ELETTRA HIGHLIGHTS > 02-03

2002-03

elettra


elettra

ELETTRA HIGHLIGHTS > 02-03

2002-03

ELETTRA HIGHLIGHTS 2002-2003
EDITORIAL COMMITTEE

> Massimo Altarelli
> Carlo J. Bocchetta
> Edoardo Busetto
> Kristina Djinovic Carugo
> Andrea Goldoni
> Claudia Grubissa
> Maurizio Matteucci
> Giorgio Paolucci
> Kevin C. Prince

Graphic Design:
Studio Link (www.studio-link.it)
Print:
Graphart s.n.c.

ELETTRA HIGHLIGHTS
TABLE OF CONTENTS

It is once again a pleasure to introduce this new edition of the Highlights of the ELETTRA Synchrotron Light Laboratory. It contains a selection of the most interesting results of the year between June 2002 and June 2003. During this time, the efforts to improve the source quality and to enlarge the offer of beamlines and experimental stations around the ring, produced some very visible achievements. The installation of the superconducting third harmonic cavity allowed an improvement between 70 and 100% of the beam lifetime, providing a substantially higher average current to users. At the same time, users gained full access to new beamlines, both on bending magnets (Materials Science Beamline) and on insertion devices (APE), while two other lines (XAFS, for absorption spectroscopy, and IUVS, the Inelastic Ultraviolet Scattering Beamline) collected the first data.

Results on new and old beamlines confirm the high scientific quality of the ELETTRA output. On subjects as diverse as the pathogenic agent of the SARS disease or the symmetry of the electronic states of high-Tc superconductors, our users are pushing forward the frontiers of knowledge. We are determined to keep developing the facility, in spite of the present difficult financial situation, with the completion of beamlines under construction and with major projects, such as the new Booster injector, or the FERMI@ELETTRA free electron laser in the VUV and soft x-ray region. We are as confident as ever that quality, as witnessed for example by our success in the competition for European funds, is the best guarantee of the future of the Laboratory.

I hope you will find reading these Highlights an informative and pleasant experience.

> **Massimo Altarelli**
Managing Director

RESEARCH HIGHLIGHTS

RESEARCH HIGHLIGHTS
TABLE OF CONTENTS

LIFE SCIENCES

STRUCTURAL PROPERTIES

ELECTRONIC AND MAGNETIC PROPERTIES

SURFACES AND NANOSTRUCTURES

IMAGING STUDIES

INSTRUMENTATION DEVELOPMENT

CRYSTAL STRUCTURES OF CORONAVIRUS MAIN PROTEINASES (3CL^{pro}) HELP DESIGN ANTI-SARS DRUGS

> K. Anand, R. Hilgenfeld
Institute of Biochemistry, University of Lübeck, Ratzeburger Allee 160, 23538 Lübeck, GERMANY

INTRODUCTION

Since February 2003, almost 8500 people worldwide have been diagnosed with SARS, and 914 have died of the disease. A new coronavirus has been isolated from affected tissue of SARS patients and identified as the infectious agent. So far no treatment is known for infections by this newly emerging pathogen. Although the epidemic has been contained by now, its re-emergence is very likely, and the discovery and development of anti-SARS drugs should be a high priority.

Coronaviridae are positive-strand RNA viruses that have been united with the families *Arteriviridae* and *Roniviridae* in the order *Nidovirales*. Coronavirus have the largest viral RNA genome known to date (about 30,000 bases). As much as roughly two thirds of this genome encode the replication machinery that is necessary for reproduction of the virus in infected host cells. In an initial step of this process, the viral RNA is translated into two very large polyproteins, each comprising several thousand amino acid residues. These polyproteins are subsequently cleaved into individual, functional proteins. The vast majority of these cleavages are mediated by the viral main proteinase, M^{pro} (also named 3CL^{pro}). This enzyme is itself initially a part of the polyprotein and has to be liberated from that inactive precursor by autocleavage, in a poorly understood mechanism.

Owing to its essential role in virus replication, the main proteinase is an attractive target for the design of anticoronaviral inhibitors, including anti-SARS drugs. Detailed structural knowledge of the active site and substrate specificity pockets of the

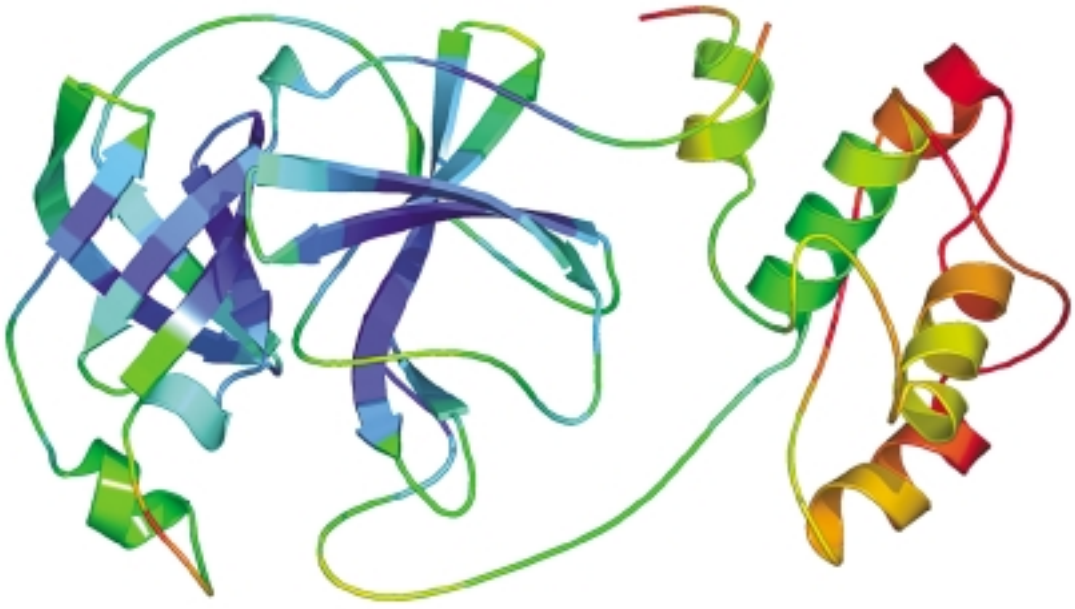

Figure 1. HCoV M^{pro} monomer coloured according to temperature factor

enzyme is the prerequisite for designing such drugs. We have determined crystal structures for the M^{pro} from human coronavirus 229 E [1] as well as from porcine coronavirus (transmissible gastroenteritis virus) [2]. Very recently, we have also solved the crystal structure of SARS coronavirus M^{pro}, in collaboration with Prof. Rao's group at Tsinghua University, Beijing, China [3].

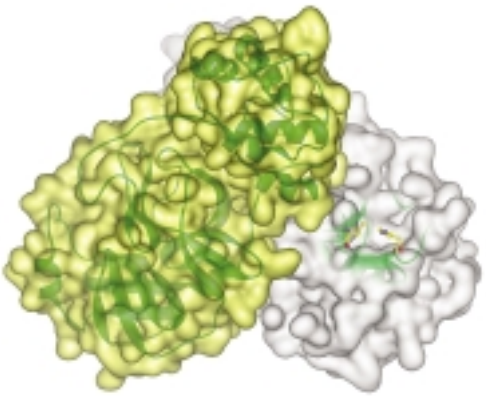

Figure 2. Dimer of SARS-CoV M^{pro}

MATERIALS AND METHODS

The use of synchrotron radiation was essential in all these studies. Diffraction data from a selenomethionine derivative were collected at four different wavelengths at the XRD beamline of ELETTRA. The structure was solved at 2.54 Å resolution and refined to an R value of 19.7%. We also collected native data from crystals of transmissible gastroenteritis virus M^{pro} at the same beamline, to 1.96 Å resolution, and solved this structure (R = 21.0 %). Other diffraction data sets were collected at DESY, Hamburg, and at the Beijing Synchrotron Radiation Facility, Beijing. For SARS-CoV M^{pro}, we determined three structures at pH values of 6.0, 7.6, and 8.0; these have resolutions between 1.9 Å and 2.4 Å, with R factors between 21.1% and 22.6%.

RESULTS AND DISCUSSION

The structures show that the coronavirus main proteinase consists of three domains, of which two distantly resemble the β-barrels of chymotrypsin while the third has a unique α-helical fold (Figure 1). Comprising a Cys-His catalytic dyad in its catalytic

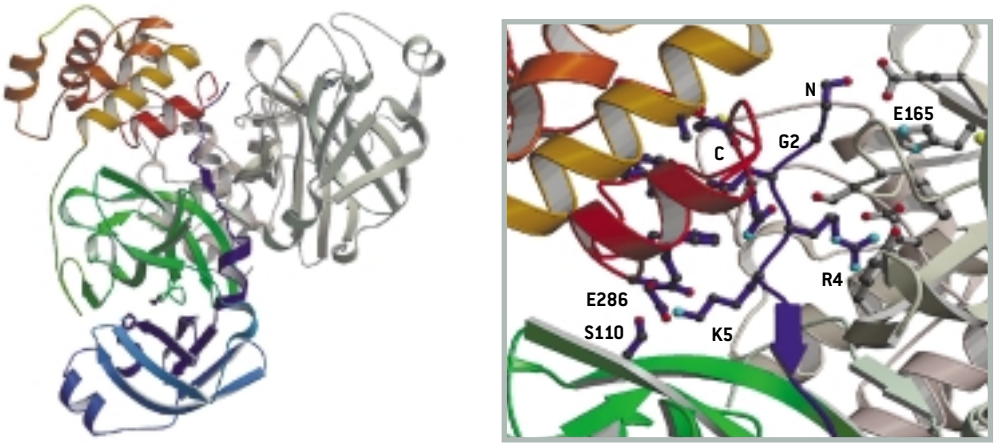

Figure 3. Left: Dimer of TGEV Mpro. One monomer is shown in colours and the other in grey. In the coloured molecule, the colour changes from blue (N-terminus and domain I) via green (domain II) to orange/red (domain III). Right: The N-terminal segment of the coloured monomer squeezes in between domains II (green) and III (orange/red) of its own molecule and domain II of the neighbouring monomer in the dimer. The very amino terminus forms a salt bridge with Glu165 of the other monomer. This glutamate residue lines the S1 substrate binding pocket of the grey monomer. Thus, the amino-terminal segment ("N-finger") is essential to hold the substrate-binding site of the other monomer in the dimer in an active conformation. Deletion of the first five amino-acid residues leads to complete inactivation of the enzyme [2].

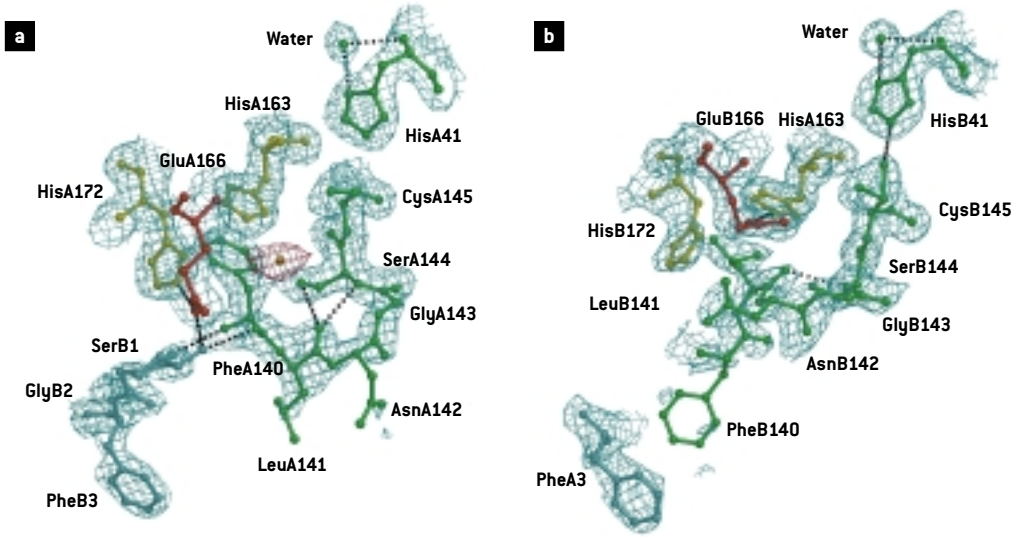

Figure 4. Molecule **a** (active site intact) and Molecule **b** (active site collapsed)

centre, the substrate-binding site is located between domains I and II. Although quite remote from the immediate substrate-binding site, the third domain is essential for proteolytic activity of the enzyme, as we found when we deleted it [2].

In the crystal as well as at higher concentrations in solution, the M^{pro} is a dimer (Figure 2). The amino terminus plays an important role in dimerization, by forming very specific contacts with domain III of its parent molecule, and domain II of the neighbouring molecule in the dimer (Figure 3). The latter interaction keeps the active site of the other domain in an active conformation. Accordingly, we observe a total loss of enzymatic activity upon deletion of the first five amino acid residues [2].

Interestingly, this delicate mode of interaction is seen to break down when SARS coronavirus M^{pro} is crystallized at lower pH (about 6.0). Under these conditions, the protonation of a histidine residue in the substrate-binding site changes, leading to a collapse of the specificity pocket and the catalytic site (Figure 4). When the same

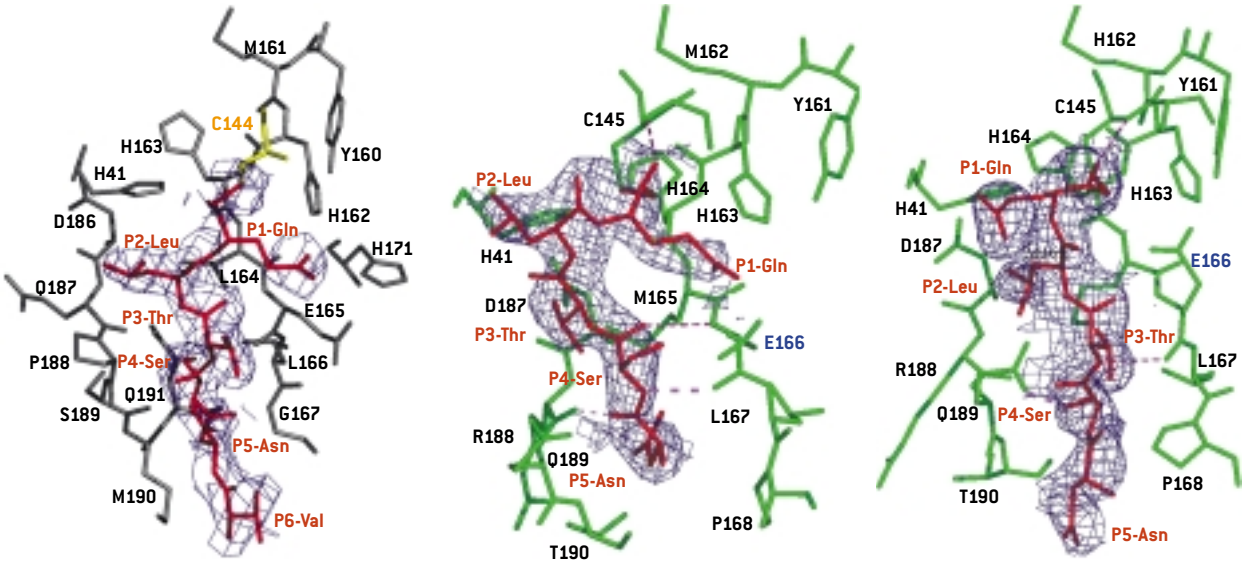

Figure 5. Porcine coronavirus M^{pro}, and molecules A and B of SARS-CoV M^{pro} in complex with the hexapeptidyl chloromethyl ketone inhibitor

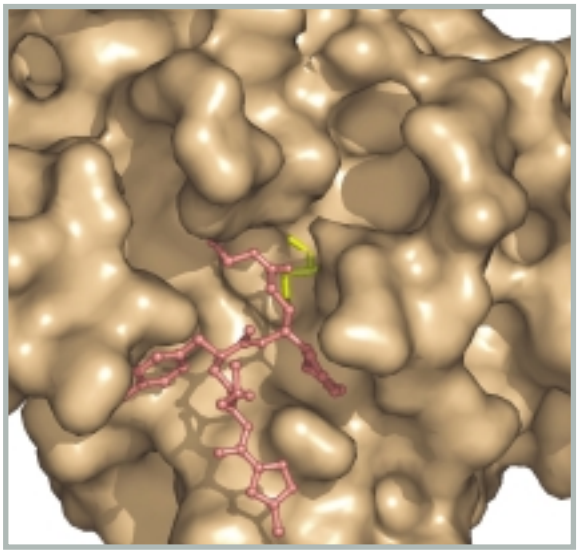

Figure 6. Compound AG7088, developed as an inhibitor for human rhinovirus 3C proteinase, fits into the active site of SARS coronavirus main proteinase.

crystals are equilibrated with a buffer of pH > 7, the molecule adopts the active conformation again. This pH-dependent switch allows us to speculate about the conformation of the enzyme in the inactive polyprotein precursor.

We have also determined structures of inhibitor complexes of porcine and SARS coronavirus main proteinases that provide a useful basis for anti-SARS drug design [1,3]. We synthesized a hexapeptidyl chloromethyl ketone inhibitor the amino acid sequence of which was derived from one of the cleavage sites of the M^{pro} in the polyprotein. These crystal structures, determined at 2.4-2.5 Å resolution (R values of 19.1% and 21.6%), provide us with a detailed picture of the interaction between the polyprotein substrate and the enzyme (Figure 5). On the basis of this template, we searched the Protein Data Bank for inhibitor complexes of cysteine proteinases and found, much to our surprise, one example where the inhibitor displays a binding mode very similiar to our hexapeptidyl chloromethyl ketone, although the target enzyme, human rhinovirus 3C proteinase, is quite different from the coronavirus main proteinase. We then modelled this inhibitor, AG7088, into the active site of the M^{pro} and found a reasonable fit (Figure 6). Our proposal that this compound, which is in clinical trials for the treatment of the common cold, could be a good starting point for the design of anti-SARS drugs [1], was corroborated shortly after we had published it. AG7088 is now being modified in several industrial laboratories in order to improve its efficiency in inhibiting the SARS coronavirus main proteinase.

References

[1] K. Anand, J. Ziebuhr, P. Wadhwani, J. R. Mesters, and R. Hilgenfeld; *Science;* 300, 1763-1767, (2003).

[2] K. Anand, G. Palm, J. R. Mesters, J. Ziebuhr, and R. Hilgenfeld; *EMBO J.;* 21, 3213-3224, (2002).

[3] H. Yang, M. Yang, Y. Ding, Y. Liu, Z. Lou, L. Sei, Z. Zhou, S. Ye, H. Pang, G. G. Gao, K. Anand, M. Bartlam, R. Hilgenfeld, and Z. Rao; *Proc. Natl. Acad. Sci.; USA* 101, in press (2003).

THE CRYSTAL STRUCTURE OF PGIP (POLYGALACTURONASE INHIBITING PROTEIN), A LEUCINE-RICH REPEAT PROTEIN INVOLVED IN PLANT DEFENCE

> A. Di Matteo, L. Federici, K.A. Johnson, C. Savino, D. Tsernoglou
Department of Biochemical Sciences, University of Rome "La Sapienza" and CNR Institute for Molecular Biology and Pathology, Rome, ITALY

> B. Mattei, G. Salvi, G. De Lorenzo, F. Cervone
Department of Plant Biology, University of Rome "La Sapienza", Rome, ITALY

INTRODUCTION

Plants have evolved successful defence mechanisms against the attack of a wide range of pathogenic microorganisms. As they lack a circulatory system of antibodies, their defence relies on the capability of each cell to recognize the presence of pathogens and subsequently activate defence responses. Many of the recognition events occur in the plant cell wall, which is the first barrier to come into contact with the invading organisms. The majority of microorganisms need to breach this barrier to gain access to the plant tissue and produce enzymes that degrade the cell wall polymers [1]. Among the cell wall degrading enzymes produced by phytopathogenic fungi, an important role is played by the endopolygalacturonases (EC 3.2.1.15) that cleave the linkages between D-galacturonic acid residues in non-methylated homogalacturonan, a major component of pectin. Polygalacturonases (PGs) are among the first enzymes secreted by phytopathogenic fungi and their action on the outer component of the cell wall is a prerequisite for further wall degradation by other degrading enzymes [2].

Polygalacturonase-inhibiting proteins (PGIPs) are extracellular plant proteins, ionically bound to the plant cell wall which limit the fungal invasion by counteracting PG activity [2]. Their inhibitory activity favours the accumulation of fragments of homogalacturonan (i.e. oligogalacturonides), which act as elicitors of plant defence responses [3]. Plants have evolved PGIPs with different recognition capabilities against the many PGs secreted by pathogenic fungi. Moreover the expression of various PGIPs is regulated and is induced by different stress-related molecules through separate transduction pathways [4].

PGIPs are members of the leucine-rich repeat (LRR) protein family, a class of proteins specialized in protein-protein interaction. Plants have selected the LRR fold for their "immune" functions and recognition of non-self molecules [5]. Several plant resistance gene products or defence related receptors display LRR motifs of the extracytoplasmic type homologous to that of PGIP [6]. Up to date there is no structural information available on plant LRR proteins and, given the peculiarity of this repeat, any attempt of modelling based on the structure of LRR proteins of different subfamilies (animals and microbes), was unsatisfactory.

The crystal structure of PG from the phytopatogenic fungus *Fusarium moniliforme* (*Fm*PG) has been previously determined by our group at 1.7Å resolution [7]. Now we have solved the crystal structure of the isoform 2 of PGIP (PGIP2) from *Phaseolus vulgaris* (common bean) at 1.7Å (Figure 1). This is the first structure of a plant LRR protein and represents a model for studying the structural organization and the mode of interaction of other plants LRR proteins. The structure also provides a molecular basis for understanding how PGIP inhibits polygalacturonases.

MATERIALS AND METHODS

PGIP2 from *Phaseolus vulgari,* was overexpressed in *Nicotiana benthamiana* plants infected with PVX virus purified and concentrated [8]. PGIP2 crystallized in two crystal forms (A and B), both belonging to the $P2_12_12$ space group but with different unit cell dimensions. Form A (Native2 in Table 1) had cell dimensions: a=139.59 Å, b=65.64 Å, c=37.23 Å and diffracted to 2.5 Å resolution. Form B (Native1 in Table 1) diffracted better (up to 1.7Å resolution) and showed the following cell dimensions: a=134.84 Å, b=65.45 Å, c=34.64 Å. Data for crystal form B to 1.7 Å resolution were collected at the XRD1 beamline at ELETTRA. Data for crystal form A to 2.5 Å resolution were collected at BW7A beamline of the DESY Synchrotron (Hamburg, Germany). Reflection intensities were integrated and scaled using DENZO/SCALEPACK. Different heavy atoms derivatives were tested using synchrotron radiation at ELETTRA. Phases were determined by single isomorphous replacement and anomalous scattering (SIRAS) method. A suitable heavy atom derivative was obtained soaking a crystal in a solution containing 1 mM K_2OsO_4 for 6 hours and data were collected at DESY Synchrotron.

Heavy metal Patterson search with the derivatized and native crystals of the form A was performed using the program SOLVE and 3 peaks were found leading to an overall figure of merit of 0.45 in the 25-2.5 Å shell. Density modification was carried out with RESOLVE, yielding a figure of merit of 0.65 at 2.5 Å resolution. The resulting electron density map was sufficiently connected to allow us building a partial model out of two thirds of the residues and to fit most of side chains using the program QUANTA. This partial model was then used to solve the structure at 1.7 Å with native data from the form B by molecular replacement using AmoRe.

Refinement was carried out with REFMAC and water residues were added into the Fo-Fc density map, contoured at 4σ, with the X-SOLVATE tool of QUANTA. Several cycles of refinement, manual rebuilding and addition of solvent molecules, led to a crystallographic R factor of 0.194 and a free R factor of 0.244 for a complete model of PGIP2 consisting of 313 residues (1-313), 323 water molecules, four N-acetyl glucosamine residues (one linked at the a Asn35, two at Asn112 and another one to Asn274).

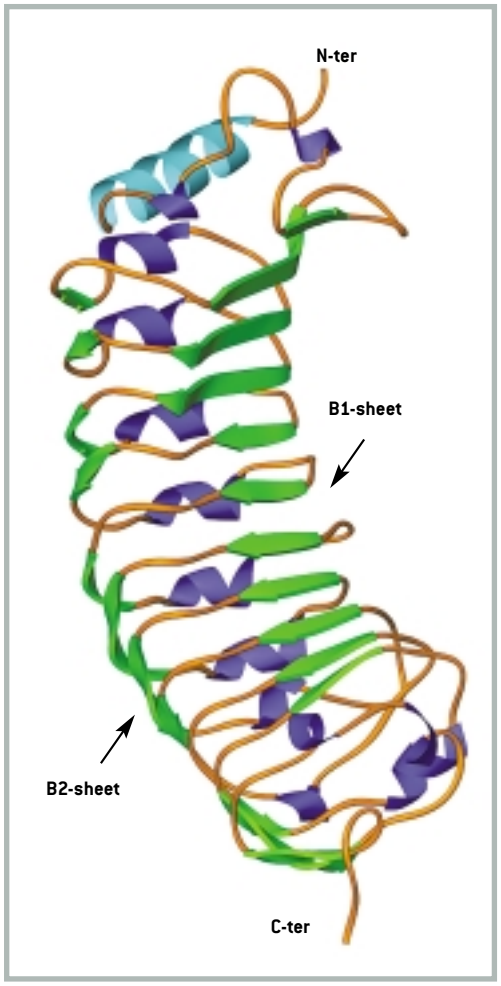

Figure 1. Ribbon representation of the structure of PGIP2. Sheets B1 and B2 are colored in green. Helices are colored in blue (light blue for the N-terminal α-helix and dark blue for helices 3_{10} in the LRR central portion of the molecule)

RESULTS AND DISCUSSION

PGIP2 structure displays the typical LRR curved and elongated shape, described for the porcine ribonuclease inhibitor [9]. The central LRR domain, folded in a right-handed superhelix consists of a set of ten tandemly repeating units, each made by 24 residues matching the extracytoplasmatic LRR plant specific consensus sequence LxxLxx**LxxLxLxx**NxLt/sGxIPxx. A long parallel β-sheet (B1) occupies the concave inner side of the structure and is conserved among all LRR subfamilies. On the opposite side of the protein, nine 3_{10}-helices are almost parallel to the sheet B1. An additional extended parallel β-sheet (B2) charac-

terizes the fold of PGIP2. This is absent in the majority of other LRR proteins, in which helices and β-sheet B1 are connected simply by loops or β-turns .The central LRR domain of PGIP2 is flanked by two small cysteine-rich domains at the N-terminal and C-terminal sides which contribute to cap the hydrophobic core of the protein (Figure 1).

PGIP2 inhibits fungal PGs through the formation of bimolecular complexes and the residues of PGIP2 critical for its affinity and recognition capability are located in the sheet B1 [7]. In a recent study, we have observed that the interaction between the *Fm*PG and PGIP2 is mediated by at least two positively charged residues of the enzyme (Arg267 and Lys269), which are located at the edge of its active site and are involved in substrate binding. The involvement of these two residues in the interaction with PGIP2 provides an explanation for the competitive inhibition observed [7].

Examination of the electrostatic potential surface of PGIP2 reveals a negative pocket, formed by the charged residues Asp131, Asp157, Asp203, located approximately in the centre of the sheet B1 where the residues determining the affinity and specificity of PGIP2 are known to reside [10] (Figure 2). Interestingly the three aspartic residues are highly conserved in all PGIPs. The pocket is sufficiently large and deep to accommodate the positively charged residues Arg267 and Lys269 on the surface of the enzyme and may completely cover its active site thus preventing access to the substrate. The residue Gln224 of PGIP2, which has been demonstrated to be involved in the specificity of the inhibitor towards *Fm*PG, is located in the sheet B1, immediately above the negative pocket putatively involved in PG binding (Figure 2). We hypothesize that this residue may interact with an unidentified partner residue of *Fm*PG to correctly lock Arg267 and Lys269 into the negative pocket.

The structures of FmPG and PGIP2 revealed useful to drive site-directed mutagenesis and provided a solid framework to interpret the available functional data. Moreover we expect that the structure of PGIP2 will be useful for understanding the mode of interaction of PGIPs, as well as for designing better inhibitors with tailor-made specificities.

ACKNOWLEDGMENTS

We thank Maurizio Brunori for his encouragement and valuable advice. This research was supported by the European Communi-

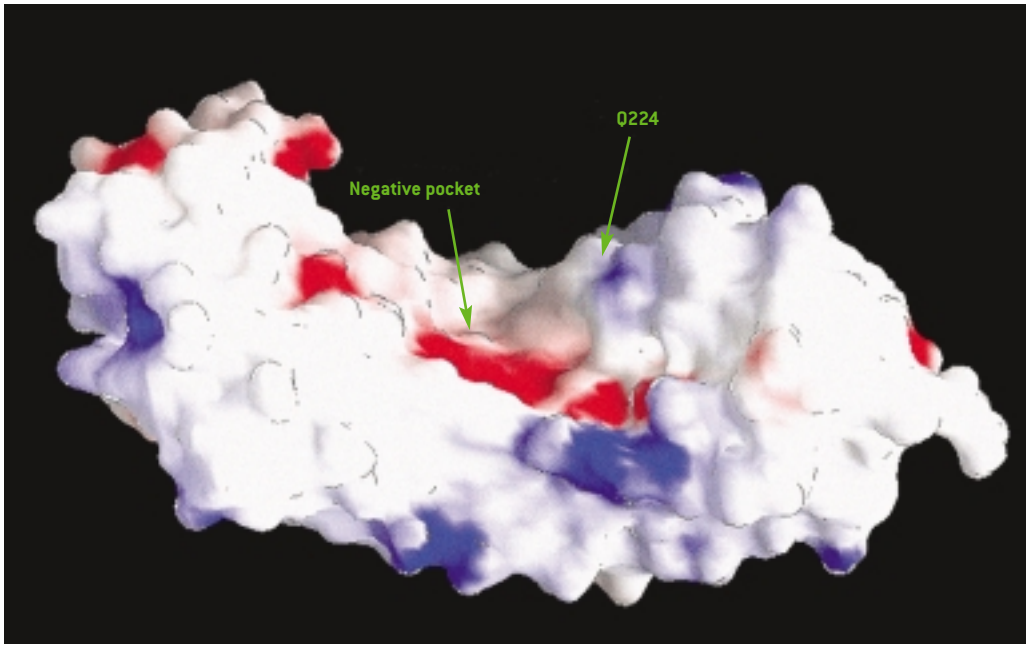

Figure 2. Electrostatic potential surface representation of PGIP2. Regions of negative and positive potential are shown in red and blue, respectively. A wide negative pocket, putatively involved in polygalacturonase recognition, is located in the middle of the inner concave surface of the protein. The residue Gln224, crucial for PGIP2 specificity, is also indicated.

Data collection	Nativ1	Nativ2	K_2Os_4
Space group	$P2_12_12$	$P2_12_12$	$P2_12_12$
Unit cell dimensions	a=134.86 b=65.45 c=34.64	a= 139.59 b=65.64 c= 37.23	a= 139.72 b=65.81 c=37.47
Wavelength (Å)	0.95	0.9537	0.8431
Resolution limits (Å)	30.0-1.7	25.0-2.5	25.0-2.5
Reflections			
Total (N)	330460	656453	367444
Unique (N)	35377	25439	12694
Completeness (last shell)	93.2 (65.5)	87.1 (86.0)	93.1 (86.7)
Average I/σ (last shell)	11.4	15.3	13.4
R_{merge} (%)	0.064 (0.45)	0.080 (0.312)	0.125 (0.317)
Derivative			
Concentration (mM)			1
Soaking time (hours)			6
FOM (before DM)			0.45
FOM (after DM)			0.65
Refinement statistic			
Resolution (Å)		25.0-1.7	
R_{work} (%)		0.194	
R_{free} (%)		0.244	

$R_{sym} = S_{hkl}\Omega|I> - I/(S_{hkl}I)|\Omega$. $R_{cryst} = S_{hkl}\ \Omega F_o(hkl) - F_c(hkl)\ \Omega/S_{hkl}\ F_o(hkl)$. R_{free} is R_{cryst} for 5% of the reflections excluded from the refinement.

Table 1. Data collection, phasing and refinement parameters.

ty Grant QLK3-CT99-089, the Institute Pasteur Fondazione Cenci Bolognetti, and the Armenise-Harvard Foundation. We also acknowledge the valuable help of the staff of the XRD1 beamline of ELETTRA.

References

[1] F. Cervone, M.G. Hahn, G. De Lorenzo, A. Darvill, P. Albersheim; *Plant Physiol.;* 90, 542, (1989).

[2] G. De Lorenzo, R. D'Ovidio, F. Cervone; *Annu. Rev. Phytopathol.;* 39, 313, (2001).

[3] B.L. Ridley, M.A. O'Neill, D. Mohnen; *Phytochem.*; 57, 929, (200,1).

[4] S. Ferrari, D. Vairo, F. M. Ausubel, F. Cervone, G. De Lorenzo; *Plant Cell.*; 15, 93, (2003).

[5] J.L. Dangl, J.D. Jones; *Nature;* June 14, 411(6839), 826, (2001).

[6] A.V. Kajava; *J. Mol. Biol.*; 277, 519, (1998).

[7] L. Federici, C. Caprari, B. Mattei, C. Savino, A. Di Matteo, G. De Lorenzo, F. Cervone, D. Tsernoglou; *Proc. Natl. Acad. Sci. U. S. A;* 98, 13425, (2001).

[8] A. Di Matteo, L. Federici, B. Mattei, G. Salvi, K. A. Johnson, C. Savino, G. De Lorenzo, D. Tsernoglou, and F. Cervone; *PNAS;* 100, 10124, (2003).

[9] B. Kobe, J. Deisenhofer; *Nature*; 366, 751, (1993).

[10] B. Mattei, M.S. Bernalda, L. Federici, P. Roepstorff, F. Cervone, A. Boffi; *Biochemistry;* 40, 569, (2001).

REVISED CRYSTAL ANALYSIS OF NOVEL RNA MOLECULES FOR MOLECULAR MEDICINE

> M. Vallazza, V. A. Erdmann
Freie Universität Berlin, FB Biologie, Chemie, Pharmazie, Institut für Chemie, Thielallee 63, D-14195 Berlin, GERMANY

> S. Klussmann
NOXXON Pharma AG, Max-Dohrn-Strasse 8-10, D-10589 Berlin, GERMANY

> M. Perbandt, C. Betzel
Universitätsklinikum Hamburg-Eppendorf, Institut für Biochemie und Molekularbiologie I, c/o DESY, Notkestrasse 85, D-22603 Hamburg, GERMANY

INTRODUCTION

The diverse functions of ribonucleic acids as information carrier (mRNA), adapter (tRNA), scaffold and catalyst (rRNA) reflect the key position within the living cell and their essential significance for life itself. Previously discovered catalytic properties of ribozymes (molecular scissors), the highly specific binding capability of aptamers (which is comparable with antibodies) as well as small RNAs, termed RNAi and regulators, make possible new applications in biotechnology and molecular medicine [1]. The inherent structural and functional potentials of these molecules are employed in the fast evolving area of RNA technologies causing a great need for folding motifs to design functional RNAs [2]. So far, only 400 ribonucleic acids have been crystallized and structurally investigated (Figure 1). On the contrary, 1.300 DNA and nearly 22.000 protein structures have been characterized by X-ray diffraction and NMR spectroscopy (referring to the nucleic acid data bank (NDB) and the protein data bank (PDB)). We are currently contributing to the RNA technologies by crystal analysis of novel RNA classes like Spiegelmers, racemates and small interfering RNAs (siRNA).

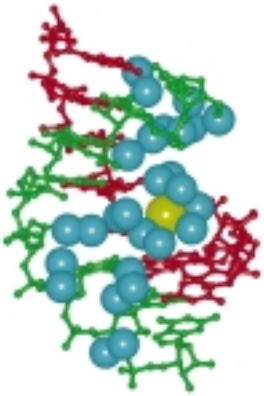

Figure 1. Helical RNA structure [10] stabilized by water molecules (blue) and a Ba^{2+} ion (yellow).

Nucleic acid molecules in the mirror-image or L-configuration do not exist in nature and therefore display an extremely high biostability. Empirically developed in our laboratory [3,4], the identification of functional L-oligonucleotides (so called Spiegelmers) represents a novel approach of RNA based drug discovery. In the first step, a D-RNA aptamer is selected against the unnatural enantiomeric form of a target by the SELEX procedure. In the second step, the mirror-image RNA which specifically recognizes the natural target is chemically synthesized. In comparison, other post-SELEX modifications (like phosphorothioates or locked nucleic acids) often change the biological activity [5,6]. Furthermore, Spiegelmers do not cause an immunogenic response [7].

Due to the relevance of both enantiomeric forms of high-affinity RNA molecules (termed aptamers and Spiegelmers), the simultaneous crystallization of a racemate might accelerate the structure solution. In accordance with Wallach's rule, racemic crystals tend to be about 1 % more tightly packed than their chiral counterparts. Additionally, the potential crystallization in centrosymmetric space groups greatly facilitates use of direct methods for solution of the phase problem: since the centrosymmetric arrangement possesses inverse symmetry elements, only the two alternatives 0° and 180° for the phase of each reflection need to be considered [8].

Finally, we are going to approach the phenomenon of RNA interference (RNAi) by crystallizing parts of the RNA-induced silencing complex (RISC). RNAi is a response to dsRNA which triggers the sequence specific gene silencing. It has been cultivated as means to manipulate gene expression experimentally and to probe gene function on a whole-genome scale [9].

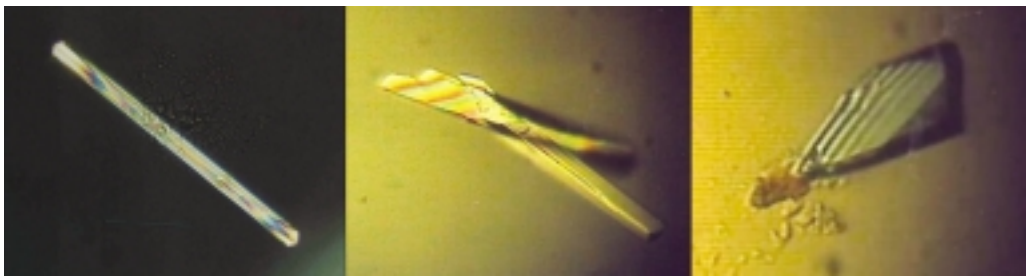

MATERIALS AND METHODS

The *Thermus flavus* 5S rRNA helix E was synthesized, pre-incubated, crystallized and structurally characterized as previously described [10]. Spiegelmers were produced with the phosphoramidite chemistry as well, purified by ion-exchange HPLC and analyzed by applying the same specific extinctional coefficients $e_{E3\text{-}79}$ = 62167 $l*mol^{-1}*cm^{-1}$ and $e_{E3\text{-}90}$ = 60171 $l*mol^{-1}*cm^{-1}$ [7,10]. siRNAs were purchased from Qiagen-Xeragon. Crystallization set-ups were performed in the hanging drop at 18°C with commercial and self-developed screening protocols [11]. Data were collected at 100 K with synchrotron radiation of the 5.2R ELETTRA X-ray diffraction beamline. The programs DENZO, AMoRe and REFMAC were used for data processing, molecular replacement and refinement.

RESULTS AND DISCUSSION

In order to get a deeper insight into the structural features of mirror-inverted RNA motifs, the regular RNA duplex r(CUGGGCGG)•r(CCGCCUGG) was crystallized in the mirror-image configuration and in the racemic mixture for the first time. Surprisingly, the crystallization hits revealed a low similarity of less than 5 % between D-RNA and Spiegelmer, D-RNA and racemate as well as Spiegelmer and racemate. Only three conditions (1.4 %) promoted the growth of all crystal species. Furthermore, a different quality of D-, L- and D/L-crystals grown under the same condition was revealed by X-ray diffraction studies so that enantiomeric crystals of non-identical origin had to be analyzed (Figure 2).

The D-RNA helix was crystallographically translated to the left-handed L-RNA by applying the centre of inversion operator, and the crystal structure of this Spiegelmer was determined at 2.2 Å resolution. In contrast to the D-RNA, crystal packing of two L-molecules in the asymmetric unit forming pseudo-continuous infinite helices, the disappearance of a wobble-like G:C^+ base pair and a reduced hydration (1 solvent molecule per 10.4 nucleic acids atoms) were newly described for the Spiegelmer structure (Figure 3) [12]. The detailed analysis of water arrangements regarding the exclusive appearance of D-ribose in naturally occurring ribonucleic acids was delayed by the crystal quality. However, the structure analysis and refinement of the racemic mixture is these days in progress and interesting results can be expected (Table 1).

The pharmaceutical characterization of several Spiegelmers binding targets such as GnRH, Nociceptin and the α-calcitonin gene-related peptide (αCGRP) gave rise to the expansion of crystallization experiments [5]. For example, the neuropeptide αCGRP is a potent endogenous vasodilator thought to be implicated in the genesis of migraine attacks [13]. Intercepting αCGRP by means of a Spiegelmer could treat them. The first complex crystals displayed an unusual, but non-interpretable diffraction pattern (Figure 4).

Last, the successful crystallization of small interference RNAs is presented. Crystals of a pain suppressing siRNA directed against the mRNA of the vanilloid receptor subtype I (VR1) [6] diffracted to 1.2 Å, whereas the crystals of a second siRNA targeting the prolyl hydroxylase (PHD) mRNA achieved 4.0 Å (Figure 5). The use of RNAi to control the expression of PHD provides an effective tool for the characterization of angiogenic pathways involved in

Figure 2. The different crystal morphology of D-RNA (left), Spiegelmer (middle) and racemate (right) is caused by different crystallization conditions. The D-RNA crystal was grown to a size of 0.05 x 0.05 x 0.8 mm by equilibrating 0.125 D-RNA, 40 mM Na-cacodylate (pH 6.0), 80 mM KCl, 20 mM $BaCl_2$, 12 mM $SpCl_4$ and 5 % (v/v) MPD against 30 % (v/v) MPD reservoir solution. A rod-shaped crystal (0.07 x 0.07 x 0.67 mm) - obtained by incubating a drop of 0.125 mM L-RNA, 0.05 M Na-HEPES (pH 7.5), 1 % (v/v) PEG 400 and 1 M $(NH_4)_2SO_4$ against a reservoir having the twice concentration - was cryo-protected by 15 % (v/v) glycerol in 0.085 M Na-HEPES (pH 7.5), 1.7 % (v/v) PEG 400, 1.7 M $(NH_4)_2SO_4$ and used for X-ray structure analysis. Crystals of racemic RNA were grown to dimensions of 0.2 x 0.2 x 0.5 mm from 0.125 mM D/L-RNA, 0.05 M MES (pH 6.5), 5 mM $CoCl_2$ and 0.9 M $(NH_4)_2SO_4$ and cryo-protected by 20 % (v/v) glycerol in 0.1 M MES (pH 6.5), 10 mM $CoCl_2$ and 1.8 M $(NH_4)_2SO_4$.

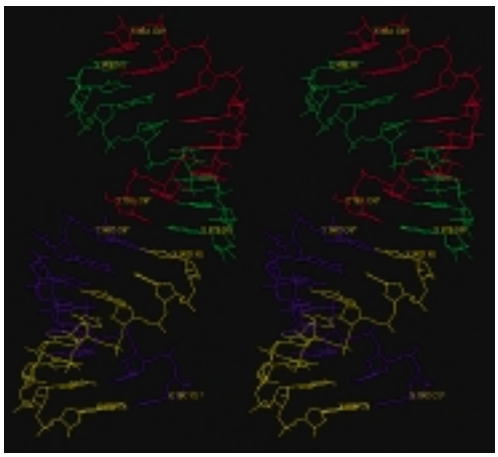

Figure 3. The Spiegelmer molecules A and B of the asymmetric unit are interacting in the head-to-tail fashion.

cancer development and the understanding of the regulation mechanisms of HIF (hypoxia-inducible factor) hydroxylases [14].

CONCLUSIONS

Emerging applications of mirror-image oligonucleotides led us to structural investigations of this novel RNA class. Although enantiomers should expose identical chemical and physical features in accordance to van't Hoff's postulate based on symmetry, the crystallization process required different conditions for well-diffracting enantiomeric crystals. Similar, but not identical conditions were also observed while crystallizing the mirror-image protein D-monellin [15]. Consequently, the diverse solutions exerted an important influence on the crystal structure, therefore being responsible for some features that distinguish Spiegelmer from the D-RNA structure. As hypothesis, the different crystallization behaviour might be explained by the parity violating energy difference of ribose enantiomers which theoretically amounts to 10^{-14} J/mol in favor of the D-RNA [16]. This fact proposed by the electroweak quantum chemistry allows two possible conclusions: firstly, the L-RNA made of antimatter (not that made of matter) actually represents the isoenergetic mirror-image of the natural occurring (matter) D-RNA, causing a deviation in the physical behaviour between matter enantiomers. The clear difference during phase transition from the liquid to the solid state could serve as an indication that the parity violating effects are enlarged. Secondly, the gradient of the free energy to be minimized as the thermodynamic requirement of the crystallization process is increased to a slightly higher level due to the higher Gibbs energy of the Spiegelmer. That fact might change the crystallization.

The significance of solvent molecules within the tertiary RNA structure could be pointed out. It is supposed that a chiral water network represents another parameter influencing the structure formation of enantiomers and their crystal packing [15].

To sum up, mirror-image structures are

Table 1. Crystal data and refinement statistics.

	D-RNA	Spiegelmer	Racemate
Space group	R32	R32	P2
Cell parameters (Å)			
a =	41.9	45.7	41.9
b =	41.9	45.7	51.51
c =	127.1	264.6	46.94
β =	90°	90°	116.07
Mathews Coefficient	2.2	2.7	
Solvent content [%]	37.5	48.9	29.3
Mosaicity	1.1°	3.2°	1.2
Resolution range [Å]	20-1.6	20-2.2	25-2.1
No. of unique reflections	5994	6321	11330
Rsymm (final shell)	0.066 (0.291)	0.096 (0.401)	0.074 (0.513)
Completeness (%)	96.1	99.2	95.7
R-factor (R_{free})	0.183 (0.241)	0.232 (0.267)	0.238
Number of atoms			
Nucleic acid atoms	338	676	
Water oxygen atoms	80	65	

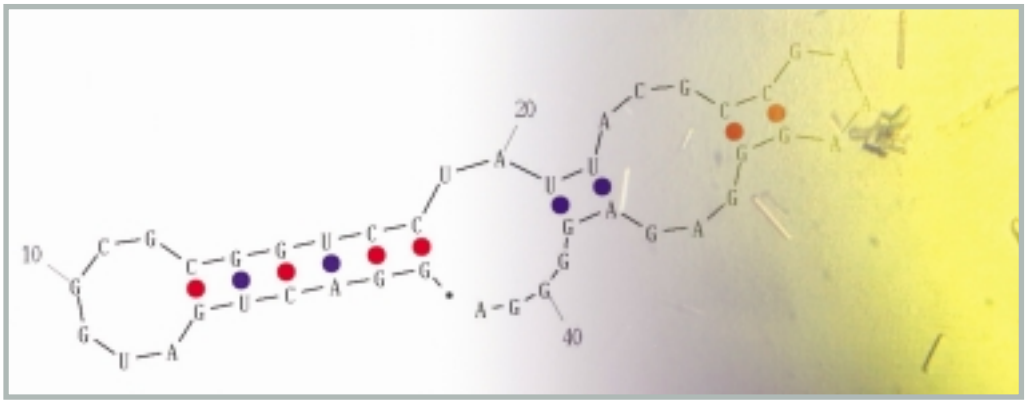

Figure 4. Secondary structure of the anti-αCGRP Spiegelmer and crystals of the L-RNA/L-peptide complex.

considered as a key to explain the genesis of biomolecular homochirality which is the requirement for the storage, distribution and utilization of genetic information. Furthermore, the characterization of folding motifs (like the G:C$^+$ bp) and the definition of structural elements involved in target interactions (like the G:U bp) include the essential knowledge to be applied for the optimization of these high-affinity binding molecules.

ACKNOWLEDGMENTS

The opportunity for crystal analysis at the 5.2R X-ray diffraction beamline of ELETTRA is gratefully acknowledged. This work was partly supported by grants from the Deutsche Luft- und Raumfahrtagentur (DLR) and the National Foundation for Cancer Research (NFCR).

References

[1] B.A. Sullenger and E. Gilboa; *Nature*; 418, 252, (2002).

[2] V.A. Erdmann and J.P. Fuerste; *Euro-biotech*; 2000, 104, (1999).

[3] S. Klussmann, A. Nolte, R. Bald, V.A. Erdmann and J.P. Fuerste; *Nature Biotechnology*; 14, 1112, (1996).

[4] A. Nolte, S. Klussmann, R. Bald, V.A. Erdmann and J.P. Fuerste; *Nature Biotechnology*; 14, 1116, (1996).

[5] A. Vater and S. Klussmann; *Curr. Opin. Drug Discov. Devel.*; 6, 253, (2003).

[6] A. Gruenweller, E. Wyszko, B. Bieber, R. Jahnel, V.A. Erdmann and J. Kurreck; *Nucl. Acids Res.*; 31, 3185, (2003).

[7] B. Wlotzka, S. Leva, B. Eschgfaeller, J. Burmeister, F. Kleinjung, C. Kaduk, P. Muhn, H. Hess-Stump and S. Klussmann; *PNAS*; 99, 8898, (2002).

[8] C.P. Brock, W.B. Schweizer and J.D. Dunitz; *J. Am. Chem. Soc.*; 113, 9811, (1991).

[9] G.J. Hannon; *Nature*; 418, 244, (2002).

[10] M. Perbandt, M. Vallazza, C. Lippmann, C. Betzel and V.A. Erdmann; *Acta Cryst. D;* 57, 219 (2001).

[11] M. Vallazza, S. Banumathi, M. Perbandt, K. Moore, L. DeLucas, C. Betzel and V.A. Erdmann; *Acta Cryst. D;* 58, 1700, (2002).

[12] M. Vallazza, M. Perbandt, S. Klussmann, C. Betzel and V.A. Erdmann; *Submitted to Acta Cryst. D;* (2003).

[13] J.M.L. Hakala and M. Vihinen; *Protein Engineering*; 7, 1069, (1994).

[14] C.W. Pugh and P. J. Ratcliffe; *Nature Medicine*; 9, 677, (2003).

[15] L.W. Hung, M. Kohmura, Y. Ariyoshi and S.H. Kim; *Acta Cryst. D;* 54, 494, (1998).

[16] G.E. Tranter; *Chem. Phys. Lett.*; 135, 279, (1987).

Figure 5. Crystals of siRNAs directed against the VR1 mRNA (left) and the PHD mRNA (right).

CRYSTAL STRUCTURE OF NICKEL-CONTAINING SUPEROXIDE DISMUTASE

> J. Wuerges*

International School For Advanced Studies, Via Beirut 2-4, 34014 Trieste, ITALY
Structural Biology Laboratory, Sincrotrone Trieste-ELETTRA - S.S. 14 km 163,5, in AREA Science Park , 34012 Basovizza, Trieste, ITALY

> J. Lee*, Y. Yim, S. Kang

Laboratory of Biophysics, School of Biological Sciences, Seoul National University, Seoul 151-742, Republic of KOREA
Institute of Microbiology, Seoul National University, Seoul 151-742, Republic of KOREA

> H. Yim

Institute of Microbiology, Seoul National University, Seoul 151-742, Republic of KOREA

> K. Djinovic Carugo

Structural Biology Laboratory, Sincrotrone Trieste-ELETTRA - S.S. 14 km 163,5, in AREA Science Park, 34012 Basovizza, Trieste, ITALY

* These authors contributed equally to this work

INTRODUCTION

Oxygen metabolizing organisms have to face the toxicity of superoxide radicals [1] (O_2^-) which are generated by a single electron transfer to dioxygen. Superoxide dismutases (SOD) are dedicated to keep the concentration of O_2^- in controlled low limits thus protecting biological molecules from oxidative damage. Superoxide dismutases are almost ubiquitous metallo-enzymes which dismute the superoxide radical anion (O_2^-) to molecular oxygen (O_2) and peroxide (H_2O_2). Until recently three metal species have been found [2,3] ; copper- and zinc-containing SOD (Cu,ZnSOD), with copper as the catalytically active metal, manganese-containing SOD (MnSOD), and iron-containing SOD (FeSOD). Recently, a new superoxide dismutase containing nickel, NiSOD, was purified from several *Streptomyces* species [4,6] (aerobic soil bacteria). The dissimilarity of NiSOD to known SODs was indicated by the lack of sequence homology as well as by immunological and spectroscopic properties [4,5,7,8,9]. The catalytic activity of NiSOD [7], however, is on the same high level as that of Cu,ZnSOD at about $10^9 M^{-1}s^{-1}$ per metal centre.

Here we present the crystal structure of NiSOD from *Streptomyces seoulensis* [10] which was solved by the multiple-wavelength anomalous dispersion (MAD) method and refined to the resolution of 1.68 Å for a crystal form with one enzyme molecule per asymmetric unit ('small cell') and to 1.6 Å resolution for a crystal form containing two NiSOD molecules in the asymmetric unit ('big cell').

Table 1. Three NiSOD crystal forms.

Crystal form	Form I	Form II	Form III
Space group	$P2_12_12_1$	R3	$P2_12_12_1$
Cell dimensions, Å	112.3 113.8 128.6	189.4 189.4 159.9	65.2 119.3 121.0
No. molecules/ a.u.$	12	18	6
Matthews Volume$	V_M= 2.6 Å^3 Da^{-1}	V_M= 2.3 Å^3 Da^{-1}	V_M= 3.0 Å^3 Da^{-1}
Solvent content$, %	51	46	57

$ Using the molecular mass of NiSOD of 13.2 kDa and a molecular density value of 1.3 g cm^{-3} to estimate the solvent content of the crystal form.

MAD data set§	Wavelength, Å	Resolution range, Å	Completeness¶, %	R_{anom}†, %	$\langle I / \sigma(I) \rangle$¶	$R_{sym}$$¶, %	Redundancy
Form I		31.1 – 2.2					
Pk	1.4827		99.7 (99.7)	4.2	11.9 (3.3)	5.6 (18.7)	4.7
Pi	1.4859		99.5 (99.5)	4.1	11.3 (3.4)	6.2 (22.4)	4.6
Re	1.2398		99.8 (98.7)	3.3	13.3 (5.5)	4.8 (13.6)	4.6
Form III		44.0 – 2.0					
Pk	1.4863		98.6 (98.6)	3.2	9.3 (2.2)	5.2 (21.7)	6.3
Pi	1.4756		98.5 (97.0)	2.9	6.7 (1.9)	6.2 (27.5)	6.3
Re	0.9392		99.2 (98.5)	2.4	6.3 (2.8)	7.5 (20.9)	8.0

High resolution data sets	X-ray source	Resolution range, Å	Completeness‡, %	$\langle I / \sigma(I) \rangle$¶	$R_{sym}$$‡, %	Redundancy
Form I	ESRF, ID14-2	42.6 – 1.6	98.9 (97.6)	13 (2.8)	8.0 (26.0)	3.7
Form III	ELETTRA XRD1	34.3 – 1.68	99.1 (96.0)	11 (2.1)	4.3 (27.6)	6.6

§ Pk = peak energy, Pi = inflection point, Re = remote energy data. ¶ Values in parentheses are for the outer resolution shell: 2.32 - 2.2 Å (form I), 2.11 – 2.0 Å (form III).
† $R_{anom} = \Sigma_{hkl} | I_+ - I_- | / \Sigma_{hkl} | I_+ + I_- |$. $ $R_{sym} = \Sigma_{hkl} \Sigma_i | I_i - \langle I \rangle | / \Sigma_{hkl} \Sigma_i | I_i |$. ‡ Values in parentheses are for the outer resolution shell: 1.69 – 1.6 Å (form I), 1.76 – 1.68 Å (form III).

Table 2. Processing and reduction statistics of MAD data sets for crystal forms I and III. Below, statistics of data to higher resolution than for the corresponding MAD data.

MATERIALS AND METHODS

Crystallization trials were carried out by the hanging-drop vapour-diffusion method at 4°C and 20°C. Initial screens utilized premixed conditions (Crystal Screen I and II, Hampton Research) which were subsequently refined to improve crystal growth. NiSOD crystallizes in more than one form and, only those crystal forms are described which exhibited a quality suitable for collection of complete X-ray data sets to higher resolution than 5 Å. In all these cases, 1 µl of protein solution was mixed with an equal amount of crystallization reagent and the 24 well plates (purchased from Hampton Research) were stored at 20°C.

Crystal form I. The first crystals of NiSOD grew readily from a premixed crystallization reagent consisting of 2 *M* ammonium sulphate and 5% isopropanol (Crystal Screen II, Hampton Research). The small amount of isopropanol proved to be necessary for crystal growth. The pH of this condition is 5.25. Plate-like crystals with approximate dimensions of 0.21 x 0.21 x 0.05 mm^3 appeared after 1-2 weeks.

Crystal form II. Needle-shaped crystals were obtained after 8-10 days from 1.85 *M* ammonium sulphate and 0.1 *M* sodium acetate, pH 5.25, showing an approximate length of 0.3 mm and diameter of 0.03 mm (Figure 1*b*). Macroseeding these needle crystals to crystallization drops containing 1 µl of 1.78 *M* ammonium sulphate, 0.1 *M* sodium acetate and 1 µl fresh protein solution was tried to increase the crystal size. No significant crystal growth could be observed, but instead a new crystal form III appeared after 5-6 weeks in the macroseeding drops, showing a different morphology and space group. A small improvement in needle diameter to 0.04 mm was obtained by adding a thin layer of oil mixture (silicon and paraffin oil purchased from Hampton Research, in 1:1 or 2:3 ratio) of 0.2-0.3 ml volume on top of the reservoir.

Crystal form III. Rod like crystals with typical dimensions of approximately 0.5 x 0.2 x 0.2 mm^3 were first obtained as by-product of macroseeding form II crystals as described above. This way of growing form III crystals was reproducible, but more convenient growth conditions were found to be 1.85 *M* ammonium sulphate, 0.1 *M* sodium acetate, pH 5.25, and 10% glycerol from which crystals grew in 5-6 weeks.

Multiple wavelength anomalous dispersion (MAD) data sets were collected on cryo-cooled (100 K) crystals of each of the three crystal forms at the Ni K-edge. Cryoprotecting solutions were prepared as the respective crystallization conditions and additionally 20% v/v glycerol. Crystal characteristics are summarized in Table 1. MAD data processing and reduction statistics are given in Table 2.

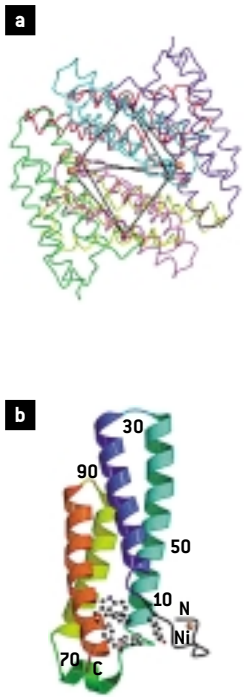

Figure 1. a) C_α-trace representation of a hexamer viewed along a twofold symmetry axis, emphasizing the octahedron-like Ni ion arrangement (black lines). **b)** Ribbon representation of a NiSOD subunit. The N-terminal loop hosting the Ni ion protrudes from the body of the four-helix bundle. Residues involved in aromatic stacking are shown in ball-and-stick representation.

The heavy atom partial structure was solved using automated Patterson methods, revealing 12 sites per asymmetric unit. Electron density maps calculated with experimental phases and structure factor amplitudes were not interpretable in any region of the asymmetric unit despite the promising FOM for this crystal form I. Native as well as anomalous and dispersive difference Patterson maps were calculated for the MAD data. All maps of crystal form I showed an outstanding peak (20% of the origin peak height) at u = 0.05, w = 0 in the v = Harker section. This peak indicated the presence of pseudo-translation, a special type of non-crystallographic symmetry (NCS), which hindered the structure solution [11].

Interpretable electron density maps of NiSOD were obtained using the peak and inflection point data to 2.0 Å resolution of a MAD experiment on crystal form III which did not indicate the presence of pseudo-translation. One Ni-ion per 117 amino acids (13.2 kDa) could be successfully used as anomalous scatterer for MAD phasing. Initial phases were improved by solvent flattening, histogram matching and averaging the density of six NCS related molecules per asymmetric unit to permit the complete interpretation of the electron density. Structural model for form III consisting of one hexamer was refined to 1.68 Å resolution (R = 17.7%, Rfree = 20.0%). This model was subsequently placed twice in the crystal form I, and refined to 1.6 Å resolution (R = 18.4%, Rfree = 20.2%).

RESULTS AND DISCUSSION

Biologically functional unit of NiSOD is a hexamer exhibing a globular shape in which all protein atoms lie in a hollow sphere with outer diameter of 72 Å and inner diameter of 23 Å (Figure 1a). Ni ions are arranged as a distorted octahedron with distances along edges between 23.4 and 27.7 Å. Subunit interactions are mainly of hydrophobic character since approximately two thirds of residues in the interface have non-polar side chains. The subunit structure of NiSOD reveals a four-helix bundle in the all-antiparallel topology (Figure 1b). The four-helix body of a subunit is not involved in stabilizing the respective N-terminal loop since within a subunit there is no direct contact between residues of the protein core and this loop. Thus, the interactions between the subunits, rather than the subunit's shape on its own, are crucial for stabilization of the active site loop.

The structures of NiSOD in both crystal forms initially revealed a square-planar Ni coordination by the amino group of His 1, the amide group of Cys 2, and two thiolate groups, Cys 2 and Cys 6 (Figure 2a). It has been observed [12] that radiation-induced changes of the redox state can take place during X-ray data collection. The reduction of the initially resting NiSOD through the course of X-ray irradiation became evident from a difference Fourier omit map calculated with an initial fraction of data collected in a MAD experiment ('low-dose' data sets, see Methods). The structure of the active site corresponding to low-dose exposure to X-rays shows the presence of the fifth Ni ligand – His1 (Figure 2b). On the other hand the structure of chemically reduced enzyme (using sodium thiosulphate as reducing agent) corresponds to the 'high-dose' crystal structure.

Upon approaching the active site, the access is first impeded by the side chains of Pro 5 and Tyr 9 and then obstructed by a remarkable arrangement of the loop's backbone nitrogen atoms. As a result, a small pocket is formed in the enzyme's surface which can account for substrate specificity. Calculation of solvent accessible areas for active site atoms reveals that the Ni ion and four of five ligands are essentially buried. A non-zero accessible area was obtained solely for His 1 N which amounts to only about 1.1 $Å^2$. Both S-ligands are protected from direct contact with substrate or product molecules, preserving the vulnerable thiolate ligands from oxidation and thus reconciling the apparent implausibility of a Ni-thiolate complex as an agent of protection against oxidative stress. Channels to the hexamer's interior pass through the midpoint between two Ni sites but do not allow direct contact with the metal centre. At this stage, based on the accessible areas for active site atoms, only an outer sphere electron transfer between the superoxide anion and the Ni ion can be suggested.

We have shown that NiSOD is a homo-

hexamer of four-helix-bundle subunits and represents a novel class of SODs. Based on the fact that among Ni-containing proteins investigated so far only redox-active enzymes feature thiolate ligation but neither the hydrolytically active urease nor auxiliary proteins for Ni related cellular tasks, thiolate ligation was suggested to be required for the function of redox-active Ni centres at physiological redox potentials [9]. The coordination of Ni by backbone nitrogen atoms as found in NiSOD has been observed very rarely in proteins. Very recently it was found in the active site (A-cluster) of a bifunctional CO dehydrogenase/ acetyl-CoA synthase [13,14]. The fact that O_2^- can reduce and subsequently reoxidize the Ni centre requires this centre to possess a redox potential in-between those of the couples (O_2^-/O_2) and (O_2^-/H_2O_2), about 0.3 V vs. normal hydrogen electrode (NHE). An important point of NiSOD's catalytic mechanism is the ability of the Ni(II/III) redox couple to reach this potential value by means of the Ni coordination described here.

ACKNOWLEDGMENTS

Work performed at Seoul National University was supported by a research grant from the Korea Science and Engineering Foundation and by a research fellowship of the BK21 project.

References

[1] B. Halliwell, J.M.C. Gutteridge; *Free Radicals in Biology and Medicine* (Oxford University Press, New York, 1999).

[2] I. Fridovich, Superoxide Radical and Superoxide Dismutases; *Annu. Rev. Biochem.;* 64, 97-112 (1995).

[3] D. Bordo, *et al.*, Cu,Zn Superoxide Dismutase in Prokaryotes and Eukaryotes. in *Handbook of Metalloproteins*, (ed. Messerschmidt, A., Huber, R., Poulos, T. and Wieghardt, K.), 1284–1300 (Wiley, England, 2001).

[4] M.E. Stroupe, M. DiDonato, J.A. Tainer; Manganese Superoxide Dismutase. in *Handbook of Metalloproteins*, (ed. Messerschmidt, A., Huber, R., Poulos, T. and Wieghardt, K.), 941–951 (Wiley, England, 2001).

[5] A.F. Miller, Fe-Superoxide Dismutase. in *Handbook of Metalloproteins* (ed. Messerschmidt, A., Huber, R., Poulos, T. and K. Wieghardt) 668-682 (Wiley, England, 2001).

[6] H.-D. Youn, *et al.* Unique Isozymes of Superoxide Dismutase in *Streptomyces griseus*. *Arch. Biochem. Biophys.;* 334, 341-348, (1996).

[7] H.D. Youn, E.J. Kim, J.H. Roe, Y.C. Hah, and S.-O. Kang, A novel nickel-containing superoxide dismutase from *Streptomyces spp. Biochem J.;* 318, 889-896, (1996).

[8] E.J. Kim, H.P. Kim, Y. C. Hah and J.H. Roe, Differential expression of superoxide dismutases containing Ni and Fe/Zn in *Streptomyces coelicolor*. *Eur. J. Biochem.;* 241, 178-185, (1996).

[9] S.B. Choudhury, *et al.* Examination of the Nickel Site Structure and Reaction Mechanism in *Streptomyces seoulensis* Superoxide Dismutase. *Biochemistry;* 38, 3744-3752, (1999).

[10] J.W. Lee, J.H. Roe and S.-O. Kang, Nickel-containing Superoxide Dismutase. *Methods Enzymol.;* 349, 90-101, (2002).

[11] J. Wuerges, J.W. Lee, S.O. Kang and K. Djinovic Carugo, Crystallization of a Nickel-containing Superoxide Dismutase and Preliminary Phase Determination by MAD at the Ni K-edge. *Acta Crystallogr. D* ; 58, 1220-1223, (2002).

[12] G.I. Berglund, *et al.* The catalytic pathway of horseradish peroxidase at high resolution. *Nature;* 417, 463-468, (2002).

[13] T.I. Doukov, T.M. Iverson, J. Seravalli, S.W. Ragsdale and C.L. Drennan, A Ni-Fe-Cu Center in a Bifunctional Carbon Monoxide Dehydrogenase/Acetyl-CoA Synthase. *Science;* 298, 567-572, (2002).

[14] C. Darnault, *et al.* Ni-Zn-[Fe4-S4] and Ni-Ni-[Fe4-S4] clusters in closed and open subunits of acetyl-CoA synthase/carbon monoxide dehydrogenase. *Nat. Struct. Biol.;* 10, 271-279, (2003).

[15] P.J. Kraulis, MOLSCRIPT: a program to produce both detailed and schematic plots of protein structures. *J. Appl. Crystallogr.;* 24, 946-950, (1991).

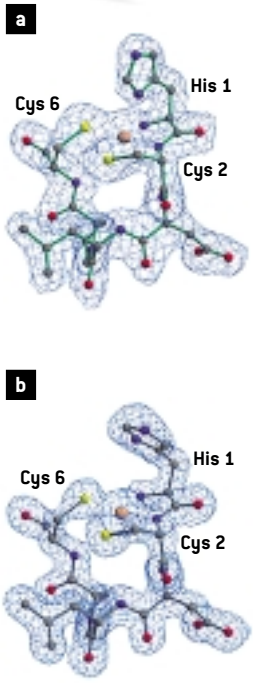

Figure 2. Electron density maps of the NiSOD active site. **a)** 'high-dose' structure. **b)** 'low-dose' structure. Figures were prepared with MOLSCRIPT [15].

A STRUCTURAL EVOLUTION STUDY OF THE ANISOTROPIC NEGATIVE THERMAL EXPANSION MATERIAL $NbOPO_4$ AT HIGH PRESSURES

> G.D. Mukherjee, V. Vijaykumar, B.K. Godwal
High Pressure Physics Division, Bhabha Atomic Research Centre, Mumbai, INDIA

> S.N. Achary, A.K. Tyagi
Applied Chemistry Division, Bhabha Atomic Research Centre, Mumbai, INDIA

> A. Lausi, E. Busetto
Sincrotrone Trieste-ELETTRA - S.S. 14 km. 163,5 in AREA Science Park, 34012 Basovizza, Trieste, ITALY

INTRODUCTION

In recent years, structural investigations of materials that exhibit Negative Thermal Expansion (NTE) have generated considerable interest due to the usefulness of these materials as constituents in composites [1]. By employing them, the composite thermal expansion can be tuned to any desirable value. Ceramic processing methods and grain interaction stresses in the composites can produce changes in the local pressures in the material. For practical applications the constituents of the composite should not undergo phase transformations at such pressures. Therefore, high pressure studies of NTE materials have assumed a significant technological importance. High pressure investigations on MX_2O_8 and $R_2(WO_4)_3$ (M = Zr, Hf; X = W, Mo, V; R = Sc, Lu, Ho) classes of materials, which show isotropic NTE, have revealed the existence of phase changes and amorphization; both reversible and irreversible [2-5]. NTE in these materials is due to the presence of low frequency rigid modes facilitated by their open network structure with corner linking octahedra and tetrahedra [2-4]. Theoretical investigations show a close relation between pressure–induced amorphization and NTE in these tetrahedrally bonded network structures [6]. Therefore, the high-pressure behaviour of NTE materials is also of significant current interest in basic sciences.

$NbOPO_4$ belongs to an unexplored subgroup of materials that exhibit anisotropic NTE at high temperature [7]. Under ambient conditions $NbOPO_4$ has been synthesized having a monoclinic structure (a = 13.097 Å, b = 5.280 Å, c = 13.228 Å, β = 120.334°) [8] and also in a tetragonal structure (a = 6.389 Å, c = 4.105 Å), which is 18% denser than the monoclinic phase [9]. Both phases of $NbOPO_4$ are based on NbO_6 octahedra and PO_4 tetrahedra, which share corners to form three-dimensional networks. The two-fold co-ordination of oxygen atoms in the structure facilitates transverse motion of oxygen in the Nb – O – P linkages and results in negative thermal expansion [7]. Both the phases undergo reversible transitions: monoclinic to an orthorhombic phase at 292° C and tetragonal (Space Group: P4/n) to another tetragonal phase (Space Group: P4/nmm) at 200° C [9]. The transition is observed to be of displacive type, which is first order in the

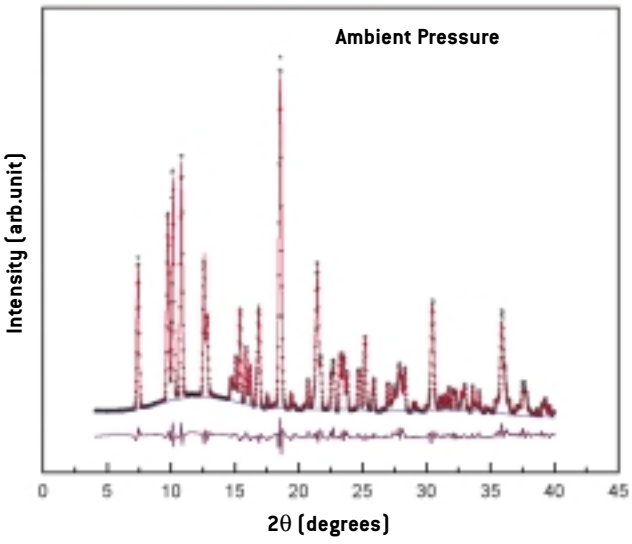

Figure 1. Rietveld fit of ADXRD data taken at ambient pressure using capillary of monoclinic $NbOPO_4$ with Pt as pressure calibrant.

case of monoclinic phase and apparently second order in the case of tetragonal. An interesting aspect of the material behaviour is that only the high temperature phase after the transition exhibits anisotropic NTE behavior [7, 9]. Because of the large volume difference between monoclinic and tetragonal phases at ambient temperature, and the presence of anisotropic NTE at high temperature, compression is expected to have a profound effect on the structure of this material.

Here we report the results of X-ray powder diffraction investigations of monoclinic $NbOPO_4$ at high pressure (ambient temperature).

EXPERIMENTAL

Monoclinic $NbOPO_4$ was synthesized by the reaction of Nb_2O_5 and phosphoric acid at 1300° C and then air quenching the sample [7]. After the characterization of the sample at ambient pressure, high pressure Angle Dispersive powder X-Ray Diffraction (ADXRD) measurements were carried out at the powder X-ray Diffraction beamline of ELETTRA. Monochromatized X-rays were used of wavelength 0.729126 Å. For high pressure experiments, fine powdered samples of monoclinic $NbOPO_4$ were loaded in a Mao-Bell-type diamond anvil cell (DAC), which has been designed and constructed in BARC [10]. A pair of diamond anvils with almost identical culet diameter of about 400 µm was used in the DAC. A hardened steel gasket with a central hole of diameter 150 µm and thickness 60 µm contained the sample. A mixture of methanol – ethanol (4:1) was used as the pressure transmitting medium. The pressure was determined *in situ* by using Pd powder as a pressure calibrant. Images of the powder diffraction rings were collected with a Mar345 image plate detector from MarResearch. The images were integrated over the entire powder rings using the FIT2D software [11] and converted to the normal 2θ *vs.* intensity diffraction pattern. The obtained powder patterns were further corrected for the absorption from the diamond anvils. The Rietveld structural refinements of the spectra were carried out using the GSAS software [12].

Name	x/a	y/b	z/c
Nb(1)	0.0628	0.2440	0.3658
Nb(2)	0.5623	0.2442	0.1967
P(1)	0.3451	0.2569	0.4078
P(2)	0.1578	0.7726	0.0663
O(1)	0.2110	0.2376	0.3664
O(2)	0.9044	0.2209	0.3621
O(3)	-0.0017	0.5297	0.2583
O(4)	0.1477	0.4804	0.5189
O(5)	0.1216	-0.0553	0.4745
O(6)	0.7151	0.2332	0.3446
O(7)	0.4152	0.2823	0.0366
O(8)	0.4886	0.4618	0.2542
O(9)	0.6223	0.0184	0.1143
O(10)	0.6279	0.5550	0.1569

Table 1. Atomic coordinates for monoclinic $NbOPO_4$ at ambient pressure.

RESULTS AND DISCUSSION

The ambient pressure and room temperature ADXRD data of $NbOPO_4$ collected using a capillary were indexed to a monoclinic lattice with unit cell parameters: a = 13.091 Å, b = 5.279 Å, c = 13.230 Å and β = 120.615°, which agrees excellently with reported values [8]. A Rietveld refinement (using bond constraints) of our room temperature data was carried out in space group $P2_1/c$ with the trial positional parameters reported in the literature [7], which resulted in an excellent fit with a typical R factor of 3% (Figure 1). Our refined positional parameters (Table 1) are found to be in good agreement with those published.

Typical X-Ray powder patterns collected up to 21 GPa and the pattern after pressure releases are shown in Figure 2. Comparison of the ADXRD pressure evolution patterns shows a gradual amorphization of monoclinic $NbOPO_4$ with the sample lines broadening and merging with the background as the pressure increases. A careful inspection of the powder patterns shows that, with application of pressure, the line-broadening is initiated from the lines corresponding to low d values. The high pressure ADXRD patterns were also refined using the GSAS software by using the lattice parameters and the atom position parameters obtained from the Rietveld refinement of the ambient pressure pattern. Figure 3 shows an excellent refinement of the data obtained at 0.3 GPa pressure. The excellent fit of the pattern results because the data

FIGURE 2

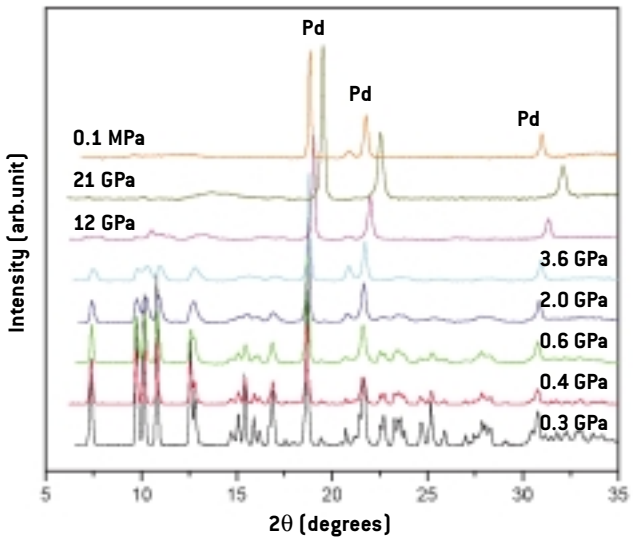

FIGURE 3

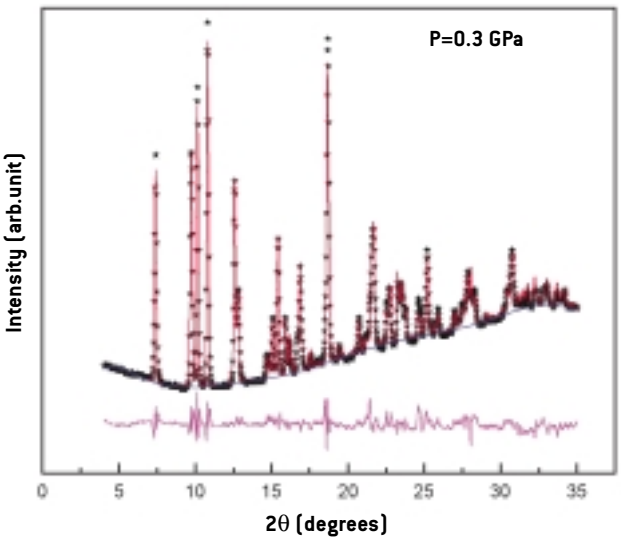

Figure 2. Typical high pressure ADXRD patterns taken using the modified Mao-Bell-type DAC.

Figure 3. Rietveld fit of ADXRD data taken at 0.3 GPa of monoclinic $NbOPO_4$ with Pd as pressure calibrant.

obtained at ELETTRA have a very good signal to noise ratio as compared to laboratory X-ray sources. The refined lattice parameters are shown in Figure 4 at various pressures up to 6 GPa. Above 6 GPa indexing the powder patterns and their refinement did not yield any meaningful result because of the excessive broadening of the X-ray lines, indicating the onset of amorphization. Figure 5 shows the pressure (P) vs. volume (V) curve for the monoclinic $NbOPO_4$ up to 6 GPa. The lattice parameters show a small anomaly at about 0.57 GPa:

i) the cell parameter *a* increases slightly and then falls, ii) the cell parameter *b* decreases rapidly up to 0.57 GPa and then falls slowly with a slope change; iii) the cell parameter *c* does not show any appreciable change in its value. Angle β starts increasing from 0.57 GPa. As mentioned in the introduction the crystal structure of monoclinic $NbOPO_4$ is based on NbO_6 octahedra and PO_4 tetrahedra, which share corners to form three-dimensional networks which leave quite a large open space. The two adjacent corners of NbO_6 octahedra are used to form zigzag chains along the *b* – axis [7,8]. An initial large compression of the b-axis is probably caused by a rotation of NbO_6 polyhedra to reduce the length of the chains along this direction and accommodate the volume reduction in the material by partial filling up of the open spaces. This is also evident from a slight decrease in the angle β. However, as is clear from Figure 5, no anomaly is observed in volume. The P ~ V curve was analyzed using the Birch – Murnaghan equation of state [13] and the values of the bulk modulus B_0 and its pressure derivative B_0' are estimated to be 66.3 GPa and 1.44 respectively.

From the powder ADXRD pattern of the pressure released sample shown in Figure 3, it is evident that the pressure induced amorphization observed in monoclinic $NbOPO_4$ is irreversible. This is probably due to the kinetic hindrance of transformations toward a denser phase, which needs a restructuring of the existing bonds. This has been verified by the fact that monoclinic $NbOPO_4$ transforms to the 18% denser tetragonal phase when quenched from 5.5 GPa and 1000° C [14].

CONCLUSIONS

In conclusion, we have reported high pressure ADXRD measurements up to 21 GPa pressure on monoclinic $NbOPO_4$ using a Mao Bell type diamond anvil cell (DAC) at the powder X-ray Diffraction beamline at ELETTRA. The observation of small anomalies in the variation of lattice parameters

at a pressure around 0.57 GPa is not seen in volume variation. An irreversible, pressure induced, amorphization has been observed in the material. From the pressure vs. volume data the values of B_0 and B_0' are estimated to be 66.3 GPa and 1.44 respectively.

References

[1] C.N. Chu, N. Saka and N.P. Suh; *Mater Sci. Eng.*; 95, 303, (1987).

[2] H. Liu, R.A. Secco, M. Imanaka and G. Adachi; *Solid State Commun.*; 121, 177, (2002) and references therein.

[3] D.V.S. Muthu, B. Chen, J.M. Wrobel, A.H.K. Anderson, S. Carlson and M.B. Kruger; *Phys. Rev.* B; 65, 064101, (2002).

[4] B. Chen, D.V.S. Muthu, Z.X. Liu, A.W. Sleight and M.B. Kruger; *Phys. Rev.* B; 64, 214111, (2001).

[5] H. Liu, R.A. Secco, N. Imanaka and G. Adachi; *Solid State Commun.*; 121, 177, (2002) and references therein.

[6] R.J. Speedy; *J. Phys.: Condens. Matter*; 8, 10907, (1996).

[7] T.G. Amos and A.W. Sleight; *J. Solid State Chem.;* 160, 230, (2001).

[8] A. LeClaire, H. Chahboun, D. Groult and B. Raveau; *Z. Kristallogr.*; 177, 277, (1986).

[9] T.G. Amos, A. Yokochi and A.W. Sleight; *Solid State Chem.*; 14, 303, (1998).

[10] V. Vijaykumar and S. Meenakshi; BARC Technical Report (Library and Information Services Division, BARC, 2000).

[11] A. Hammersley; FIT2D V10.3 Reference manual V4.0, ESRF, Grenoble, France, (1998).

[12] A.C. Larson and R.B. von Dreele; "LANCE." Los Alamos National Laboratory, Los Alamos, NM, 1994.

[13] F. Birch; *J. Geophysics Res.;* 57, 227, (1952).

[14] G.D. Mukherjee, A. Karandikar, V. Vijaykumar and B.K. Godwal (To be published).

FIGURE 4

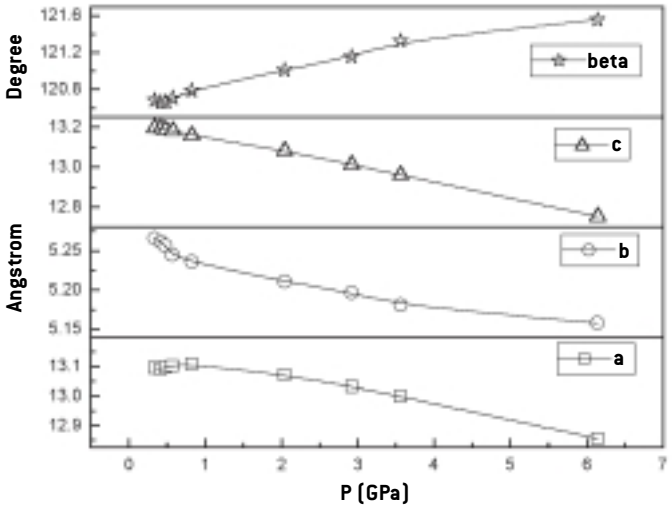

Figure 4. Pressure variation of lattice parameters of $NbOPO_4$ obtained from Rietveld refinement of high pressure ADXRD patterns. The solid lines are a guide for eye.

FIGURE 5

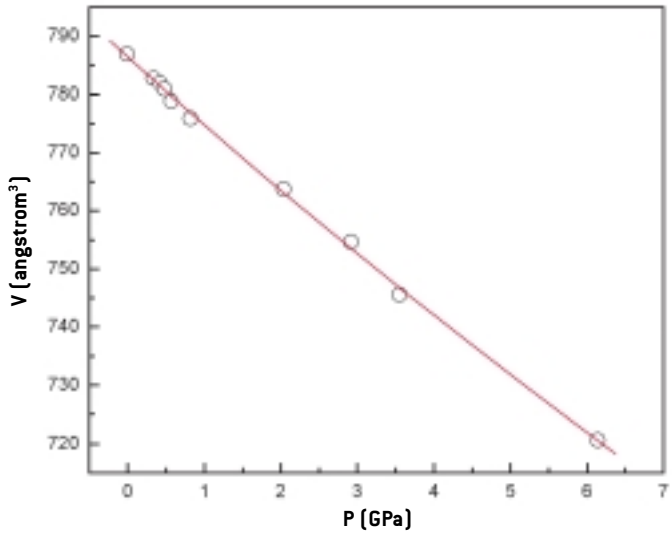

Figure 5. P vs. V curve for $NbOPO_4$. The solid line is a guide for eye.

IN-SITU SAXS INVESTIGATIONS OF THE FORMATION OF MESOSTRUCTURED SPIDER-WEB LIKE SILICA MONOLITHS

> N. Hüsing, D. Brandhuber, C. Raab, V. Torma
Institute of Materials Chemistry, Vienna University of Technology, Getreidemarkt 9/ 165, A-1060 Vienna, AUSTRIA

> H. Peterlik
Institute of Materials Physics, University of Vienna, Boltzmanngasse 5, A-1090 Vienna, AUSTRIA

> M. Steinhart
Institute of Macromolecular Chemistry, Academy of Sciences of the Czech Republic, Heyrovsky Sq. 2, 16206 Prague, CZECH REPUBLIC

> M. Kriechbaum
Institute of Biophysics and X-ray Structure Research, Austrian Academy of Sciences, Schmiedlstraße 6. A-8010 Graz, AUSTRIA

> S. Bernstorff
Sincrotrone Trieste-ELETTRA - S.S. 14 km 163,5, in AREA Science Park, 34012 Basovizza, Trieste, ITALY

INTRODUCTION

The beautiful silica exoskeletons of diatoms and radiolaria are only some examples for the outstanding capability of nature to specifically design inorganic structures on various length scales. The basic concept behind these biomineralization processes relies on the application of templates or structure-directing agents such as biopolymers to spatially pattern the deposition of inorganic solids.[1] The synthetic chemist applies these concepts from biomineralization processes to different types of materials, e.g. zeolites with periodic microporous structures are prepared by using single molecules as templates [2]. Larger structures, such as can be found in ordered mesoporous oxides, are synthesized by using supramolecular templates such as liquid-crystal aggregates of surfactants, and features in the micrometer regime can be deliberately designed by using micromoulding methods with emulsion droplets, latex spheres or bacterial threads [3, 4].

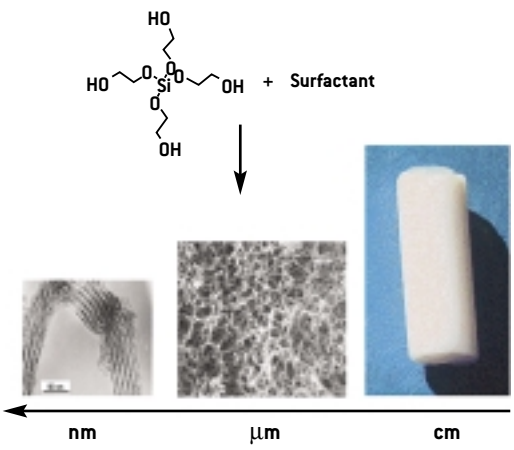

Figure 1.
Top: Schematic representation of the precursors. Bottom: The monolith and its web-like structure in the micrometer range composed of mesoscopically arranged hollow silica channels forming the strings of the web (as obtained by optical photography (right), scanning (middle) and transmission electron microscopy (left)).

For many applications the synthetic chemist seeks to copy the properties of natural materials. Porous materials for example with a hierarchical organization of the network (as found in almost all biominerals) are desired for a broad variety of applications, including chromatography and catalysis, due to the multiple benefits that arise from each of the pore size regimes [5]. However, despite the enormous progress in the synthesis of porous inorganic materials with control of pore sizes from Ångstrom to micrometers, the preparation of materials with a simultaneous tailoring of morphology (monoliths, fibres, films, powders) and pore structures on different length scales still remains a challenging task.

In our approach, a novel sol-gel precursor molecule (an ethylene glycol modified silane, EGMS) is used. Sol-gel reactions of this silica precursor within liquid-crystal

aggregates of an amphiphilic block copolymer in purely aqueous solution lead to the formation of *hierarchically porous silica monoliths* with macropores in the range of 200 to 800 nm and periodically arranged mesopores with a repeating unit distance of 11 nm (Figure 1) [6].

By means of time resolved Small Angle X-ray Scattering (SAXS) we studied the inorganic network formation and the build-up of ordered mesostructures as well as the sensitivity of the built-up structures to the different processing steps. Among these were solvent exchange first to methanol, then to liquid carbon dioxide and finally supercritical drying in carbon dioxide at a temperature of 45 °C and a pressure of 120 bar.

EXPERIMENTAL

In a typical synthesis procedure, wet gels were prepared by adding an ethylene glycol modified silane (EGMS, tetrakis(2-hydroxyethyl) orthosilicate) to a homogeneous mixture of the surfactant Pluronic P123 (BASF) and water, in a molar ratio of EGMS:P123:water=1:0.03:23. Gelation occurred within five minutes and the wet gel bodies were allowed to age at 30 °C for seven days in the mother solution. After solvent exchange first to methanol and then to liquid carbon dioxide, drying of the wet gels was performed by supercritical extraction with carbon dioxide (p_c=73.6 bar, T_c=31 °C).

The time-dependent high-pressure measurements were performed at the Austrian high-flux SAXS beamline at ELETTRA using a fixed wavelength λ=0.077 nm, with a camera length of 204 cm, equipped with a 150 mm linear wire PSD (Gabriel-type gas detector), which provided an effective q-range 0.008 - 4 nm^{-1} [7]. Here q is the magnitude of the momentum transfer ($q=4\pi\sin(\vartheta)/\lambda$ with 2ϑ being the scattering angle). The high-pressure X-ray cell was made of stainless-steel with diamond windows (0.5 mm thick) and a sample volume of approximately 30 mm^3 and flow-through capability (Figure 2). In the sample stage the cell was sandwiched between two copper blocks through which thermostated water circulated. Both temperature and pressure were computer-controlled [8]. CO_2 was used both as solvent and pressurizing agent. The cylinder containing CO_2 in the liquid-state was connected via a valve to a high-pressure network, which allowed us to increase or decrease the pressure in the sample cell.

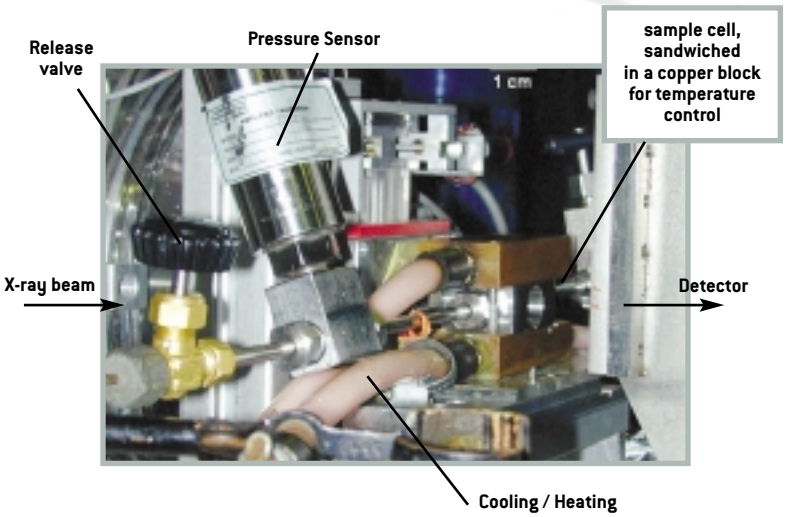

Figure 2. High pressure sample cell for *in-situ* SAXS measurements during supercritical drying with carbon dioxide

The SAXS measurements were carried out during the gelation process, thus continuously following network and mesophase formation. Preformed gels were investigated at different times during aging (1 to 7 days), followed by *in-situ* measurements of the solvent exchange process to methanol (of gels that had been aged for seven days). For these measurements, liquid samples and also preformed gel samples were placed in a home-made flow-through cell with a sample volume of about 1 cm^3. For supercritical extraction with liquid carbon dioxide, the wet gels were placed in the high-pressure cell. After solvent exchange from methanol to liquid carbon dioxide at 20 °C and 70 bar, the temperature and pressure were raised computer-controlled to 45 °C and 100 bar.

RESULTS AND DISCUSSION

Figure 1 shows schematically the synthesis procedure which relies on hydrolysis and polycondensation reactions of the ethylene glycol modified silane in the hydrophilic domains of the surfactant/water liquid-crystalline arrangement. The photograph (right) shows a typical white crack-free monolith as obtained after drying and calcination. The very unique hierarchical network structure is displayed in the scanning and transmission

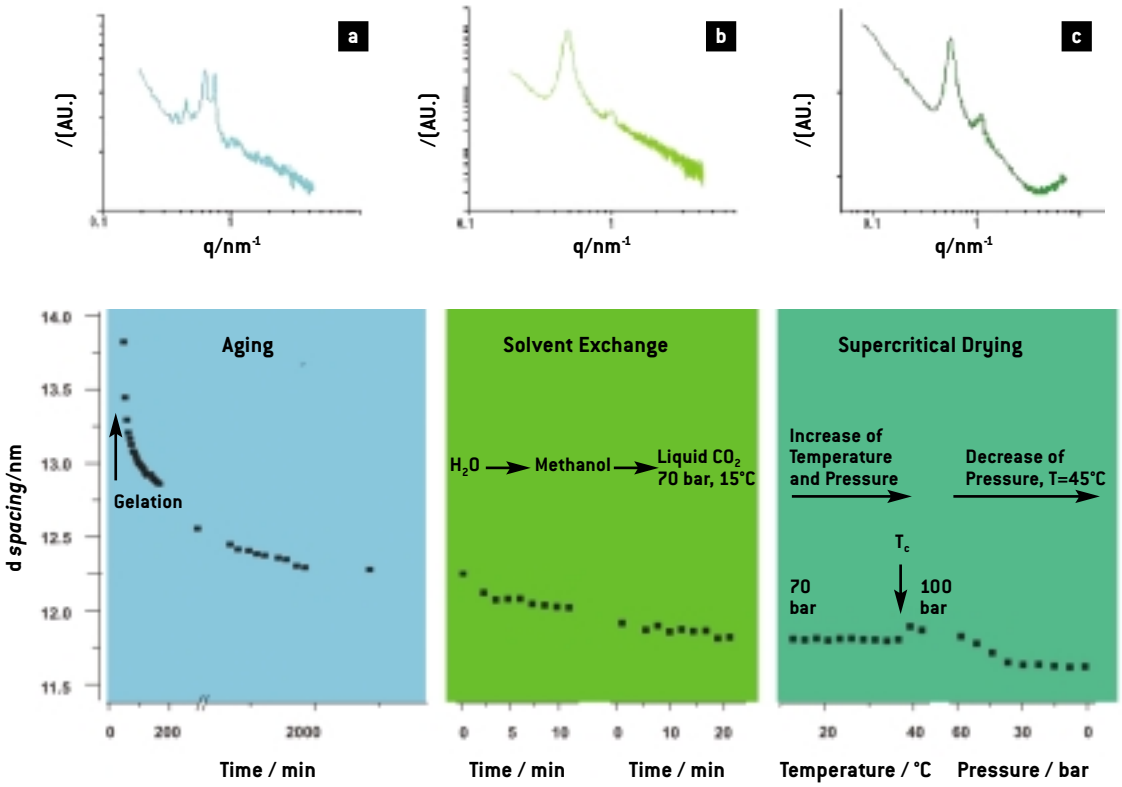

Figure 3. SAXS pattern of the water/surfactant mixture **a)**, shortly after gelation **b)** and after supercritical drying **c)**, (top) and the evolution of the corresponding *d*-spacing during gel formation (30 sec/ measurement), solvent exchange from ethylene glycol/water mixture to methanol (in the liquid cell) to liquid carbon dioxide (in the high pressure cell) with preformed gels (30sec/ measurement) and supercritical drying with carbon dioxide (10sec/ measurement, bottom).

electron micrographs. The silica backbone forms a spider-web like structure with macropores in the range of 200-800 nm in diameter (Figure 1, bottom middle) in which every string of the web is composed of periodically arranged, hollow silica channels with a repeating unit distance of about 10 nm (Figure 1, bottom left). The material is in addition characterized by low densities (ca. 0.1 $g \cdot cm^{-3}$) and high specific surface areas of above 1000 $m^2 \cdot g^{-1}$.

Figure 3 shows representative SAXS patterns (top part) of a) the surfactant/ water mixture, b) during the formation of the gel network after addition of the ethylene glycol modified silane, and c) a dried sample. The scattering curves show at least one distinct reflection due to the periodic arrangement of the surfactant/ water liquid crystal as well as of the evolving mesostructured silica phase. The changes in the repeating unit distance (*d*-spacing) calculated from this reflection represent best the formation and evolution of the mesostructures during the whole synthesis.

The addition of the silane to the surfactant/water mixture significantly disturbs the long range order of the supramolecular arrangements, (three well resolved reflections change to one broad maximum of low intensity). Even after the formation of a three-dimensional inorganic network (gelation) in the surfactant/ water mixture the evolution of the silica-surfactant mesophase continues which can be seen by the significant decrease of the repeating unit distance. To complete the cooperative self-assembly process and network condensation the gels were subjected to an aging procedure in the mother liquid (water/ ethylene glycol) for seven days at 30 °C. Preformed gels were measured repeatedly during the aging procedure. Prior to drying of the wet gels a solvent exchange process of aqueous ethylene glycol to methanol was performed. During all these processes, the long-range order in the material becomes more pronounced and a significant decrease in the repeating unit distance is observed, which corresponds well to a higher degree of cross-linking in the inorganic network and loss of surfactant during solvent exchange.

The most crucial step in the preparation of large porous monoliths is drying, since evaporation of the pore liquid leads to large shrinkage or even collapse of the whole gel body. One typical procedure to prevent cracking is drying with supercritical fluids. Here, the building-up of a gas/ liquid interface is avoided during drying, hence no capillary pressures evolve. In this study, an *in-situ* SAXS study of a supercritical drying process with carbon dioxide was performed, comprising an extraction step with liquid carbon dioxide to exchange methanol, an increase in temperature to 45 °C while simultaneously increasing the pressure (100 bar), thus transferring carbon dioxide into the supercritical state, and finally a venting step to ambient pressure. These experiments were performed on previously prepared and aged wet gel samples in the high pressure cell, which is displayed in Figure 2.

None of the solvent exchange and drying steps are detrimental to the mesostructure of the silica monoliths. Interestingly, the transition from liquid to supercritical CO_2 at 31 °C and ca. 80 bar leads to a small increase in the repeating unit distance, which cannot be explained at the moment. Venting the system to ambient pressure again results in a contraction of the gel network and a final *d*-spacing of 11.6 nm.

CONCLUSIONS

The formation of highly porous silica monoliths with uniform periodic mesopores relies on the compatibility of the liquid crystalline surfactant/ water phase with the inorganic network forming species. In addition, the stability of the network during surfactant removal and drying of the monoliths is of importance. We were able to follow the whole process towards a mesostructured silica monolith, including drying in supercritical carbon dioxide using a high pressure cell set-up.

So far, only the influence of the synthesis process on the periodic mesostructure has been discussed. The quite unusual fibrous, spider-web like structure is probably formed via a second-level phase separation process. This will be the topic of a forthcoming publication.

References

[1] S. Mann; *Biomineralization: Principles and Concepts in Bioinorganic Materials Chemistry*; Oxford University Press, (2001).

[2] *Handbook of Porous Solids*, Ed. F. Schüth, Wiley-VCH, Weinheim, (2002).

[3] C.T. Kresge, M.E. Leonowicz, W.J. Roth, J.C. Vartuli, J.S. Beck; *Nature;* 359, 710, (1992).

[4] B.T. Holland, C.F. Blanford, A. Stein; *Science*; 281, 538, (1998).

[5] J.H. Smatt, S. Schunk, M. Linden*; Chem. Mater.;* 15, 2354, (2003).

[6] N. Hüsing, C. Raab, V. Torma, H. Peterlik, A. Roig; *Chem. Mater.;* 14, 2690, (2003).

[7] H. Amenitsch, S. Bernstorff and P. Laggner, *Rev. Sci. Instrum.;* 66, 1624, (1995); H. Amenitsch, S. Bernstorff, M. Kriechbaum, D. Lombardo, H. Mio, M. Rappolt, P. Laggner, *J. Appl.Cryst.;* 30, 872, (1997).

[8] M. Steinhart, M. Kriechbaum, K. Pressl, H. Amenitsch, P. Laggner, S. Bernstorff, *Rev. Sci. Instrum.*; 72/2, 1540-1545, (1999). http://www.ibr.oeaw.ac.at/beamline/publications.html, *Annual Report of the Austrian SAXS-beamline* (2000), p. 27-29.

ARPES OF Bi2212 USING CIRCULARLY POLARIZED LIGHT: NO EVIDENCE FOR A TIME-REVERSAL SYMMETRY BREAKING

> S.V. Borisenko, A.A. Kordyuk, T. Kim, A. Koitzsch, M. Knupfer, J. Fink
Institute for Solid State and Materials Research, IFW-Dresden, D-01069 Dresden, GERMANY

> H. Berger
Institute of Physics of Complex Matter, EPFL, CH-1015 Lausanne, SWITZERLAND

> S. Turchini, C. Grazioli
Istituto di Struttura della Materia, Consiglio Nazionale delle Ricerche, in AREA Science Park, 34012 Trieste, ITALY

INTRODUCTION

The puzzle of High-Temperature Superconductivity (HTSC) is still not unraveled. The variety of specific points, lines and regions in the "normal state" part of the phase diagram of high Tc superconductors, clearly demonstrates not only the complexity of the problem but also the absence of its detailed understanding [1]. It is therefore important to realize which of the features of the phase diagram are really universal boundaries of particular phases and which just designate intermediate states with properties defined by the proximity to well established phases such as, for instance, superconductivity. A recent angle-resolved photoemission (ARPES) study [2] found evidence of time-reversal symmetry breaking below the so called T*-line, implying the existence of a well defined phase transition in underdoped cuprates. The importance of the issue appeals to the confirmation of already existing data since the observation of the effect is an extremely demanding experiment [2, 3]. In fact, a number of artifacts must be ruled out before one can state that exactly the time-reversal symmetry breaking is responsible for the non-vanishing dichroism in the mirror plane. It was already suggested [4] that the ~3% asymmetry effect observed in the underdoped samples can be explained by changes of the well known incommensurate modulation, reported [2] to be also of the order of 3%, as a function of temperature. Therefore, analogous experiments carried out on systems with reduced interference of the temperature-sensitive structural modifications would be of special interest today together with the development of an improved experimental methodology aiming at more precise and reliable investigations of circular dichroism effects in low energy photoemission.

Here we present the results of an ARPES investigation of the $(Pb,Bi)_2Sr_2CaCu_2O_{8+d}$ (Pb-Bi2212) cuprates known to have no 5x1 superstructure. In addition to the temperature dependent analysis, we consider the symmetry of the dichroic signal (details of its momentum distribution) with respect to the momentum distribution of the total photocurrent, calculated as a sum of the spectra taken with right- and left-hand circularly polarized excitation and therefore equivalent to the photocurrent measured using unpolarized light. Application of the method to the Pb-Bi2212 compounds demonstrates that the reflection antisymmetry of the dichroic signal with respect to the mirror planes remains insensitive to both temperature and doping level. The obtained results demonstrate that the signatures of time-reversal symmetry violation in pristine Bi2212, as determined by ARPES, are not a universal feature of all cuprate superconductors.

EXPERIMENTAL

The experiments were performed at the "Circular Polarization" beamline, 4.2R, of ELETTRA using approximately 90% circularly polarized (CP) light from the elliptical wiggler-undulator. Spectra were collected in

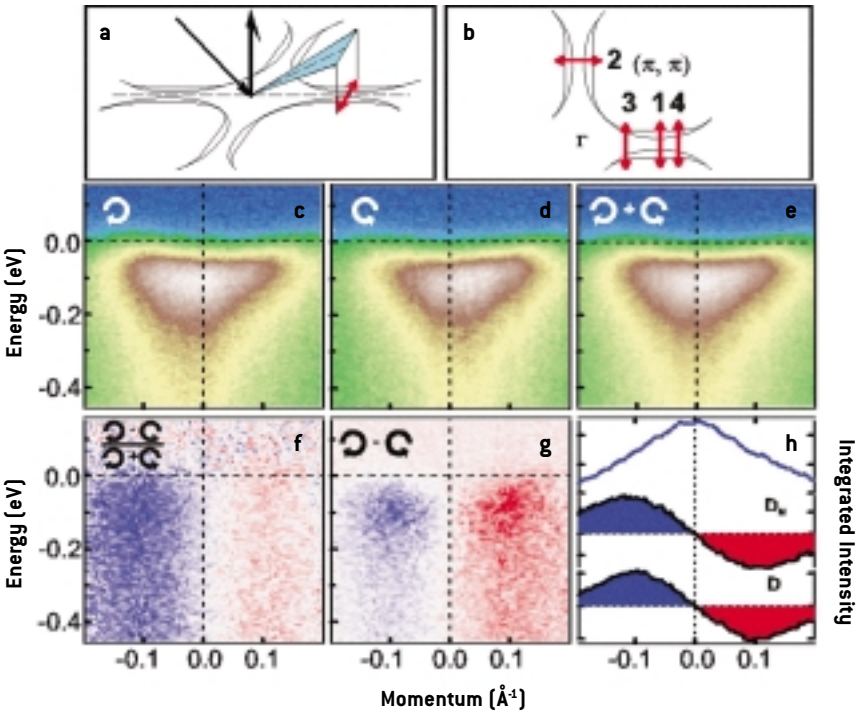

Figure 1. a) Schematic layout of the experiment. **b)** Cuts in **k**-space corresponding to the recorded spectra. **c)** and **d)** EDMs taken using the light of positive **c)** and negative **d)** helicity. **e)** Sum of EDMs shown in panels **c)** and **d)**. **f)** The normalized difference. **g)** The difference. **h)** Integrated intensities corresponding to panels **e)**, **f)** and **g)**. For details see text.

the angle-multiplexing mode of a SCIENTA SES-100 electron-energy analyzer. The overall average resolution in (**k**, ω)-space was set to 0.01 Å^{-1} x 0.02 Å^{-1} x 40 meV. An essential advantage of this experimental set-up based on the latest achievements of synchrotron radiation technologies is that no mechanical movement is involved in the process of switching the helicity of the incoming radiation. Only the direction of the current in the coils of the wiggler-undulator needs to be reversed, which takes approximately 30 seconds. This enables the successive recording of the spectra using light of both polarizations with the other experimental parameters remaining unchanged. Direct imaging of the beam spot (typical linear size ~ 300 μm) on the sample surface using the transmission mode of the same electron-energy analyzer has demonstrated its perfect (< 10 μm) spatial stability with respect to multiple switching of the helicity [5]. We note here that such experimental conditions are obviously more favorable for the dichroism studies than those reported in reference [2], where not only the polarizer is rotated resulting in residual beam movement but also the experimental chamber needs to be adjusted every time the helicity is changed.

High-quality single crystals of 5x1-superstructure-free, underdoped (T_c=77 K) and overdoped (T_c=70 K) Pb-Bi2212 were mounted on a three-axis stepper motor driven cryo-manipulator allowing a precise (0.1°) positioning of the sample with respect to the analyzer's entrance slit. Alignment of the crystals was done by recording characteristic spectra with pronounced **k**-dependence. The stability of the sample orientation was further controlled by a digital camera with a sensitivity to the relative movement of the sample of the order of 0.1°. The excitation energy was chosen to be hν=50 eV for two reasons: (i) the emission from the antibonding band is strongly enhanced near the (π, 0)-point in comparison with that from the bonding band thus effectively reducing the number of features in the spectra [6]; (ii) the (3π, 0)-point becomes accessible in normal incidence geometry at an emission angle of 45°. Intensity variations of the synchrotron radiation were controlled by continuously monitoring the ring current. If jumps of more than 1% were observed during the data

acquisition, measurements were repeated. The data were collected at 300 K, 100 K and 30 K.

RESULTS AND DISCUSSION

The basic idea of our approach is the same as previously suggested and experimentally tested [2, 3] but there are important differences which we discuss in the next paragraph. According to the proposed criterion, one needs to control the value of the dichroic signal corresponding to the emission within a mirror plane. If this signal is zero, the time-reversal symmetry is preserved, if not - it is broken. For this, the vectors of photon incidence, electron emission and the normal to the sample surface should lie in this mirror plane. Such a significant modification (proposed earlier [7]) of the criterion was required because of the strong dichroism observed in the case when the experimental geometry possesses a "handedness", i.e. when at least one of the three mentioned vectors is not in the mirror plane. Such an effect, regardless of its origin, which has been argued to be geometric [3], can be used to track down the temperature dependence of the intrinsic dichroism (if any). The geometric effect is odd with respect to reflection in a given mirror plane and an intrinsic dichroism, expected to be even, should then result in an effective "rotation" of this mirror plane upon entering the pseudogap regime of underdoped samples, as was observed for pure Bi2212 in [2], where the corresponding angle was estimated to be 2.3°.

The essentials of our approach to test the time-reversal invariance of the electronic states in Pb-Bi2212 are depicted in Figure 1. As shown in Figure 1(a) we record the photoemission intensity simultaneously for **k**-vectors from the cuts crossing the mirror plane at a right angle (red arrows). Resulting Energy Distribution Maps (EDM) taken at room temperature using the right- (I^+) and left-hand (I^-) CP light are shown in Figure 1(c) and (d) respectively. One easily notes an asymmetric character of both distributions with respect to the zero **k**-values representing the mirror plane. Panels (f) and (g) show normalized, $(I^+-I^-)/(I^++I^-)$, and simple, I^+-I^-, differences of the EDMs shown above. Here one sees how the dichroic signal is distributed as a function of energy and momentum. Its essentially homogeneous character (Figure 1f) seems to be in agreement with its geometric origin. Figure 1(h) concludes the presentation of the data set condensing it into the three curves which are the main basis of our data analysis - (i) momentum distribution curves (MDC) corresponding to the total photocurrent (one example is shown as a solid blue line), (ii) integrated normalized difference ($\mathbf{D}_N$) and (iii) integrated simple difference (**D**). MDCs are needed to precisely determine the **k**-location of the mirror plane. The other two curves were obtained by integration within the energy interval of -450 to 100 meV of the corresponding distributions from the panels (f) and (g). This example clearly shows that the dichroic signal is zero in the mirror plane.

We stress two important points here. We *first* determine the position of the mirror plane with a precision of 0.002 $Å^{-1}$ by considering MDCs of the total distribution (Figure 1e) and then plot $\mathbf{D}_N$ and **D** in these coordinates. In other words, we believe that the best accuracy in alignment could be achieved using "internal" reference points, such as experimental dispersion derived from the MDCs maxima of the total spectral weight. It is worth noting that these reference points are obtained in static conditions, i.e. without any movement of the sample or the analyzer, which is ruled out when using a smaller detector at lower photon energies as in Ref. 2, where neither the procedure itself nor the accuracy of the momentum scale determination was reported.

The second point is that, once the signal has been recorded in a relatively wide momentum interval, it is easy to note the non-monotonic character of both $\mathbf{D}_N$ and **D** dependencies (Figure 1(h)). Locations of the extrema as well as their absolute intensities can be determined with a high precision using a fitting procedure: these are symmetric with respect to the origin when the sample is properly aligned. We have systematically studied the line shape of $\mathbf{D}_N$ and **D** as a function of misalignments of different types. Both turned out to be extremely sensitive: not only the curves did not pass through the origin imitating the presence of

the intrinsic dichroism, but at the same time their maxima and minima were no longer symmetric with respect to zero. This observation opens up an additional possibility to check the reflection invariance of the dichroic signal. For instance, if some sort of a misalignment resulting in a non-zero value in the mirror plane is compensated by the intrinsic dichroism expected as a result of the time-reversal symmetry violation, one can identify such an unlikely case of "accidental zero" by observing the locations and absolute intensities of the extrema of $\mathbf{D}_N$ and $\mathbf{D}$ -curves.

Now we apply our approach to check whether there is an effect in the superconducting state of the overdoped sample - the issue which was not addressed before. First we compare in Figure 2 the total intensity distributions with the $\mathbf{D}_N$ and $\mathbf{D}$ curves measured at 100 and 30 K. In this case we observe an antisymmetric behaviour of both $\mathbf{D}_N$ and $\mathbf{D}$ which is not sensitive to the temperature (Figure 2c). In the panel (d) we plot again the data with a more detailed momentum scale, comparable with the one used for data presentation [2]. As seen, the accuracy of our experiment is better and allows us to draw a conclusion about the absence of the effect of the mirror plane "rotation" in the overdoped sample upon entering the superconducting state.

Figure 2 (e-g) illustrates that the additional condition described above is satisfied. Data are taken now along the cut closer to the Γ-point. This results in more clearly pronounced extrema of $\mathbf{D}_N$, whose momentum location we determine by fitting these parts with gaussians. The left maximum resides at -0.115±0.003 Å^{-1} whereas the right minimum is at 0.113±0.001 Å^{-1}.

The data recorded on underdoped samples are presented in Figure 3. The first row shows EDM's of total intensity together with $\mathbf{D}_N$ -curves recorded perpendicular to the two mirror planes Γ - (π, 0) and Γ - (0, π) in the pseudogap state. As seen from the panel (c) the dichroism in the mirror plane is negligible. At zero momentum, linear fits cross the vertical axis at 0.16% and -0.41%, respectively, which is within the error bars (< 0.5%). These values are far smaller than the dichroism value of ~ 4% reported in [2] for the pseudogap regime. In panel (d) we compare dichroic signals recorded along the cut 3 (Figure 1 (b)) measured at 100 K and 30 K and again, as follows by applying both criteria, there is no visible deviation from zero. Panels (e) and (f) represent the data taken in normal incidence geometry.

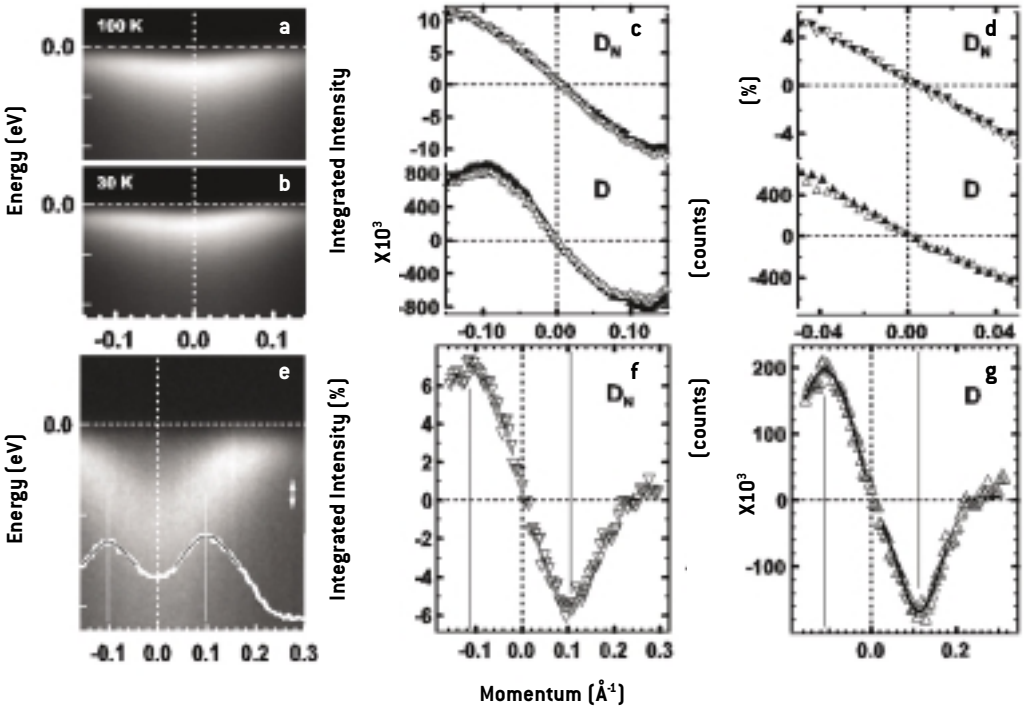

Figure 2. Overdoped sample. **a)**, **b)** EDMs of the total intensity taken along the cut 4 (see Figure 1b) at 100 K and 30 K. **c)** and **d)** Corresponding dichroic signals. **e)** EDM taken along the cut 3 in the superconducting state and MDC (white line, obtained by the integration of the spectral weight within the energy range shown by the double-headed arrow) used to determine the origin of the momentum scale. **f)** and **g)** Corresponding dichroic signals with pronounced **k**-dependence which allows a self-check procedure.

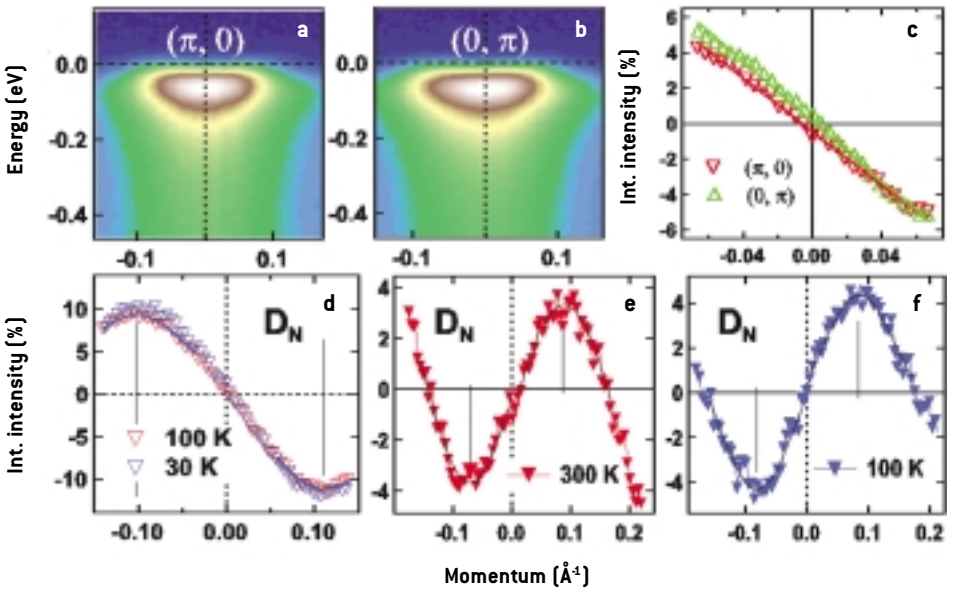

Figure 3. **a)** and **b)** EDMs of the total photocurrent along the cuts through the (π, 0)- and (0, π)-points (cuts 1 and 2) taken at 100 K and **c)** corresponding $\mathbf{D_N}$ - curves together with linear fits. **d)** $\mathbf{D_N}$ - curves for the cut 3 measured at 100 K and 30 K. **e)** and **f)** Normal incidence $\mathbf{D_N}$ - curves taken at 300 K and 100 K. For details see text.

Due to the relatively large emission angle (45°), reduced "handedness" of the experiment (because of the co-planarity of the three aforementioned vectors) and radial matrix element effects, the signal is weaker and more problematic for the application of the absolute intensity criterion. Linear fits in the vicinity of zero momentum, cross the vertical axis at -0.63% and 0.18% respectively which is slightly more than the experimental uncertainty (~ 0.5%) for the room temperature curve. This is exactly the case when one can apply additionally the line shape criterion discussed above. Fitting the extrema of the normal incidence curves measured at 300 and 100 K we find that the "zero" is shifted by less than 0.009 Å^{-1} at room temperature and by less than ±0.004 Å^{-1} in the pseudogap regime. This means that the reason for the small dichroism in the mirror plane is the residual misalignments. A qualitatively similar picture was observed for other underdoped samples (results are not reported here).

The accuracy of our experiments can be estimated in two ways. We distinguish between the temperature dependent measurements where error bars are given by the size of the relative shift of the $\mathbf{D_N}$-curve and measurements of a single $\mathbf{D_N}$-curve at a given temperature where the accuracy is defined by the absolute **k**-value at which the dichroism is zero or by the absolute dichroism value at **k**=0. In both cases typical values are of the order of 0.004 Å^{-1}, which in terms of the dichroism is ± 0.3% or in terms of the degree of the mirror plane "rotation" would be ± 0.3°. Note that our additional criterion allows us to identify and account for the major source of the errors - misalignments. In some particular cases (e.g. Figure 3 e, f) the quality of the gaussian fits defines the precision of the experiment (± 0.005 Å^{-1}).

Our studies of pure Bi2212 single crystals led us to the following conclusions. Because of the 5:1 superstructure present in Pb-free Bi2212 samples, the dichroic signal measured at the (π, 0)-point is not equal to zero already at the room temperature. According to our measurements it is ~ 3.7% and the $\mathbf{D_N}$ line crosses the momentum axis away from the (π, 0)-point which is easy to understand since the additional dichroism related to the two diffraction replicas crossing the Fermi level along this cut is not compensated. This is because diffraction replicas originate from the different Brillouin zones where the corresponding photoemission signal is widely known to be different due to the matrix element effects. If one, however, starts to measure the evolution of the dichroism at the point where it is zero at room temperature, i.e. not at the (π, 0)-point, it is

not surprising that at lower temperatures the dichroism can become non-zero. Moreover, this effect will be doping dependent since in the overdoped samples diffraction replicas are less important as they cross the Fermi level further away from the (π, 0)-point than in underdoped samples.

The obtained results do not rigorously disprove the existence of the time-reversal symmetry breaking phase in the pseudogap part of the cuprates' phase diagram. We simply find no experimental evidence for the specific pattern [3] of circulating currents in the studied compounds according to the theoretical proposal and in contrast to the experimental observation of the effect in pristine Bi2212 [2]. One should notice, however, that the reason for non-observation of the effect can in our case be due to domains of size smaller than 300 μm.

While the present results put strong constraints on the possible scenarios involving the circulating currents, in some particular cases the obtained information is not sufficient to make a conclusive statement. For instance, while the antiferromagnetic pattern of currents required by the d-density wave instability [8] is invariant upon reflections in the Γ - (π, 0) plane, reflections in the Γ - (π, π) plane result in a pattern of currents which can be obtained by shifting the initial one by one unit cell vector (i.e. this plane is a glide plane) and therefore cannot be distinguished from the mirror plane reflection in a photoemission experiment. In this case, perhaps, a more detailed knowledge is required as for the energy and momentum distribution of the dichroic signal.

ACKNOWLEDGMENTS

We are grateful to C. Varma for numerous stimulating discussions and to R. Hübel for technical support. We acknowledge the support of the European Community - Access to Research Infrastructure action of the Improving Human Potential Programme. HB is grateful to the Fonds National Suisse de la Recherche Scientifique.

References

[1] e.g. J.L. Tallon and J.W. Loram; *Physica*; 349, 53, (2001)

[2] A. Kaminski *et al.*; *Nature*; 416, 610, (2002).

[3] M.E. Simon and C.M. Varma; *Physical Review Letters*; 89, 247003, (2002).

[4] N.P. Armitage and J. Hu, *cond-mat/0303186* (unpublished).

[5] This has been checked for two perpendicular directions, rotating the analyzer by 90°.

[6] A.A. Kordyuk *et al.*; *Physical Review Letters*; 89, 077003, (2002).

[7] C.M. Varma; *Physical Review B*; 61, R3804, (2000).

[8] S. Chakravarty *et al.*; *Physical Review B*; 63, 094503, (2001).

MICROMAGNETIC STUDIES WITH X-RAY MAGNETIC CIRCULAR DICHROISM PHOTO EMISSION ELECTRON MICROSCOPY (XMCDPEEM)

> E. Bauer, A. Pavlovska
Sincrotrone Trieste-ELETTRA - S.S. 14 km 163,5, in AREA Science Park, 34012 Basovizza, Trieste, ITALY
Department of Physics and Astronomy, Arizona State University, Tempe, AZ 85287, USA

> S. Cherifi
Sincrotrone Trieste-ELETTRA - S.S. 14 km 163,5, in AREA Science Park, 34012 Basovizza, Trieste, ITALY
Laboratoire Louis Neel, CNRS, 38042 Grenoble Cedex 9, FRANCE

> S. Heun, A. Locatelli
Sincrotrone Trieste-ELETTRA - S.S. 14 km 163,5, in AREA Science Park, 34012 Basovizza, Trieste, ITALY

> R. Belkhou
LURE, Université Paris-Sud, 91898, Orsay Cedex, FRANCE

> J.A.C. Bland, M. Kläui*, C.A.F. Vaz
Cavendish Laboratory, University of Cambridge, Madingley Road, CB3 0HE, United Kingdom

> L.J. Heyderman
Laboratory for Micro- and Nanotechnology, Paul Scherrer Institute, CH-5232 Villigen PSI, SWITZERLAND

> J. Shi, W. C. Uhlig
Department of Physics, University of Utah 115 S. 1400 E. #201 Salt Lake City, UT 84112-0830, USA

**current affiliation: Fachbereich Physik, Universität Konstanz, Universitätsstr. 10, D-78457 Konstanz, Germany*

INTRODUCTION

The magnetic domain structure of ferromagnetic materials has been an exciting subject of solid state physics, materials science and engineering for many years [1]. During the last several decades attention has increasingly focused on the domain structure of thin films, in particular of films with micron and submicron lateral dimensions because of their importance in high density nonvolatile memory devices ("magnetic bits or elements"). Numerous methods have been developed to image domain structures, ranging from magneto-optic imaging for elements in the 10 μm range to electron holography that allows imaging in the 10 nm range [1]. Although the feasibility of domain imaging with XMCDPEEM was already demonstrated 10 years ago [2], the resolution at that time could not compete with that of magnetic force microscopy (MFM) so that MFM became the major imaging method. As a result of the improvement of cathode lens photoemission electron microscopes and the increasing availability of high brightness undulator beamlines with variable polarization, XMCDPEEM has become an important tool for imaging magnetic elements. For these reason efforts have been made to develop XMCDPEEM at the Nanospectroscopy beamline, using the Spectroscopic Photo Emission and Low Energy Electron Microscope (SPELEEM) attached to this beamline.

The first results were obtained still without energy filter [3], while those reported here are in part without, and in part with energy filter. The goal of the present study was to obtain a better understanding of the domain structure of two very different elements in zero external field, in the virgin and in the demagnetized state, that is in remanence. A well-defined reproducible remanent state is important for the nonvolatility of memory devices.

EXPERIMENTAL

The studies were made with the SPELEEM in the XMCDPEEM mode and – for imaging the topography – in the LEEM mode. XMCDPEEM uses for imaging the secondary electrons (SE) produced by the Auger electrons that fill the 2p hole created in the photo ionization process. The transition probability from the $2p_{1/2}$ and $2p_{3/2}$ levels to the spin-polarized empty 3d states depends upon the helicity $\boldsymbol{\sigma}$ of the incident circular polarized light. Therefore the SE yield, which is proportional to $\boldsymbol{\sigma} \bullet \mathbf{M}$ – where **M** is the local magnetization –, changes upon reversal of the helicity. When SE images taken with opposite helicity are subtracted, the helicity-independent structural contrast is eliminated in the resulting image and only the helicity-dependent magnetic contrast, which gives the direction and – to a certain extent also the magnitude of the local magnetization **M** – remains.

Two types of magnetic element patterns were studied. One was a set of rectangular Co patterns from the Department of Physics of the University of Utah, the other several sets of Co ring patterns from the Cavendish Laboratory of the University of Cambridge. Both were prepared by electron beam lithography, the rectangular patterns on an Al-coated flat Si substrate using a bylayer resist, the ring patterns on a pre-patterned Si substrate as described in detail in [4]. All Co films were polycrystalline and were covered with a protective Au layer 2.5 nm thick on the rectangles and 1.5 nm on the rings. The Au layer was partially removed by sputtering before imaging. The rectangular elements were in the virgin state, that is they were not exposed (intentionally) to a magnetic field, while the ring samples had been exposed to the saturation field and the resulting remanent state was observed.

RESULTS AND DISCUSSION

We present first some results for the rectangular elements. They were 0.25 µm, 0.5 µm and 1 µm wide, with aspect ratios of 1:1, 2:1, 3:1 and 4:1, so that the size of the smallest element was 0.25×0.25 µm², that of the largest 4×1 µm². The images were taken without energy filter. Figure 1 gives an overview of the dependence of the domain structure on the aspect ratio at fixed width (1 µm); Figure 2 illustrates the dependence on the element width at fixed aspect ratio. The overviews (a) – (d) in Figure 1 show a large variety of domain patterns instead of simple closure structures with minimum energy. In the images e) – h) some of the domain patterns can be seen in more detail. For the square element the symmetrical vortex structure i) is the lowest energy configuration but the images show also many distorted vortices and stripe patterns. With increasing aspect ratio an increasing number of domain configurations is found. An example is the symmetric vortex pair with opposite magnetization j) instead of the simple closure structure k) for the aspect ratio 2:1. The increasing complexity with increasing aspect ratio can be understood as follows. During film growth domains can nucleate quasi-simultaneously at many places in the element, preferentially at the corners or edges. When the growing domains meet, there is no external field that would cause growth of one domain at the expense of the others and the configuration determined by the nucleation is frozen in,

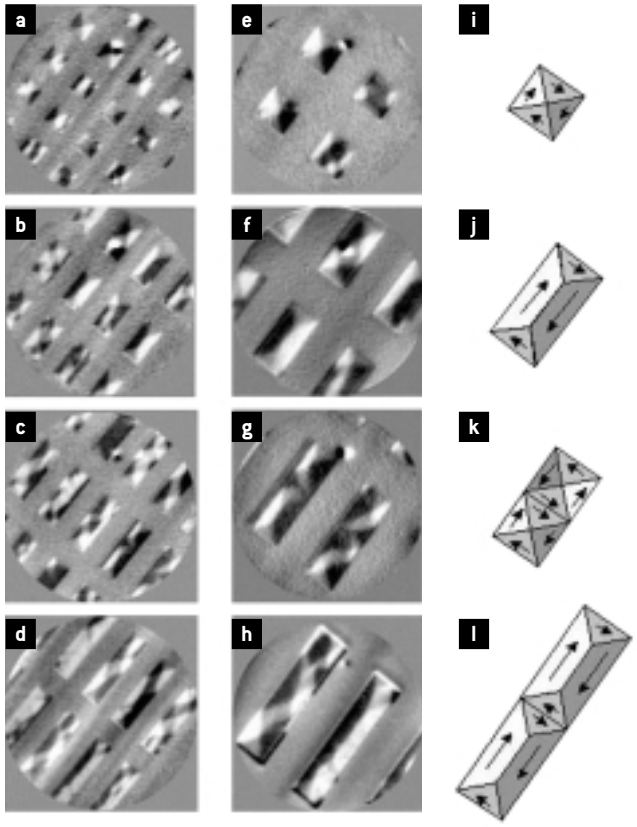

Figure 1. XMCDPEEM images of the magnetic domain structure of 15 nm thick and 1 µm wide polycrystalline Co elements with aspect ratios from 1:1 to 4:1. **a) – d)**: overview, **e) – h)**: selected regions, **i) – l)**: some simple **M** distributions. In all images **M** is parallel to the in-plane component of $\boldsymbol{\sigma}$ in the black regions, antiparallel in the white regions and perpendicular to it at the neutral grey level. The black-white dot in the upper part of the images results from a defect on the channel plate and the image shift correction; the stripes in the nonmagnetic background are caused by the beam drift between the images taken with opposite helicity.

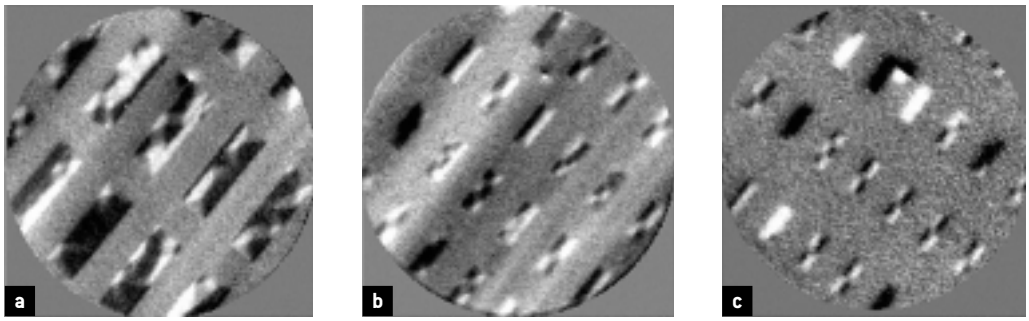

Figure 2. XMCDPEEM images of elements with constant aspect ratio but width decreasing from 1 µm **a)** via 0.5 µm **b)** to 0.25 µm **c)**. Field of view 10 µm **(a,b)** and 5 µm **c)**.

except for some rearrangements for local energy minimization.

This observation of the virgin state is also relevant for magnetic switching which usually does not occur via simple magnetization rotation but also by nucleation so that similar intermediate states can occur. The question arises then to what extent the domain structure becomes simpler with decreasing dimensions, which decreases the number of nucleation sites. Figure 2 gives the answer for an aspect ratio 3:1. Even at the smallest width (0.25µm) up to three domains are visible, together with two-domain and single-domain patterns. The resolution is insufficient to identify the individual domains but they are most likely vortex domains as seen in the larger elements. Smaller elements will be the subject of future work with the energy filter-equipped instrument in order to determine the size at which all elements are single-domain in the virgin state.

A quite different problem was addressed in the study of the ring-shaped elements that have attracted considerable interest recently [4]: how does the remanent state domain structure depend upon ring width, film thickness, distance between rings and magnetic history? This question was investigated by studying patterns of 34 nm and 10 nm thick rings with 1.6 µm outside diame-

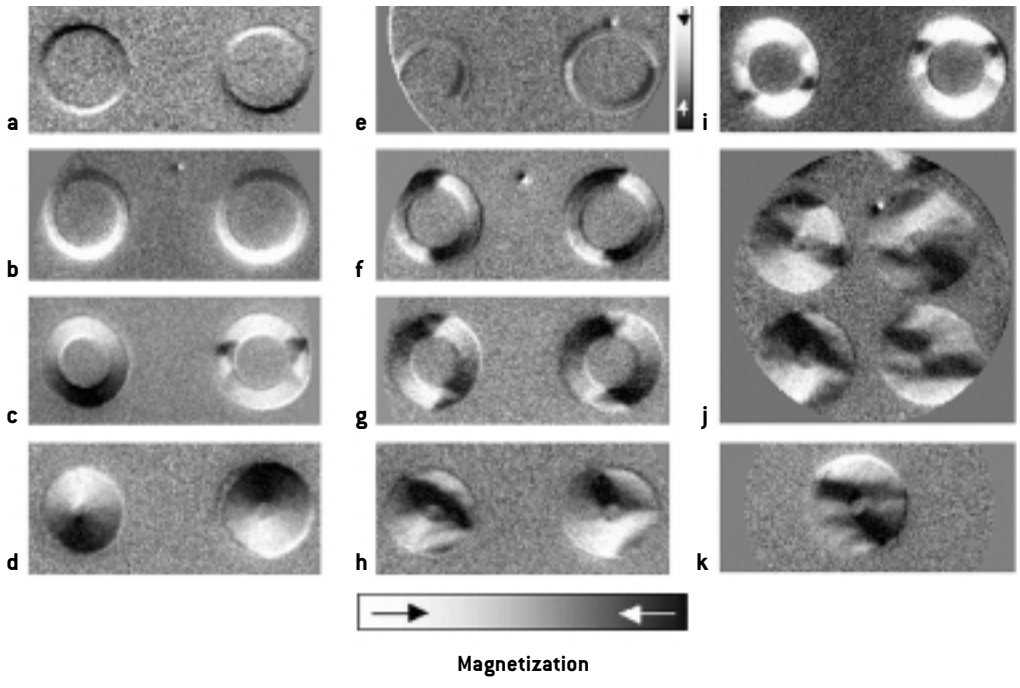

Figure 3. XMCDPEEM images of ring-shaped elements with 1600 nm outside diameter. **a) – d)**, **i)**: 34 nm thick rings, all others: 10 nm thick rings. The widths are from top to bottom 100 nm, 200 nm, 350 nm and 700 nm. The right side illustrates some cases discussed in the text.

ter and widths of 700, 350, 200 and 100 nm. Figure 3 illustrates the result of this study by a number of typical domain configurations, which were obtained by imaging at remanence after a field of less than 1 kOe had been applied. The images a) – d) and i) are from 34 nm thick films, the other images from 10 nm thick films. The ring width increases from top to bottom from 100 nm to 700 nm. In the 100 nm and 200 nm, 34 nm thick films only the vortex state was observed with both clockwise and counterclockwise circulation. This is due to the fact that the applied field was high enough to switch the 100 nm and 200 nm wide rings into the vortex state but not into the "onion state" that will be discussed below [4]. No influence of the distance between the rings was seen except when they touched. In the case of touching rings, effectively an anti-dot array is created and then the magnetic domains extended over several rings. For the 350 nm wide rings the applied field lies within the switching field distribution from the vortex to the onion state. Thus some rings have already switched into the so-called onion state, which is characterized by two head-to-head domain walls as seen in Figure 4 b) and c). The rings with higher switching field have remained in the vortex state, so that both states occur simultaneously, in a ratio of about 4:3. In the onion state the magnetization on opposite sides of the ring points in the same direction so that two head-to-head domains walls are formed. The wide rings have vortex head-to-head walls (Figure 4 b)) and as shown in image i) of Figure 3, there are two possible orientations of the vortex walls (in Figure 4 b) the circulation in the left vortex is clockwise, in the right vortex counterclockwise). The spin structure of the vortex walls is very well reproduced by the micromagnetic simulations in Figure 4. For extremely wide rings (Figure 3 d)) the onion state is not stable at remanence as shown by hysteresis loop measurements [4]. So even though the rings had been switched into the onion state by the applied field, they have reverted to the vortex state upon lowering the field as seen in Figure 3 d).

The 10 nm thick rings have lower switching fields, which means that all the rings have been switched into the onion state as seen in Figure 3 e) – h). The few rings with 100 nm width that have survived the preparation process undamaged are predominantly in the onion state with transverse head-to-head walls (as simulated in Figure 4 c), the rings with 200 nm and 350 nm width f), g) are exclusively in the onion state with transverse walls and those with 700 nm width h), j), k) have a complex domain structure that is presently being studied with micromagnetic simulations. As long as the rings do not touch, the distance between them has no noticeable influence on the domain structure as illustrated in image j) of Figure 3.

CONCLUSIONS

From these ring studies the conclusion can be drawn that wide and thick rings show onion states with vortex head-to-head walls, whereas narrow and thin rings exhibit transverse walls in agreement with micromagnetic simulations. Very wide and thick rings do not exhibit a stable onion state at zero field and here the lowest energy state is the vortex state.

The results demonstrate the superiority of XMCDPEEM over SEMPA (scanning electron microscopy with polarization analysis) that is more time-consuming and over MFM that tends to modify the domain structure and is more difficult to analyze.

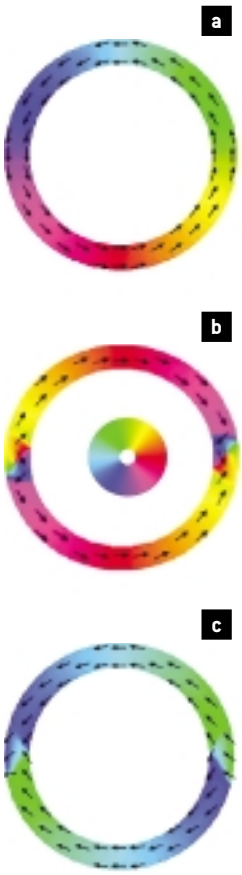

Figure 4. Micromagnetic simulations of the dominant spin structures in rings. **a)** vortex state, **b)** onion state with vortex head-to-head walls and **c)** onion state with transverse head-to-head walls.

References

[1] A. Hubert and R. Schaefer; *Magnetic Domains;* (Springer, Berlin 1998)

[2] J. Stoehr et al; *Science;* 259, 658, (1993)

[3] A. Locatelli et al; *Surf. Rev. Lett.*; 9, 171, (2002)

[4] M. Klaeui et al; *J. Phys.: Condens. Matter;* 15, R985, (2003)

DOPING-DEPENDENT ELECTRONIC STRUCTURE OF Na-MANGANITES DETERMINED BY RESONANT X-RAY EMISSION

> M. Platè
Dipartimento di Fisica, Università di Pavia, Via Bassi 6, 27100 Pavia, ITALY

> F. Bondino, M. Zacchigna, M. Zangrando
INFM-TASC, Beamline BACH, AREA Science Park, 34012 Basovizza, Trieste, ITALY

> I. Alessandri
Lab. di Strutturistica Chimica, Università degli Studi di Brescia, 25123 Brescia, ITALY

> D. Cocco, M. Matteucci, K.C. Prince
Sincrotrone Trieste-ELETTRA - S.S. 14 km 163,5, in AREA Science Park, 34012 Basovizza, Trieste, ITALY

> A. Comin
Dipartimento di Matematica e Fisica, Università Cattolica del Sacro Cuore, Brescia, ITALY

> F. Parmigiani
INFM-TASC, Beamline BACH, AREA Science Park, 34012 Basovizza, Trieste, ITALY
Dipartimento di Matematica e Fisica, Università Cattolica del Sacro Cuore, Brescia, ITALY

INTRODUCTION

High-storage-density magnetic devices require materials with a large magneto-resistance (MR) near room temperature. The recent discovery of doped manganites – $Ln_{1-x}A_xMnO_3$ - (Ln = Lanthanides; A = alkali or alkaline earth metals) promises to satisfy this technological demand. For this reason an intense effort has been devoted to synthesizing new doped manganites and to understanding the origin of the unique properties shown by these intriguing materials [1].

In these mixed oxides the colossal magnetoresistance phenomenon is accompanied by a wide range of exotic behavior such as magnetic ordering, a metal-insulator transition, charge and orbital ordering. In addition, depending on temperature, pressure and doping, they exhibit very rich phase diagrams, including insulating antiferromagnetic, paramagnetic and metallic ferromagnetic phases [1].

The beautiful complexity of these phenomena arises from the interplay among several competing structural and electronic mechanisms, not fully understood, such as double exchange and cooperative Jahn-Teller (J-T) distortions. In particular, ambiguities and missing information about the interplay between occupied and unoccupied states as well as controversies concerning the strength of the electronic correlations and the size of the energy band gap need to be addressed.

A powerful technique to investigate the elementary excitations in solids with element specificity is Resonant Inelastic X-ray emission Spectroscopy (RIXS). In RIXS an incident x-ray photon excites a core electron to the absorption threshold, and the x-ray emission resulting from the decay of the excited state is energetically analyzed. In recent years this spectroscopy has progressed remarkably, becoming an extremely effective tool to study low-energy neutral electronic transitions, charge transfer (CT) excitations, inter-band transitions and energy band dispersion [2].

The aim of this experiment was to study the X-ray emission from $La_{1-x}Na_xMnO_3$ (x = 0, 0.08 and 0.15) compounds. In these manganites the J-T effect, that favors the double exchange and hence the ferromagnetic pairing of the spins, is less pronounced with respect to systems doped with divalent alkaline-earth ions (Ca and Sr).

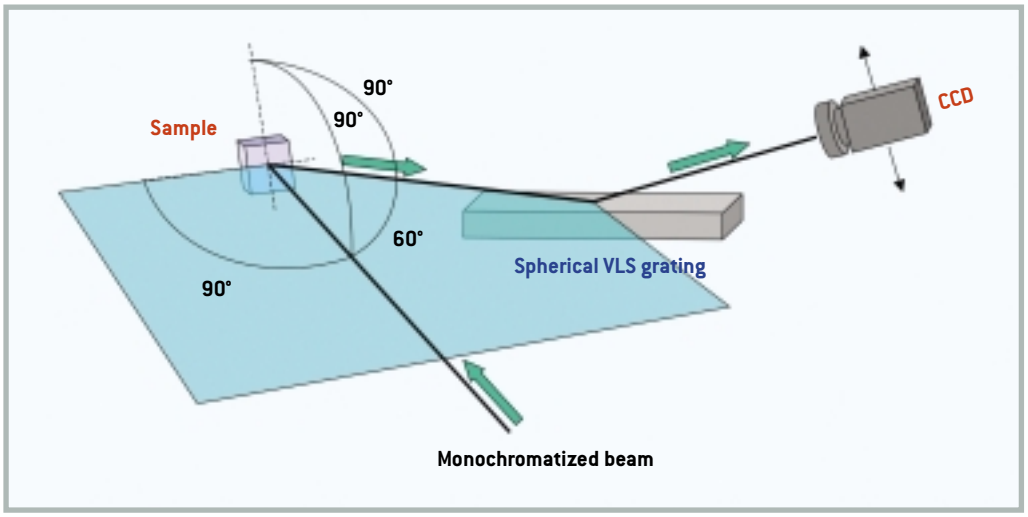

Figure 1. Experimental set-up and scattering geometry for RIXS measurements at the BACH beamline.

EXPERIMENTAL

The experiment was performed at the Beamline for Advanced diCHroism (BACH) [3] of ELETTRA. The resonant emission spectra were acquired with the ComIXS fluorescence spectrometer [4]. The spectrometer, based on an innovative optical design, is equipped with a detector consisting of a CCD camera with 20x20 μm^2 pixels, and two variable line spacing spherical gratings of central groove density 4800 l/mm (optimized for the 20-200 eV region) and 19200 l/mm (optimized for 150-1200 eV). The spectrometer exploits the small spot size, high flux and controllable polarization of BACH. The small spot size of the radiation on the sample (15x250 μm^2) allows the use of an entrance-slitless design and the collection of a solid angle of about 30×10 $mrad^2$.

The Mn L_3 emission spectra were recorded in fourth order diffraction with the 4800 l/mm grating and second-order diffraction with the 19200 l/mm grating. The energy bandwidth of the incident photon beam for RIXS was set at 0.7 eV at the Mn L_3 threshold, which corresponds to high flux and a resolving power of ~930. XAS spectra were obtained in total electron yield mode, measuring the sample drain current with a photon resolution of 0.28 eV. The incident photon energies were calibrated using the elastic peak measured in the x-ray emission spectra.

The scattering geometry and the experimental set up for the RIXS measurements are shown in Figure 1. The spectra were collected both with vertical polarization (*i.e.* the electric vector of the incident radiation perpendicular to the scattering plane highlighted in Figure 1) and horizontal polarization (*i.e.* the electric vector in the scattering plane).

The samples were 150 nm thin films of $La_{1-x}Na_xMnO_3$ (x = 0, 0.08 and 0.15) grown *ex-situ* on polycrystalline Al_3O_2 by radiofrequency magnetron sputtering. $LaMnO_3$ was obtained from La_2O_3 and Mn_2O_3, while $La_{1-x}Na_xMnO_3$ samples were prepared adding Na_2CO_3 to the lanthanum and manganese oxides. Details of the sample preparation are reported elsewhere [5]. The transition temperature T_c from the ferromagnetic metallic phase to the paramagnetic insulating phase was ~250 K and ~200 K for the x=0.15 and x=0.08 samples [5].

RESULTS AND DISCUSSION

Figure 2 b) shows the Mn $L_{3,2}$ RIXS spectra obtained with the 4800 l/mm grating, using vertically polarized radiation from the x= 0.08 sample at 300 K. In this configuration the peak at zero energy loss, i.e. the elastic peak, is visible in almost all the spectra, allowing an accurate calibration of the energy scale. The RIXS raw data are plotted against an energy loss scale relative to the

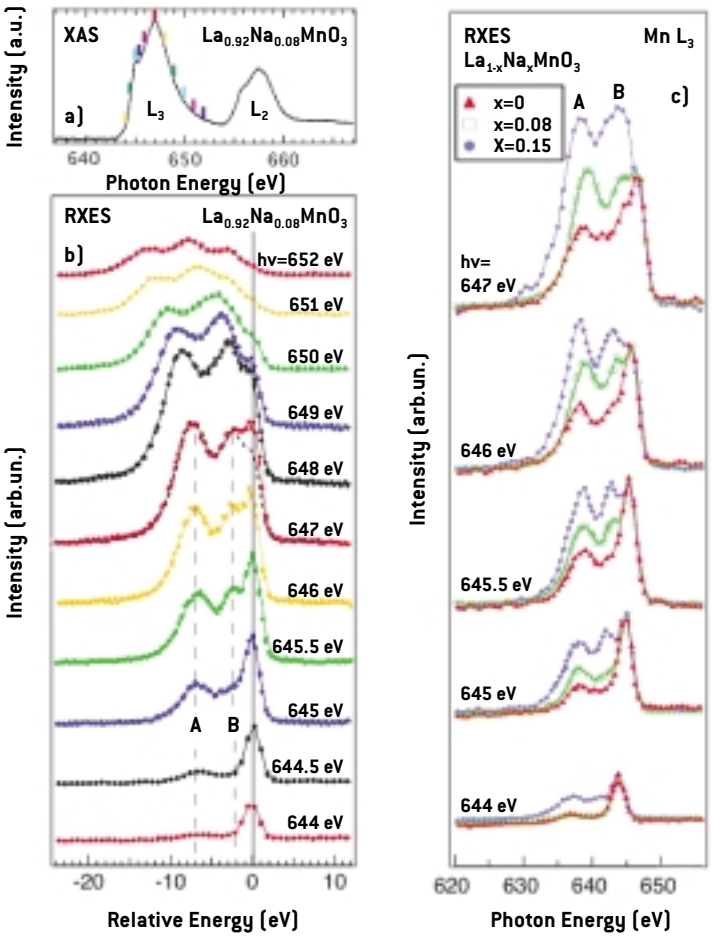

Figure 2. a) Mn $L_{3,2}$-edge XA spectrum of $La_{0.92}Na_{0.08}MnO_3$ at 300 K. **b)** RIXS spectra measured with the 4800 l/mm grating and vertical polarization from the same $La_{0.92}Na_{0.08}MnO_3$ sample at different excitation energies across the Mn L_3 threshold at 300 K. One of the spectra recorded with horizontal polarization is shown (black dotted line, at 640 eV excitation energy). The RIXS raw data are plotted against the transferred energy (curves are offset for clarity) and the excitation energies are indicated with ticks in the XA spectrum. **c)** Variation of the Mn 3d → 2p RIXS spectra of $La_{1-x}Na_xMnO_3$ with the doping concentration (x=0, 0.08 and 0.15).

elastic peaks. The excitation energies are indicated with ticks in the XAS spectrum shown in Figure 2 a).

Raman and fluorescence-like features can be easily identified. The fluorescence-like features appear at constant emission energy (hence, as dispersing peaks in the figure).

Resonating inelastic loss features appear at constant energy, below the elastic peak. Two well-resolved inelastic emission structures are observed between excitation energies 644 eV and 647 eV: a broad structure A at about 6-9 eV and another broad structure at about 2-4 eV below the elastic peak. The energy position of these inelastic losses is similar to those found in the Mn L_3 RIXS of $Eu_{1-x}Ca_xMnO_3$ and $Pr_{0.5}Sr_{0.5}MnO_3$ [6]. For the sake of comparison, some spectra were recorded with horizontal polarization, *i.e.* with the electric vector of the incident light in the scattering plane. In Figure 2 b), one of these spectra is displayed as a dotted line at hν = 647 eV. As expected from dipole transition selection rules [7], the elastic peak is strongly suppressed, confirming the assignment of this peak to the elastic channel.

Figure 2 c) shows the doping-induced changes in the electronic structure of $La_{1-x}Na_xMnO_3$. The spectra are displayed on an emission energy scale and the data are normalized to the elastic peak.

A set of higher resolution Mn L_3 spectra was obtained by using the 19200 l/mm grating. Figure 3 shows these spectra together with a possible decomposition of the individual spectral structures after Gaussian fitting with six components. The spectra are displayed against the transferred energy and the data are normalized to the photon flux. The single components have been respectively labeled with the letters E, B2, B1, A2, A1, D. The component on the far right is E

and refers to the elastic peak. Then four inelastic peaks can be resolved: a peak B2, which is located at -2.1 eV; a component B1 at -3.3 eV; A2 at -7.0 eV and A1 at -9.8 eV. Finally, a peak D, at constant emission energy, is detected at 635.4 eV.

The results of recent *ab-initio* partial DOS calculations for distorted orthorhombic $LaMnO_3$ derived from spin polarized density functional theory and the schematic diagram of the observed transitions are shown in Figure 4 [8].

According to these calculations, the dominant contribution to the density of states (DOS) close to the E_F is given by Mn $e_g\uparrow$-like bands, split by a strong electron-phonon coupling of the Jahn-Teller type. Mn t_{2g} electrons are well localized at –2 eV. Emission B [Figure 2 (b,c)] can be associated with *dd* transitions from the occupied t_{2g} electrons to the e_g-like empty states. Note that in RIXS spectroscopy the optically dipole forbidden *dd* transitions have a strongly enhanced cross-section.

Peak B is significantly more intense in the doped samples. This effect can be explained considering the weaker hybridization of the t_{2g} and O 2*p* electrons due to a less pronounced structural distortion induced by the doping ions. The strong enhancement of peak B in the doped samples can also be explained by the higher density of empty $e_g\uparrow$ states in the lower part of the CB related to the presence of the Mn^{4+} ions. This interpretation is consistent with the band observed in optical conductivity measurements at 2.3 eV and associated with the presence of Mn^{4+} and/or O^- self-trapped holes in possible non-stoichiometric $LaMnO_3$ samples [9].

Both the Mn- t_{2g}- and $e_g\uparrow$ bonding bands, hybridized with O 2p states, give a broad contribution in the occupied DOS around 5-6 eV. Peak A in Figure 2 (b, c) can be assigned to an electronic excitation from this band to the empty $e_g\uparrow$ band.

Finally, a loss structure appears at constant emission energy [peak D in Figure 3], however the origin of this feature require further investigations.

For a more detailed assignment of the spectral structures obtained from the Gaussian fitting, it is useful to compare the Mn L_3 RIXS data with resonant photoemission valence-band spectra (RPES) measured on $La_{1-x}Ca_xMnO_3$ manganites [10]. The latter spectra were decomposed using seven Gaussian-like features centred at 1.7 eV, 2.9 eV, 4.1 eV, 5.8 eV, 7.8 eV, 9.6 eV, 11.1 eV. In particular, the 2.9 eV and 4.1 eV emission features are assigned to Mn 3d states with t_{2g} and e_g ($3z^2$-r^2) symmetry respectively, and can be identified with the A2 and A1 RIXS spectral components. The 7.8 eV and 9.6 eV features are assigned to Mn 3d-O_{2p} π- and σ-bonds, and match well the B2 and B1 structures in the RIXS spectra.

It is also meaningful to compare the RIXS spectra with optical conductivity measurements for alkali-doped and undoped $LaMnO_3$. Optical conductivity essentially probes the same elementary excitations observed in RIXS but without elemental selectivity and different selection rules [11]. The optical absorption spectra display several broad bands at ~1.9-2.3, 4.6, 7, 9, 17 and 25 eV. The features at about 4.6 eV, 17 eV and 25.0 eV are not detected in RIXS spectra, for any doping. This observation leads to the conclusion that Mn ions are not directly involved in these transitions.

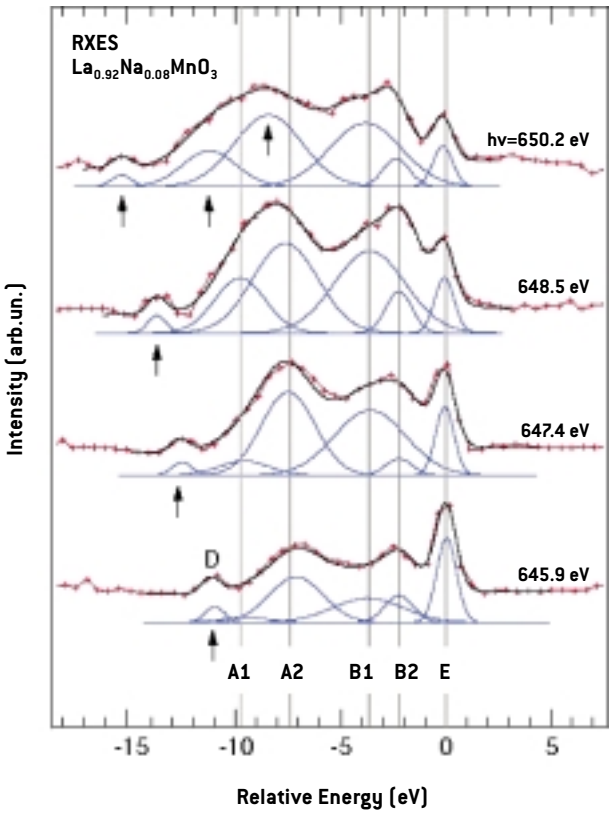

Figure 3. Experimental RIXS spectra (lines with markers) measured in second-order of diffraction with the 19200 l/mm grating at various incident photon energies and Gaussian fit of the inelastic peaks.

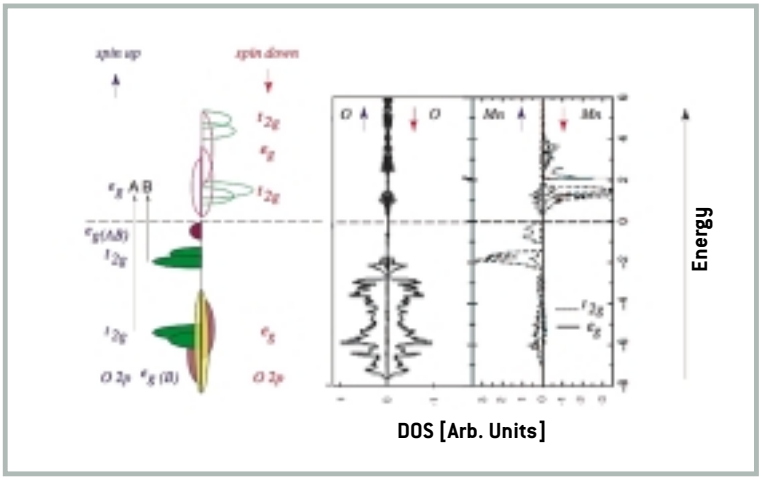

Figure 4. Mn 3d and O partial DOS for A-antiferromagnetic $LaMnO_3$ with orthorhombic $GdFeO_3$ structure obtained by full-potential linearized augmented plane-wave LSDA calculations. Adapted from ref. [8]

CONCLUSIONS

Here we have reported some of the first electronic structure results with the new ComIXS spectrometer, based on an innovative optical design, and mounted on the BACH Beamline at ELETTRA. The novelty of this work is the observation of significant variations of the low-energy electronic excitations for different carrier doping concentration. We explain these effects considering the weaker hybridization of the t_{2g} and O2p electrons due to a less pronounced structural distortion in the substituted samples and to the higher density of empty e_g majority states in the lower part of the conduction band. In this respect, the present RIXS data confirms the optical conductivity data at 2.3 eV where the presence of Mn^{4+} and O^- self trapped holes associated with non-stoichiometric $LaMnO_3$ was postulated.

ACKNOWLEDGMENTS

This work was supported by the INFM LdS-BACH project. We gratefully acknowledge M. Finazzi and G. Zampieri for useful suggestions and fruitful discussion.

References

[1] J.M. D. Coey et al.; *Adv. in Phys.;* 48, 167, (1999). E. Dagotto, *"Nanoscale Phase Separation and Colossal Magnetoresistance"*; Springer-Verlag (2002).

[2] See *J. Elect. Spectrosc. Rel. Phenom.*; 110-111, (2000).

[3] M. Zangrando, M. Finazzi, G. Paolucci, G. Comelli, B. Diviacco, R.P. Walker, D. Cocco, F. Parmigiani; *Rev Sci. Instrum.*; 72, 1313, (2001); M. Zangrando *et al.*; *Rev Sci. Instrum.;* submitted.

[4] D. Cocco, M. Matteucci, K. Prince, M. Zangrando; *Proceedings SPIE* 4506; 46, (2001).

[5] L. Malavasi, I. Alessandri, M.C. Mozzati, P. Ghigna, G. Chiodelli, C.B. Azzoni, G. Flor; *Phys. Chem. Chem. Phys.;* 5, 2274, (2003); C. Mozzati; unpublished results.

[6] E.Z. Kurmaev et al.; *J. Elect. Spectrosc. Rel. Phenom.;* 103, 793 (1999); E.Z. Kurmaev et al.; *J. Elect. Spectrosc. Rel. Phenom.;* 96, 187, (1998).

[7] M. Nakazawa, H. Ogasawara, A. Kotani, *Surf. Rev. and Lett.;* 9, 1149, (2002).

[8] P. Ravindran et al.; *Phys. Rev. B;* 65, 64445, (2002).

[9] N.N. Kovaleva et al., *Physica B;* 312, 737, (2002); *J. Exp. Theor. Phys.;* 94, 178, (2002).

[10] J. Zhang, D.N. McIlroy, P.A. Dowben, S.H. Liou, R.F. Sabirianov, and S.S. Jaswal, *Solid State Commun.;* 97, 39, (1996).

[11] T. Arima et al., *Phys. Rev. B ;* 48, 17006 (1993); Y. Okimoto et al., *Phys. Rev. B ;* 55, 4206 (1997); J.H. Jung et al., *Phys. Rev. B;* 55, 15489, (1997).

ELECTRON-VIBRON COUPLING IN LARGE ORGANIC MOLECULES

> R. Fink
Physikalische Chemie II, Universität Erlangen, Egerlandstraße 3, 91058 Erlangen, GERMANY

> D. Hübner, A. Schöll, E. Umbach
Experimentelle Physik II, Universität Würzburg, Am Hubland, 97074 Würzburg, GERMANY

> K.C. Prince
Sincrotrone Trieste-ELETTRA - S.S. 14 km 163,5, in AREA Science Park, 34012 Basovizza, Trieste, ITALY
INFM-TASC, Gas Phase Beamline at ELETTRA, 34012 Basovizza, Trieste, ITALY

> R. Richter
Sincrotrone Trieste-ELETTRA - S.S. 14 km 163,5, in AREA Science Park, 34012 Basovizza, Trieste, ITALY

> M. Coreno
CNR-Istituto di Metodologie Inorganiche e dei Plasmi, Area della Ricerca di Roma1, Monterotondo Scalo, ITALY
INFM-TASC, Gas Phase Beamline at ELETTRA, 34012 Basovizza (Trieste), ITALY

> M. Alagia
CNR-ISMN, Sezione Roma1, P. le A. Moro 5, 00185 Rome, ITALY

INTRODUCTION

The coupling of electronic transitions to vibronic excitations in molecules has been extensively studied in molecular physics with particular focus on valence electron excitations. With respect to core excitations, i.e. with excitations in the XUV regime, almost all studies with vibronic resolution were performed for di- (e.g., O_2 [1], CO [2,3]) or tri-atomic molecules (e.g., CO_2 [2,4]). Larger molecules like formaldehyde were investigated only recently [5]. Vibrational resolution in NEXAFS investigations of polymers (polystyrene) is due to local excitations in the respective functional groups [6].

For larger molecules the increased number of normal modes is usually believed to lead to an unresolvable superposition of fine structures. Only if one or few vibronic modes preferentially couple to the electronic excitation they might be resolved. So far the largest organic molecule with resolved fine structure at the O K-edge is the above mentioned formaldehyde. Here we report on high-resolution NEXAFS results for ANQ (acenaphthenequinone, structural formula see Figure 1, mass 182 amu) obtained in gas phase experiments at the ELETTRA Gas Phase Photoemission Beamline [7], which will be compared to ANQ data in the solid state [8].

EXPERIMENTAL

The experiment was performed at the Gas Phase Beamline [7] in a high vacuum chamber with a base pressure of 1 $\cdot 10^{-6}$. This beamline has a high spectral resolution ($E/\Delta E$=10000 at 540 eV [9]) which is necessary to resolve the vibrational fine structure in the absorption signal. The signal was detected using two channeltrons in a total counting yield mode for electrons and ions, respectively. For high resolution spectra a fixed mirror scan was performed with 5 meV steps in order to take advantage of the full monochromator resolution. Energy calibration was obtained with respect to O_2 (530.8 eV [10]) which was measured simultaneously in an absorption chamber behind the ANQ gas cell. The intensity normalization was done using the I_0 signal also recorded in parallel by a photodiode. The ANQ powder was sublimated at 430 K to achieve a reasonable flux such that a good signal-to-noise ratio could be achieved. The absolute energy calibration by using the maximum of the oxygen π^* resonance envelope is not straightforward. Many different

	Γ_L	Γ_G	E_A	E_V	ΔE_{FC}	$\chi h\nu'$	$h\nu'$	$h\nu_0$
Gas phase	97 meV	144 meV	529.00 eV	530.14 eV	1.14 eV	3.2 meV	200meV	390 meV
Solid state	97 meV	156 meV	528.98(1) eV	530.08(1) eV	1.10(2) eV	2.6(1) meV	200 (2) meV	383(10) meV

Table 1. All parameters from the peak fitting of the ANQ O 1s -> LUMO NEXAFS resonance in the gas phase as compared to the solid state results: Lorentzian (Γ_L) and Gaussian (Γ_G) line width, energy of the adiabatic (E_A) and vertical (E_V) transition, Franck-Condon shift (ΔE_{FC}), anharmonicity ($\chi h\nu'$), and vibronic energy in the core-excited ($h\nu'$) as well as in the ground state ($h\nu_o$).

values in the literature are reported so far ranging from 531.06 [13], 530.8 [9] to 530.521 eV [14]. The energy 530.8 eV was chosen because the resulting value for ANQ of 530.14 eV is only 60 meV off that of the solid state calibration (530.08 eV) in [8] which was done very accurately using calibrated Ag substrate lines. In Ref. [8] calculations of NEXAFS resonances are presented using the GSFC3-code developed by Kosugi [10,11]. The calculations yielded good results for both the energetic position and the intensity of bound π^* states of large organic molecules.

RESULTS AND DISCUSSION

In Figure 1 the high-resolution O K-edge NEXAFS spectrum of gas phase ANQ is shown together with peak fitting results and a solid state spectrum [8] of ANQ multilayers (top). From the above mentioned ab-initio calculations [8] it is known that only one electronic transition, the O 1s -> LUMO excitation, is responsible for this resonance. Thus, the fine structure of this single resonance can unambiguously be attributed to a vibronic coupling to the O 1s π^* excitation. The resonance has been fitted with Voigt peaks assuming the validity of the Franck-Condon principle based on a harmonic potential for the electronic ground ($V_{pot} = \alpha (R-R_E)^2$) and excited ($V_{pot}' = \alpha (R-R_E')^2$) state, respectively (R is the normal coordinate of the observed vibrational mode, R_E describes the equilibrium distance and α the harmonicity; the apostrophe ' indicates parameters in the electronically excited state). As boundary condition a single Gaussian and a single Lorentzian width were used for all fine structure peaks, and only these two values were varied. With these assumptions no satisfactory fitting result was obtained, as for the solid state case (compare [8]). Therefore a new approach was made taking an anharmonicity of the excited state potential into account (e.g., a Morse potential). Now the peak positions of the vibrational levels were additional free parameters. It turns out that for this assumption a very good description of the experimental data is achieved as can be seen from the essentially flat residuum in Figure 1 (enlarged by a factor 4). The energy positions of the fitted Voigt profiles indicated by the bar graphs on the bottom of Figure 1 clearly indicate the anharmonicity of the excited state potential since the distances between the vibrational levels decrease for increasing energy. Using an anharmonic Morse-potential $E(R) = E_D [1-e^{-a(R-R_E)}]^2$ the expansion for a small anharmonicity results in the energy eigenvalues $E_n = h\nu'\cdot(n+1/2) - \chi h\nu' (n+1/2)^2$ which is the sum of a harmonic potential plus an additional anharmoncity $\chi h\nu'$. This anharmonicity factor can be deduced from the fit in Figure 2 resulting in a value of 3.2 meV. This value is comparable to those found for other molecules like CO where it was found to be 1.7 meV [1]. The result and the perfect agreement between fit and data definitely justifies the approach with an anharmonic potential.

Additional information can be drawn from Figure 2. The lowest vibrational level ($\nu' = 0$) of the excited state is found at E_A = 529.0 eV, and therefore the vibronic energy in the excited state is 200 meV. The energy of the so called vertical transition which is the maximum of the measured envelope of the vibronic progression is E_v= 530.14 eV. From $\Delta E_{FC} = E_v - E_A$ we derive the Franck-Condon shift ΔE_{FC} = 1.14 eV, and hence the energy of the vibronic ground state can be estimated as 390 meV using the empirical formula $h\nu_o = h\nu' \cdot (\Delta E_{FC}/1.2 + 1)$. This energy fits only to a CH stretching mode at 381-386 meV [15] known from FTIR data and from Density Functional Theoretical calculations (GAUSSIAN 98 program packet).

The comparison of the gas phase results

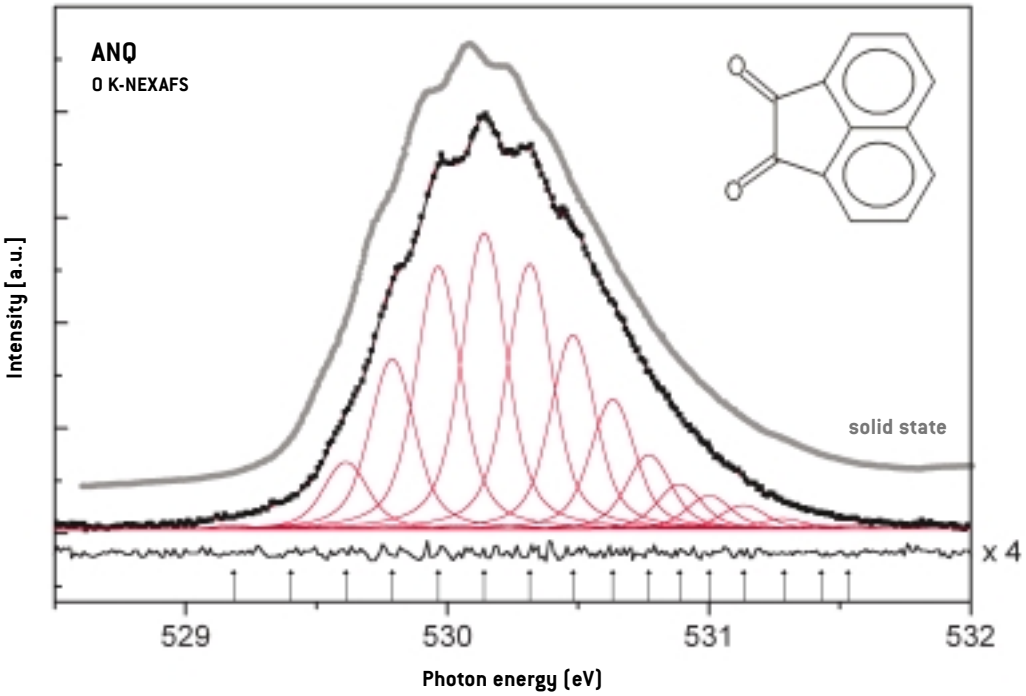

to those of the solid film which were independently determined reveals small differences as summarized in Table 1. The vibrational energies in the excited states hν' do not differ at all. The asymmetry of the Morse potential is slightly, but significantly larger in the gas phase experiment which may be a hint that the intermolecular interaction in the solid phase affects the excited state potential as well. The smaller Gaussian width indicates contributions from inhomogeneous broadening and/or phonons in the solid state spectra but this difference is surprisingly small. Another difference between gas phase and solid state spectra is of course the signal-to-noise ratio which is due to the much smaller density of molecules in the gas phase within the probed volume as compared to the solid film. However, a higher flux of molecules in the gas phase set-up would spoil the chamber environment and is therefore limited. Despite the larger error bars for the gas phase data no other assignment is possible: the O 1s excitation into the LUMO preferentially couples to only one vibration and that is a CH stretch vibration since there are no other ground state vibrations above 230 meV available.

CONCLUSIONS

The interesting aspects of these gas phase experiments are four-fold: First, ANQ is so far the largest organic molecule which unambiguously shows vibronic fine structure at the O K-edge. Second, an anharmonic potential in the first electronic excited state is found which can well be described by a Morse potential. Third, the derived vibronic excitation is only consistent with a C-H stretching mode in ANQ as derived from comparison with FTIR data and with DFT calculations. This in turn means that the local excitation at the O-atom of the carbonyl group directly couples to CH-modes via the delocalized electronic system. Fourthly, the similarity of the gas phase and solid state spectra clearly indicates that in this particular system the electron-vibron coupling is not drastically affected by neighbouring molecules.

ACKNOWLEDGMENTS

We thank N. Kosugi for sharing his GSCF3 program with us. This work is financed by the BMBF under contract 05 KS1 WWA 5. Travel support was provided by the European Union under the access to large scale fa-

Figure 1. Comparison of the O K-edge NEXAFS spectra of ANQ in the condensed phase (top) and gas phase (black dots) measured at ELETTRA's Gas Phase Beamline. Voigt profiles with identical line width were fitted to the gas phase spectra indicating the vibronic levels in the first electronic excited state. The unequal distances are indicated by bars in the lower section to visualize the anharmonicity of the potential of the excited state. The structural formula of ANQ is depicted in the top right. The energy scale was calibrated using a value of 530.8 eV [9] for the first O_2 NEXAFS resonance.

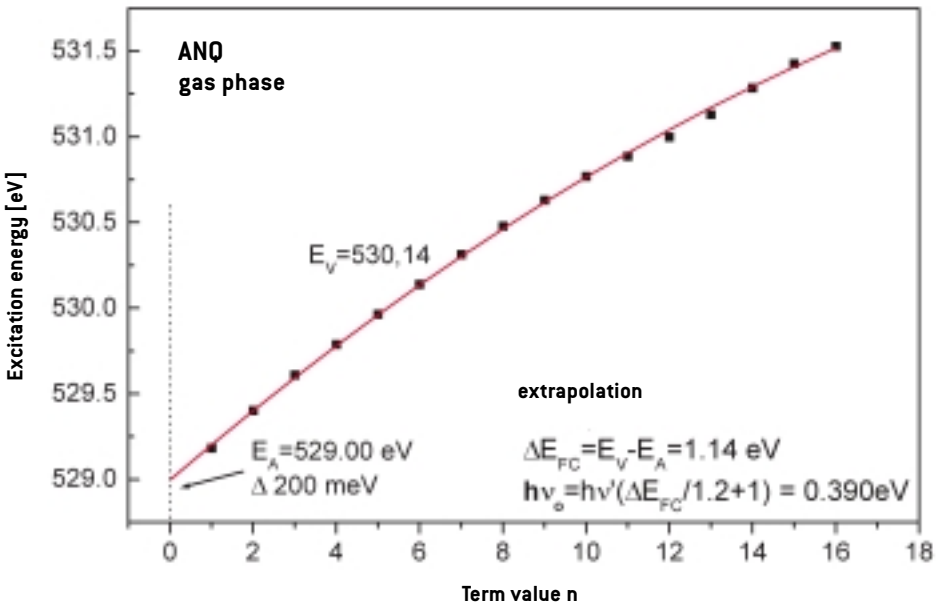

Figure 2. Energetic positions of the fitted resonances plotted versus the term value n. From the fitted red curve $E_n = h\nu' \cdot (n+1/2) - \chi h\nu' \cdot (n+1/2)^2$ the parameters E_0, $h\nu'$, the anharmonicity term $\chi h\nu'$ and the value of E_A can be deduced.

cilities, contract no. HPRI-CT-1999-00033. One of us (E.Umbach.) would like to thank the Fond der Chemischen Industrie for support.

References

[1] M. Coreno, M. de Simone, K.C. Prince, R. Richter, M. Vondracek, L. Avaldi, R. Camilloni; *Chemical Physics Letters;* 306, 269, (1999).

[2] Y. Ma, C.T. Chen, G. Meigs, K. Randall, F. Sette; *Physical Review* A; 44, 1848, (1991).

[3] Y. Jugnet, F.J. Himpsel, P. Avouris, E.E. Koch; *Physical Review Letters*; 53, 198 (1984).

[4] H. Koppel, F.X. Gadea, G. Klatt, J. Schirmer, L.S. Cederbaum; *Journal of Chemical Physics;* 106, 4415, (1997).

[5] K.C. Prince, R. Richter, M. de Simone, M. Coreno; *Surface Review Letters*; 9 159, (2002). A.B. Trofimov et al.; *J. Phys. B At. Mol. Opt. Phys.;* 36, 3805, (2003).

[6] H. Ade, St. Urquhart; *Chemical Physics Letters*; 322, 412, (2000).

[7] K.C. Prince, R.R. Blyth, R. Delaunay, M. Zitnik, J. Krempasky, J. Slezak, R. Camilloni, L. Avaldi, M. Coreno, G. Stefani, C. Furlani, M. de Simone, S. Stranges; *Journal of Sychrotron Radiation*; 5, 565, (1998).

[8] A. Schöll et al.; submitted to *Chemical Physics Letters.*

[9] R.R. Blyth, R. Delaunay, M. Zitnik, J. Krempasky, R. Krempaska, J. Slezak, K.C. Prince, R. Richter and M. Vondracek, R. Camilloni, L. Avaldi, M. Coreno, G. Stefani, C. Furlani, M. de Simone, S. Stranges, M.-Y. Adam; *Journal of Electron Spectroscopy and Related Phenomena*; 101-103, 959, (1999).

[10] A.P. Hitchcock, C.E. Brion; *Journal of Electron Spectroscopy and Related Phenomena*; 18, 1, (1980).

[11] N. Kosugi et al.; *Theoretical Chimica Acta;* 72, 149, (1987).

[12] N. Kosugi, H.Kuroda; *Chemical Physics Letters;* 74, 490, (1980).

[13] K.C. Prince, R. Richter et al.; *Journal of Physical Chemistry* A; 107, 1955, (2003).

[14] Y. Saitoh., H. Kimura, et al.; *Review of Scientific Instruments;* 71, 3254, (2000).

[15] Sigma-Alrich, FTIR spectroscopy reference 1(2), 82A.

SURFACE ELECTROMIGRATION PATTERNS IN A CONFINED ADSORBED METAL FILM: Ga ON GaN

> A. Barinov, L. Gregoratti, B. Kaulich, M. Kiskinova
Sincrotrone Trieste-ELETTRA - S.S. 14 km 163,5, in AREA Science Park, 34012 Basovizza, Trieste, ITALY

INTRODUCTION

Application of an electric field to a confined adsorbed metal film creates a diffusion bias and therefore can considerably affect the morphology of the surface or the interface. This phenomenon is known as Surface Electromigration (SE). Coupled to a complex surface dynamics governed by the interplay of adsorbate–surface and adsorbate–adsorbate interactions, it can lead to qualitatively different scenarios of surface behavior. In the case of surface electromigration the migration direction with respect to the electric field is specific to individual atoms. Moreover, the migration rate is coverage dependent and usually higher than that observed in the bulk [1].The main difficulty in quantitative description of SE is that the specific directional motion due to the electric field is accompanied by multidirectional thermal diffusion and the latter may dominate at high temperatures [2]. Another obstacle is that the presence of irregularities on the surface does not permit a straightforward application of atomic scale models of diffusion for understanding transport phenomena taking place on a larger mesoscopic scale. An experimental method well adapted for large scale dynamics studies, in addition to having spatial resolution, should on one hand allow averaging among the atoms of the same sort and on the other hand discriminate different phases of the material, the surface dynamics of which is under investigation.

EXPERIMENTAL

Using the scanning photoemission microscope (SPEM) at ELETTRA we tackled a model system, electromigration of a Ga confined film on a GaN (0001) surface aiming at shedding light on the following unanswered questions: (i) how the surface microstructure may affect the lateral distribution of the electromigrating species and (ii) how the superimposed thermal diffusion alters this distribution. Analysis of Ga 3d lineshapes allows identification of Ga states on the GaN surface, the first ML or interface gallium, called Ga-I phase and the metallic one, Ga-M phase which grows on top (Figure 1a). This has enabled us to follow spatial distribution of the two states inside the patch during and after thermal treatments and electromigration.

RESULTS AND DISCUSSION

Experimental results show that the development of different concentration profiles of the migrating Ga adatoms, involving formation of three-dimensional islands, and non-uniformity of the diffusion barriers beyond the edge of the confined Ga bilayer. The effects of directional electromigration and 'random' thermal diffusion are determined separately. The main temperature effect is

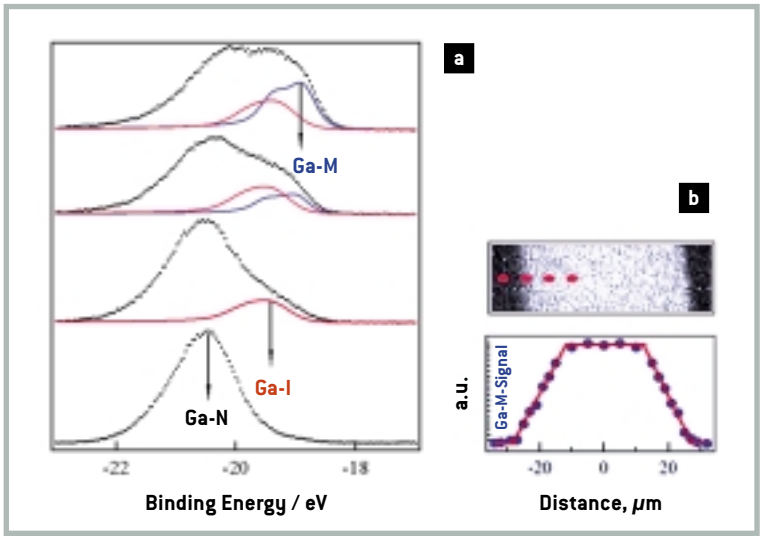

Figure 1. Ga 3d spectra **a)** taken from corresponding points of the image **b)** that shows concentration profile of Ga-M species, measured after deposition of Ga on a GaN substrate at room temperature.

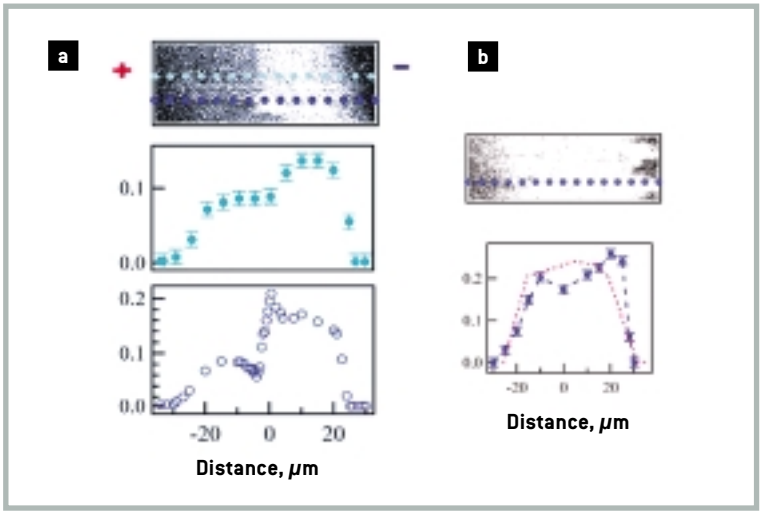

Figure 2. Ga-M images and the concentration profiles measured along the dashed lines, illustrating the Ga mass transport induced by the electric field at 200^0 C **a)** and 400 ^{0}C **b)**. In **b)** the red dashed line shows the profile measured in the absence of electric field.

the rearrangement of the top metallic Ga layer due to thermally activated diffusion favouring island formation, in a homogeneous manner, i.e. preserving the concentration profile shape of Ga-M, illustrated in Figure 1b, but with decreased intensity. The interfacial Ga-I phase appears less mobile and its intensity remains intact at the temperatures of the experiment.

The behaviour of the Ga confined bilayer on a GaN (0001) surface in the presence of an applied electric field is made clear by the concentration profiles measured across the Ga patch that has undergone electromigration. At temperature below 400 ˚C, the application of an electric field of 100 V/cm across the patch affects only the shape of the Ga-M concentration profile, as shown in Figure 2a. In this rearrangement the migration of the Ga-M atoms is confined only on top of the 'immobile' interfacial Ga-I phase. Only at the temperatures above 400 ˚C can expansion of the patch be observed as irregular protrusions along the electric field. The behaviour of the Ga confined bilayer on a GaN (0001) surface in the presence of an applied electric field has also revealed the important role of the surface microstructure and the adatom bonding configuration in SE-related effects occurring in adsorbed metal films. We suggest a scenario of low temperature electromigration that involves incorporation of electrically driven Ga-M atoms into immobile islands and island nucleation sites at surface defects. A simple model of general validity can explain the experimentally observed different EM-induced concentration profiles developed in the different regions of the confined film (Figure 2) in terms of variations in the density of vacancies and in the distribution of trapping centres (for a detailed discussion [3]).

At higher temperature the islands can function as sources of mobile atoms, and the borders become penetrable. These two facts generally lead to a situation where 'unrolling carpet' diffusion takes place. In our case this type of diffusion occurs at 400 ˚C revealing the defective nature of the GaN surface. Mobile species that manage to overcome the Ga-I plateau in the areas having a locally small diffusion barrier, provide a further mode of migration through a decrease of the diffusion barrier, and lead to the formation of the observed protrusions in Figure 2b.

CONCLUSIONS

In summary, the behaviour of the Ga confined bilayer on a GaN (0001) surface in the presence of an applied electric field has revealed the important role of surface microstructure and adatom bonding configuration in SE-related effects occurring in adsorbed metal films at different temperatures. The new findings are the strong effects of the presence of vacancies and trapping centres on the re-arrangements inside the confined bilayer during biased diffusion of the mobile atoms. We suggest a simple model of general validity which explains the experimentally observed different EM-induced patterns in the different regions of the confined film in terms of variations in the density of vacancies and in the distribution of trapping centres.

References

[1] J.M. Zhou, S. Baba, and A. Kinbara; *Thin Solid Films,* 98; 109, (1982).

[2] D. Kandel and E. Kaxiras; *Phys. Rev. Letts.*; 76, 1114, (1996).

[3] A. Barinov, L. Gregoratti, B. Kaulich, and M. Kiskinova, *Chem. Phys. Chem.;* 3, 1019, (2002).

GAS ADSORPTION ON SINGLE-WALLED CARBON NANOTUBES: EFFECTS OF CONTAMINANTS AND ENVIRONMENTAL MONITORING

> A. Goldoni, L. Petaccia, S. Lizzit
Sincrotrone Trieste-ELETTRA - S.S. 14 km 163,5, in AREA Science Park, 34012 Basovizza, Trieste, ITALY

> R. Larciprete
Sincrotrone Trieste-ELETTRA - S.S. 14 km 163,5, in AREA Science Park, 34012 Basovizza, Trieste, ITALY
CNR-IMIP - Zona Industriale, 85050 Tito Scalo (PZ), ITALY

INTRODUCTION

The nanocapillary properties of single-walled carbon nanotubes (SWCNTs) and their large specific surface area make these nanostructures potential materials for gas and energy storage. By accompanying such nanocapillarity with the capability of being sensitive to the adsorbed molecules, SWCNTs would certainly appear as the ideal systems for the realisation of nano-sensors for gas detection [1-6]. Indeed, recent theoretical [2-4] and experimental [5-6] reports claim that an exposure to ppm of molecules such as O_2, NO_2 and NH_3, can significantly affect the electronic and transport properties of the SWCNTs.

The positive point of these results is that nanotubes could be used as sensitive chemical sensors, offering several advantages in terms of active area, sensitivity and miniaturization compared to conventional devices based on metal-oxide materials and polymers. On the other side, the sensitivity to oxygen suggests that many of the measured electronic properties, thought to be intrinsic of nanotubes, may instead be due to extrinsic factors such as air exposure. Moreover, SWCNTs have been touted for their immense promise as components of future nano-computers and other nano-electronic devices. The fabrication of such nanotube-based devices will be complicated by their sensitivity to oxygen (or air).

The adsorption and interaction of gases with single-walled carbon nanotubes may influence the electronic and transport properties of SWCNTs as a consequence of the possible charge reorganization on bond for-

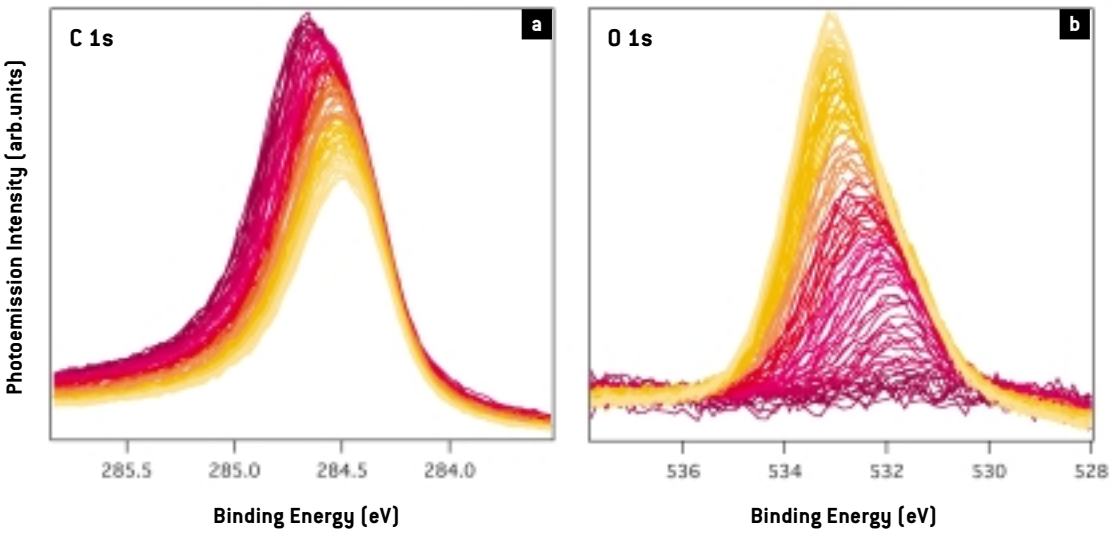

Figure 1. C 1s **a)** and O 1s **b)** spectra of the *bucky paper* flashed at 1800 K (Ni particles removed, but the Na photoemission signal still visible) measured while exposing the sample, kept at 150 K, to O_2 at a partial pressure of 10^{-7} mbar.

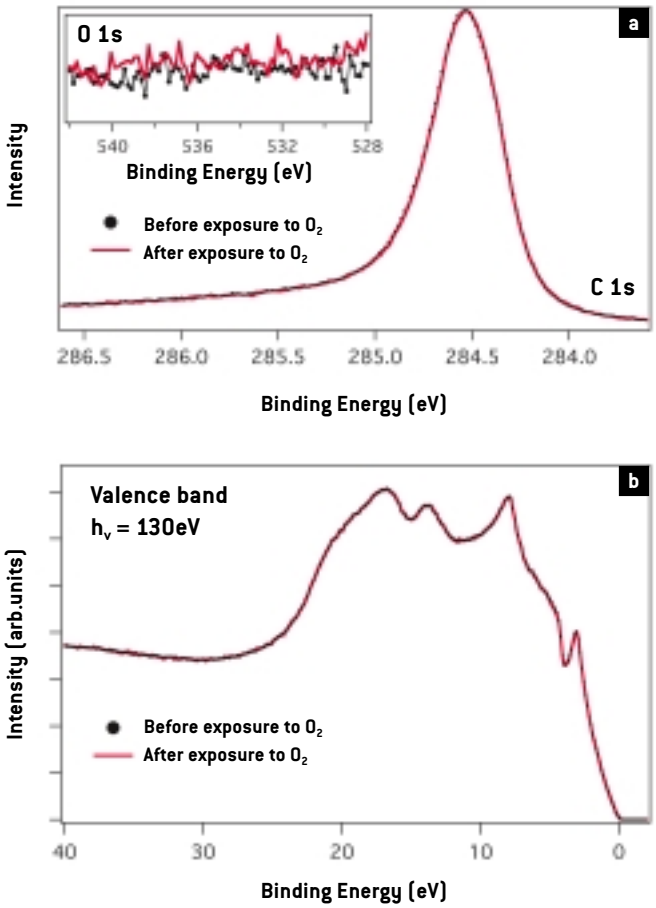

Figure 2. C 1s and valence band spectra of the clean SWCNT *bucky paper* before and after exposure at 150 K to one thousand of Langmuir of O_2 at a partial pressure of 10^{-6} mbar. Inset: spectral region were the O 1s emission should be expected.

mation. The gas molecules can interact directly with the SWCNTs *via* physisorption (interaction through dispersive van der Waals forces) or chemisorption (formation of chemical bonds). They could also indirectly affect the SWCNTs' properties by interacting with already present donors and/or acceptor centres due to contaminants bonded to the nanotube. Indeed, in spite of the already mentioned potential technological application of SWCNTs, the cleanliness of the sample is a delicate and crucial point that is often neglected, or at least not sufficiently taken into account, in experiments aimed at determining the nanotube properties.

The majority of techniques used to grow SWCNTs yield material containing tubes mixed with other entities, ranging from amorphous carbon, residual material from the graphite targets used in arc discharge or laser ablation, fullerenes and aromatic compounds. Moreover, the metal catalyst particles (Fe, Ni, Co) typically needed for nanotube growth also remain trapped in the material. Before being suitable for any further use the "as produced" material has to be purified [7-9]. The purification sequence usually starts with treatments in medium or strong acid baths to induce oxidation processes that remove the amorphous carbon part and attack the weakest sites in the SWCNTs, opening the caps and leaving their edges decorated with unsaturated, and therefore reactive, bonds. Prolonged and/or repeated baths can also dissolve the metal particles and produce an ensemble of entangled tubes, which are still unfeasible for the fabrication of a free-standing and compact sample. These baths, however, besides reducing the average nanotube length, can induce defects in the tube network damaging the graphene lattice. Moreover, catalyst residues can survive moderate acid attacks and remain in the material as round particles with diameter ranging from 2 to 50 nm. For further handling and manipulation, the SWCNTs are dispersed in surfactant solutions, filtered through μ-pore membranes, washed in NaOH and then dried to form a mat, so-called *bucky paper*. This is a free-standing, easy to handle, assembly of SWCNTs which can be manipulated and used for experiments as a normal bulk sample.

In spite of accurate protocols for contaminant elimination, apart from the presence of solid particles trapped in the *bucky paper*, traces of acids and surfactants can remain in the material adsorbed on the tube walls or trapped within the bundles. In a recent study [10], by using several techniques such as X-ray emission, photoemission microscopy and high-resolution photoemission spectroscopy, we investigated the presence of contaminants and impurities in a commercial purified *bucky paper* sample (stated purity > 90% vol.) and we determined the cleaning procedure in ultra-high-vacuum (UHV) conditions needed to eliminate these species. We were able to relate the nature, the amount and the distribution of such contaminants to the effects on the electronic and chemical properties of the SWCNT bundles. In particular, we found a large amount of Na, most likely a residue of the surfactant (Sodium Lauryl Sulfate) and of the NaOH bath, and catalyst particles (Ni in our case). These contaminants were completely removed only after a high temperature flash (1800 K) followed by a pro-

longed (> 2 h) annealing at 1270±30 K. After this treatment, minor quantities of other impurity elements (S and Si) remained in the material as localised clusters that do not interact with the SWCNTs and do not interfere with their properties.

Here, using fast photoemission spectroscopy, we address the issue of gas interaction with SWCNTs by looking for variation in the electronic spectra of SWCNTs and checking the presence of spectroscopic features indicative of gas adsorption while exposing the sample to gas molecules. First, using the exposure to oxygen as a key example, we will show that even traces of reactive contaminants (Na in this case) may influence the interaction of gases with SWCNTs. After complete removal of these contaminants the core level spectra of SWCNTs become insensitive to O_2, CO, H_2O and N_2, while a strong sensitivity to NH_3, NO, NO_2 and also SO_2 is observed, indicating SWCNTs could be powerful chemical gas sensors of these toxic molecules. The measurements were performed at the SuperESCA beamline, with the *bucky paper* sample mounted on a manipulator that allows cooling to 150 K and annealing up to 1800 K.

RESULTS AND DISCUSSION

Figure 1a shows the effect on the C 1s core level spectrum observed by exposing a sample, where small traces of Na were still present, to molecular oxygen. During the exposure the C 1s core level gradually shifted to lower binding energies, narrowing the line width. Simultaneously, a peak appeared in the photoemission binding energy region where the O 1s emission is expected, its intensity increasing with O_2 exposure (Figure 1 b). These changes in the photoemission spectra were completely reversible: by annealing the sample, mass selected thermal desorption spectra and O 1s photoemission spectra indicated that oxygen was released and correspondingly the C 1s spectrum evolved towards its initial shape and binding energy. Since the physisorption probability of molecular oxygen on SWCNTs in ultra-high-vacuum conditions is practically zero above 100 K [11], the released oxygen should have been chemisorbed. The changes observed in the C 1s core level during the oxygen exposure might be associated with a charge transfer from the carbon system to the bonded oxygen and apparently confirm a strong sensitivity of the SWCNT electronic properties to O_2. However, this is incorrect and the observed behaviour must be related to the presence of Na contaminants. Indeed, Figure 2 shows the C 1s core level and valence band photoemission spectra of a clean sample (i.e. after Na contaminant elimination) before and after exposure to 10^5 L of O_2. Both spectra remained absolutely unchanged after the exposure to oxygen and no O 1s core level peak, indicative of adsorbed oxygen species, was observed. The same happened in the case of N_2 and CO. In the case of H_2O, ice formed at 150 K on the sample, but the line shape and binding energy of the C 1s core level remained unaffected while dosing water, apart from the reduction of photoemission intensity due to the growing ice layer. It is worth noting that the C 1s spectrum of this sample remained unaffected also after air exposure at atmospheric pressure at both room and lower temperature. The above observations indicate that N_2, CO, H_2O and O_2 interact with clean SWCNTs *via* weak dispersion forces only and do not affect the electronic spectra (properties) of SWCNTs. In the particular case of O_2, this observation contrasts with the experiment of Collins et al. [5] and with some theoretical investigations [2], but agrees with more recent experiments [11] and calculations [12].

However, the exposures of the clean SWCNT sample to NH_3, NO, NO_2 and SO_2 molecules were accompanied by clear changes in the carbon photoemission features. These changes reflect new carbon chemical surroundings and sizable charge redistribution between the adsorbed species and the SWCNTs. Figure 3 shows the C 1s spectra measured in real-time with fast-photoemission during the exposure to NO, SO_2, NH_3, and NO_2 respectively. In all of the four cases the C 1s peak shifts and changes shape as the exposure time increases. The shift is toward lower binding energy and of comparable size in the case of NO, NO_2 and SO_2. In the case of NH_3 the shift is smaller and in the opposite direction, i.e. toward higher binding energies. If these binding energy shifts are ascribed to shifts of the nanotube chemical potential, the NO,

NO_2 and SO_2 molecules bound to SWCNTs act as charge acceptors, while the NH_3 molecules act as charge donors. In the case of NO_2 and NH_3 these observations are in full agreement with those reported by Kong et al. [6] and with recent calculations [3].

In Figure 4 we report the evolution of N 1s and S 2p photoemission spectra while exposing the sample to NO_2 and SO_2, respectively. Both spectra show the presence of several peaks that have to be ascribed to molecular species bonded to the SWCNTs. Systematic studies of SO_2 and NO_2 absorption on metal and oxide surfaces [13-16] indicate that in the case of N 1s spectra, the low binding energy component (401.5 eV) is due to NO species, while the component at 404 eV can be associated with a small fraction of NO_2 molecules and the most intense peak at 407 eV with NO_3 species. The S 2p spectra can be understood considering the tendency of SO_2 to form several species when chemisorbed on surfaces (namely S, SO, SO_3 and SO_4) and to easily react with water to form H_2SO_x acids [15, 16]. Apart from the broad peak at ~ 159 eV of binding energy, due to the sulfur clusters already present in the sample, the most intense S 2p doublet first appearing in the spectrum at ~ 167.3 eV (S $2p_{3/2}$) should correspond to chemisorbed SO_3 molecules. It is worth noting that in the very first spectra the signal coming from the precursor SO_2 molecules at ~ 165 eV is visible. The photoemission signal coming from the chemisorbed SO_3 molecules grows until saturation when a second broad peak appears as a bump at higher binding energy, and grows while moving towards higher binding energies. This second peak is due to the formation of H_2SO_x molecules.

Thermal desorption experiments (not shown here [10]), where the desorption of the nitrogen and sulfur oxide species has been followed in real time with fast-photoemission, indicated that the NO_2 molecules are physisorbed since the corresponding N 1s photoemission peak is already lost at 180 K, while the remaining NO and NO_3 species are chemisorbed and completely removed only above 800 K. In the case of SO_2, the acid peak is lost first with the formation of SO_4 at about ~ 300 K and then of atomic S above ~ 400 K. The SO_4 signal is already lost above 450 K, with the dissociation of the molecule and the formation of atomic S and O_2 molecules. The atomic S and the remaining chemisorbed SO_3 molecules are removed together above ~ 500 K and the process is complete above 800 K, when only the signal coming from the already present sulfur clusters remains visible.

Finally, we note from core level measurements that clear variations in the electronic properties of SWCNTs are detectable well above the noise level (1% of variation) after exposing the sample to ~ 40 L of NO, NO_2, SO_2 and NH_3. An exposure of 40 L means an exposure to a partial pressure of 10^{-5} mbar (i.e. 10 ppb of toxic molecules in air at atmospheric pressure) for about 4 seconds. In other words, SWCNT bundles at 150 K are able to feel the presence of 10 ppb of toxic gas in air in 4 s. For comparison, a typical solid-state sensor based on conducting polymers can detect a few ppm of NO, NO_2, SO_2 or NH_3 in a typical response time of 1 minute at room temperature, while the best commercial detectors based on metal oxides are sensitive to 30-100 ppb with a typical response time longer than 1 minute [17, 18].

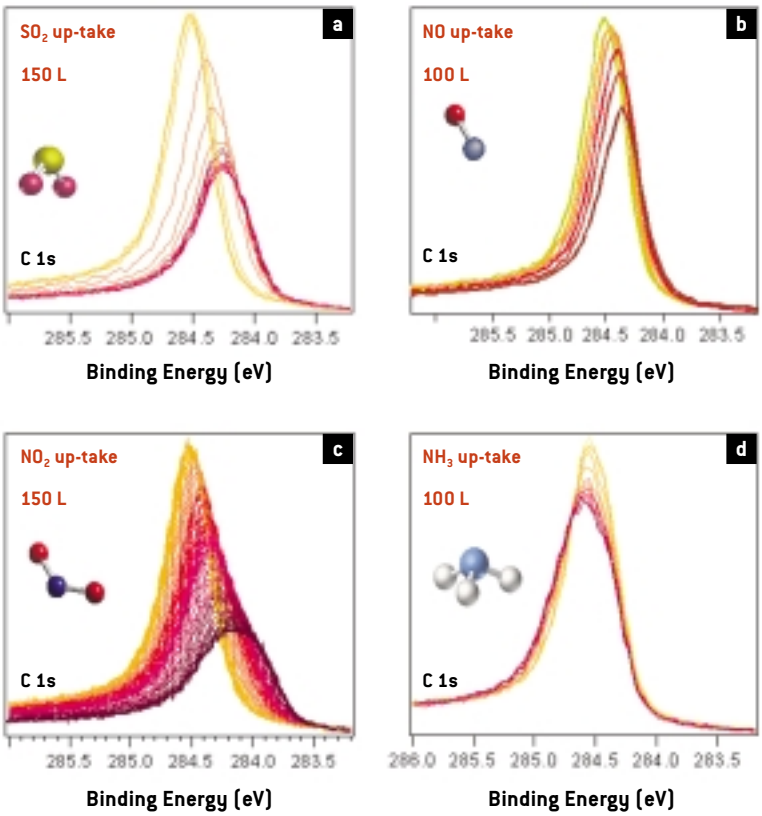

Figure 3. C 1s spectra of the clean SWCNT *bucky paper* measured while exposing the sample at 150 K to SO_2 **a)**, NO **b)**, NO_2 **c)** and NH_3 **d)** at partial pressures of about 10^{-8} mbar.

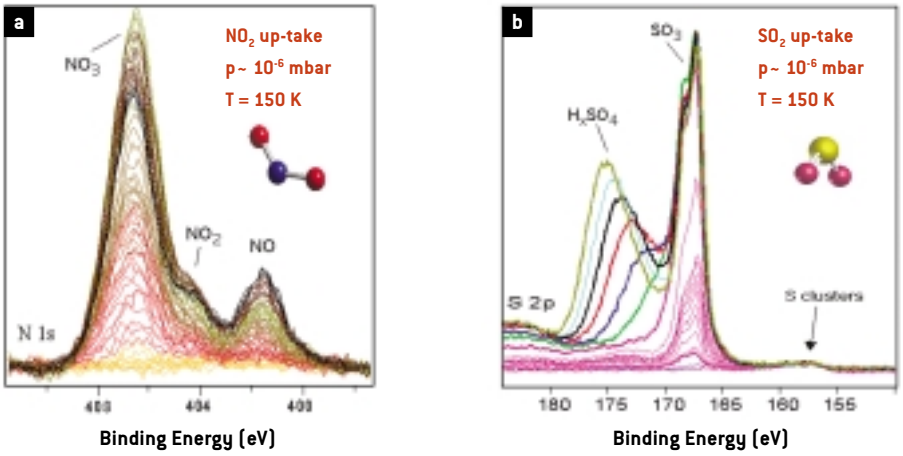

Figure 4. N 1s **a)** and S 2p **b)** spectra taken by fast photoemission on the clean SWCNTs kept at 150 K during the exposure to NO_2 and SO_2, respectively, at a partial pressure of 10^{-8} mbar.

CONCLUSIONS

In conclusion, we suggest that SWCNTs could find use as powerful chemical gas sensors of toxic molecules, being sensitive to environmentally significant quantities of hazardous gases like NO, NO_2, SO_2 and NH_3. Our results, however, indicate that many supposedly intrinsic properties measured on "as-prepared" or mildly annealed in vacuum nanotubes may be severely compromised by the presence of catalyst particles and contaminants. In particular, there is strong evidence that gas molecules present in air (e.g. O_2, H_2O and N_2) interact weakly with SWCNT bundles, through dispersion forces only and not by the formation of chemical bonds. We observe that the electronic structure, as reflected in the photoemission spectra of clean SWCNTs at 150 K, is not influenced by the exposure to these molecules. On the other hand, the data reported here demonstrate strong catalytic activity of purified SWCNTs to remove/trap nitrogen and sulfur oxide species. This is extremely important in environmental pollution catalysis since the NO_x and SO_x species released into the atmosphere are responsible for the acid rain that corrodes monuments and kills vegetables.

References

[1] O.K. Varghese *et al.* ; *Sens. Actuators* B; 81, 32, (2001).

[2] S.H. Jhi, S.G. Louie, M.L. Cohen ; *Phys. Rev. Lett.*; 85, 1710, (2000).

[3] H. Chang *et al.*; *Appl. Phys. Lett.*; 79, 3863, (2001); J. J. Zhao *et al., Nanotechnology;* 13, 195, (2002).

[4] S. Peng, K. Cho; *Nanotechnology*; 11, 57, (2000).

[5] P.G. Collins *et al.; Science;* 287, 1801, (2000).

[6] J. Kong *et al.; Science;* 287, 622, (2000).

[7] M. Monthioux *et al.; Carbon;* 39, 1251 (2001).

[8] I.W. Chiang *et al.*; *J. Phys. Chem.* B; 105, 1157, (2001).

[9] M. Moon *et al.*; *J. Phys. Chem.* B; 105, 5677, (2001).

[10] A. Goldoni *et al.*, *submitted for publication.*

[11] H. Ulbricht, G. Moos, T. Hertel; *Phys. Rev.* B; 66, 075404, (2002).

[12] P. Giannozzi, R. Car, G. Scoles; *J. Chem Phys.;* 118, 1003 (2003).

[13] T. Jirsak, M. Kuhn and J.A. Rodriguez; *Surf. Sci.*; 457, 254, (2000); J.A. Rodriguez *et al.; J. Phys. Chem.* B; 104, 319, (2000); J.A. Rodriguez et *al.* ; *J. Chem. Phys.*; 112, 9929, (2000).

[14] J.A. Rodriguez *et al.* ; *Chem. Phys. Lett.;* 330, 475 (2000); J. Schmitz and R.J. Baird; *J. Phys. Chem* B; 106, 4172, (2002).

[15] H. Lu *et al.*, *Vacuum;* 49, 171, (1998).

[16] T. Jirsak, J.A. Rodriguez ; *Langmuir*; 16, 10287, (2000); J.A. Rodriguez *et al.*, *Surf. Sci .;* 477, L279, (2001).

[17] S.J. Qin *et al.*, *Sensors and Actuators B;* 66, 240, (2000).

[18] T.K. H. Starke, G.S.V. Coles, H. Ferkel, *Sensors and Actuators B;* 85, 239, (2002).

AN XPS SPECTROMICROSCOPIC STUDY OF Mo-S BASED NANOTUBES

> J. Kovac, A. Zalar, M. Remskar, A. Mrzel, D. Mihailovic
Jozef Stefan Institute, Jamova 39, 1000 Ljubljana, SLOVENIA

> L. Gregoratti, M. Kiskinova
Sincrotrone Trieste-ELETTRA - S.S. 14 km 163,5, in AREA Science Park, 34012 Basovizza, Trieste, ITALY

INTRODUCTION

Due to small dimensions, low dimensionality and high anisotropy nanotubes exhibit a large variety of mechanical and electronic properties, which makes them an excellent material for nanotechnological applications. Despite the fact that most attention has been dedicated to the study of C nanotubes, inorganic nanotubes have already been fabricated. Among them single-wall $MoS_{2-x}I_y$ ($0<x<1$, $y<1$) nanotubes, synthesized for the first time by some of the authors of this work, represent the smallest known inorganic nanotubes [1, 2]. These Mo-S based nanotubes show interesting electron field-emission characteristics [3], very low shear modulus [4], a potential use for Li-ion batteries [5] and interesting electron spin resonance phenomena [6]. They were synthesized by a catalyzed transport reaction involving C_{60}. On the basis of X-ray and electron diffraction data a model structure was proposed consisting of sulphur-molybdenum-sulphur cylinders with diameter of 0.96 nm. It was shown that the $MoS_{2-x}I_y$ nanotubes grow in twisted chiral bundles perpendicular to the substrate surface. The self-assembly of the bundles of nanotubes into various regular geometrical shapes was observed indicating an attractive interaction among the nanotubes and the possibility of handling single tubes. The bundles are a few tens of microns long, from 100 to 500 nm wide and composed of individual, parallel and ordered nanotubes.

However, the structural characterization of these nanotubes is not sufficient for understanding their electronic properties which, as in the case of C-nanotubes, should be determined to a great extent by the chemical bonding within and between the MoS_2 units. A main obstacle for thorough characterization of the chemical and electronic properties of the $MoS_{2-x}I_y$ tubes is that, to probe these properties, appropriate "microscopic" analytical tools are needed. The high photon flux of the third generation synchrotron light source ELETTRA combined with the high spatial resolution (100 nm) achievable at the ESCAmicroscopy beamline allowed us to localize the nanotube bundles (~ 10 microns long and up to 0.5 micron wide) and select areas for systematic laterally resolved photoemission measurements along the axes of the tubes, providing important details about the electronic properties and chemical bonding of these dichalcogenide based nanotubes.

Figure 1. Scanning electron microscope (SEM) image of bundles of aligned $MoS_{2-x}I_y$ nanotubes.

Figure 2. Scanning photoemission image (38x38 μm) of bundles of the $MoS_{2-x}I_y$ nanotubes taken with Mo 3d signal.

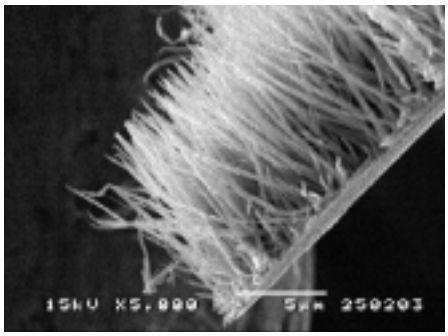

FIGURE 1

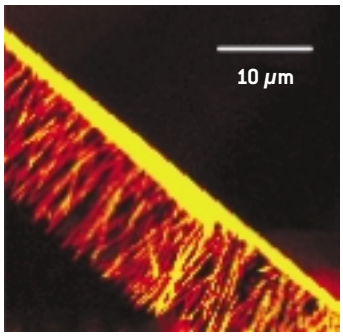

FIGURE 2

FIGURE 3

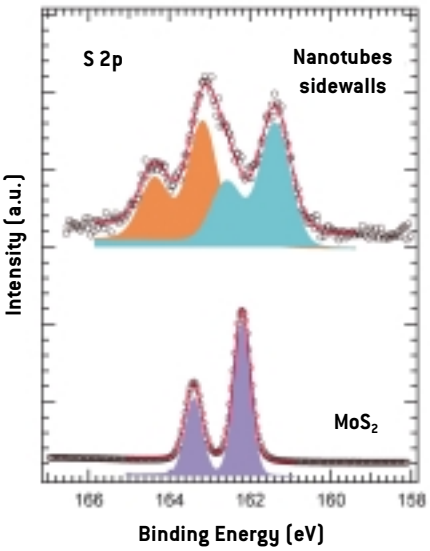

FIGURE 4

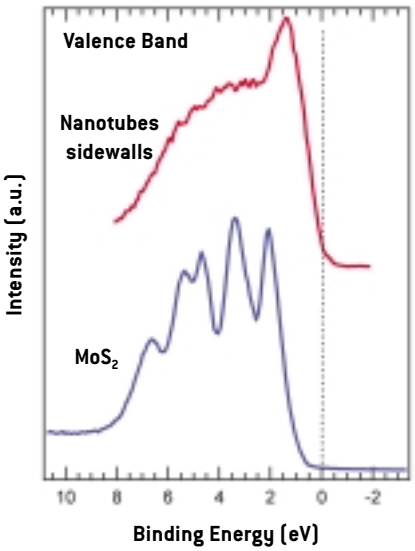

Figure 3. S 2p photoemission spectra from nanotubes sidewalls and from MoS_2 crystal

Figure 4. Valence band spectra from nanotubes sidewalls and from MoS_2 crystal

EXPERIMENTAL

The $MoS_{2-x}I_y$ nanotubes were prepared by the iodine transport method using C_{60} as the growth promoter [1]. The transported material, in the form of foil was mounted into the Mo sample holder and analysed by scanning photoemission microscope (SPEM) at the ESCAmicroscopy beamline. The energy of the photon beam was 496 eV.

RESULTS AND DISCUSSION

Figure 1 shows a scanning electron microscope (SEM) image of bundles of aligned $MoS_{2-x}I_y$ nanotubes. A similar area of the sample was analysed also by the SPEM microscope. A cross-sectional image obtained by Mo 3d photoelectrons is shown in Figure 2. The S 2p, Mo 3d, I 4d and the valence band spectra were taken at the tips and sidewalls of the tubes. All of them are strongly affected by the low dimensionality of the $MoS_{2-x}I_y$ nanotubes and they differ significantly from the corresponding spectra taken on the reference MoS_2 crystal. Figure 3 shows a comparison between the S 2p spectra from the sidewalls of the nanotubes and from the MoS_2 crystal. The spectrum from the nanotube sidewalls is broader and clearly shows the presence of at least two S 2p doublets. We suggest that the two S 2p components from nanotubes reflect inner and outer positions of sulphur atoms in strongly bent S-Mo-S sheets in nanotubes as well as a bonding of outer sulphur atoms to the iodine atoms at interstitial positions between the tubes. The valence band spectra from the nanotubes (Figure 4) show a finite density of electronic states at E_F that makes electronic properties of the $MoS_{2-x}I_y$ nanotubes different from those of the MoS_2 crystal. The metallic character of these tubes suggests possible applications as molecular wires.

CONCLUSIONS

In this report we have shown the capabilities of laterally resolved photoemission to study electronic properties and chemical bonding of $MoS_{2-x}I_y$ nanotubes.

ACKNOWLEDGMENTS

The experiment at ELETTRA was supported by the ICTP-ELETTRA Users Program.

References

[1] M. Remskar *et al.; Science*; 292, 47, (2001).

[2] M. Remskar *et al.; Advanced Materials;* 15, 237, (2003).

[3] V. Nemanic *et al.; Applied Physics Letters*; 82 (25), 4573, (2003).

[4] A. Kis et al.; *Advanced Materials*; 15, 733, (2003).

[5] R. Dominko et al.; *Advanced Materials;* 14, 1531, (2002).

[6] D. Arcon et al.; *Physical Review B*; 67, 125423, (2003).

AN ELECTROCHEMICALLY CONTROLLED SURFACE REACTION

> B. Luerßen, H. Fischer, J. Janek
Physikalisch-Chemisches Institut Justus-Liebig-Universität Gießen, Heinrich-Buff-Ring 58, 35392 Gießen, GERMANY
> S. Günther
Institut für Physikalische Chemie und Elektrochemie Universität Hannover, Callinstr. 3-3A, 30167 Hannover, GERMANY
> L. Gregoratti, M. Kiskinova
Sincrotrone Trieste-ELETTRA - S.S. 14 km 163,5, in AREA Science Park, 34012 Basovizza, Trieste, ITALY

INTRODUCTION

Over the last twenty years, special attention was directed to the electrochemical promotion of catalysis (EPOC). Electrochemical polarisation of catalytically active materials offers the unique possibility of in situ control of their reactivity. Nevertheless, the underlying processes at the three phase boundary between metal, solid electrolyte and the gas phase as well as the microscopic mechanism of the promotion are not yet unambiguously resolved. The scanning photoelectron microscope (SPEM) at the ESCA microscopy beamline provides the possibility to image morphological and chemical changes of surfaces during catalytic processes as can be seen in the examples below.

EXPERIMENTAL

For our investigations we used a model system consisting of an YSZ single crystal (YSZ = yttria stabilized zirconia) and a dense platinum electrode prepared via pulsed laser deposition (PLD). The experimental setup of the electrochemical cell Pt/YSZ/Pt is depicted schematically in Figure 1. If the working electrode is polarized anodically, oxygen ions are transported through the solid electrolyte and deposited at the three phase boundary.

The lack of oxygen permeability of these PLD electrodes can be shown by making use of the capability of the SPEM to image changes in the topography of a surface. In the present case the Pt 4f intensity was monitored while mechanically scanning the sample with respect to the focused photon beam and collecting photoelectrons of the corresponding selected kinetic energy with a hemispherical analyzer. Then the working electrode was polarized anodically for a few minutes. The changes of the surface area are shown in Figure 2. The longer we polarize the more oxygen accumulates between the electrode and the solid electrolyte. Since the Pt electrode acts as a barrier for the oxygen penetration towards the electrode surface the electrochemically induced pressure of the accumulated oxygen rises significantly (part (a) of Figure 2 illustrates the process schematically). Therefore, an increasing number of bubbles becomes visible and can be imaged with the spectromicroscope in situ (parts (b) – (d) of Figure 2). It is important to note that the formation of bubbles is an indirect proof for the low permeability by oxygen of the dense platinum electrode.

In Figure 3 we make use of the chemical sensitivity of the SPEM in order to image the spillover of oxygen through a hole in the electrode onto the platinum surface. Due to the fast surface *diffusion* of oxygen on platinum it is not possible to observe the oxygen diffusion process directly. Therefore, we chose an indirect way of imaging a surface *reaction*. For this purpose, we deposited a thin carbon film on the platinum electrode by exposing the surface to ethylene at elevated temperatures, about 400 °C. The analyzer spot was focussed on a hole in the platinum electrode (marked with a circle in Figure 3). Two types of image sets were taken by collecting C 1s and Pt 4f photoelectrons. In the latter imaging mode the contrast of the C 1s images is reversed since the

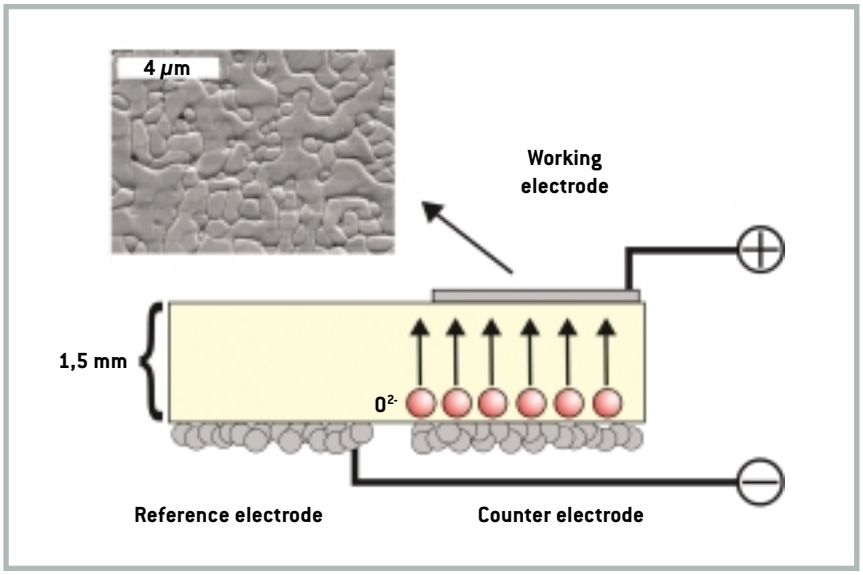

Figure 1. Experimental setup for the electrochemical experiments at the ESCA Microscopy beamline. During anodic polarization oxygen is transported towards the working electrode. The SEM image shows the working electrode which was prepared by pulsed laser deposition (PLD).

Pt 4f photoelectron yield is reduced by the covering carbon layer.

At the beginning of the experiment (Figure 3, time t_1) the surface was almost completely covered with carbon. Therefore, the C 1s image was homogeneously bright. The corresponding Pt 4f image appears dark due to the above mentioned signal damping of the covering carbon layer.

Then we polarized the platinum electrode so that oxygen is formed at the hole which acts in this case as a three phase boundary between the electrolyte, the electrode and the gas phase. The surface reaction ($C + 2\ O_{ad} \rightarrow CO_2$) starts, and the surface is successively cleaned of carbon. With increasing time (t_1 + 3 min and t_1 + 6 min in Figure 3) the C 1s image darkens – starting from the hole – and the Pt 4d image lightens. This surface reaction can be con-

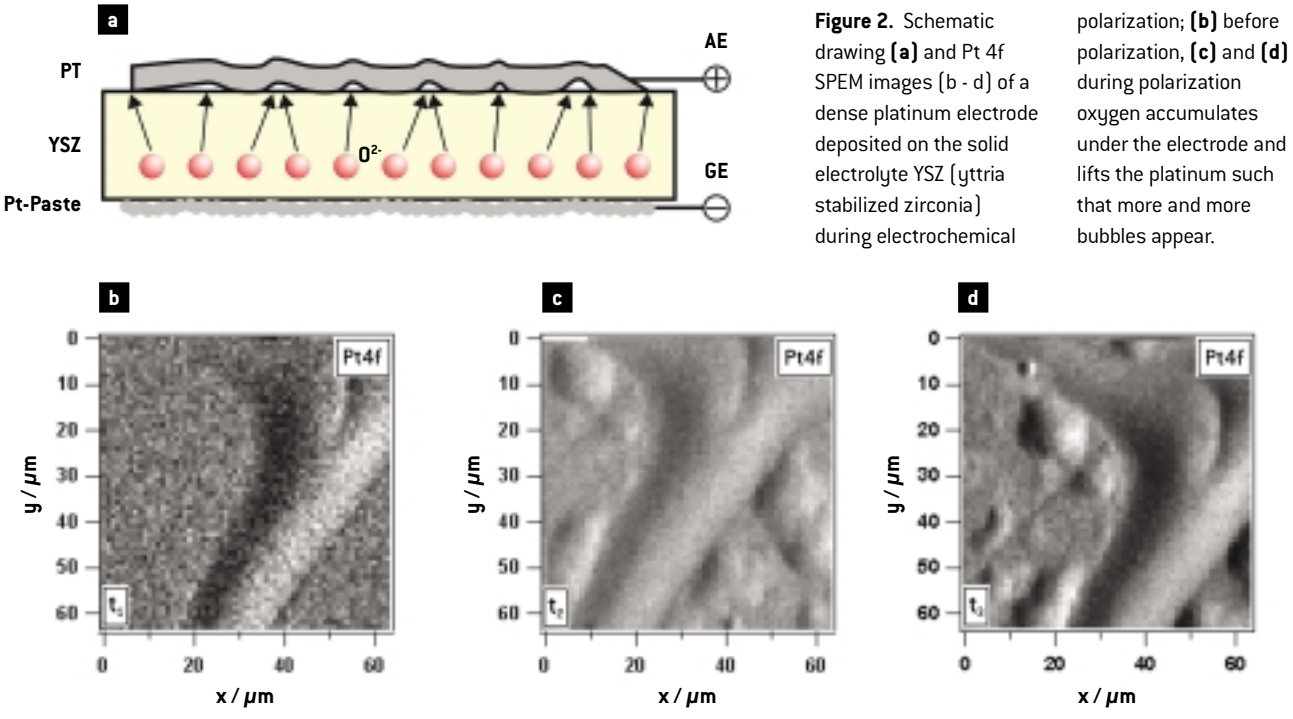

Figure 2. Schematic drawing **(a)** and Pt 4f SPEM images (b - d) of a dense platinum electrode deposited on the solid electrolyte YSZ (yttria stabilized zirconia) during electrochemical polarization; **(b)** before polarization, **(c)** and **(d)** during polarization oxygen accumulates under the electrode and lifts the platinum such that more and more bubbles appear.

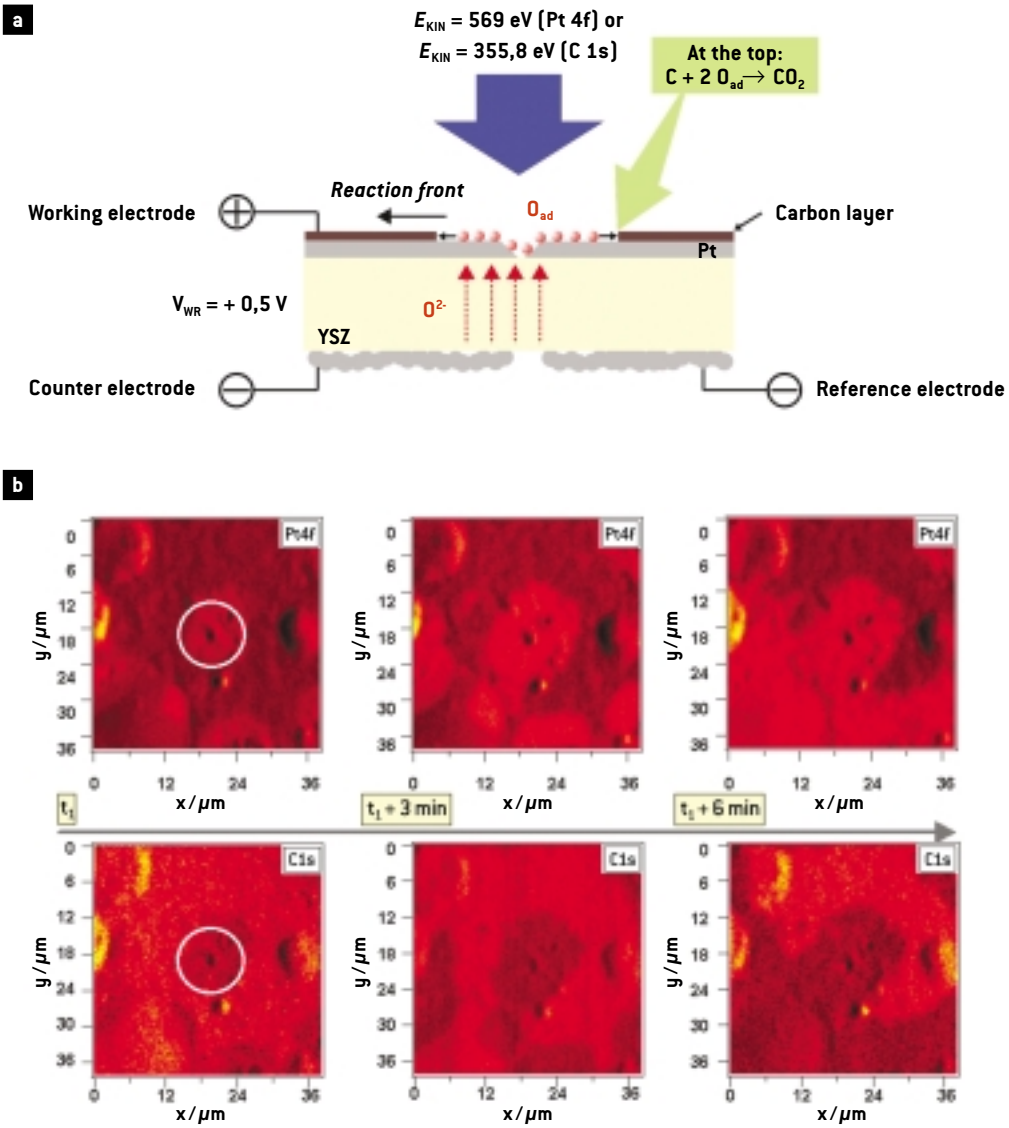

Figure 3. Schematic drawing **(a)** and Pt 4f and C 1s SPEM images **(b)** of the electrochemically controlled surface reaction C + 2 O_{ad} → CO_2 on platinum. During anodic polarization the platinum electrode is successively cleaned from carbon. Therefore, the C 1s images darken (less carbon is detected) and the Pt 4f images light up.

trolled electrochemically: A polarization stop brings to an end the surface reaction.

CONCLUSIONS

To our knowledge, these data represent the first direct images of an electrochemically induced surface reaction and impressively demonstrate the application of SPEM to electrochemical problems and the possibilities of electrochemical control of a catalytic surface reaction.

References

[1] C.G. Vayenas, S. Bebelis, C. Pliangos, S. Brosda, D. Tsiplakides, and T. S. Stein; *Electrochemical Activation of Catalysis: Promotion, Electrochemical Promotion, and Metal-Support Interactions;* (Plenum Pub. Corp., April 2002).

[2] C.G. Vayenas, S. Bebelis, and S. Neophytides; *J. of Phys. Chem.;* 92, 5083, (1988).

CALORIMETRY AT A SURFACE USING HIGH RESOLUTION CORE-LEVEL PHOTOEMISSION

> S.C. Santucci
Dipartimento di Fisica, Università di Perugia, Via A. Pascoli 1, 06123, Perugia, ITALY
> A. Goldoni, R. Larciprete, S. Lizzit, M. Bertolo, C. Masciovecchio
Sincrotrone Trieste-ELETTRA - S.S. 14 km 163,5, in AREA Science Park, 34012 Basovizza, Trieste, ITALY

INTRODUCTION

The study of the behaviour of surfaces is an important task in solid-state physics. Due to the present tendency toward nanostructure science, where the surface dominates over the bulk, the quantitative measurement of the surface properties has become fundamental. While important bulk thermodynamic information is typically obtained *via* calorimetric techniques, the measurements of the same physical quantities at the surface is not a trivial task.

Here, we illustrate an experimental method, based on high-resolution core level photoemission, which allows the quantitative evaluation of the surface internal energy. As a pioneering application of this method, we addressed the solid-to-liquid phase transition in Li(110) whose vapor pressure allows us to perform the ultra-high-vacuum photoemission experiments also in the liquid phase and for which the possible occurrence of surface premelting is still an open question. Moreover, lithium is representative of the class of simple metals and is a good test case for different theoretical approaches to solid-to-liquid transition dynamics.

We measured the temperature dependence of the Li 1*s* core level lineshape starting from 22 K, crossing the bulk melting transition at 453 K [1], up to 600 K, that is about 150 K into the liquid phase. This is the first time that such a measurement is carried out in so wide a temperature range. As in many other materials, distinct and simultaneous bulk and surface investigation is allowed by the presence of core level electrons having different binding energies for the surface and deeper layer atoms (surface core level shift). In the frame of the Debye model, a quantitative one-to-one correspondence can be established between the temperature dependent broadening of the bulk photoemission peak and the internal energy of the solid, which allows a direct comparison with the published calorimetric specific heat data. By assuming that a similar relationship holds for the thermal broadening of the surface core level peak, the temperature-dependent surface internal energy can be obtained.

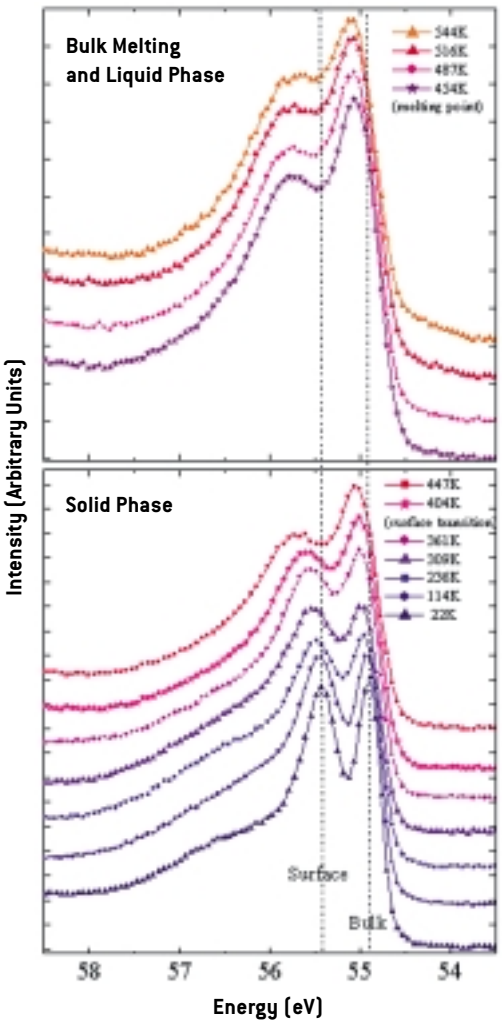

Figure 1. Li 1s core-level photoemission spectra as a function of temperature. Lower panel: bulk solid phase. Upper panel: bulk liquid phase. Vertical dotted lines are guides for the eye. Due to residual water in the experimental chamber, an oxide peak appears in the low temperature spectra as a consequence of a partial surface oxidation. The presence of this oxide peak (accounted for using a Gaussian peak in the fitting procedure) does not affect the results of this report.

EXPERIMENTAL

The measurements were performed in the ultra-high-vacuum (~ $5x10^{-11}$ mbar) experimental chamber of the SuperESCA beamline. Li(110) films (about 20 layers thick) were grown *in situ* onto a clean Ni(100) crystal kept at 22 K. Li 1*s* core level photoemission spectra were obtained with a photon energy of 94 eV and collecting the electrons at 40° from the normal direction, using a double-pass hemispherical analyser with an energy resolution of 80 meV. The temperature was measured using a calibrated thermocouple welded to the Ni sample, with an uncertainty of ±1 K. The experimental setup allowed the collection of core level spectra every 52 s. The liquid phase was kept stable by introduction of Ar at $5x10^{-8}$ mbar.

RESULTS AND DISCUSSION

A selection of Li 1*s* photoemission spectra, representing the whole thermal history of our sample, is shown in Figure 1. There are two main components visible in the spectra, the sharpest one at lower binding energy corresponding to the bulk atoms, the broader one at higher binding energy corresponding to surface atoms. Already from a visual inspection of the spectra it is clear that the two components broaden and the peak maxima shift toward higher binding energy as the temperature increases. For the range of temperature investigated here, the main contribution to the thermal broadening of the core level line width comes from the phonons distribution [2, 3], while the excitation and distribution of electrons near the Fermi level is mainly responsible for the asymmetric line shape of the peaks giving a tail at higher binding energy (Doniach-Sunjic lineshape [4]).

To quantify the temperature dependent phonon broadening and binding energy shift of bulk and surface peaks, the spectra were reproduced by means of a standard curve-fitting procedure using components having a

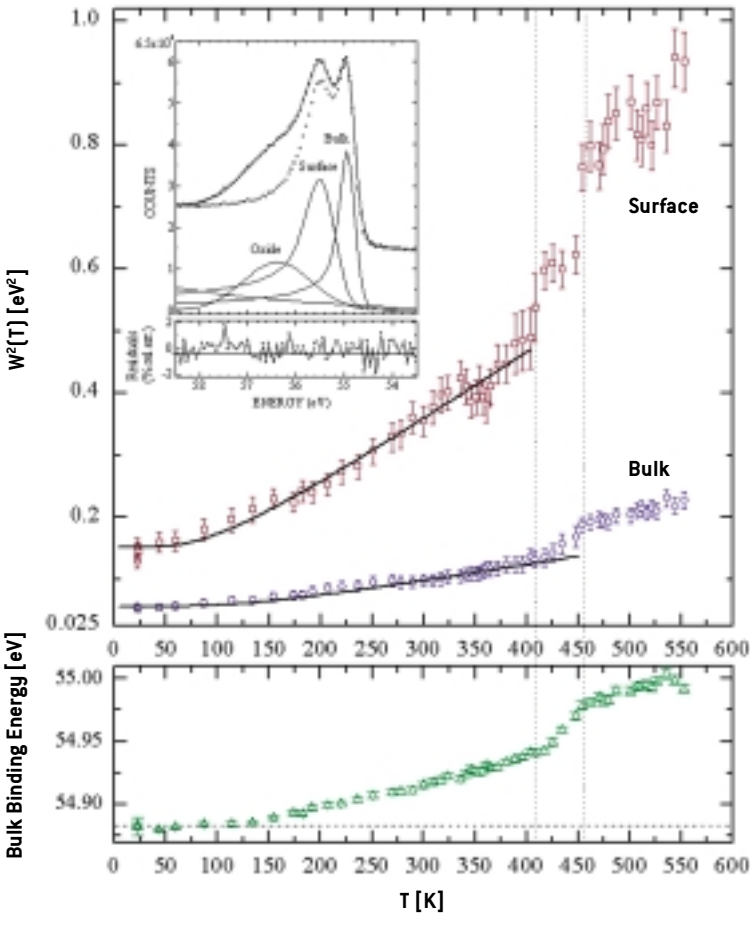

Figure 2. Upper panel: Temperature dependence of the squared Gaussian contribution (phonon broadening) to the core level linewidth for bulk (blue circles) and surface (red squares) peaks. The corresponding fit using the core level phonon broadening theory - eq.(1) and eq.(4) for bulk and surface, respectively - are superimposed as solid lines. Inset: The 300 K spectrum (solid circles) with the fit function superimposed (line) and bulk, surface, oxide and background contributions. The same spectrum, with oxide peak having been subtracted, is shown in open circles. Residuals are reported as relative errors. Lower Panel: The thermal shift of the bulk peak binding energy.

Doniach-Sunjic lineshape [4] convolved with a Gaussian function. The full width at half maximum of the Gaussian function, corrected by the temperature independent instrumental resolution, is the phonon contribution W(T) to the core level linewidth. In Figure 2 we report the square of the obtained W(T) for the bulk and surface peaks (top panel) and the binding energy of the bulk peak (bottom panel) as a function of temperature.

Bulk Analysis

For bulk atoms, the temperature dependent phonon contribution to the core level linewidth has been calculated theoretically by Hedin and Rosengren on the basis of the Debye model for the lattice vibrations [3]. The squared phonon broadening W^2 is given by:

$$W^2(T) = W_0^2 \left[1 + 8 \left(\frac{T}{\theta_D} \right)^4 \int_0^{\theta_D/T} dx \frac{x^3}{e^x - 1} \right] \quad (1)$$

where θ_D is the bulk Debye temperature and W_0 is the zero-temperature squared phonon width. This equation, which we tested for the first time down to the asymptotic region lying around 22 K and up to the melting transition, turned out to give an excellent fit of our bulk solid-phase data. We obtained $\theta_D = 470 \pm 25$ K and $W_0^2 = (51 \pm 2) \times 10^{-3}$ eV^2, in good agreement with values estimated by experiments performed in a reduced temperature range (78-280 K [5]), and with the phonon spectrum of Li [6].

By comparing Eq.(1) to the Debye formula for the lattice internal energy *U(T)* [7], it is straightforward to deduce the following relation, valid for a mole of bulk atoms:

$$U(T) = -\frac{9R}{8}\theta_D + \frac{9R}{8}\frac{\theta_D}{W_0^2} W^2(T) \quad (2)$$

Here R is the ideal gas constant.

By means of equation (2) we can calculate U(T) from our experimental data. In Figure 3a we show the quantitative good agreement between the published calorimetry measurements of the Li internal energy [1] and U(T) calculated from our experimental bulk data.

In order to further corroborate our core level analysis, we also calculated U(T) from the bulk binding energy thermal shift, which is linearly related to the thermal expansion of the solid and, hence, to the specific heat [7, 8]. The result is again in very good agreement with the published calorimetric measurements and is shown in Figure 3a.

Surface Analysis

We have shown that in the bulk case our approach parallels the standard calorimetric measurements, giving quantitative values of U(T). Now, the question is whether we can use in a similar way the surface core level data to obtain the surface internal energy, whose contribution is not detectible macroscopically using standard calorimetric techniques because of the relatively small number of surface atoms compared to the bulk.

For a two dimensional array of atoms (a surface), the phonon contribution to the internal energy *per* mole within the Debye model is:

$$U_S(T) = 4R \frac{T^3}{(\theta_D^{(S)})^2} \int_0^{\theta_D^{(S)}/T} dx \frac{x^2}{e^x - 1} \quad (3)$$

Here is the surface Debye temperature and R is again the ideal gas constant.

Following the work of Hedin and Rosengren [3], it is possible to extend eq. (1) to the core level phonon broadening of the *surface* atoms, keeping in mind that we are now dealing with the phonon density of states in a two-dimensional array of atoms. The temperature dependence of the core level linewidth can be written as:

$$W_S^2(T) = W_{0S}^2 \left[1 + C_S \left(\frac{T}{\theta_D^{(S)}} \right)^3 \int_0^{\theta_D^{(S)}/T} dx \frac{x^2}{e^x - 1} \right] \quad (4)$$

with C_S to be determined experimentally.

Fitting the surface data reported in Figure 1 to eq. (4), we obtained excellent agreement with $C_S = 4.0 \pm 0.2$; $\theta_D^{(S)} = 310 \pm 10$ K, and $W_{0S}^2 = (15 \pm 2) \times 10^{-2}$ eV^2. Consequently, the relation between the internal energy and the phonon contribution to the core level linewidth becomes:

$$U_S(T) = R\theta_D^{(S)} \left[\frac{W_S^2(T)}{W_{0S}^2} - 1 \right] \quad (5)$$

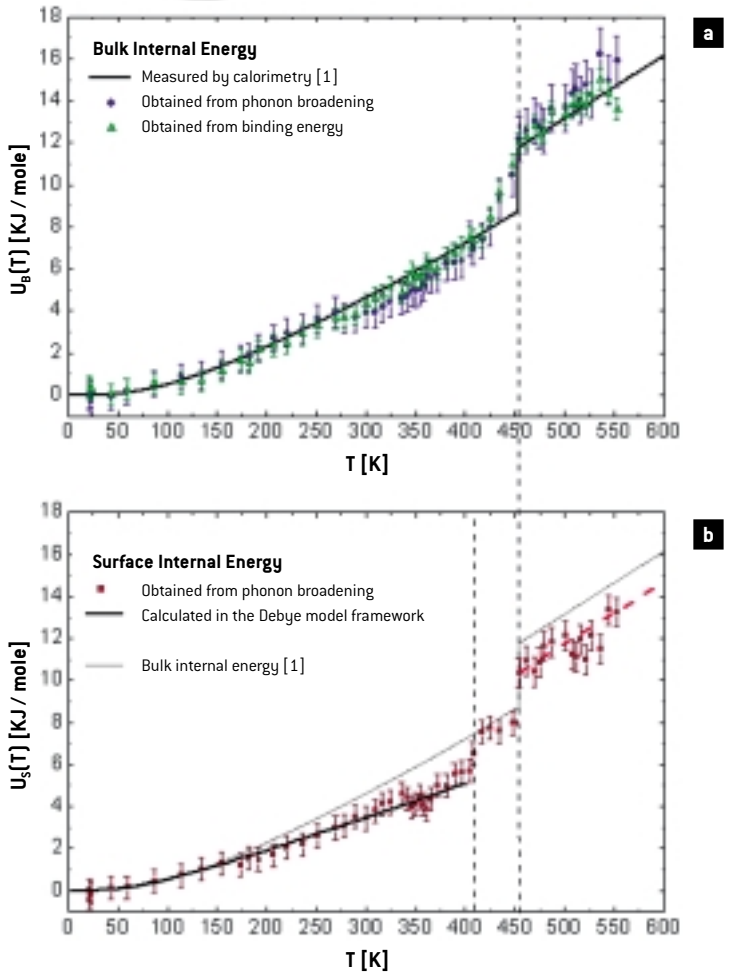

Figure 3. a) Bulk internal energy as measured *via* calorimetry (solid line) [1], obtained from phonon broadening (blue circles) and binding energy shift (green squares) of the bulk component in our temperature dependent photoemission data. **b)** Surface internal energy obtained from the phonon broadening of the surface peak (red dots) using eq. (5). The thick solid black line is the theoretical surface internal energy, calculated with eq.(3). For comparison the bulk internal energy as measured *via* calorimetry [1] is also shown (thin line).

In Figure 3b we show the surface internal energy obtained substituting our experimental data in eq. (5), superimposed on the surface internal energy calculated according to eq. (3). The bulk U(T), obtained via calorimetric measurements, is also shown for comparison. Two anomalies (jumps) are clearly visible, which are the hallmarks of temperature driven phase transitions. The transition at 453 K, visible also in the bulk data, corresponds to the bulk melting [1]. The observed jump (2.5 KJ/mole), corresponding to the latent heat at the transition, parallel to the bulk measurements, confirms that eq. (5) gives a quantitative estimation of U(T).

The jump occurring at 404 K, i.e. ~ 50 K below the bulk melting point, is visible in the surface data only. It corresponds, therefore, to a surface phase transition. According to the last-decade studies about melting mechanisms [9] and the first-order of the transition observed, we assign this transition to the surface pre-melting, although quite debated for a closed surface like Li(110).

CONCLUSIONS

In summary, we have shown a method based on high-resolution core level photoemission spectroscopy that, within the framework of the Debye model, can be used to obtain the internal energy (specific heat) of a sample. This is the crucial point, because photoemission spectroscopy can be extremely surface sensitive, but not in the usual sense that due to the low escape depth of photoelectrons the information comes from a skin of few layers below the surface. Rather it is in the sense that the surface atoms can be chemically and electronically distinguishable from the atoms of the layer underneath, producing distinct features in the photoemission spectra. Since high-resolution X-ray photoemission allows one to disentangle and simultaneously record the core level peaks corresponding to bulk and surface atoms, the bulk and surface internal energies can be obtained. While for bulk atoms this approach should parallel the standard calorimetric measurements (it can be considered as a validity check of the method), it has the unique characteristic of quantitatively measuring the internal energy of the surface atoms whose contribution is not detectible macroscopically due to their low number compared to bulk atoms.

References

[1] C.B. Alcock, M.W. Chase and V.P. Itkin; *J. Phys. Chem. Ref. Data;* 23, 385, (1994).

[2] L. Hedin; *X-ray spectroscopy*; (L.V. Azaroff - Mc Graw Hill,1974), p.227-283.

[3] L. Hedin and A. Rosengren; *J. Phys.* F; 7, 1339, (1977).

[4] S. Doniach and M. Sunjic; *J. Phys.* C; 3, 185, (1970).

[5] D.M. Riffe and G. K. Wertheim; *Phys. Rev.* B; 61, 2302, (2000).

[6] J.K. Freericks, S. P. Rudin and A. Y. Liu; *Physica* B; 284-288, 425, (2000).

[7] N.W. Ashcroft and N.D. Mermin; *Solid State Physics*; (Saunders College Publishing, 1976).

[8] M. Riffe, G.K. Wertheim, D.N.E. Buchanan and P.H.Citrin; *Phys. Rev.* B; 45, 6216, (1992).

[9] J.G. Dash; *Rev. Mod. Phys.*; 71, 1737, (1999); and references therein.

CHARACTERIZATION OF PHASE EVOLUTION UNDER LOAD BY MEANS OF PHASE CONTRAST IMAGING USING SYNCHROTRON RADIATION

> S. Besseghini, F. Stortiero, G. Carcano, E. Villa
CNR-IENI Dept. Of Lecco Corso Promessi Sposi 29, 23900 Lecco, ITALY

> L. Mancini, G. Tromba, F. Zanini, F. Montanari
SYRMEP Group Sincrotrone Trieste - ELETTRA - SS 14 km 163 in AREA Science Park, 34012 Basovizza, Trieste, ITALY

> G. Airoldi
Università di Milano Bicocca, Dipartimento di Scienza dei Materiali, Via Cozzi 53, 20100 Milano, ITALY

ABSTRACT
In the last few years many studies have been done on the characterization of the phase evolution, during martensitic transformation of shape memory alloys (SMAs). From the experimental point of view this topic has many difficulties. Detailed information is needed on the very small modifications locally induced by the transforming interface and, at the same time, on the phase evolution in the sample as a whole. Microscopic techniques give detailed information on local interfaces, twinning and self-accommodation structures, but in order to develop a complete description of the link between the microscopic and macroscopic levels, proper techniques must be identified and verified which can describe the intermediate level.

In this paper we report on the application of Phase Contrast Imaging (PCI) in the study of the phase evolution during pseudoelastic transformation in NiTiCu shape memory alloys. PCI is a quite novel technique, which gives image information linked to very small differences in the density of the material under analysis. The method has some clear advantages when compared with common microscopic techniques: (a) no special preparation of the sample is needed, (b) the investigated area is very large, (c) it allows the setting up of complex experimental apparatus.

In order to perform stress-strain tests on NiTiCu samples, an "ad-hoc" experimental set-up was prepared. With this, control of different parameters and data acquisition during tests were ensured by dedicated software, developed in the LabVIEW language, while images of the sample were acquired.

INTRODUCTION
The interest in SMAs has been increasing owing to the functional properties of these materials such as pseudoelasticity and Shape Memory Effect. These effects are of interest both for basic research and for the development of new applications. Many investigations were undertaken on the most common shape memory systems (e.g. NiTi, CuZnAl) with the aim of understanding the complex relation between the microscopic and macroscopic behaviour of these materials. In a successful experiment, a thermal imaging technique has been used for detecting small local temperature variations due to latent heat of transformation [1].

Another successful approach was the characterization of Cu-Zn-Al single crystals

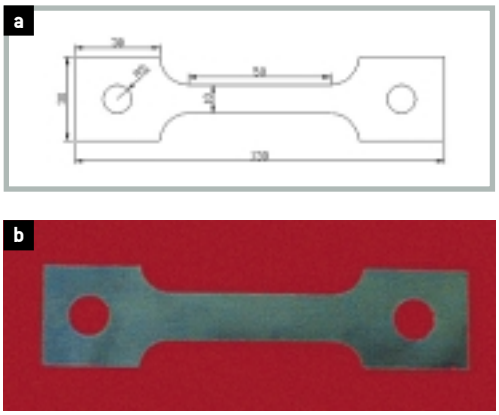

Figure 1. a) schematic view of the sample laser cut from the rolled foil. The sample thickness was 0.1 mm. **b)** is a photograph of the real sample. The two holes have been cut to increase connection in the grips.

[1] A_F =Temperature of the end of the austenite transformation

M_F = Temperature of the end of the martensite transformation

by using synchrotron X-ray diffraction topography technique [2].

In this paper we present a characterization of phase evolution under load by means of synchrotron radiation PCI. The high transverse coherence of radiation delivered from third generation synchrotron light sources like ELETTRA allows us to overcome the usual restriction of radiography to absorption-induced contrast, and to visualize object features that affect the phase of a transmitted X-ray beam. In this imaging mode, the sample is illuminated by a monochromatic hard X-ray beam, and a position-sensitive detector is set at a distance typically between 1 cm and a few m from the specimen. Free space propagation transforms the phase modulation of the transmitted beam into an amplitude modulation [3]. Contrast basically stems from interference between parts of the wavefront that have experienced different phase shifts. The technique has been demonstrated to be useful both for the characterization of very thin biological structures as well as of light metals [4] and metal matrix composites [5].

In this case we used PCI in an attempt to identify the growth mechanism of Stress Induced Martensite (SIM) during mechanical characterization of a $Ni_{45}Ti_{50}Cu_5$at% alloy in the pseudoelastic regime.

EXPERIMENTAL

We used $Ni_{45}Ti_{50}Cu_5$ at% prepared at CNR-IENI laboratories. We prepared, by hot rolling and cold rolling with intermediate anneals, a thin ribbon (25x0.1 mm^2) with residual cold deformation (estimated as thickness reduction) of about 30%. Small pieces (about 200 mm in length) were submitted to a thermal treatment of 1.8 Ks at a temperature of 723 K. Owing to geometrical constraints imposed by the special apparatus described below, a sample like that shown in Figure 1 was laser cut from the thermally treated piece.

The samples were electropolished in order to eliminate surface oxide, formed during the thermal treatment.

The transformation temperatures of the sample were assessed by means of calorimetric characterization. For this purpose a Seiko DSC 220C calorimeter, equipped with a liquid nitrogen stage, was used. The analysis were performed at a scanning rate of 5 °C/min over the temperature range -50 °C / + 150 °C. The calibration of the temperature scale was obtained by comparison with the melting point of pure elements: In and Hg.

In order to perform stress-strain tests an "ad-hoc" experimental set-up was prepared. A schematic view of the apparatus is reported in Figure 2. During tests several parameters can be measured: strain by means of a Linear Variable Differential Transformer (LVDT)[1], force by means of a loading cell, electric resistance by means of four probes directly mounted on the measuring sample. The entire experimental set-up was mounted in the hutch of the SYRMEP beamline and a sequence of images during a complete pseudoelastic cycle was acquired by means of photographic plates or a 2048x2024 pixels CCD detector (pixel size = 14 μm).

First of all PCI was applied to a stress-free sample which underwent only a thermal transformation. Images of the sample at a temperature well above A_F were acquired. They were compared with images of the same specimen area at a temperature well below M_F. In this way it was possible to appreciate the differences between the two images that are related to the martensitic transformation. This procedure allowed us to identify the best experimental parameters for PCI.

Afterwards a complete pseudoelastic cycle was performed. Both during the loading and unloading of the branches the cycle

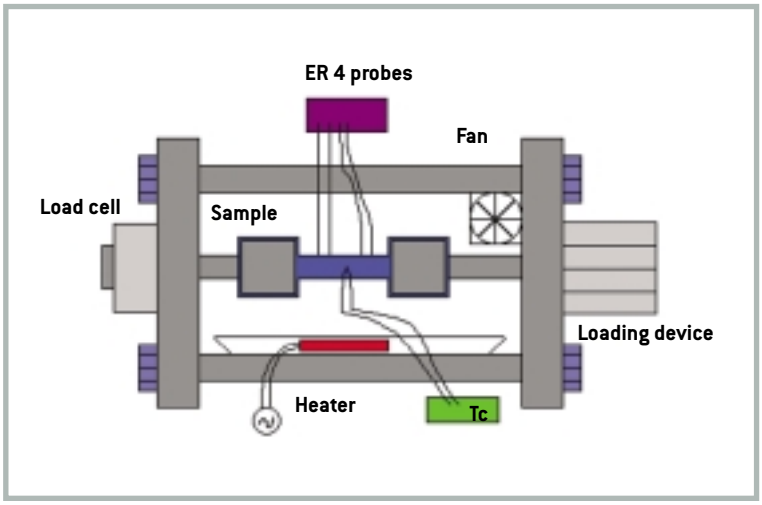

Figure 2. Schematic view of the special apparatus developed to perform PCI characterization. The whole apparatus has a maximum length of 230 mm and a maximum width of 150 mm.

FIGURE 3

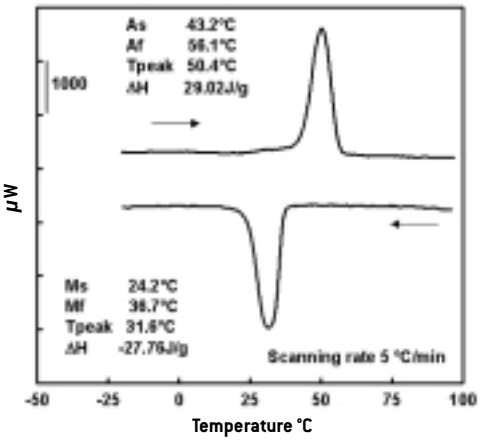

FIGURE 4

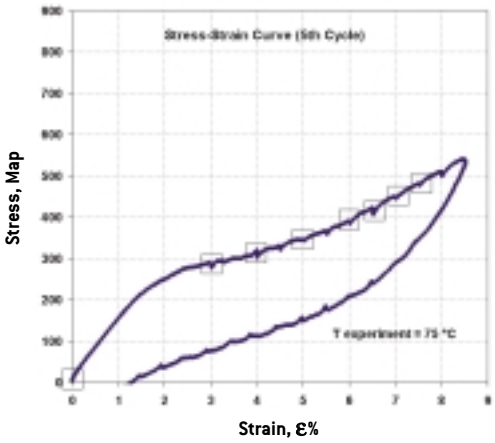

was stopped at specific points (e.g. pseudoyield point, half value of the transformation strain, end of the pseudoelastic plateau) and a radiograph was taken. The pseudoelastic cycle was measured at a temperature of 20 °C above the A_F temperature.

RESULTS AND DISCUSSION

Figure 3 shows a typical thermogram of the material. Figure 4 is the stress-strain measurement performed on the sample mounted in the special device at a test temperature of 75 °C. While the calorimetric curve is the one expected, the stress-strain one deserves some comments. It was not possible to observe a pseudoelastic cycle with a straight loading plateau. In any case, it is possible to recognize two slope changes which can be related to the start of the stress induced transformation (at about 2% of strain) and to the onset of elastic deformation of the SIM (roughly at 6-7% of strain).

In order to evaluate the resolution limit of PCI and the influence of the surface of the specimen, some preliminary tests were performed. First of all a comparison was conducted between the images taken by conventional optical microscopy and the phase contrast technique. Preparing the sample according to the needs of optical microscopy [6] is detrimental for PCI. In fact chemical etching has the effect of increasing the evidence of surface structures. As a consequence it is much more difficult to appreciate bulk modifications due to the transformation. An example is reported in Figures 5 a) and b).

The fine structure which is evident in the optical micrograph, is present even in the PCI image but it is so fine and dispersed that other structures are blurred. Without chemical etching, bulk features related to the phase transformation are easily identified. One example is reported in Figure 6.

Here the same sample area (the white spot visible at bottom right of the two photos is a reference mark) has been photographed in the two phases, fully austenite ($T>A_F$) and fully martensite ($T<M_F$). The effect of the transformation is observed by formation of a fine dispersed structure which is shown in Figure 6 b). It is worthwhile to recall that the observed structure is not related only (as in the case of optical microscopy) to the formation of surface relief, but is directly related to the bulk structure of the transformed sample. When the specimen was observed at different temperatures without any chemical etching no visible modification of the surface was detected.

The structure shown in Figure 5 b) is not changed by changing temperature. Assuming that this is the real structure of martensite and not an artefact due to chemical etching one must conclude that this is stabilized at the surface so that no information on temperature related phase evolution can be drawn from it.

According to the parameters obtained by this preliminary investigation a complete

Figure 3. Calorimetric characterization of the sample used for PCI characterization. The main transformation parameters are reported in the graph.

Figure 4. Typical stress strain curve as measured in the sample installed in the special apparatus. Boxes highlight the strain values at which the phase contrast image was acquired.

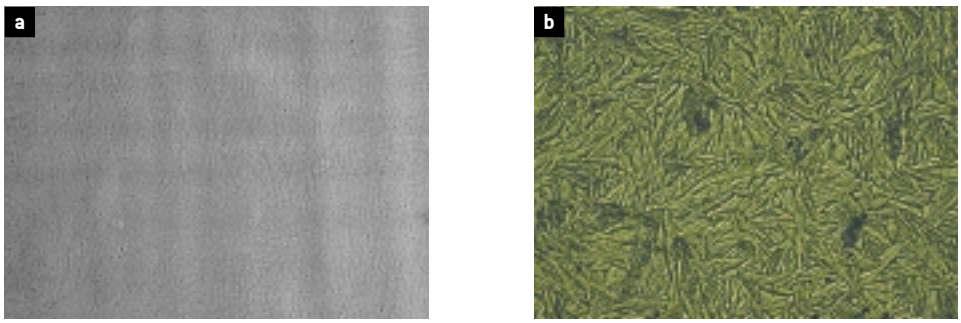

Figure 5. a) PC image of a sample with the surface prepared for optical microscopy observed in phase contrast; **b)** optical microscope image of the surface of the sample. See text for details.

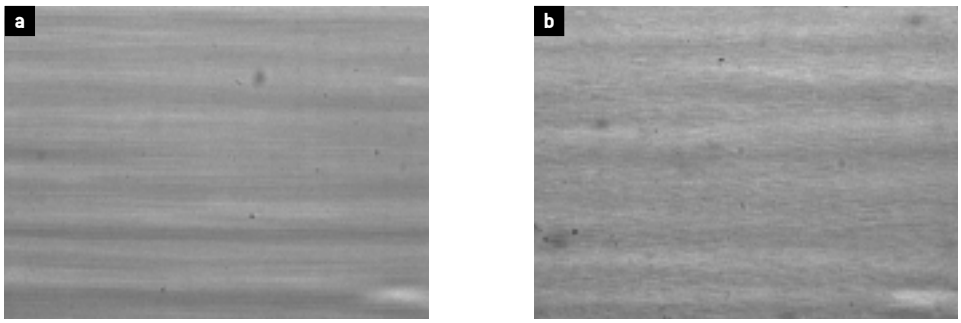

Figure 6. PC images of the NiTiCu sample in the austenitic phase at $T>A_F$ **a)** and in the martensitic phase **b)**. The two images have been taken from the same sample area using as reference the white spot, bottom right.

pseudoelastic cycle has been characterized by PCI. On the basis of the mechanical characterization performed, some points have been identified (represented by boxes in Figure 4) at which the PCI observations were performed. In the sequence of photographs of Figure 7 the images taken at different strain levels are compared. To better appreciate the modifications induced by increasing strain, photographs have been post-processed.

In each image, some lamellae are present. For low values of the strain (say up to 4-5%) they do not change in shape or in apparent intensity. At a deformation of about 6% there is an increase in the intensity (the lamellae are darker, i.e. they are more radiation-opaque). From about 6.5% they change slightly in shape, at 7% they are clearly thinned and, eventually, at 7.5% there is no evidence of these lamellae.

The intensity variation due to lamellae evolution is underlined by the curve in Figure 8 where the intensity evolution versus imposed deformation is shown.

The lamellae which disappeared at the end of the loading, retransform during unloading. In fact they are still present at the beginning of the following cycle. Images reported in Figure 7 refer to the 5th complete pseudoelastic cycle to which the sample was submitted. As a consequence the behaviour can be considered quite reproducible.

CONCLUSIONS

The PCI technique proved successful even in the characterization of purely thermally activated transformations.

Interesting results were obtained in the characterization of a pseudoelastic cycle performing PCI during the formation of SIM. We have found that some structure exists which is stable up to a strain value which is similar to the measured maximum transformation strain. Once this value is passed, the structure disappears but is still present after unloading. Further work is needed to clearly correlate this behaviour to the properties of the underlying martensitic transformation.

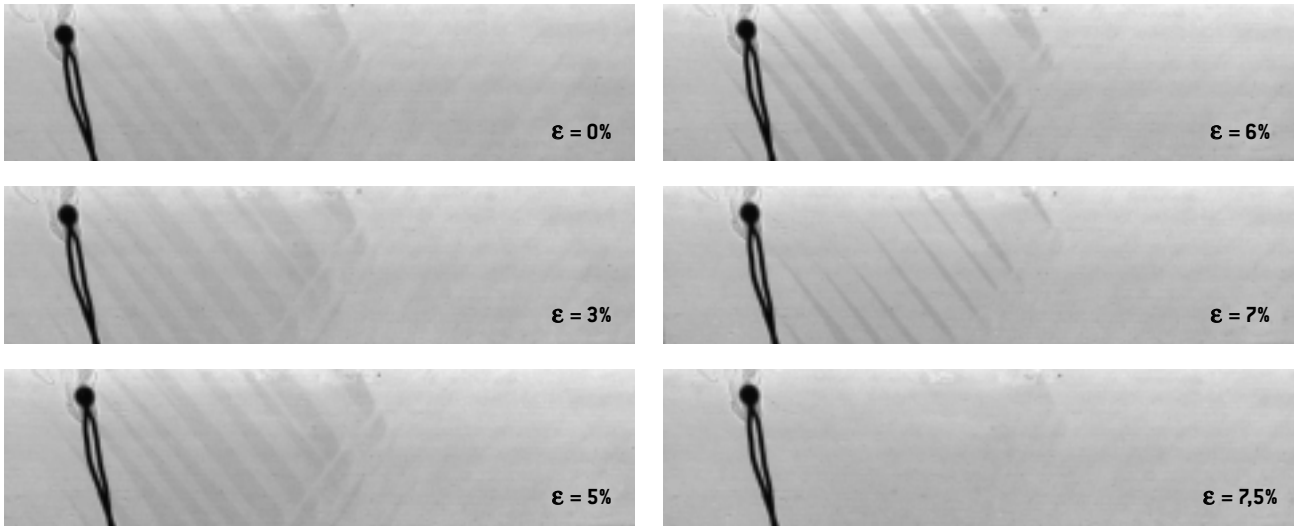

Figure 7. PC images of the sample at different values of imposed strain. The images have been processed in order to enhance the contrast contribution coming from the different phases.

References

[1] J.A. Shaw, S. Kyriakides, *Int. Jour. Plast.*; 13, 837, (1998).

[2] Gastaldi *et al.* Proceedings of Esomat Aussois 1991, *Journal de Physique IV*; Colloque 4, 1, 341, (1991).

[3] P. Cloetens, R. Barrett, J. Baruchel, J.P. Guigay and M. Schlenker, *J. Phys. D: Appl. Phys.*; 29, 133, (1996).

[4] L. Salvo, P. Cloetens et al.; Nuclear Instruments and Methods in *in Phys. Res. B.;* 200, 273-286, (2003).

[5] E. Marie et al.; *Acta Mater.;* 49, 153, (2001).

[6] J.M.Gallardo et al.; *Prakt. Metallogr.;* 36, 1, (1999).

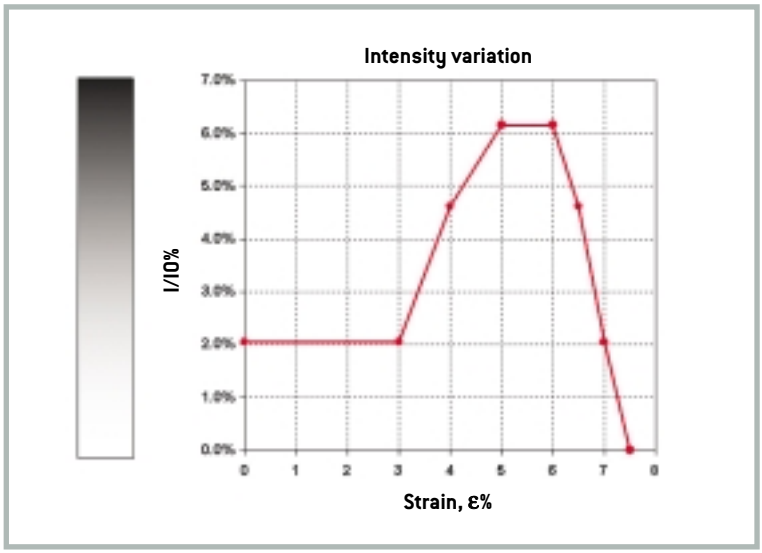

Figure 8. Intensity evolution of Lamellae vs. the imposed strain.

HIGH RESOLUTION Ca/P MAPS OF BONE ARCHITECTURE

> M. Tzaphlidou
Lab Medical Physics, Medical School, University of Ioannina, 45110 Ioannina, GREECE
> R. Speller, G. Royle, J. Griffiths
Department of Medical Physics & Bioengineering, University College London, 11-20 Capper Street, London WC1E 6JA, UK

INTRODUCTION

Reliable measures of the dynamic and static strength of the skeleton is a requirement for a rational approach to the clinical problem of skeletal diseases. It is generally accepted that a measurement of bone mineral content is an appropriate estimate of bone quality and most current clinical techniques make an estimate of bone mineral density without considering the role played by the different chemical components that are present. The aim of this work was to measure the Ca/P ratio in different kinds of bones and to seek information on whether this ratio changes with bone abnormalities. This is because changes in the amounts of Ca and P in biological apatites do not go hand-in-hand; therefore, a decrease in bone density may be due to a decrease in either Ca or P, or to dissimilar decreases in both. Consequently, the determination of the Ca/P ratio may provide a sensitive measure of bone mineral changes and may add to our understanding of the changes in bone diseases.

The range of Ca/P values in different parts of the same bone or in different bones can be estimated most accurately by in vitro studies. As a new clinical method has been put forward for assessing the skeletal Ca/P ratio *in-vivo* [1-3], it is important that *in-vitro* data from intact bones should be obtained for comparison with those derived from the *in-vivo* measurements. Synchrotron sources provide new, more accurate possibilities to assess bone mineral content from intact bone samples. Using a monoenergetic X-ray beam, as provided by a synchrotron facility, 3-D maps of the linear attenuation coefficient within the sample, unaffected by beam hardening can be generated in a CT procedure. When produced with high spatial resolution these data sets provide the ability to map different chemical components [4, 5] throughout the volume of the bone sample.

It is known that the mechanical strength of bone depends first of all on the condition of the cortical bone [6]. Hence, in the present study, cortical bone from the femoral neck and tibia regions was analyzed with two objectives in mind:

Firstly, to estimate the bulk Ca/P ratio for intact bones as a basis for comparison with *in vivo* studies.

Secondly, to study regions most affected by bone disease and to identify the significance of the distribution of the Ca/P ratio.

MATERIALS AND METHODS

Bone samples

The results in this report come from two visits (15 shifts) to the SYRMEP beamline at ELETTRA. In the first visit, cortical right tibia samples from normal 1-year old lambs and 3-years old sheep were analysed. In the second visit, cortical bone from the right tibia and femoral neck from normal 7 month old rabbits, and cortical bone from the right tibia from osteoporotic (induced by inflammation) age-matched rabbits were measured. These samples were chosen as a model for evaluating the sensitivity of the Ca/P ratio estimates as they covered different animals, different sites and different bone conditions.

For the second visit the samples of cortical bone from the femoral neck and tibia were obtained from four, 7 month old female rabbits. In two of them inflammation-mediated osteoporosis was induced by

subcutaneous injections of magnesium silicate (talcum) [7]. Two age-matched animals without injections served as controls. In all cases the samples were taken as a whole cross-section of the femoral neck and tibia from the right side. All samples were held in thin walled plastic tubes of 10 mm diameter. A section approximately 4 mm long was imaged for each sample.

Equipment and techniques

MicroCT data sets were collected using the CT set-up on the SYRMEP beamline. This consists of a high resolution rotary table mounted upon high resolution translators and cradles. This allows precise alignment of the rotation axis of the sample with the detector pixels. The detector is an X-ray sensitive Photonic Science CCD camera and was operated in a mode that provided 28 µm square pixels. A full data set consisted of 360 views over 180° and for each sample data were collected at 20 and 28 keV Two calibration phantoms containing $Ca(HPO_4).2H_2O$ and $Ca(H_2PO_2)_2H_2O$ as bone substitutes were also imaged.

Analysis

From the 3-D data sets, multiple 2-D slices (example in Figure 1) were reconstructed with a slice thickness of ~30 µm using a filtered back-projection routine. All of the software was written in IDL and typically a full data set would contain 140 slices. Analysis of these images was carried out in two ways:

- for each slice, regions of interest were grown around suitable sites and were converted to Ca/P ratios using the data collected from the calibration phantoms. Bulk estimates for the Ca/P ratio were then computed as the mean and standard deviation of the Ca/P ratio values from the individual slices;
- for selected bone sites the spatial distribution of the Ca/P ratio was studied by forming contour plots using the appropriate slices.

RESULTS

Table 1 summarises the results from the analysis of the bulk Ca/P ratios. Results show a significant difference between osteoporotics and age-matched normals (this agrees with other estimates for these quantities [2]) as well as differences between different bone sites and different animals. These variations with different animals and different sites indicate the importance of selecting suitable animal models when applying results to human studies.

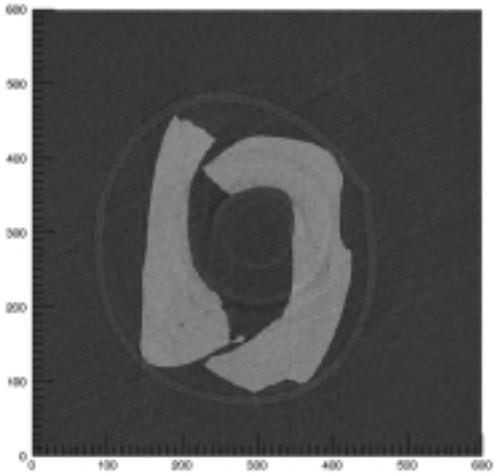

Figure 1. MicroCT image of normal rabbit tibia cortical sample

Differences between estimates made at 20 and 28 keV are not significant but can be used to remove any dependence upon the physical density of the sample.

However, an important aspect that is unique to the measurements made at a synchrotron source such as ELETTRA is the ability to map the spatial distribution of the Ca/P ratio. This has been investigated by using contour plots for selected slices where the local gradients exhibited in the contour plots are a measure of the changing Ca/P ratio and hence can be used to study the changing distribution. Figure 2 shows examples of the Ca/P contour plots for different bone types, sites and bone conditions taken from the 28 keV images. Contours have been plotted at Ca/P ratios of 60%, 80%, 85%, 90% and 97% of the maximum values in the image.

DISCUSSION

The experiments described in this report, using the ELETTRA synchrotron radiation microtomography system on the SYRMEP beamline, were designed to confirm and extend previous results on bone and to use the spatially dependent measurements to look at the distribution of Ca and P throughout the sample.

Bone type	Mean Ca/P (20keV)	Mean Ca/P (28keV)
Femoral rabbit(1)	1.55±0.18	1.54±0.37
Femoral rabbit(2)	1.22±0.19	1.14±0.26
Tibia rabbit(1)	1.88±0.06	1.84±0.31
Tibia rabbit(2)	1.79±0.05	1.97±0.05
Tibia osteoporotic(1)	1.45±0.04	1.67±0.18
Tibia osteoporotic(2)	1.66±0.06	1.75±0.13
Tibia lamb(1)	1.01±0.04	0.96±0.05
Tibia lamb(2)	1.19±0.04	1.05±0.06
Tibia sheep(1)	1.28±0.04	1.17±0.07
Tibia sheep(2)	1.55±0.05	1.65±0.04

Table 1. Bulk values of the Ca/P ratio measured at 20 and 28 keV.

Ca/P content and bone condition

A new method has been developed at the University of Ioannina for the estimation of the *in vivo* Ca/P ratio in the human radius. This approach uses a modified dual energy X-ray absorptiometry system [3]. Using this instrument a significant difference in the mean Ca/P ratio between post-menopausal osteoporotic patients and pre-menopausal controls has been observed and from studies in rabbits, a significant decrease in the tibia Ca/P ratio in animals with inflammation-mediated osteoporosis has also been found [2]. Our results at ELETTRA confirm that a statistically significant decrease is observed in rabbit tibia Ca/P ratio for osteoporotic samples suggesting that there is a relationship between bone loss and a lowered Ca/P ratio (Table 1).

Ca/P ratio and bone type

Others performing measurements on intact bones by neutron activation analysis have shown that the Ca/P ratio depends upon the kind of bone studied [8-11]. Our mean values for Ca/P ratio, at both energies, in cortical femoral neck are lower than those in tibia. It is our opinion that the lower values obtained in the femoral neck are due to the influence of the organic matrix, particularly that of red marrow. In some samples taken from the proximal part of the femur, red marrow contributes up to 75% of the whole marrow [12]. The P content of red marrow is high and thus, as femur contains significantly more red marrow than tibia, the P content of femur will be higher than that of tibia. We suggest that this accounts for the lower Ca/P ratio obtained in cortical femoral neck bone in comparison with the Ca/P value obtained for the cortical tibia bone. In addition, as the cortical bone does not only contain mineral (hydroxyapatite) but also organic matter, this results in a decrease of the Ca/P values in comparison to the stoichiometric value for hydroxyapatite (2.16).

Ca/P spatial distribution and bone condition

The spatial distribution of the Ca/P ratio can be seen in Figure 2. It appears that normal bone shows less variation in the distribution of Ca/P as demonstrated by the near absence of contours throughout the bone volume. However, the osteoporotic examples show a higher density of Ca/P contours in general, but also demonstrate regions of significantly higher Ca/P gradient changes. These changes are not fully understood but could be due to local exchanges of the elements Ca and P. A further interesting observation is the variation in the contour density within a single sample. It can be seen in Figure 2 that a sample which is judged to be 'osteoporotic' from the bulk estimate of the Ca/P ratio may show regions of 'osteoporotic' behaviour and regions of 'normal' behaviour. Further work is required to confirm and understand these observations and their full interpretation is still ongoing.

CONCLUSIONS

In conclusion, synchrotron radiation microtomography is potentially an outstanding *in vitro* technique to map different bone chemical components and to detect changes

brought about by bone diseases. As has been reported [8,10], Ca/P ratio may provide greater reliability for diagnosis of bone disorders and hence microtomography may become a valuable technique to be used during bone therapeutic and diagnostic trials.

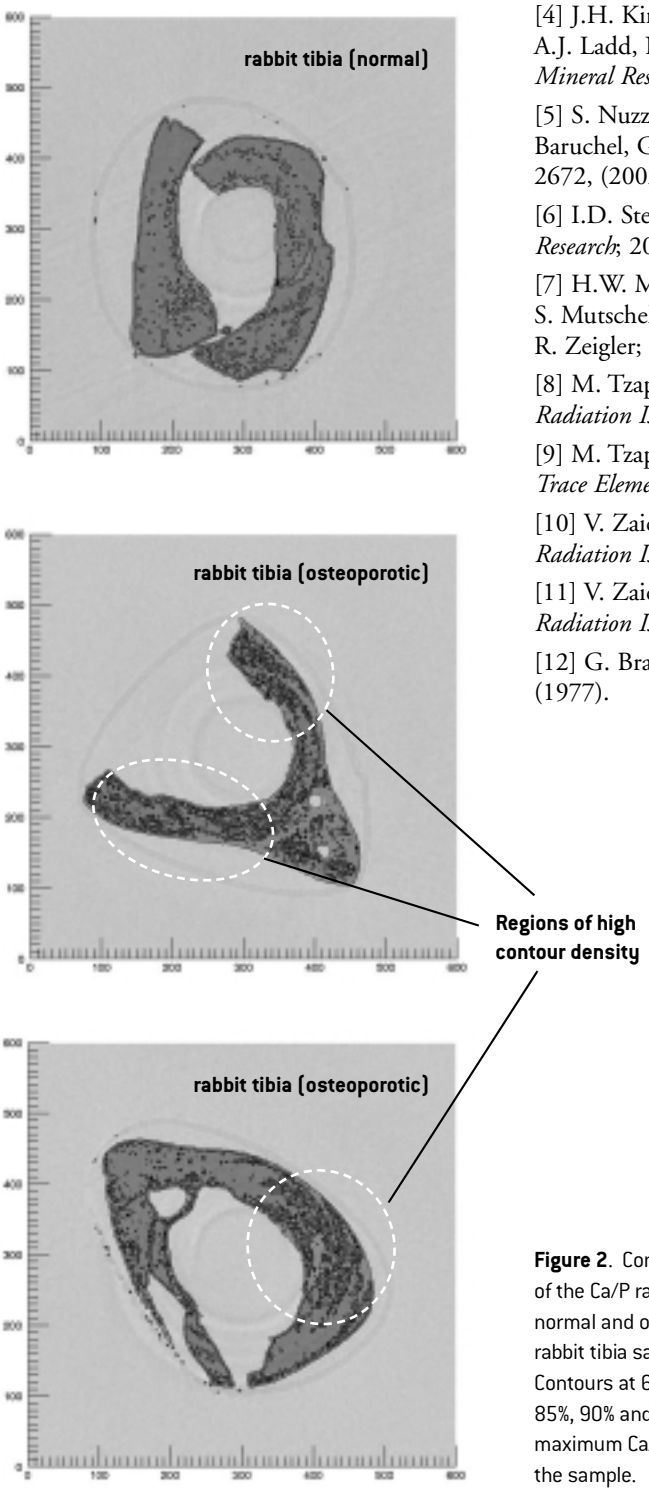

Figure 2. Contour plots of the Ca/P ratio for normal and osteoporotic rabbit tibia samples. Contours at 60%, 80%, 85%, 90% and 97% of maximum Ca/P within the sample.

References

[1] G. Fountos, S. Yasumura, D. Glaros; *Medical Physics*; 24, 1303, (1997).

[2] G. Fountos, E. Kounadi, M. Tzaphlidou, S. Yasumura, D. Glaros; *Applied Radiation Isotopes*; 49, 657, (1998).

[3] G. Fountos, M. Tzaphlidou, E. Kounadi, D. Glaros; *Applied Radiation Isotopes*; 51, 273, (1999).

[4] J.H. Kinney, D.L. Haupt, M. Balooch, A.J. Ladd, N.E. Lane; *Journal of Bone Mineral Research*; 15, 1981, (2000).

[5] S. Nuzzo, F. Peyrin, P. Cloetens, J. Baruchel, G. Boivin; *Medical Physics*; 29, 2672, (2002).

[6] I.D. Stein, G. Granik; *Calcified Tissue Research*; 20, 61, (1976).

[7] H.W. Minne, J. Pfeilschiften, S. Scharla, S. Mutschelknauss, A. Schwarz, B. Krempien, R. Zeigler; *Endocrinology*; 115, 50, (1984).

[8] M. Tzaphlidou, V. Zaichick; *Applied Radiation Isotopes*; 57, 779, (2002).

[9] M. Tzaphlidou, V. Zaichick; *Biological Trace Element Research*; 93, 63, (2003).

[10] V. Zaichick, M. Tzaphlidou; *Applied Radiation Isotopes*; 56, 781, (2002).

[11] V. Zaichick, M. Tzaphlidou; *Applied Radiation Isotopes*; 58, 623, (2003).

[12] G. Brandt; *Medical Welt*; 28, 1307, (1977).

PHASE CONTRAST MICROTOMOGRAPHY OF ARCHAEOLOGICAL GLASSES

> S. Gerlach, H. Römich, E. Lopéz
Fraunhofer-Insitut für Silicatforschung Würzburg, GERMANY

> F. Zanini, L. Mancini
SYRMEP Group, Sincrotrone Trieste-ELETTRA, S.S. 14, km. 163,5 in AREA Science Park, 34012 Basovizza, Trieste, ITALY

> L. Rigon
Dipartimento di Fisica, Università degli Studi di Trieste, Istituto Nazionale di Fisica Nucleare, Trieste, ITALY

INTRODUCTION

During burial in soil, archaeological glasses develop corrosion products that appear as a thin surface layer of variable thickness which ranges from nanometers up to a few millimetres. Corrosion degradation may affect the fragment homogeneously or it may be concentrated in spots and local cracks. Depending on the impact of different environmental situations (soil composition, humidity, pollutants, micro-organisms, etc.) the corrosion process can lead to significant changes in the chemical composition and morphology of degraded areas.

The aim of our project was to explore the possibility of microtomography as a new technique for non-destructive analysis of corroded archaeological glass objects. For our study we used a highly coherent X-ray beam available at the SYRMEP bending magnet beamline of ELETTRA. Phase Sensitive (PS) microtomography [1,2] is a promising method to determine the three-dimensional corrosion patterns of archaeological glasses and also to control the distribution and status of materials used for conservation purposes on the surface and in the micro-porous structure of fragile objects.

Results obtained by PS microtomography are compared with those achieved from conventional analysis and traditional desktop-micro-tomography of identical samples.

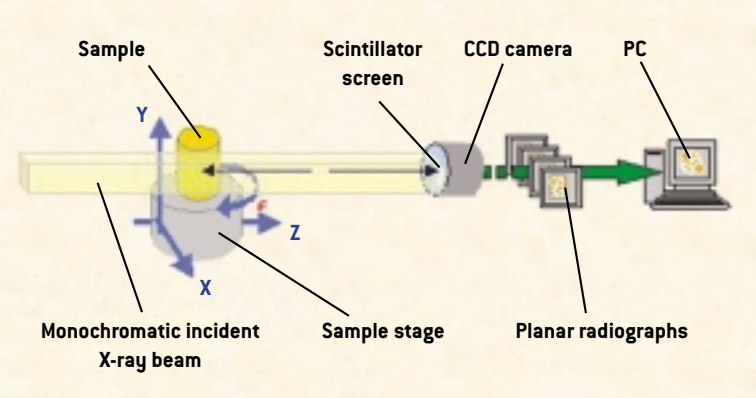

Figure 1. Schematic view of the experimental set-up used for μCT at the SYRMEP beamline of ELETTRA.

STATE-OF-THE-ART

Non-destructive techniques and fast analysis methods are in great demand in the field of archaeology. Optical microscopy is frequently used as a first and simple tool for characterising the surface of archaeological objects. For more precise investigations with higher magnification and for detecting the extent of corrosion on the object's surface, scanning electron microscopy (SEM) is applied. If the thickness of a corrosion layer needs to be evaluated by SEM, the sample has to be embedded, cut and polished, which is a destructive technique. Moreover, the method is time-consuming and delivers pictures from only one single cut, which might not be representative for inhomogeneously corroded fragments.

For the characterisation of samples treated for conservation purposes, the penetration of a coating or a consolidant (polymer) into the micro-cracks of the corrosion layer has to be controlled in order to guarantee suitable adhesion between the polymer and the surface of the glass object. For this problem, no adequate method is available so far.

Computed X-ray tomography (CT) is an imaging technique with major potential applications in the cultural heritage domain. When corrosion layers have to be

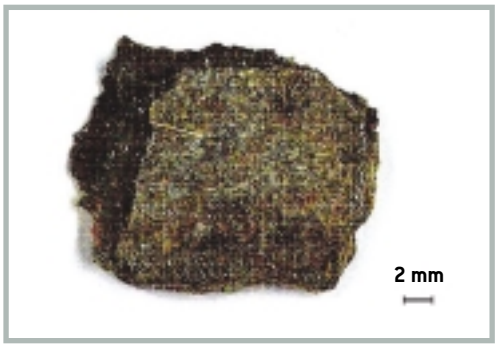

Figure 2. Heavily corroded fragment (OLM2).

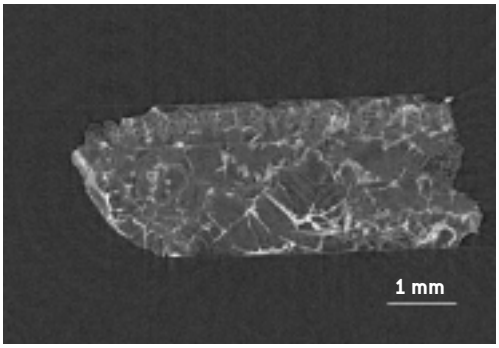

Figure 3. Reconstructed slice of a heavily corroded fragment (OLM2). Corrosion channels and the laminated structure of the leached glass are clearly visible.

detected, resolutions in the range between 0.1 and 1.0 millimetres are of special interest: this can be achieved with commercially available instruments. For the analysis of altered glass a 10 micrometer-scale is obligatory. Within a European project ("Monitoring the corrosion state of glass objects by optimized micro-computerized X-ray-tomography", SMT4-CT98-2261) the potential of µCT for archaeological glass has been explored [3, 4]. In this project a desktop tomography scanner was used (equipment manufactured by Skyscan, Belgium), which provided interesting results for heavily corroded samples where the absorption contrast was high enough between the uncorroded bulk and the corrosion layer. For the detection of polymers it turned out that the contrast between the corroded surface and the organic polymer could not be adjusted appropriately.

EXPERIMENTAL

The advent of third-generation synchrotron radiation sources such as ELETTRA is now making possible, by exploiting the X-ray coherence, a novel form of radiography, in which, by Fresnel diffraction, contrast arises from phase variations across the transmitted beam. With this technique, the edges of the inhomogeneities present in the investigated sample determine local phase shifts and can be directly imaged. Phase-sensitive (PS) radiography [1, 2, 5] and its three-dimensional development, PS µCT [6], are attracting increasing attention due to the possibility to obtain image information in the presence of very small differences in the densities of the materials under analysis [7].

From an experimental point of view PS µCT is based on the recording of X-ray transmission images (radiographs) on a CCD detector placed at an adjustable distance from the sample (Figure 1). The free space X-ray propagation transforms phase modulation into amplitude modulation as described by the Fresnel interference model.

The SYRMEP beamline optical system is based on a double-crystal silicon (111) monochromator which works in an energy range between 8 and 35 keV. The beamline provides, at a distance of about 20 m from the source, a monochromatic X-ray beam with a maximum area of (150 x 6) mm^2. The detector used is a 2048 x 2024 pixel CCD detector (pixel size = 14 µm, field of view 28 x 28 mm^2).

The tomographic experiments at SYRMEP included original archaeological glasses and model glasses simulating the corrosion process of glasses after exposure in the soil [8]. The samples varied in their chemical composition and their corrosion state. Some of the samples were treated with consolidation or conservation materials (Araldite", Silicon-Zirconium-Alkoxide). A total number of 8 tomograms were record-

Figure 4. Reconstructed slice of a model glass covered by a thick organic polymer layer (Araldite®).

ed after setting the appropriate parameters for measurement at 25 keV energy, 720 rotations and a distance between the sample and the detector of 66 cm.

RESULTS AND DISCUSSION

Due to the high material contrast of this technique, a number of interesting features have been visualised in the reconstructed tomograms. Defects inside the glass and the corrosion layers, including thin laminated substructures, have been resolved. A thick organic polymer coating and a comparatively thin inorganic coating applied on a fairly corroded glass surface were imaged.

Figure 2 shows an overview of the waterlogged fragment OLM2 from the Middle Ages provided by the Museum of London. The fragment is dark brown and seems completely degraded, although from the surface it cannot be seen how far the corrosion proceeds into the glass. PS microtomography on this fragment (Figure 3) enables a view inside this heavily corroded glass. A complex system of cracks and channels through the whole piece, determined by strong corrosion, can be detected. A sequence of views into this original glass makes clear that there is no unaltered glass core left. Even the laminated structure, typical of leached glass material, is resolved. This alteration layer consists of a sequence of thin layers with different chemical compositions caused by diffusion and precipitation processes of the glass components during corrosion in the soil.

Organic or inorganic coatings are used as consolidation and conservation materials to prevent the glass objects from further deterioration and damage. In order to test the adhesive properties, a non-destructive method is required to observe the interface between the coating and the surface. Model samples with different surface characteristics are used in laboratory studies to simulate the originals during destructive testing. Figure 4 shows the reconstructed slice of a model glass treated with the common conservation polymer Araldite®. This experiment proved that PS µCT provides appropriate material contrast to characterise and visualise the effectiveness of conservation treatments with organic polymers.

Figure 5 gives an example of the detection of inorganic polymers used for consolidation of fragile glass objects. This consolidant is based on a mixture of Silicon-Zirconium-Alkoxides (SZA). Due to its low viscosity this material does not cover the surface but consolidates the structure by penetrating into the pores. PS µCT enables the detection of a very thin layer (thickness below 1 micrometer) on the surface of the sample. Furthermore, it can be seen clearly how the SZA penetrates into the crack on the upper surface in Figure 5. The channel is completely and perfectly filled with the consolidation material without formation of defects like cavities.

The results show that this method is far more complete and practical as compared with conventional analytical methods, such as scanning electron microscopy, where several parameters like resolution, material contrast and a long preparation have to be taken into account. The most striking advantage of tomography is that it is a non-destructive method, which is of special importance for any kind of investigation in the field of cultural heritage. Although the resolution of SEM is higher and more appropriate for the detection of sub-structured layers, the material contrast is stronger in the case of tomography. SEM requires time-consuming preparation of a cross section with embedding and polishing, and is a 2D destructive technique. Tomography

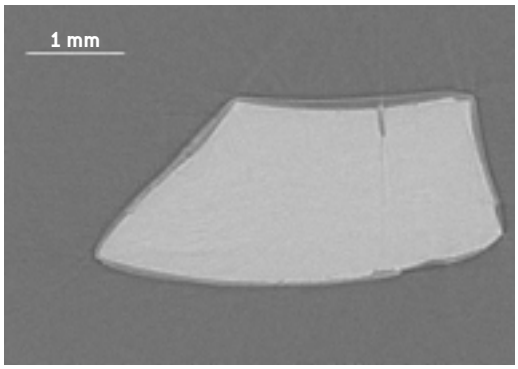

Figure 5.
Reconstructed slice of a model glass treated with an inorganic polymer based on Silicon-Zirconium-Alkoxides.

provides the possibility to record a series of pictures and to reconstruct damage patterns three-dimensionally, which is an essential aspect for inhomogeneously corroded fragments. Desktop-tomography allows routine analysis with easy-to-handle equipment. However, the resolution is significantly lower and the material contrast less accurate as compared to the PS µCT performed at the SYRMEP beamline.

CONCLUSIONS

These preliminary experiments done on one original and selected model glass illustrate the potential of phase sensitive µCT to study corroded glasses and conservation materials. This X-ray imaging technique is extremely promising, it is non-destructive, it allows the visualization of the 3D structure of corrosion patterns and the detection of conservation materials within fragile original objects. The development of conservation materials may gain new impetus, if a new non-destructive method is available to evaluate the effectiveness of treatments on originals. Further research is needed to optimise the resolution and to adjust the method for detecting a sequence of treatments for a variety of different fragments.

References

[1] A. Snigirev, I. Snigireva, V. Kohn, S. Kuznetsov and I. Schelokov; *Rev. Sci. Instrum.*; 66, 5486, (1995).

[2] P. Cloetens, R. Barrett, J. Baruchel, J.P. Guigay, M. Schlenker; *J. Phys. D: Appl. Phys.*; 29, 133, (1996).

[3] H. Römich; E. López; F. Mees; P. Jacobs; E. Cornelis; D. Van Dyck; T. Doménech Carbó; Proc. 7th International Conference on Non-destructive Testing and Microanalysis for the Diagnostics and Conservation of the Cultural and Environmental Heritage; Antwerp, Belgium, publ. by University of Antwerp, 1, (2002).

[4] H. Römich; S. Gerlach; P. Mottner; F. Mees F.; P. Jacobs; D. Van Dyck; T. Domenech Carbó; Proc. MRS Symposium II, 2003, in print.

[5] J. Baruchel, P. Cloetens, J. Härtwig, W. Ludwig, L. Mancini, P. Pernot, M. Schlenker; *J. Synchrotron Rad.*; 7, 196, (2000).

[6] P. Cloetens, M. Pateyron-Salomé, J.Y. Buffière, G. Peix, J. Baruchel, F. Peyrin and M. Schlenker; *J. Appl. Phys.*; 81, 5878, (1997).

[7] L. Mancini, E. Reinier, P. Cloetens, J. Gastaldi, J. Härtwig, M. Schlenker and J. Baruchel; *Phil. Mag. A;* 78, 1175, (1998).

[8] H. Römich: Simulation of corrosion phenomena of historical glasses on model glasses: an update, Proc. conference. The Surface: a Bug in New an Old Glasses – GS 2000, Rivista della Stazione Sperimentale del Vetro, ISSN: 0391-4259, 9, (2000).

X-RAY AND e-BEAM LITHOGRAPHY OF THREE DIMENSIONAL ARRAY STRUCTURES FOR PHOTONICS

> F. Romanato, E. Di Fabrizio
TASC-INFM, LILIT beamline at Sincrotrone Trieste-ELETTRA - S.S. 14 km 163,5, in AREA Science Park, 34012 Basovizza, Trieste, ITALY

> M. Galli
INFM and Dip. di Fisica "A. Volta" Università di Pavia, Via Bassi 6, 27100 Pavia, ITALY

INTRODUCTION

Moulding the flow of light represents one of the goals of photonics and to achieve this result, new artificial materials are being developed: Photonic Crystals (PC). These are the optical analogues of semiconductors. In the same way as in semiconductors the energy gap splits into allowed electronic states, in PCs the light propagation is governed by the frequency band structure that opens a gap between allowed propagation modes [1]. Three dimensional (3D) PCs have been shown to provide a full directional control of the light in the gap frequency range. Several interesting optical devices have been envisaged with this peculiar characteristic. The most basic and, at the same time, innovative example is represented by a *waveguide* characterized by zero propagation loss also through paths with sharp corners [1].

However, the realization of a waveguide in a 3D PC represents a challenge from a fabrication point of view. To the original difficulty for the realization of 3D PCs with lattice parameters comparable to wavelengths of interest for telecommunication, is added the problem of creating a linear hole that acts as waveguide in the 3D lattice structure. At present 3D periodic arrays showing the designed optical energy band structure have been demonstrated, sometimes also with mass production compatible techniques [2,3,4,5], but the realization of waveguide 'defects' in the 3D PC is far from being achieved. Preliminary results have been reported where the "defect" realization is based on a pioneering *layer-by-layer stacking* technique that is complex, imprecise, as well as time consuming [6].

Here we present a new fabrication strategy. The waveguide has been introduced in a 3D periodic array by means of a combination of electron beam and multiple exposure *tilted* X-ray lithography performed at the LILIT beamline at ELETTRA. In a first step we have developed X-ray lithography to a reliable and mass production compatible technology for 3D PCs fabrication. We apply this fabrication method to metallic 3D PCs; this can be advantageous in the high frequency region (greater than 100 THz) where metals become almost completely reflecting [7] (Figure 1). Then we have addressed the issue of waveguide realization and here we present the first structures obtained (Figure 2). The method that we have developed, and patented, allows

Figure 1. Nickel 3D photonic crystal obtained by 4-fold X-ray exposure of a square pattern array.

Figure 2. Linear defect acting as a waveguide embedded in a 3D metallic photonic crystal.

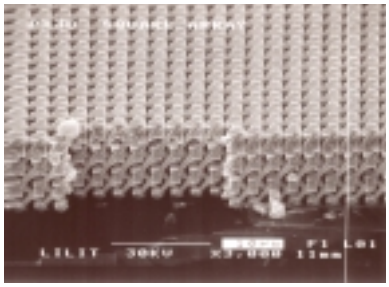

FIGURE 1

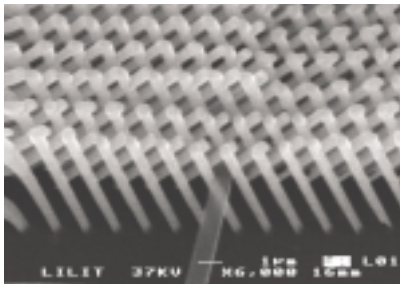

FIGURE 2

FIGURE 3

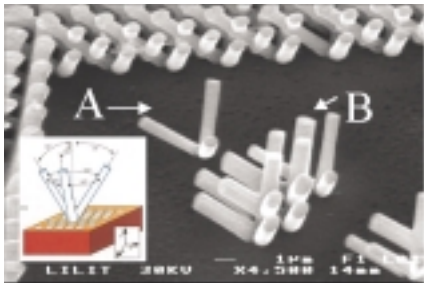

FIGURE 4

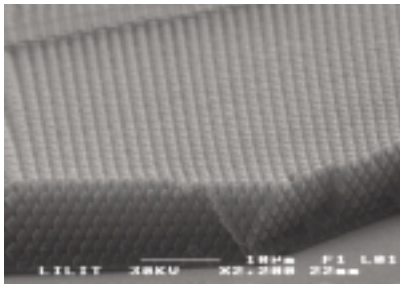

FIGURE 5

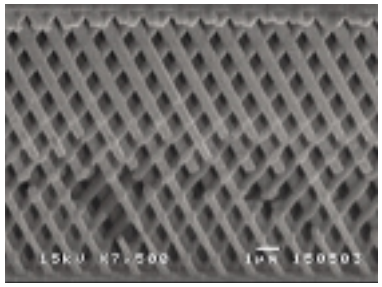

the realization of arbitrary shaped defects with the necessary position accuracy and precision with respect to the 3D lattice.

EXPERIMENTAL

Proximity X-ray lithography was performed at the LILIT beam line [8] at ELETTRA. The LILIT beamline is designed for both soft and hard X-ray lithography. It is possible to choose the optimum energy window of the energy spectrum provided by the bending magnets (from a few hundred eV to 25 keV). For the present work, a *medium* hard spectrum was selected (from 500 to 4 keV) in order to facilitate the exposure of resists thicker than 15 μm.

Electron Beam Lithography (EBL) was performed for the generation of the mask pattern by means of a JEOL 6400 at 30 keV. Several X-ray masks have been used for this experiment. They typically consist of an 800 nm gold film supported on a self standing 1 μm thick Si_3N_4 membrane which is patterned with a square or triangular array of circular holes with lattice parameters between 1 and 2 μm.

The idea underlying the realization of a three dimensional lattice by X-ray lithography is based on unconventional exposure geometry. Typically, the mask+sample system is mounted *perpendicular* to the beam. During exposure, the X-ray beam is shadowed by the mask that projects its pattern on the resist providing vertical, digital-like, lithographic profiles. For the realization of a 3D lattice, on the contrary, the mask+sample set is mounted *tilted* in front of the X-ray beam and successively exposed performing azimuthal rotation around the axis perpendicular to the mask+sample set. From the frame of reference of the sample each opening of the X-ray mask can be considered as a collimated light source that exposes the resist along different directions generating different holes (inset in Figure 3). A special sample holder allows the mounting of the *tilted* mask+sample *system* onto the stage of the X-ray stepper, thus ensuring a permanent and fixed contact between mask and sample.

In order to generate metallic structures, after the exposure of the sample spun with PMMA resist of different thicknesses (from 1 μm to 10 μm), the patterned area was filled by electro-plating deposition with gold and finally cleaned from residues.

RESULTS AND DISCUSSION

An example of three successive exposures is shown in Figure 3. A single hole generates a tetrahedral tripod-like structure (structure A). When the mask openings are close enough, the light paths overlap and the pillars intersect (structure B). When the X-ray mask openings are organized in a plane array and the exposure directions are along the major axis of the associated 3D lattice structure, then the exposed pillars organize themselves in a 3D lattice (lattice surrounding structure A and B). Specifically, if the planar array has triangular geometry and three exposures take place every 120 rotation degrees, the lattice that is generated is the called the Yablonovite lattice [9]. Gold and Nickel 3D photonic crystals with 3 fold (Yablonovite) and 4 fold rotation symmetry have been fabricated with a lattice parameter ranging from 3 μm to 500 nm. It is important to underline that this is a fabrication technique compatible with mass production, and that can expose in one shot areas as large 2000 mm^2 (Figure 4).

For real devices, not only the lateral di-

Figure 3. Yablonovite lattice generation by multi exposure tilted X-ray lithography. A) Tripod-like structure generate by a single hole in the X-ray mask. B) Five crossing tripods generated by 5 close holes. Inset: Geometry defining the lattice of a Yablonovite structure.

Figure 4. X-ray lithography can generate large, defect free, mass production compatible 3D photonic crystals.

Figure 5. Yablonovite lattice of crossing pillars generates up to 14 parallel lattice planes.

mension but also the 3D PC thickness plays an important role: it must be large enough to provide full 3D optical behavior. Several critical thicknesses have been reported depending on the specific structure and material used. Fleming *et al.* [10] have shown that a metallic structure of four lattice planes parallel to the substrate is enough to completely open the band gap. This number certainly is too low for semiconductor PCs. The rule of thumb that the thickness must be much larger than the wavelength (i.e. of the lattice parameter) requires that the number of lattice planes must be greater than at least 6-8. Moreover, in view of the goal of introducing a waveguide in the middle of the lattice structure, the critical number of lattice planes, N_c, doubles, since it is required to place them above and below the waveguide.

From a lithographic point of view, a constraint on N_c becomes a condition on PC thickness, i.e. on the length of the metallic pillars. This means that, for a lattice parameter between 1 and 2 μm, the PC thickness must range between 12 and 18 μm keeping constant the pillar diameter that typically ranges from 0.3 μm to 1 μm. Such a structure can easily be obtained by X-ray lithographic *tilted* exposures. An example of a successful nickel made Yablonovite structure, is shown in Figure 5. The length and diameter of the pillars are respectively 25 μm and 0.55 μm generating up to 14 parallel lattice planes.

Preliminary optical characterizations performed on the sample shown in Figure 1 are reported in Figure 6. The experimental reflectance spectra show several sharp features, which display a well-defined dispersion in their energy position as the angle of incidence is varied, both for TE (Figure 6a) and TM polarizations (Figure 6b). These kinds of resonances, which are very similar to those observed in 2D and 3D dielectric photonic crystals [11,12], are likely to be associated with the excitation of the 3D photonic bands of the metallic sample. The observation of such structures is a clear indication of the very good quality and true three dimensionality of the samples. In particular, the sharp minimum observed at low energy in the TM reflectance spectra, may be related to the excitation of a surface-plasmon-polariton, while the other step-like features are most probably associated with the excitation of the allowed photonic modes of the metallic 3D structure. The photonic band dispersion may be determined from the energy position of the structures observed in the reflectance curves as a function of the wavevector $k=(\omega/c)\sin\theta$ of the incoming radiation field. However, the unambiguous interpretation of the experimental spectra would require the development of a theoretical model and subsequent comparison of experimental measurements to calculated photonic bands.

On the basis of the previous results, we

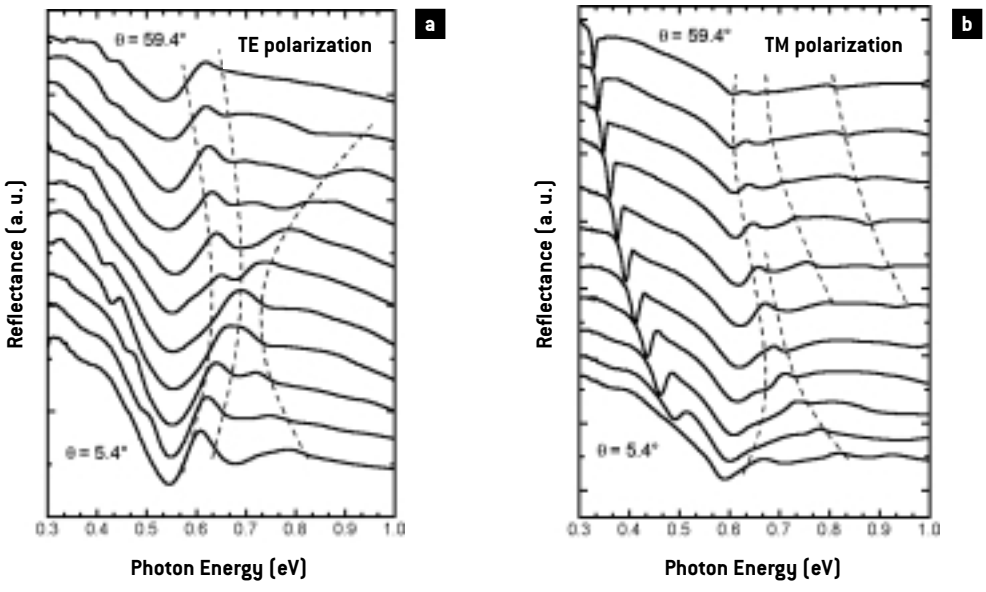

Figure 6. Variable angle reflectance of the sample shown in fig. 3 a) for light incident along the G-X orientation, for **a)** TE and **b)** TM polarizations. The angle of incidence was varied from 5.4° to 59.4° in steps of 5.4°. The curves are shifted vertically for clarity.

addressed the issue of the realization of a waveguide in a 3D lattice structure; an example is reported of a waveguide inside a Yablonovite nickel-made structure (Figures 2 and 7). The possibility to introduce linear controlled tube-like defects is based on a two-resist process described elsewhere [13]. The complete independence of the defects from the 3D lattice is remarkable; the defect is embedded in the structure defining a perfect tube-like defect (the resist filling the defect has been left in the structure for clarity). Self-alignment of the metallic pillars of the top and bottom positive film is perfect without the appearance of any interface pillar discontinuity. It is also important to underline that it is possible to design the defects with the degree of precision and accuracy provided by electron beam lithography and by its alignment system. This guarantees the insertion of the defect at the designed position in the 3D structure.

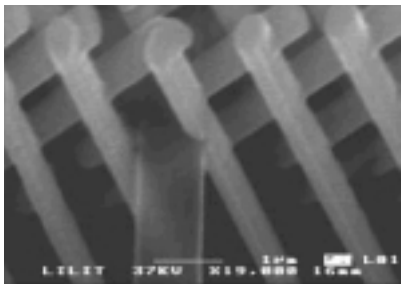

Figure 7. Detail of the waveguide entering the photonic crystal structure.

CONCLUSIONS

Metallic 3D lattices with cubic and Yablonovite structure have been fabricated by X-ray lithography. Both the method and the exposure procedure have been explained showing that a Yablonovite lattice with 1 µm pitch and 300 nm pillar diameter was achieved. Preliminary optical characterization showed that a cubic 2 µm lattice parameter has resonance features which are likely to be associated with the excitation of the 3D photonic bands of the metallic sample. A possible technique for the introduction of controlled linear defects has been studied and applied. Results of an original combination of EBL-XRL for the realization of waveguides embedded into 3D structures have shown the potential of the method.

ACKNOWLEDGMENTS

This project has been funded by INFM projects PAIS-PHO CRY (2000-2001) and PRA PHOTONIC (2002-2004).

References

[1] A. Chutinan, S. John, and O. Toader; *Phys. Rev. Lett.;* 90, (2003) 123901.

[2] M. Campbell, D. N. Sharp, M. T. Harrison, R. G. Denning, and A. J. Turberfield; *Nature*; (London) 404, 53, (2000).

[3] Y.A. Vlasov, X.Z. Bo, J.C. Sturm, D.J. Norris; On-chip natural assembly of silicon photonic bandgap crystals; *Nature*; 414, 289 - 293, (2001).

[4] E. Judith, G.J. Wijnhoven and W.L. Vos; Preparation of Photonic Crystals Made of Air Spheres in Titania; *Science;* 281, 802-804, (1998).

[5] S. Shoji and S. Kawata; Photofabrication of three-dimensional photonic crystals by multi-beam laser interference into a photopolymerizable resin; *Appl. Phys. Lett.*; 76, 2668, (2000).

[6] S. Noda, K. Tomoda, N. Yamamoto, A. Chutinan, *Science;* 289, (2000).

[7] J.G. Fleming, S.Y. Lin, I. El-Kady, R . Biswas and K.M. Ho, All-metallic three-dimensional photonic crystals with a large infrared bandgap, *Nature;* 417, 52, (2002).

[8] F. Romanato, E. Di Fabrizio, L. Vaccari, M. Altissimo, D. Cojoc, L. Businaro, S. Cabrini; LILIT beamline for soft and deep X-ray lithography at Elettra, *Microelectronic Engineering;* 57-8, 101-107, (2001).

[9]E. Yablonovitch, *Phys. Rev. Lett.*, 58, 2059, (1987).

[10] J.G. Fleming, S.Y. Lin, I. El-Kady, R . Biswas and K.M. Ho, *Nature;* 417, 52, (1987).

[11] F. Romanato, L. Businaro , E. Di Fabrizio, A. Passaseo, M. De Vittorio, R. Cingolani, M. Patrini, M. Galli, D. Bajoni, L.C. Andreani, F. Giacometti, M. Gentili, D. Peyrade and Y. Chen; *Nanotechnology;* 13 (5) 644, (2002).

[12] M. Galli, M. Agio, L.C. Andreani, M. Belotti, G. Guizzetti, F. Marabelli, M. Patrini, P. Bettotti, L. Dal Negro, Z. Gaburro, L. Pavesi, A. Liu, P. Bellutti, *Phys. Rev. B.*, 65 (11): art. no. 113111, (2002).

[13] Patent n. TO2003A000730 deposited on 23.09.2003 “Process for the fabrication of sub-micrometric complex three dimensional structures by means of two resist combinated lithography”, Inventors: F. Romanato, E. Di Fabrizio, R. Kumar.

INELASTIC ULTRAVIOLET SCATTERING BEAMLINE AT ELETTRA

> C. Masciovecchio, A. Gessini, S. Di Fonzo, A. Stolfa
Sincrotrone Trieste-ELETTRA - S.S. 14 km 163,5, in AREA Science Park, 34012 Basovizza, Trieste, ITALY

> S.C. Santucci
Università di Perugia, Dipartimento di Fisica, Via Pascoli 1, 06100 Perugia, ITALY

The recent construction of an Inelastic UltraViolet Scattering (IUVS) beamline at the ELETTRA opens new possibilities for studying the density fluctuation spectrum, S(Q,E), of disordered systems in the mesoscopic momentum (Q) and energy (E) transfer region not accessible by other spectroscopic techniques (namely Q from 0.07 to 0.3 nm^{-1} and E from 10 to 10^3 μeV). This region is of great interest for the knowledge of the properties of collective excitations in many research fields at the frontier of condensed matter physics and chemistry [1]. In order to perform IUVS spectroscopy three main requirements for the incident radiation had to be fulfilled: i) photon energy in the 5 - 11 eV range (λ ~ 240 – 110 nm), ii) incident photon flux on the sample larger than 10^{11} photons/s, iii) resolving power of the order of 10^5 to 10^6, necessary to resolve the typical phonon-like excitations in the energy range of interest. Because of the high flux needed, the radiation source for the IUVS beamline at ELETTRA has to provide at least 10^{15} photons/s/0.1%bw. This requirement implies a very high-emitted power density, which can be harmful to the optical elements of the beamline. For this reason an exotic insertion device, the Figure-8 undulator [2] has been constructed [3] as an alternative to the standard vertical field device. The resulting power on the first optical element is thus reduced to about 20 *W* while the first harmonic delivers $1.2 \cdot 10^{15}$ photons/s/0.1%bw.

The severe requirement on the resolving power has been fulfilled by using an 8 m focal length Czerny-Turner [4] normal incidence monochromator design for both the monochromator and analyser units (Figure 1). The maximum resolving power, measured by collecting the isotropic scattered intensity from a high roughness copper surface, is 10^6 [5]. The momentum transfer can be varied in the 0.02 to 0.3 nm^{-1} range, and is determined by the incident photon energy, the choice of the scattering angle, and the refractive index of the sample. The inelastic scattering spectra are collected

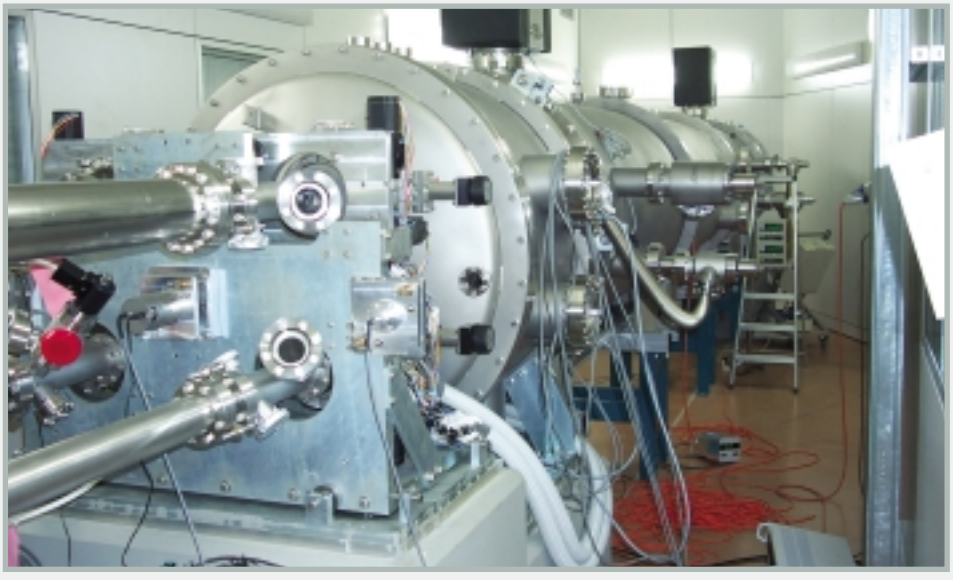

Figure 1. An overview of the vacuum chamber containing the 8 m focal length monochromator and analyser units.

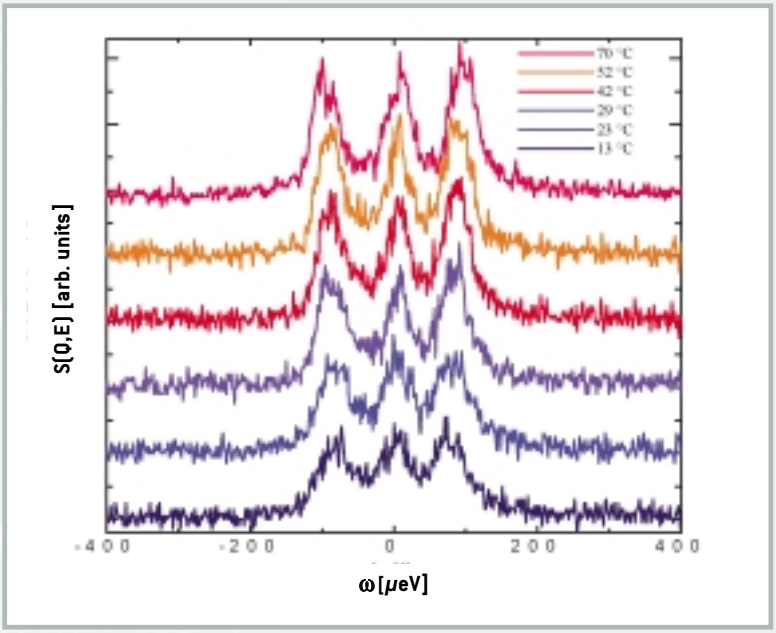

Figure 2.
Temperature dependence for the measured S(**Q**,E) on liquid water. Spectra have been taken with 6.7 eV incident photon energy and 0.09 nm^{-1} momentum transfer.

by a low noise Peltier-cooled CCD camera placed at the focal plane of the analyser, which allows to register the inelastic spectrum in one single shot, thus avoiding long-lasting monochromator scans of the diffraction angle.

In the direction of characterizing the possibilities of the IUVS beamline we have been running a series of test experiments on prototype samples such as liquid water and fused silica. As representative result of this investigations is shown in Figure 2 the temperature dependence of the measured S(**Q**,E) of liquid water from 13°C to 70°C. The incident photon energy was set at 6.7 eV and the exchanged momentum at 0.09 nm^{-1}. The exposure time of the detector for a single spectrum was 120 s. One immediately observes the presence of well-defined phonon-like excitations peaks (Stokes and AntiStokes) on the sides of the elastic central line in the spectrum and how they change their position and shape at different temperatures.

This is the first time a S(**Q**,E) of a disordered system like a liquid has been measured in the mesoscopic region spanned by IUVS. The inelastic broadening is dominated by structural (i. e. plane waves are scattered by disorder) and relaxational (a relaxation process on the atomic dynamics sets in at these frequencies) components and it is not resolution limited. This result will motivate to explore the undercooled metastable state of liquid water in the temperature range from 10°C to -30°C in the proximity of the maximum sensitivity region for liquid water, where the relaxation parameters should just fit the timescale domain of this beamline. A completely new thermodynamic region will be investigated allowing to better understand the influence of the Hydrogen bond on the structural rearrangment and by comparing these results with data extrapolated by Brillouin light and inelastic X-ray scattering [6 ,7, 8].

We acknowledge F. Sette and G. Ruocco for useful discussions, D. Cocco and M. Danailov for helping in the beamline design and alignment.

References

[1] F. Sette, G. Ruocco, M. Krisch, C. Masciovecchio, G. Monaco; *Science;* 280, 1550, (1998).

[2] T. Tanaka, H. Kitamura; *Nucl. Instr. and Meth. in Phys. Res. A;* 364, 368, (1995).

[3] B. Diviacco, R. Bracco, D. Millo and D. Zangrando; *Proc. EPAC 2002*; 2610, (2002).

[4] M. Czerny and A. F. Turner, *Z. Physik*; 61, 792 (1930).

[5] C. Masciovecchio et al. to be submitted.

[6] A. Cunsolo and M. Nardone; *J. Chem. Phys.*; 105, (1996).

[7] G. Monaco, A. Cunsolo, G. Ruocco, and F. Sette ; *Phys. Rev. E*; 60, 5505, (1999).

[8] A. Cunsolo, G. Ruocco, F. Sette, C. Masciovecchio, A. Mermet, G. Monaco, M. Sampoli, and R. Verbeni; *Phys. Rev. Lett.*; 82, 775, (1999).

THE ELETTRA VIRTUAL COLLABORATORY

> R. Pugliese, R. Borghes, F. Billè, V. Chenda, M. Turcinovich, A. Curri
Sincrotrone Trieste-ELETTRA - S.S. 14 km 163,5, in AREA Science Park, 34012 Basovizza, Trieste, ITALY

The ELETTRA Virtual Collaboratory (EVC) is a Computer Supported Collaborative Work (CSCW) system to support scientific collaboration in experiments. The term "Collaboratory" was coined by William Wulf by merging the words *collaboration* and *laboratory*, and defined as "... center without walls, in which researchers can perform their research without regard to geographical location - interacting with colleagues, accessing instrumentation, sharing data and computational resources, and accessing information in digital libraries" [1]. Scientific collaborations currently rely heavily on face-to-face interactions, group meetings, individual action, and hands-on experimentation [2]. The creation and introduction of effective CSCW systems aims at bringing the following main advantages: first, to provide remote access to expensive and hard-to-duplicate equipment (and thus reduce travel costs of research groups); second, to increase the effectiveness of the experimental activity, since more experts can participate to experiments, give useful hints and solve problems; third, to facilitate multi-institutional consortia collaborations on large-scale projects. EVC is a collaborative virtual environment (i.e., a computer system that supports human-human and human-machine communication and collaboration) for X-ray experiments developed by Sincrotrone Trieste together with the Human Computer Interaction Laboratory of the University of Udine with a partial support by Friuli Venezia-Giulia region.

The EVC is the result of an ongoing project which aims at providing researchers with the possibility of carrying out x-ray experiments remotely (i.e. through the Internet) and in a collaborative fashion. The goal of the project is to increase the effectiveness and efficiency of the experiments at the synchrotron beamlines by reducing travel costs, by increasing the number of useful collected data sets (by allowing remote experts to collaborate to the experiment), and by facilitating multi-institutional consortia collaborations.

To facilitate scientific work, collaboratory systems must support the (secure) sharing of experimental data, analysis, instruments, and interaction spaces. Several systems incorporate some of these basic features. Early collaboratories focused mostly on the sharing of large, expensive instruments such as astronomical telescopes, particle accelerators, oceanographic instruments, atmospheric observatories, and space research applications [2]. For example, the Upper Atmospheric Research Collaboratory [3] provides access to instruments in Greenland for solar wind observation, and collaborators can exchange and archive multimedia information from the instruments and the measurements analysis. More recently, collaboratory systems, e.g., [4,5], besides providing remote sharing of experimental equipment, data and computing power, are focusing also on communication tools (e.g. videoconference, whiteboards) and on *electronic notebooks*, i.e., electronic versions of a traditional paper laboratory notebook. The goal of electronic notebooks is to provide distributed access to data, as well as automated data entry, searching, and other information processing not possible in a paper notebook.

The aim of the EVC system is to provide tools that help researches to collaborate in all the typical phases of an experiment (i.e., experiment set-up, data collection, data analysis, and publication/storage of results).

The EVC interface (Figure 1) resembles a Web portal that can be accessed by different categories of users (visitors, researchers, experiment leaders, staff personnel of the experimental stations), which are offered different sets of possible actions, depending on their user category and expertise level.

Collaboration teams are led by an experiment leader (which typically, for security and safety reasons, is the one who physically carries out the experiment at the experimental station) which is able to add and remove collaborators at any time. Besides that, the EVC does not force any particular collaboration protocol, leaving to users the freedom to establish a suitable collaboration strategy (this was fundamental for the acceptance of the system).

At any phase of an experiment, collaborators can

communicate both textually and visually using a chat, which allows, besides typical messaging facilities, pasting of images (obtained from the data collection equipment) and drawing on a shared canvas. Researchers can thus see the same image and discuss about it with the possibility of drawing arrows, signs, or text on it, and have the others see what one is doing. Moreover, they can share experimental data by using a file browser tool (see Figure 2), which performs also some basic processing of the experimental data (this allows remote users to quickly estimate the suitability of the experimental parameters and of the data collection strategy).

During the *data collection* phase, collaborators have also the possibility of monitoring the experimental equipment both through video cameras and by a synoptic view of the equipment which is being used. In the *data analysis* phase, collaborators can run scientific applications using the computing resources at ELETTRA. Since these applications are typically X-Window based, they can be remotely accessed using *VNC* (Virtual Network Computing), which provides a remote graphical interface to the computing servers. An *electronic notebook* registers meaningful experiment events. Every entry has a timestamp, an associated experiment, a creator agent (program or user) and some content (text or images) which is automatically indexed and hence easily searchable.

The ELETTRA Virtual Collaboratory project started on June 2001. The first prototype was installed on ELETTRA X-ray diffraction beamline on June 2002. The system was presented at SMAU2002, the most important ICT exhibition in Italy and at the NOBUGS2002 conference (NIST Washington DC). EVC is now operating on three different experimental stations and we are planning its installation on other two by the end of this year. We are currently extending the system to support High Throughput Protein Crystallography and Far Remote Operation of the storage ring.

The authors would like to thank Kristina Djinovic Carugo, all the people of the Structural Biology Laboratory and of the Instrumentation and Measurement Software Area of ELETTRA for helpful discussions and encouragement.

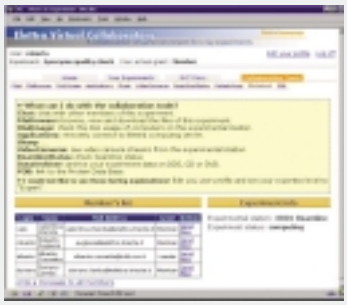

Figure 1. Working on an EVC experiment

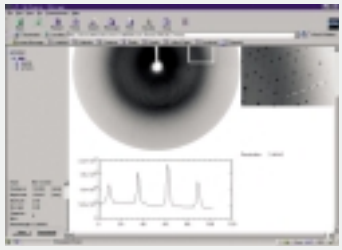

Figure 2. The scientific file browser on a diffraction image

References

[1] V.G. Cerf et al.; *National Collaboratories: Applying Information Technologies for Scientific Research;* National Academy Press: Washington, D.C., (1993).

[2] R.T. Kouzes, J.D. Myers. W.A. Wulf; *Collaboratories: Doing Science on the Internet;* IEEE Computer, (August 1996).

[3] G.M. Olson, D.E. Atkins, R.C. Thomas, A. Finholt, F. Jahanian, T.L. Killeen, A.Prakash, T.Weymouth; *The Upper Atmospheric Research Collaboratory (UARC),* Interactions, Volume 5 Issue 3, (May 1998).

[4] *The Spectro-Microscopy Collaboratory at the Advanced Light Source*, http://www-itg.lbl.gov/BL7Collab/

[5] Stanford Collaboratory for Macromolecular Crystallography, http://smb.slac.stanford.edu/collaboratory/

"AT WAVELENGTH" INSPECTION OF MULTILAYER DEFECTS IN EUV LITHOGRAPHY MASKS

> V. Farys
Laboratoire des Technologies de la Microélectronique-CNRS, c/o CEA-Grenoble, 17 rue des Martyrs, 38054 Grenoble Cedex 09, FRANCE
STMicroelectronics, 850, rue Jean Monnet, 38926 Crolles Cedex, FRANCE

> P. Schiavone
Laboratoire des Technologies de la Microélectronique-CNRS, c/o CEA-Grenoble, 17 rue des Martyrs, 38054 Grenoble Cedex 09, FRANCE

> F. Polack
Synchrotron Soleil, Synchrotron Soleil, L'Orme des Merisiers, Saint-Aubin - BP 48, 91192 Gif-sur-Yvette Cedex, FRANCE

> M. Bertolo, A. Bianco, S. La Rosa, G. Cautero
Sincrotrone Trieste-ELETTRA - S.S. 14 km 163,5, in AREA Science Park, 34012 Basovizza, Trieste, ITALY

> E. Quesnel
LETI-CEA, 17 rue des Martyrs, 38 054 Grenoble Cedex, FRANCE

INTRODUCTION

Along the way to shrinking integrated circuits down to the 32 nm node and below, one of the leading techniques for next generation lithography is Extreme Ultra Violet (EUV) lithography. This new technique introduces a gap in the manufacturing of lithographic devices. Indeed, unlike conventional lithography that uses a wavelength in the deep UV range (λ = 193 nm) and transmission optics, EUV lithography operates at the wavelength of 13.5 nm with all reflective optics. The optics (and the mask substrate) consists of Bragg interference mirrors made of a stack of 40 pairs of molybdenum and silicon layers of about 3 nm and 4 nm thickness respectively.

There are numerous critical problems to be solved before bringing EUV lithography to an industrially viable technique. One of

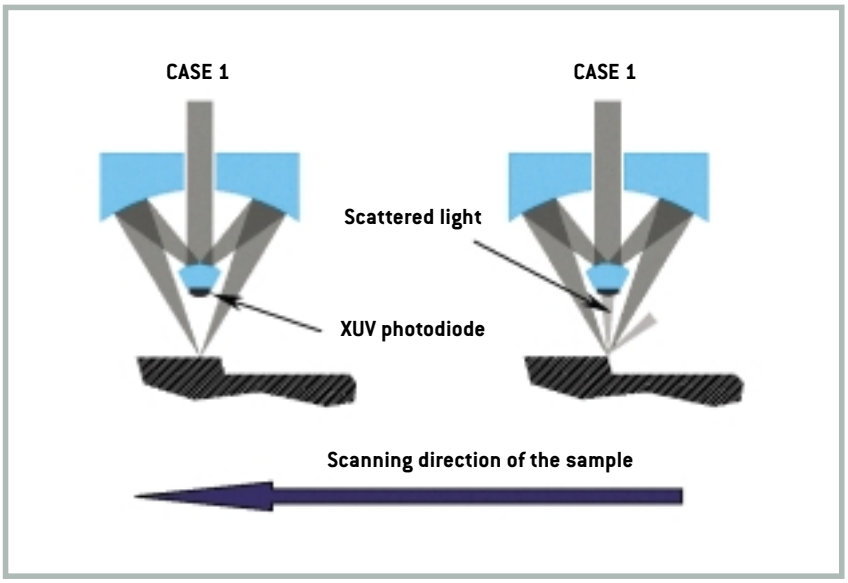

Figure 1. Principle of dark-field detection mode in scanning microscopy: the XUV photodiode detects the scattered light from the edge of the defect on the sample.
Case 1. On a flat surface the incident light is reflected into the specular direction. No signal is detected by the photodiode.
Case 2. The scattered light from the edge is detected by the photodiode.

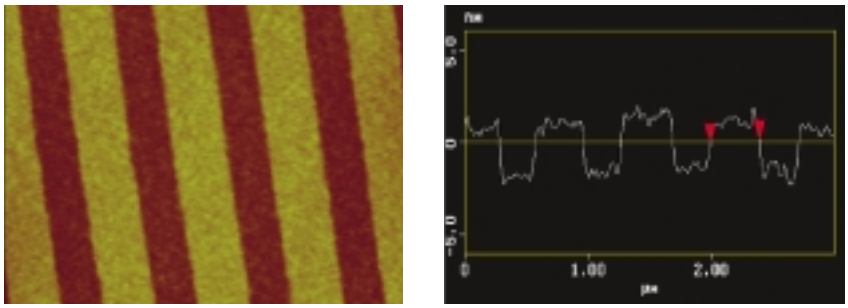

Figure 2. AFM image of the top of a multilayer with programmed defects (3.2 nm height and 700 nm pitch). The defect is perfectly replicated into the multilayer and the roughness is 0.22 nm RMS.

the major issues is the fabrication of the mask. In order to keep reasonable yield, it is essential to manufacture masks with a very low density of defects. The current requirement of the "International Technology Roadmap for Semiconductors" is 5×10^{-3} defects/cm^2 [1]. The ability to reliably detect the presence of a defect is of primary importance for the manufacturing capability of EUV lithography. This requirement is still far from being met, moreover it is expected that some defects buried in the multilayer mirror that hardly affect the surface topography (and consequently are invisible using standard inspection techniques) are likely to be printed in the resist [2].

"At wavelength" inspection is a way to detect this kind of defects. This has been demonstrated experimentally and the correlation between "at wavelength" and visible inspection has been established [3, 4]. In this paper we show that the use of dark-field microscopy combines high resolution imaging capabilities [5] with a high sensitivity to small phase variations.

In order to assess the capability of "at wavelength" inspection to identify multilayer defects, we have implemented a dark-field detection mode on the scanning Schwarzschild microscope of the Spectromicroscopy beamline, working at a wavelength of 13.1 nm. Special samples have been fabricated at the CEA-LETI facility in Grenoble, France. These microstructures consist of gratings of silicon oxide with depth ranging from 3 nm to 22 nm, on which we have deposited a multilayer of 40 pairs of Mo/Si.

In addition to the demonstration that dark-field microscopy is capable of detecting buried structures as shallow as 3 nm, the experiment yielded a deeper understanding of the delicate imaging process of dark-field microscopy. This second step was made possible by an upgrade of the scanning stage, by including the capability to tilt the sample. A fine tuning of the objective illumination by careful adjustment of the refocusing mirrors of the beamline has also provided a significant improvement of the images.

FIGURE 3

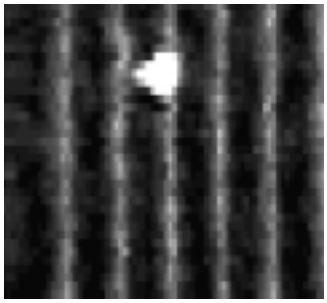

Figure 3. Image (21 μm × 22 μm) of a 3.2 nm height grating with an unintentional defect.

FIGURE 4

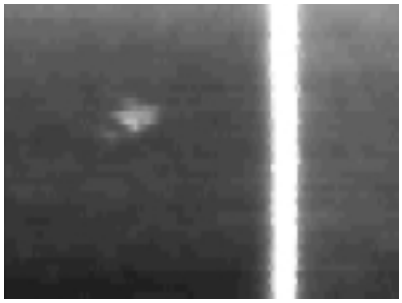

Figure 4. Image (18 μm × 13 μm) of an unintentional defect with a size of 0.4 μm × 0.16 μm, close to a step of 19.4 nm height.

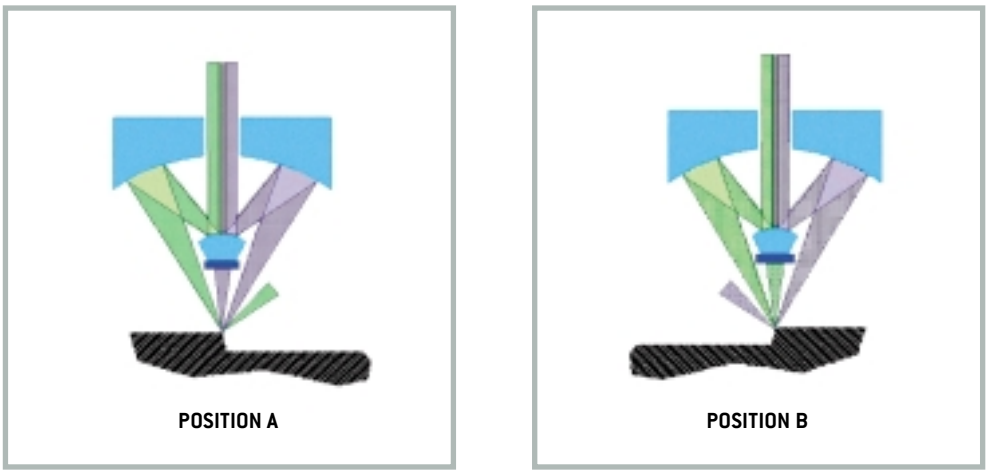

Figure 5. Scattering mechanism involved in the image formation process:
Position A) Due to the scattering process, the right edge of the feature is only imaged by the right part of the pupil illumination.
Position B) Conversely, the left edge is imaged by the left part of the pupil illumination.

EXPERIMENTAL

Principle of Dark-field Detection

To perform dark-field measurements, a photodiode was mounted on the back of the primary mirror of the Schwarzschild objective of the Spectromicroscopy Beamline. The principle of this experiment is based on the detection of the light diffracted by the defects (generally the edges) as can be seen in Figure 1. The acquisition of the image is performed by scanning the sample under a spot of 0.5 µm full width at half maximum (FWHM). When the surface is flat the light coming from the Schwarzschild objective is reflected in the specular direction and the photodiode detects no signal. When the spot encounters an edge of a defect, the light is scattered from the sample in the dark cone and is detected by the photodiode. Thus the dark pixels of the image represent flat regions of the sample, whereas bright features mark the presence of defects that are revealed by their capability of diffracting light such as absorption discontinuities or phase shifting features. In order to study this effect, we have fabricated dedicated phase objects of varying height.

Sample Fabrication

The samples were fabricated by deposition of a multilayer stack on top of features etched into silicon dioxide. For the manufacturing of the etched structure we chose to use a wet etching of hydrofluoric acid (HF) on silicon oxide. This allows a better control of the etched depth. A first series of etching was done on a full wafer of silicon oxide to determine accurately the etch rate of different HF solutions, using an ellipsometric measurement to control the thickness of silicon oxide. A deep UV stepper was used to pattern the photoresist that was subsequently used as a mask during the etching of the silicon dioxide layer. On top of these "defects" Ion Beam Sputtering was used for the deposition of 40 pairs of Mo/Si. The period of the multilayer is 6.8 nm that provides maximum reflectance for the Schwarzschild objective configuration (l= 13.1 nm, mean incidence angle = 8.93°). An Atomic Force Microscope (AFM) scan indicates that the defects are perfectly replicated on top of the multilayer, thus creating a phase object (Figure 2).

RESULTS AND DISCUSSION

The most straightforward result of our experiments is the demonstration of the extreme sensitivity of this detection technique. This is illustrated in Figure 3: even a grating with step height as small as 3.2 nm is imaged with excellent contrast.

After testing the technique on engineered defects, we looked for unintentional defects and eventually found a few. An example is

already shown in Figure 3, another can be seen in Figure 4, which shows the image of a point defect close to a step of 19.4 nm height. The point defect was subsequently analyzed by AFM. Its size is 0.4 µm × 0.16 µm. By comparison with the FWHM of the radiation spot (0.5 µm) this finding emphasizes another aspect of this technique of high practical importance: the remarkable sensitivity of the detection mechanism allows good quality imaging of features with size well below the resolution limit.

Besides establishing possible practical achievements, our experiments were dedicated to obtaining a deeper understanding of the scattering process underlying the principle of image formation in dark-field microscopy. It appears that a given feature of the sample can be imaged only by rays which have a given inclination and therefore only by a portion of the pupil illumination. This is illustrated in 1D by the sketches in Figure 5: in simple terms, it can be stated that the right edge of the feature is imaged only by the rays coming from the right (position A of the sample), whereas the opposite holds for the left edge (position B) of the feature.

An illustration of this fact is displayed in the top part of Figure 6, which shows three images of a T-shaped features (step height = 19.4 nm). These images were acquired under focus (a), at best focus (b), and beyond best focus (c). It is clearly seen that the defocusing influences the apparent size of the T-shaped feature and the crossing/retracting appearance of its corners (concave and convex corners exhibiting opposite behaviour). The reason for these findings is the extreme anisotropy of the scattering mechanism involved in the image formation process: (1) out of focus the spot on the sample is a ring; (2) different portions of the pupil (the "ring") contain rays which have different inclinations with respect to the surface normal; (3) depending

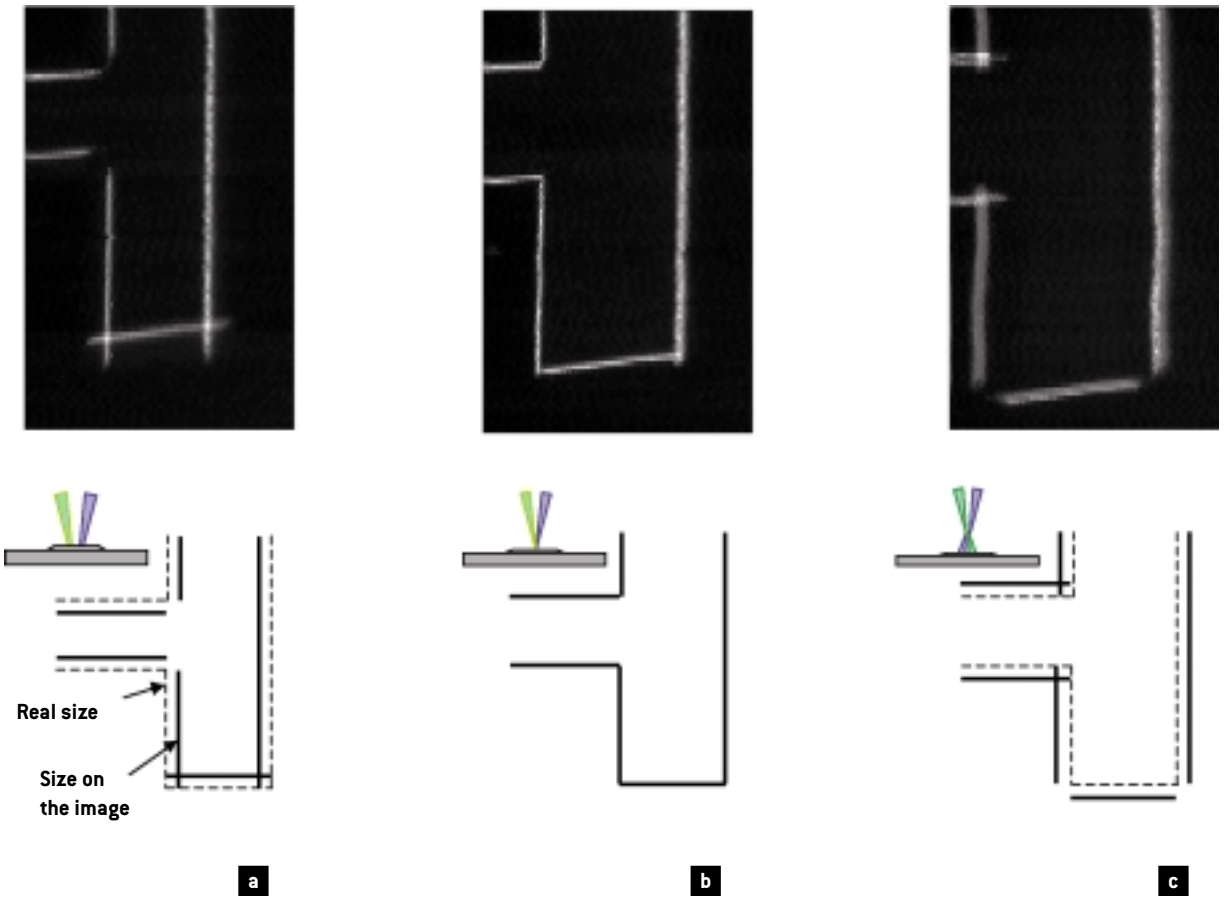

Figure 6. Top: Images (size=35 μm × 70 μm) of a T-shaped feature with step height 19.4 nm demonstrating the influence of defocusing on the image appearance: a) under focus by 50 μm, b) at best focus, c) beyond best focus by 30 μm. Middle: Sketch of the focusing conditions for the three images. Bottom: Comparison of the real and the apparent size of the features at the three focusing conditions.

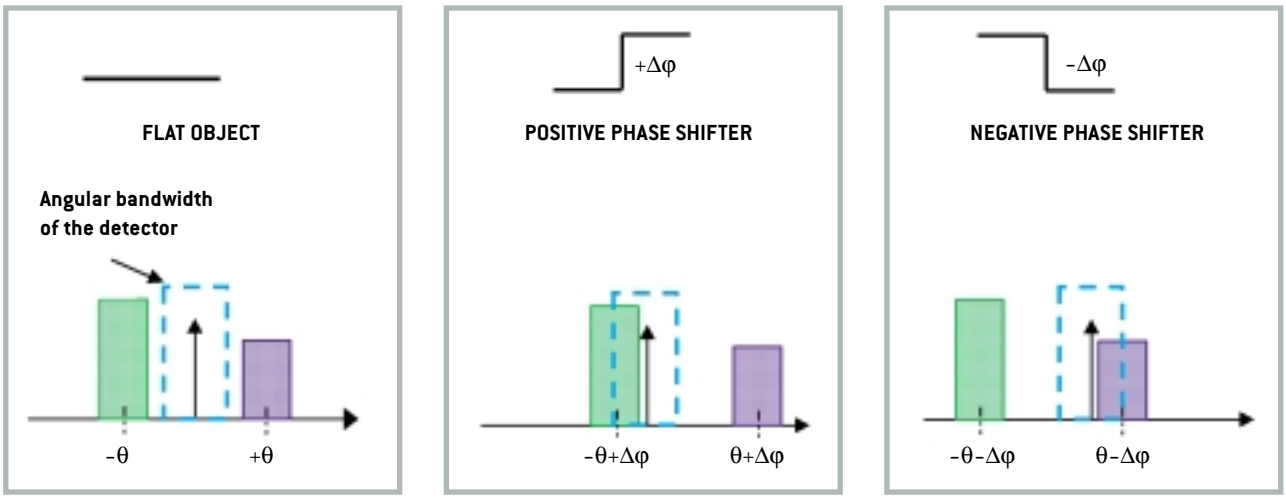

Figure 7. Representation of the scattering mechanism in spatial frequency domain for a cross section of the pupil. When a positive phase defect is imaged, the pupil suffers *a* +Δφ shift that permits the detection of the left (-θ) component of the pupil in the angular bandwidth of the detector. For negative phase shift (-Δφ) the photodiode detects the right component of the pupil illumination (+θ). The sketch depicts a case of non uniform illumination of the pupil: in the present example, the left component is more intense. Correspondingly, a positive phase shifter will appear brighter than a negative phase shifter of equal strength.

on the direction of the feature slope, the sample can be imaged only by a portion of the "ring". The implications for the *apparent* feature size are straightforward. In order to move from position A to position B (Figure 5), the sample has to be scanned by *less* than its real size in under focus (and will therefore appear *smaller* in the scanning microscope) and vice versa beyond best focus.

In more quantitative terms, the image formation process is illustrated (in 1D) in Figure 7. The pupil has two components centered at -θ (left) and +θ (right). A defect on the sample plays the role of a positive or negative phase shifter for a rising or falling edge respectively. The detector acts as a band-pass filter. When the radiation is scattered at a rising edge, the defect induces a phase change of +Δφ of the reflected spot, i.e. shifts the two components of the pupil to -θ +Δφ and +θ +Δφ, thus letting the left component (-θ +Δφ) fall inside the angular band of the detector. By the same token, a falling edge is prone to be probed (through a suitable negative shift -Δφ) by the right component of the pupil.

Figure 7 illustrates another aspect of the image formation: if the illumination of the pupil is not uniform, phase shifters of same strength and opposite sign will not have the same intensity in the image. In more simple terms, the case illustrated in Figure 7 describes an image in which a rising edge appears brighter than a falling edge of equal height. The formalism depicted in Figure 7 can be used to describe yet another aspect, namely the possibility that the sample normal is tilted with respect to the optical axis by a small angle Δψ (positive or negative), smaller than (1) the shift Δφ induced by a typical defect and (2) the angular separation between the pupil and the angular band of the detector. In this case, it will still hold that defects will appear as bright features on a dark background; however, a rising and a falling edge of equal shape will give a phase shift of Δφ+2Δψ and -Δφ +2Δψ respective-

ly. For positive $\Delta\psi$, this again corresponds to a rising edge which appears brighter than a falling edge of equal height. From a dedicated measurements series (not reported here), we quantitatively documented both aspects (change in balance of the pupil illumination and tilt of the sample).

CONCLUSIONS

We have demonstrated that dark-field microscopy is an extremely sensitive technique for the detection of multilayer buried defects: excellent contrast images were obtained on defects as shallow as 3 nm and with linear dimensions as small as 160 nm (imaging capability down to below 50 nm can be estimated). Even if large improvements are needed, especially in terms of speed, dark-field microscopy appears to be very promising for the inspection of masks for EUV lithography, which is one of the key technologies in the next generation of integrated circuit fabrication.

Besides establishing the capabilities of the technique, our experiments were dedicated to deepening the understanding of the mechanism underlying the image formation process of dark-field microscopy with particular reference to the practical effect of defocusing, balancing the pupil illumination and tilting the sample. This clarified the reason for the existence, under particular conditions, of peculiar artifacts in the images.

New experiments are planned which will be dedicated to increasing the acquisition speed and investigating isolated defects with smaller sizes and, possibly, buried in a smooth planarized multilayer, leading to a flat top of the mirror. The latter corresponds to the case of a potentially printable defect which could remain undetected when inspected at longer wavelength.

ACKNOWLEDGMENTS

We thank Cyril Vannuffel, Viviane Muffato, Pascal Besson and Mourad Idir for their contribution in this work. We are grateful to Daniele Cocco and Giovanni Sostero for providing their expertise for the alignment of the dark-field microscopy setup and to Fabio Barbo and Gilio Sandrin for their enterprising and competent technical support.

References

[1] International Technology Roadmap for Semiconductors; http://public.itrs.net.

[2] P. Schiavone, R. Payerne; *Microprocess and Nanotechnology*; Matsue, Japan, (2001).

[3] S. Jeong, M. Idir, L.E. Johnson; Y. Lin, P.J. Batson, R. Levesque, P.A Kearney, P-Y. Yan, E.M. Gullikson, J.H. Underwood, J. James H.; Bokor; *Proc. SPIE;* Vol. 3546, p. 524-530.

[4] M. Yi, T. Haga, C. Walton, J. Bokor; *Journal of vacuum science of technology*; B19, 2401, (2001).

[5] V. Farys, C. Vannuffel, E. Quesnel, V. Muffato, P. Besson, M. Idir, M. Bertolo, A. Bianco, S. La Rosa, and F. Polack; *7TH international conference on X-Ray Microscopy;* ESRF Grenoble, France, (2002).

MACHINE STATUS

MACHINE STATUS AND DEVELOPMENTS

> Carlo J. Bocchetta
Sincrotrone Trieste - ELETTRA - S.S. 14 Km.163.5 in AREA Science Park, 34012 Basovizza, Trieste, ITALY

As in previous years activities during 2002-2003 have focused on the continual improvement of source characteristics. This year has been particularly important in this respect with the putting into operation of the superconducting third harmonic cavity in combination with the bunch-by-bunch transverse feedback systems. These two developments have provided a marked increase in source brightness and lifetime. A more detailed description of the harmonic cavity can be found in this volume of the Highlights. Significant progress has also been made towards the enhancement of orbit stability through the use of higher resolution beam position monitors and advanced feedback electronics, details of which can be found below. The development of a single pass free electron laser using the linac has also evolved with activities focusing on the design studies and machine layout (see this volume for more information and [1]).

OPERATIONS

In the course of 2002 the light source was operated for 6384 hours of which 4686 were scheduled for Users. The overall User uptime for that year was 92.3% (93.6 if external disturbances are excluded) and the major sources of downtime were attributed to storms, vacuum component failure and the radio frequency (RF) systems. The operational calendar for 2003 has scheduled 6552 hours of operation of which 4920 hours dedicated to User operation. Beam energy for 2003 has been 2.0 GeV for 74% of the time and 2.4 GeV for the remaining time. Operation for Users has involved a single refill per day with a starting current of 320 mA at 2.0 GeV and 140 mA at 2.4 GeV. The overall User uptime to date has been 90.4% (92.2 excluding storms) with the main causes of downtime due to storms, the commissioning of the cryogenic system of the third harmonic cavity and the linac.

Many improvements have been made to accelerator systems during the year. On the side of control electronics and software, there has been the continued upgrade to a two level architecture that adopts new CPU boards for the front-end computers [2]. The upgrade renews control hardware that is becoming obsolete and adds new features. In the control room the high-level software program 1bm (one button machine) has been redesigned and rewritten. 1bm automates and optimises the long sequence of operations required during a refill, that includes, magnet cycling, injection, energy ramping, orbit correction and insertion device management, to mention a few. The new version has improved performance and robustness. The electronics controlling the RF phase and higher order mode (HOM) shifters have been upgraded. The RF plants have also been equipped with mains stabilisers that increase the stability of the amplitude and phase of the RF output power. An upgrade of the phase loop electronics has started that allows an increase of the correction factor of the loop, permits increased bandwidth and the possibility to perform phase modulation of the RF signals for beam manipulation. An important improvement of the effectiveness of the correction of residual closed orbit distortions from insertion devices has been initiated. For this the correction coils, associated power supplies and feedforward control hardware for section 2, 3 and 6 insertion devices will be upgraded. Moreover, the upgrade will permit correction of individual modules of the full insertion device.

For what regards mechanical upgrades, the vacuum chamber in straight section 7 was replaced. Together with the new three-meter long NEG-coated aluminium vacu-

um chamber the straight section includes two new low-gap beam position monitors (BPM) for orbit feedback systems, two additional BPMs dedicated to the multi-bunch feedback systems and the machine scrapers. The new chamber allows smaller insertion device gaps to be reached.

PHOTON SOURCES

Activities on photon sources have principally concentrated on the insertion devices for the second X-ray and IUVS beamlines and modifications to the bending magnet chamber for the infra-red beamline. The installation and final commissioning of the second Figure-8 undulator module for the IUVS beamline took place. No significant perturbation was observed on storage ring beam dynamics when closing the insertion device to the minimum gap of 19 mm and undulator control was freely allowed to beamline users. Radiation spectra measured at the experimental station show good agreement with the predicted peak wavelength and intensity [3].

The superconducting wiggler (manufactured in BINP, Novosibirsk) will produce 14 times more photon flux at 25 keV compared to the present permanent magnet device for the second X-ray diffraction beamline. The wiggler installed in the autumn of 2002 has been studied under differing operational conditions. Both the power mode (where the magnet is permanently connected to its power supplies) and the persistent current mode (where a stationary current is circulating in the superconducting coils) were successfully tested. An upgrade to the vacuum chamber (modifications to the tapers and copper liner) was scheduled for the last quarter of 2003 to lower the consumption of liquid helium. The wiggler has been installed in section 11 of the storage ring next to the superconducting third harmonic cavity. A future upgrade to both cryogenic systems foresees delivery of liquid Helium from the cavity liquefier to the wiggler dewar and also a combined helium recovery scheme.

The installation of the new infrared beamline IRSR, which is foreseen in early 2004, has required the development of a new type of exit port for the beamline itself. Modification to machine components has centred on the bending magnet vacuum chamber, the photon absorber and the photon shutter. These modifications will allow a horizontal acceptance angle of 70 mrad and 25 mrad in the vertical plane. The horizontal acceptance allows both edge and main magnet infrared radiation. The requirements of the new beamline, in particular the vertical acceptance, have also required a new vacuum chamber design based on previous experience with aluminium constructs (Figure 1). While the photon absorber was just modified, the shutter component has been completely redesigned for the layout requirements of the beamline.

An important result of 2003 is the successful operation of the storage ring free electron laser (FEL) in the so-called Q-switching mode (see these Highlights for more details and [4]). This is performed by periodically modulating the main RF oscillator in such a way that laser pulses are generated with a regular time structure (following the RF signal modulation) and with increased output intensity. This is believed to be particularly useful for the planned time-resolved experiments that would benefit from the more predictable macro-temporal structure compared to the natural regime. A procedure to energy down-ramp the storage ring was also tested and enabled to lase for the first time at 750 MeV. The advantage of low beam energy consists in a

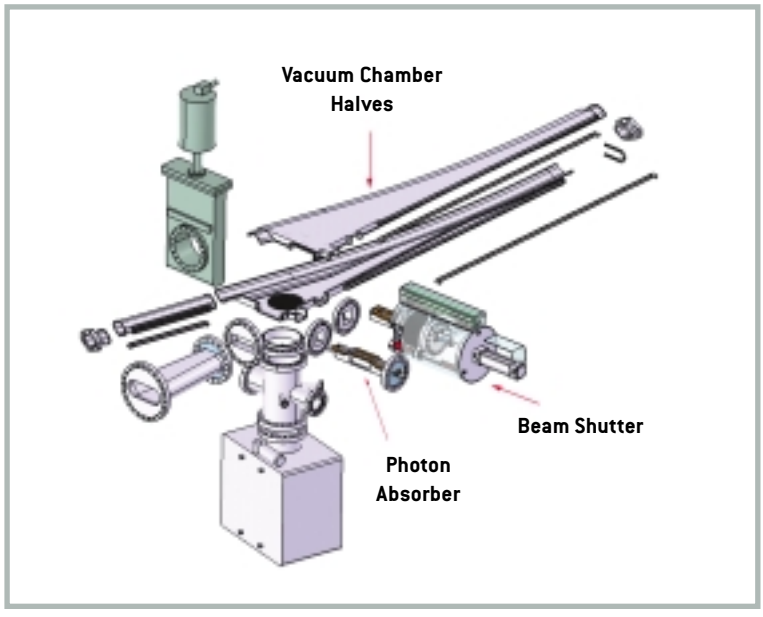

Figure 1. An exploded view of the vacuum chamber assembly for the infrared beamline showing the new beam shutter and photon absorber. The chamber is constructed of two aluminium half shells.

corresponding reduction of synchrotron radiation power that is responsible for the fast degradation of mirrors used in the optical cavity. The on-going synchrotron radiation tests of different single and multi-layer mirror samples are an important part of the European collaboration (EUFELE contract). The characterization of these samples before and after exposure allows a significant database of material properties to be built up. The database is then used to optimise the production process and the choice of materials that lead to FEL compliant mirrors for the VUV spectral region.

SUPERCONDUCTING 3RD HARMONIC CAVITY

A common problem of all intermediate energy third generation light sources is the short beam lifetime that arises from a small beam emittance. Such machines have high bunch densities and correspondingly increased elastic intra-beam collisions that lead to particle loss, i.e., the Touschek effect. To circumvent this effect the bunch is diluted by increasing its length while maintaining the all-important transverse emittance. A cavity operating at a higher harmonic of the main RF system, when appropriately phased, will lengthen the bunch without introducing increased energy spread. A superconducting third harmonic cavity was chosen and put into operation during 2003 (see these Highlights for more details and [5]). The system provides both an increase in lifetime, through bunch lengthening, and the Landau damping of longitudinal multi-bunch instabilities. The cavity is in routine operation at 2.0 GeV and 320 mA, where the improvement in beam lifetime attains to more than a factor of 3.0 and full damping of longitudinal beam instabilities is provided. The cavity has also been activated during User runs at 2.4 GeV and 140 mA, where it provides an increase in lifetime of up to 50% the nominal value.

MULTI-BUNCH FEEDBACK SYSTEMS

Activities with the transverse multi-bunch feedback system have progressed with the putting into operation of the second system acting in the horizontal plane [6]. Prior to this system, horizontal instabilities were suppressed by acting on the harmonic sextupoles to provide Landau damping. The sextupole settings, however, were not optimal for a long beam lifetime. The two transverse multi-bunch feedback systems have enhanced the effectiveness of User operation through a considerable gain in beam lifetime. Machine operation with the systems allows nominal optics to be used with a consequent increase also in dynamic aperture. In this configuration together with the operation of the third harmonic cavity a beam free of coupled-bunch instabilities is delivered to Users at all operating energies. Since installation, the operational behaviour of the two systems has been effective and reliable.

First extensive tests of the longitudinal multi-bunch feedback were performed during the start of 2003. The longitudinal feedback digital processing electronics take advantage of the same kind of hardware developed for the already operating transverse feedback, so that individual digital filters are executed for each of the 432 2-ns spaced bunches. Principal differences exist on the front end (detector electronics) and the back end (RF modulator, RF amplifier and kicker). Commissioning results have been positive and by activating the system from the beginning of the injection process up to 280 mA of longitudinally stable beam at 0.9 GeV have been accumulated. At present the system is not used for User operation since the third harmonic cavity naturally damps longitudinal instabilities when operating in bunch lengthening mode. The system has, however, been effectively operated for the suppression of longitudinal instabilities of the 4-bunch beam used by the storage ring FEL.

ORBIT FEEDBACK

The aim of the fast Local Orbit Feedback (LOF) system is to stabilize the electron beam position and angle at the corresponding ID center without affecting the rest of the orbit. The most important noise sources considered are temperature changes producing drifts on different machine equipment, closed orbit distortions generated by ID operation, mechanically and electrically

driven vibrations up to some tens of Hz, which include persistent periodic oscillations derived from the mains at 50 Hz and its harmonics.

Two 'low-gap' BPMs and four corrector magnets are used as sensors and actuators respectively [7]. The same ELETTRA standard corrector magnets normally used for orbit corrections are also employed by the fast feedback system. The -3dB cutoff frequency of the correctors is about 70 Hz, which is the main limiting factor of the feedback performance. On the other hand, the phase delay induced by the eddy currents generated in the stainless steel vacuum chamber by the AC magnetic field is negligible, resulting in one degree at 60 Hz and two degrees at 100 Hz.

The LOF processing part is hosted in a VME-based Equipment Controller. The digital beam position samples are generated at 8 kHz rate by the BPM electronics and are passed through the VME bus to a PowerPC CPU board. A task running under the Linux operating system with real-time extension executes the feedback algorithm. A multi-channel DAC converter board transforms the resulting digital output samples into analog signals that drive the corrector magnet power supplies.

The basic feedback algorithm adopted is a PID (Proportional, Integral, Derivative). An additional single-pole digital low pass filter limits the input signal dynamics to avoid non-linearities of the corrector magnet power supplies. While slow orbit drifts and lower frequency components of the beam noise spectrum are corrected by the PID controller, a different technique called 'harmonic suppression' is used to effectively remove those specific components induced by the mains. The harmonic suppression scheme (Figure 2) consists of a loop with a selective digital filter centered at the frequency to damp. The delay is calculated in order to achieve an overall system open-loop rotation of 360° at the chosen frequency. The closed-loop system behaves as a notch filter whose depth is regulated by the programmable gain. As long as the notches are completely separated from each other, multiple harmonic suppressors centered at different frequencies can be implemented and run in parallel with the standard PID regulator (Figure 2). Moreover, as the beam noise components associated to the mains are periodic and stable, their reduction is possible even if the frequency is higher than the open-loop cut-off frequency, where the phase rotation is large.

The spectra in figure 3 show the effect of the LOF with the combined action of the PID controller and harmonic suppressors at 23.5, 50, 100, 150 and 200 Hz.

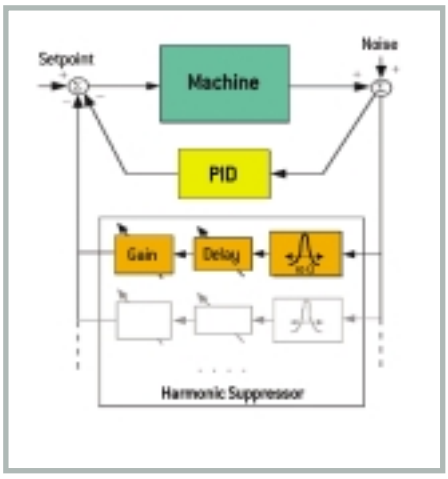

Figure 2. Block diagram of the LOF scheme showing the concurrent action of the PID controller and multiple harmonic suppressors.

Figure 3. Residual orbit sub-micron noise after application of the LOF on the SuperESCA beamline.

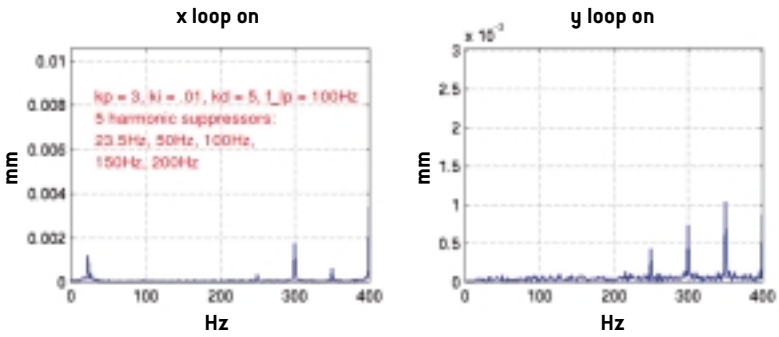

RF UPGRADE

The upgrade of the storage ring RF system is necessary to handle the RF power requirements of the full set of insertion devices and to allow operational overhead. The first phase of the upgrade is the substitution of one of the original 60 kW amplifiers with a 150 kW plant. The substituted plant will be used to power the booster RF system. The detailed evaluation of the offers received in reply to the call for tender has been completed. The upgrade, based on Inductive Output Tubes (IOT's), will use two 80 kW tubes combined by means of a switchless combiner and allows the operation of each IOT in stand-alone mode if necessary. A new improved version of the original RF cavity replaces the one in section 9. The new cavity features an upgraded cooling system that allows operation at a higher gap voltage corresponding to 60 kW of wasted power on the cavity walls. The newly designed input power-coupler also doubles the RF power to the cavity from the present 60 to 120 kW. Finally the higher order mode frequency shifter is also of a new concept, free of RF contacts, that will allow use of the full shifting range at full cavity power (60 kW).

FULL ENERGY INJECTOR

The full energy injector under construction for the storage ring is composed of a 100 MeV pre-injector linac and a 2.5 GeV booster synchrotron with a repetition frequency of 3 Hz. The 100 MeV pre-injector linac for the booster will use two 50 MeV accelerating sections donated by CERN. The in house construction of the modulator for the klystron of the pre-injector has been completed and is being tested (Figure 4). The system for beam injection into the booster is composed of a septum magnet and a fast kicker magnet, while extraction is performed by a set of bumper magnets, kickers and an extraction septum. The call for tender for the septum magnets for injection and extraction from the booster and those for the upgrade of the storage ring was made and an order placed. Delivery of all three systems is planned for early 2004. The booster will be built to operate in top-up mode necessitating reliable operation of all parts. In view of this, tests to identify critical components of the septum magnet power circuit were performed on a prototype after which the series production of six units was initiated. The design of the fast kicker magnets, based on in-vacuum ferrite magnets, has progressed and a prototype will be constructed in 2004 to test with the kicker high voltage pulsed power supply. The booster synchrotron is a two-fold symmetric lattice with long straight sections for injection and extraction. The lattice is composed of bending magnets, two types of quadrupoles and sextupoles. Specifications for the bending and quadrupole magnets have been reviewed and are now available in their final version together with those of the steerer magnets. The RF system for the booster is composed of a DESY type five cell cavity (Figure 5) powered by one of the storage ring amplifiers that will be available after the RF upgrade. The cavity was delivered at the end of May and has undergone measurements and high power RF tests in the laboratory. Development activities for other systems, such as power supplies, controls, interlocks, access control, diagnostics and vacuum have also advanced. For the diagnostics a new version of the fluorescent screen is being developed and a prototype constructed, with a combined thermal and mechanical design, for use in both transfer lines and the booster. The associated image acquisition and analysis system will be installed in the storage ring as an upgrade of the storage ring synchrotron radiation profile monitor. The first detectors adopted for the booster BPMs have also been installed on the ELETTRA linac and transfer line for characterisation with beam. Furthermore civil engineering activities, scheduled for

Figure 4. The complete modulator and klystron tank for the booster pre-injector.

Figure 5. The five cell booster cavity undergoing power tests in the RF bunker.

early 2004, will start the construction of the second part of the new injector building. This part of the building includes the electrical service area, the bridge connecting the existing control room and a part of the booster tunnel in the injection area.

References

[1] R. Bakker, *et al.; FERMI@ELETTRA: Project Update,* 25th Intl. Free Electron Laser Conference, Tsukuba, Japan, (2003).

[2] D. Bulfone, *et al., New Front-End Computers Based on LINUX-RTAI and PowerPC,* ICALEPCS 2003, Gyeongju, Korea, (2003).

[3] D. Zangrando, *et al.; Commissioning of two New Insertion Devices at ELETTRA,* Proc. Particle Accelerator Conference, Portland, Oregon, USA, (2003).

[4] G. De Ninno, *et al.*; *Q-Switching Regime of the ELETTRA Storage-Ring Free Electron Laser*, 25th Intl. Free Electron Laser Conference, Tsukuba, Japan, (2003).

[5] M. Svandrlik, *et al.; Performance of the 3rd Harmonic Superconducting Cavity at ELETTRA*, 11th Superconducting RF Workshop, Travemünde, Germany, (2003).

[6] D. Bulfone, *et al.; Bunch by Bunch Control of Instabilities with the ELETTRA/SLS Digital Feedback Systems,* ICALEPCS 2003, Gyeongju, Korea, (2003).

[7] D. Bulfone, *et al.; Exploiting Low-Gap Beam Position Monitors in Orbit Stabilisation Feedback and Feedforward Systems at ELETTRA,* J. Jap. Soc. Synchrotron Radiation Research, 197, Volume 16, (2003).

GIANT-PULSE GENERATION USING THE ELETTRA STORAGE RING FREE-ELECTRON LASER

> G. De Ninno, M. Trovò, M. Danailov, M. Marsi, B. Diviacco
Sincrotrone Trieste - ELETTRA - S.S. 14 Km.163.5 in AREA Science Park, 34012 Basovizza, Trieste, ITALY

INTRODUCTION

The maximum average lasing power that can be achieved using a storage-ring free-electron laser (SRFEL) is limited by the heating of the electron beam that is induced by the onset of the laser [1,2]. The increase of the electron-beam energy spread is indeed responsible for the diminution of the optical gain until when, at saturation, the latter reaches the level of the optical cavity losses. For applications requiring high peak power the FEL power can, however, be "concentrated" into a series of giant pulses. In this case, the peak power is considerably enhanced (from one to a few orders of magnitude) while the average power is only slightly reduced [3].

The giant-pulse operation mode of an SRFEL can be performed either by means of a radio-frequency (rf) modulation, the so-called Q-switching, or by using a gain-switching technique [3]. The first method, currently used at Super ACO [4] and UVSOR [5] and recently implemented at ELETTRA, is based on a periodically-induced longitudinal detuning between the electrons circulating in the ring and the light pulse stored in the optical cavity. When the system is detuned the lasing process is stopped. Maintaining the detuned condition for a long enough time allows the electron beam to cool down and the gain of the amplification process to recover its initial maximum value (i.e. laser-off). Once this situation is reached, the system is led back to the perfect tuning condition that is typically maintained for a period of a few milliseconds to induce the onset of the giant pulse. The system is then detuned again and the process repeated.

The GW level of intra-cavity power achieved in giant-pulse operation mode is suitable for interesting applications and in particular it allows the possibility of an efficient generation of harmonics of the fundamental wavelength [6]. Increasing interest is being shown in the use of this technique, which offers the possibility to generate tunable and coherent radiation in the UV and soft-X-ray ranges. In this respect, the use of the FEL itself as a seed can be considered complementary to the standard process for harmonic generation on SRFELs, which is based on single-pass interaction between the electron beam and an external laser [7,8].

The implementation of Q-switching at ELETTRA has led to a significant improvement of the stability and reproducibility of

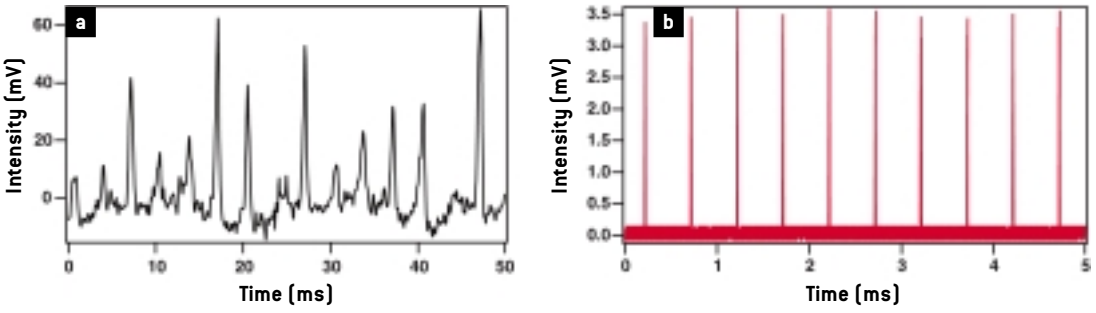

Figure 1. ELETTRA FEL signal in standard **a)** and Q-switched operation mode **b)**. The experimental setting is the following: beam energy: 900 MeV, beam current (four bunches): ≈ 10 mA, laser wavelength: 250 nm, optical gain: ≈ 7%, cavity losses: ≈ 10 5%.

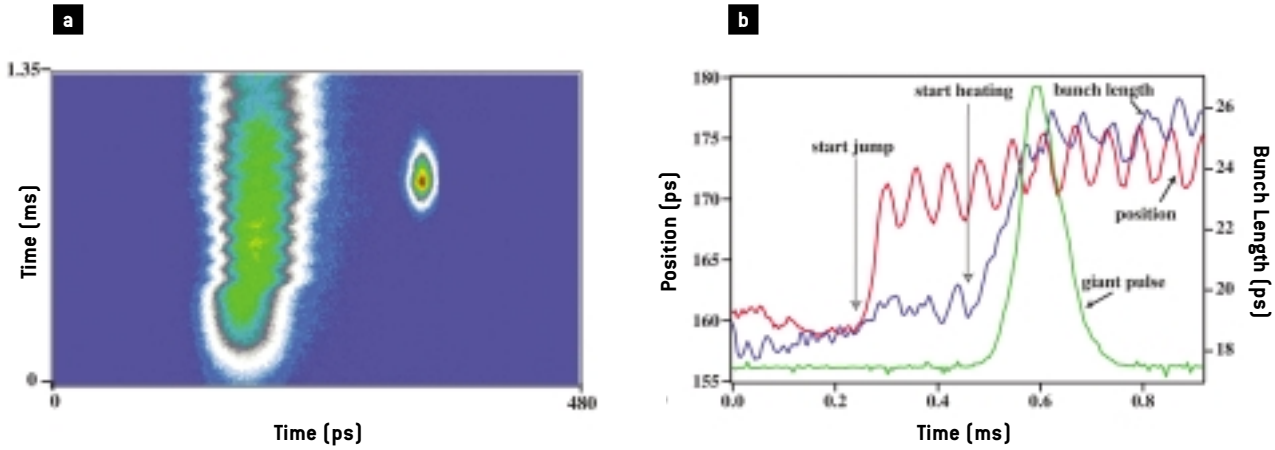

Figure 2. **a)** Streak camera image of the electron beam (left trace) and of the laser macropulse (right trace) in Q-switched operation mode. A horizontal cut provides the longitudinal distributions while on the vertical axis one can follow the evolution in time of the distribution profile. **b)** Analysis of figure **a)**. Beam current: ≈ 8 mA.

the laser signal over the standard operation mode. A systematic study has been carried out of both: the electron-beam sensitivity to the choice of the modulation parameters and the correlated source performance.

A SIGNIFICANT IMPROVEMENT OF THE ELETTRA FEL PERFORMANCE

Figure 1 shows an example of the different macro-temporal structures displayed by the FEL when operated in standard (Figure 1a) or Q-switching (Figure 1b) mode. The aperiodic character of the "natural" regime is a direct consequence of instabilities perturbing the electron beam dynamics. In particular, the dynamics of the laser is particularly sensitive to the presence of a systematic 50 Hz perturbation (and its harmonics), whose origin is presently under investigation. This slow instability may manifest itself in various unpredictable ways, e.g. as a kick or as a continuous modulation, and it can be the origin of fast synchrotron-like instabilities [9]. This lack of reproducibility is reflected in the noisy temporal structure of the laser signal (see Figure 1a). When operated in Q-switched mode, the FEL appears to be much less affected by the imperfect electron-beam stability. Figure 1b shows the significant improvement of the FEL performance in terms of peak power (an enhancement of roughly a factor of 70 with respect to the standard operation mode) and stability (fluctuations of the peak power of only a few percent). This achievement represents an important step towards the possibility of fully exploiting the source for pilot user experiments in photoelectron microscopy and time-resolved spectroscopy [10].

FEL EFFICIENCY VERSUS THE MODULATION PARAMETERS

The FEL performance in terms of (peak and average) power and stability when the system is operated in a Q-switched regime is strongly correlated with the choice of the modulation parameters, i.e. the repetition rate and slope of the rf jump that brings the system back to perfect synchronism. These parameters influence the status of the electron beam at the start of successive giant pulses. Figure 2 shows a streak camera image [11] simultaneously displaying the electron beam (perturbed by the modulation) and the generated giant pulse. One can clearly notice (Figure 2b) the main phenomena involved in the process: the excitation of synchrotron oscillations due to the rf jump, the heating of the electron-beam and the slightly-delayed start of the giant pulse.

A dedicated study [12] has shown that induced oscillations can be suppressed by means of a suitable choice of the slope of the rf jump. As for system performance as a function of the repetition rate of the modulation, Figure 3 shows the measured peak power, risetime and temporal stability (with respect to a given reference) of the giant pulse. The behaviour of the peak power is qualitatively as expected: it grows almost

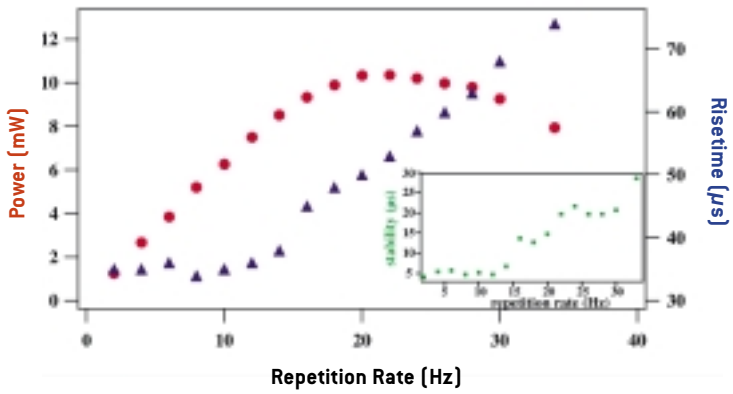

Figure 3. Peak power (circles), risetime (triangles) and stability (see inset) of the giant pulse as a function of the repetition rate of the modulation. The stability has been characterized by measuring the rms jitter of the pulse centroid with respect to the start of the modulation. Beam current: ≈ 7 mA. The energy per giant-pulse in the regime of maximum efficiency is about 600 μJ.

linearly up to a given repetition frequency beyond which the time left to the electron beam to cool down between the generation of two successive pulses becomes too short. As a consequence for higher frequencies the process becomes less efficient. A surprising result is that the threshold value, around 20 Hz, is much higher than expected. In fact, one could assume that the time necessary for the electron beam to cool down to be of the order of few synchrotron damping times, i.e. a few hundred milliseconds for the actual experimental setting and not, as shown in Figure 3, around 50 ms. The observed phenomenon, the origin of which is under investigation, suggests that electron-beam cooling between successive giant pulses is driven by a mechanism that is different and faster than (standard) synchrotron damping. As for the laser risetime, it stays almost constant for small repetition frequencies. As the frequency approaches the threshold value an increase is observed. It is worth pointing out that, since the laser risetime is inversely proportional to the net optical gain such an increase corresponds to a degradation of the amplification process. According to what is observed in the inset of Figure 3, the time jitter between two successive giant pulses is minimized when the repetition frequency is well below the threshold value.

CONCLUSIONS

The implementation of the Q-switching mode of operation has allowed a significant improvement of both the peak power and reproducibility of the storage ring free electron laser. This achievement increases the reliability of the source for user experiments and opens up interesting perspectives for harmonic generation in the UV and soft-X-ray ranges.

References

[1] N.A. Vinokurov et al.; Preprint INP77.59 Novossibirsk (unpublished), (1977).

[2] A. Renieri, *Il Nuovo Cimento*, 35, 161, (1979).

[3] I. V. Pinayev et al.; *Nucl. Instr. and Meth.*, 475, 222, (2001).

[4] T. Hara et al.; *Nucl. Instr. and Meth.*, 341, 21, (1994).

[5] M. Hosaka et al.; *Nucl. Instr. and Meth.*, 507, 289, (2003).

[6] V. Litvinenko et al.; *Nucl. Instr. and Meth.*, 507, 265, (2003).

[7] B. Girard et al.; *Phys. Rev. Lett.*, 53, 2405, (1984).

[8] R. Prazers et al.; *Nucl. Instr. and Meth.*, 304, 72, (1991).

[9] G. De Ninno et al.; *Proceedings PAC Conference,* (2003).

[10] B. Diviacco et al.; *Proceedings FEL Conference,* (2003).

[11] M. Ferianis and M. Danailov, *Proceedings AIP Conference,* (2002).

[12] G. De Ninno et al.; *Proceedings FEL Conference,* (2003).

COMMISSIONING AND OPERATION OF THE SUPERCONDUCTING THIRD HARMONIC CAVITY

> G. Penco, M. Svandrlik
Sincrotrone Trieste, S.S.14, Km.163,5 in AREA Science Park, 34012 Basovizza, Trieste, ITALY

INTRODUCTION

One of the most important challenges for ELETTRA is to increase the brightness of the source. For intermediate energy sources, a critical issue is also the beam lifetime that is dominated by large angle intrabeam elastic scattering, i.e. the Touschek effect. Consequently a reduction of the emittance also leads to an increase in the bunch density and therefore to a reduction in lifetime. The use of a cavity operating at the 3rd harmonic of the main RF frequency was therefore decided in order to lengthen the electron bunches and correspondingly increase the beam lifetime without affecting the transverse emittance [1]. The SUPER-3HC superconducting passive cavity (Figure 1), was installed during the 2002 summer shutdown together with the cryogenic plant that feeds the system with liquid Helium at 4.5 K [2]. A commissioning period followed, first for the cryogenic plant (during which ELETTRA operated with the superconducting cavity at room temperature) and afterwards, in January 2003, for the cooled cryomodule at 4.5K with beam. Routine operation of the cavity started in July 2003. The system has not only significantly increased the beam lifetime by up to a factor 3.5, but it has also completely suppressed all longitudinal coupled bunch instabilities.

CRYOGENIC PLANT COMMISSIONING AND PERFORMANCE

The cryogenic source for the cryomodule is a HELIAL 1000 refrigerator-liquefier manufactured by AIR LIQUIDE. The specified performance, that includes a 50% safety margin, is for a refrigeration power of 65 W and simultaneous liquefaction of 7.5 l/h [3]. The commissioning period of the cryogenic source lasted from the end of September 2002 to the beginning of December 2002. A series of technological issues were solved during the period that concluded with the

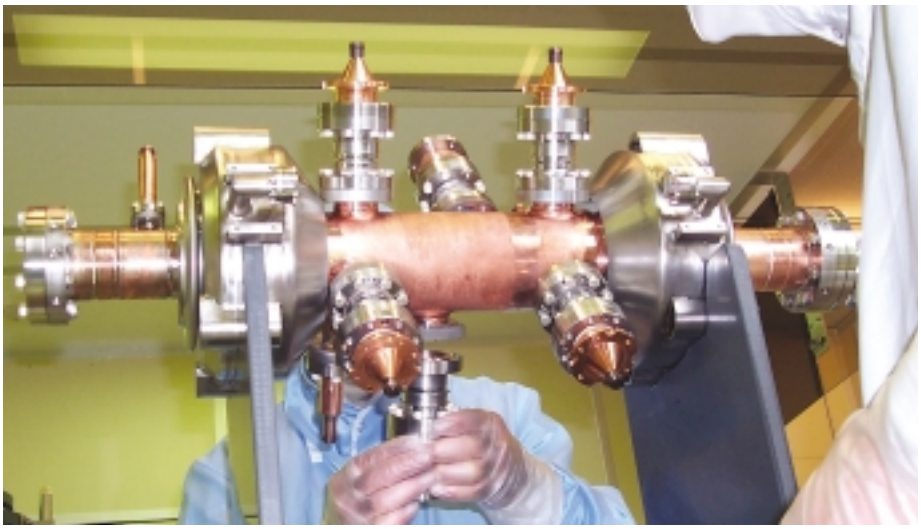

Figure 1.
The superconducting cavity being assembled at Saclay.

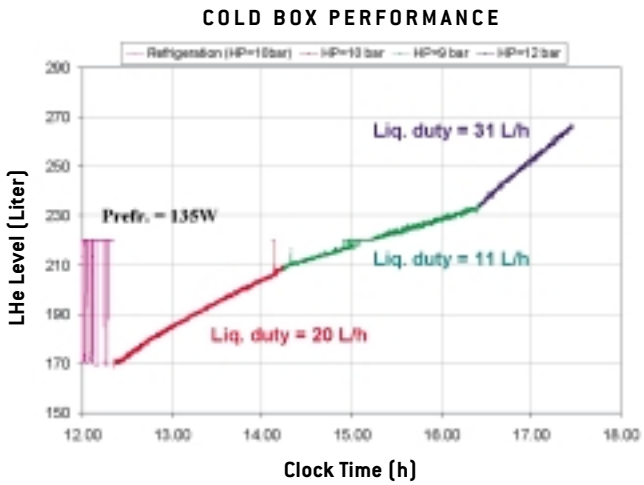

Figure 2. Acceptance test results of the HELIAL 1000.

Table 1. Liquefaction and Refrigeration performance of the HELIAL 1000.

Refrigeration Power at 4.5 K	Liquefaction Duty		
10 bar	9 bar	10 bar	12 bar
135 W	11 L/h	20 L/h	31 L/h

acceptance tests (Figure 2 and Table 1). The cryogenic source has exceeded specifications with a refrigeration power of 135 W and a liquefaction duty of more than 30 l/h at a compressor high pressure setting of 12 bar. Since the high pressure can be increased to 15 bar there are sufficient safety margins. In operating conditions, the refrigerator can sustain the full load of the operating cavity and still maintain a liquefaction capability between 10 and 20 l/h, depending on the high-pressure setting. The cryogenic system has to handle operating conditions with varying loads, which can also change rather quickly because of the dynamic radiofrequency losses in the operating cavity. The effective response of the system to these changes is performed by regulation loops.

CAVITY COMMISSIONING AND PERFORMANCE

The cavity is composed of two cells and has met the specifications both in the vertical cryostat test at CERN (Q_0 = 2x10^8 at 4.5 K and 5 MV/m) and in the loaded test in the cryomodule at Saclay (Q loaded larger than 1 10^8 at Eacc 5 MV/m) [4]. The performance specifications of the cavity are listed in Table 2. The voltage provided by the 500 MHz normal conducting RF cavities is 1.8 MV and this sets the nominal voltage of the harmonic cavity to be 600 kV. The voltage in the harmonic cavities exceeds this nominal value for a beam current of 320 mA when the cells are tuned to +60 kHz from the 3rd harmonic.

In the design of the RF structure partic-

3rd Harmonic Frequency	1498.955 MHz
Cavity tuning @ 320 mA	1499.015 MHz
Detuning, Δf @ 320 mA	+ 60 kHz
Nominal 3rd harmonic voltage	600 kV
Accelerating field gradient	3.0 MV/m
Vacuum pressure @ 320 mA	< 5 10^{-9} mbar
Parking position	1499.200 MHz
HOMs excited by the beam	None
Longitudinal HOM damping specification	f_r*$R_{//}$<7.0 kΩ*GHz
Transverse HOM damping specification	$R_\perp$ < 130 kΩ/m

Table 2. SUPER-3HC cavity performance at ELETTRA.

ular care was given to the damping of Higher Order Modes (HOM). The Q_{ext} of the HOM measured in the laboratory showed that the stringent specifications were met almost without safety margin. A very successful result of the design is that the SUPER-3HC structure does not drive any unstable coupled bunch oscillation. This is true both for users' operation at 2.0 GeV, 320 mA, and for the injection energy at 0.9 GeV. There is also no limiting effect from the harmonic cavity during the energy ramp to the final energy.

During the commissioning period of the cryogenic system, the cavity was operated at room temperature. In this operation mode, during periods of cryogenic plant downtime, the cavity is cooled by Helium gas flow or alternatively by purified compressed air. In warm operation the cavity is parked between two revolution frequencies to minimize cavity-beam interaction. However, the beam still deposits a few 100 W in the structure. At high current the interaction with the beam spectrum (Coupled Bunch Modes, CBM's) is sufficient to overheat the cavity, this decreases the cavity frequency and enhances an unstable interaction with CBM 427. It is only possible to compensate this effect at 2.4 GeV, 140 mA; as a consequence users' operations at 2.0 GeV during the commissioning phase were rescheduled at the higher energy.

After commissioning of the cryogenic system, the cavity was successfully cooled and it was possible to see that in the so-called "parked position" the cold cavity is invisible to the beam. Extensive operational experience with the system was acquired during the commissioning period to July 2003. The cryogenic plant has proved to be reliable even though occasionally interrupted by electrical power failures due to bad weather conditions. The possibility to connect the whole system to the uninterruptable power supply of the laboratory is being evaluated.

Since July the cavity has been in routine operation during the users' shifts at 2.0 GeV. The putting into operation of the cavity is optimized to fit the refill process that involves: injection at 0.9 GeV, energy ramping of the storage ring to 2.0 GeV and beam delivery to users.

BEAM STABILIZATION AND LIFETIME IMPROVEMENT

Before installation of the harmonic cavity, ELETTRA used to be operated via a controlled excitation (coherent oscillation) of a longitudinal coupled bunch mode (CBM 91 or 363). This was performed by a fine temperature tuning of one of the 500 MHz normal conducting RF cavities and prevented the onset of transverse multibunch instabilities (prior to installation of the multibunch feedbacks). At the same time this mode of operation also gave an improvement in beam lifetime. By properly control-

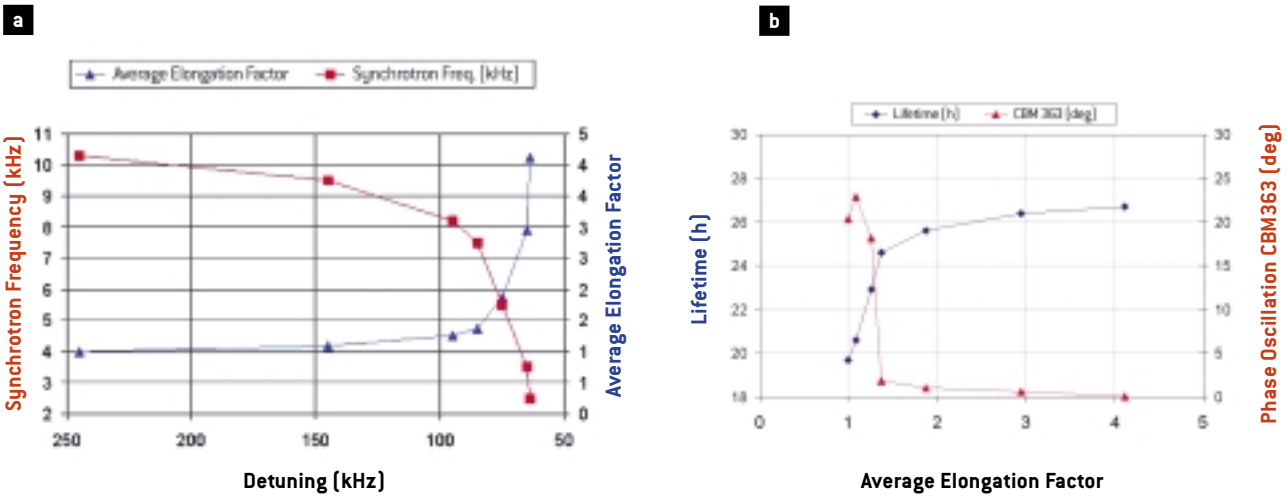

Figure 3. Effects of cavity activation, synchrotron frequency and average elongation factor **a)**, beam lifetime and stabilization **b)**.

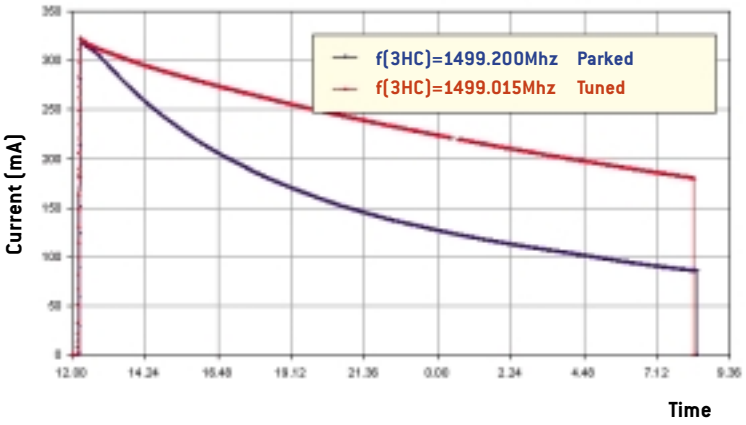

Figure 4. Effects of cavity activation, beam current decay over a day with and without cavity.

ling the instability, the deterioration of the transverse beam emittance was kept at an acceptable level for users.

In discussing the effect of the 3rd harmonic cavity on the beam we recall that although in the starting condition (2,0 GeV, 320 mA and harmonic cavity parked) the beam is transversely stable (due to the feedbacks) it is still longitudinally unstable. A typical activation process of the SUPER-3HC cavity is shown in figures 3 a) and 3 b). The plot in figure 3 a) shows the synchrotron frequency and the related average elongation factor of the bunches versus the cavity detuning frequency. The beam lifetime variation and the reduction in oscillation amplitude of CBM 363 are plotted in figure 3 b) versus the elongation factor. When the cavity is parked, the oscillation amplitude of CBM 363 is greater than 20 degrees and the lifetime is reduced to 19.7 hours as a result of this strong longitudinal instability. The effect of the 3rd harmonic cavity starts to appear at an elongation factor of 1.4 (the detuning at this point is +85 kHz) and CBM 363 starts to be damped. This Landau damping effect increases until the elongation factor reaches a value of three at which point the beam becomes longitudinally stable. Correspondingly, in the example shown, the measured lifetime is 26.7 hours which is 3.5 times the theoretical lifetime for the given storage ring optics. The effect of the 3rd harmonic cavity on the beam current decay is shown in Figure 4, where we compare a day with the 3rd harmonic cavity tuned (beam stable longitudinally) with a day when it is parked (controlled longitudinal excitation).

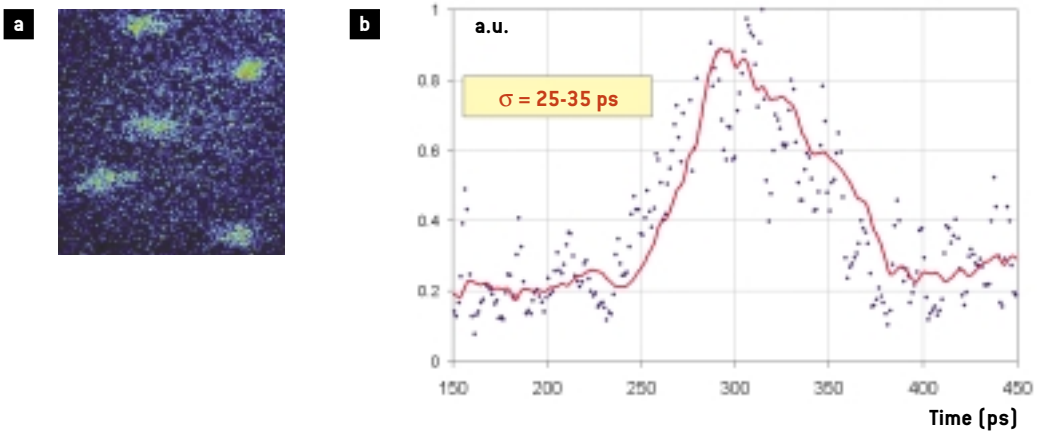

Figure 5. Unstable beam while the cavity is parked: oscillating bunches **a)**, profile of one diluted bunch, length 25 to 35 ps **b)**.

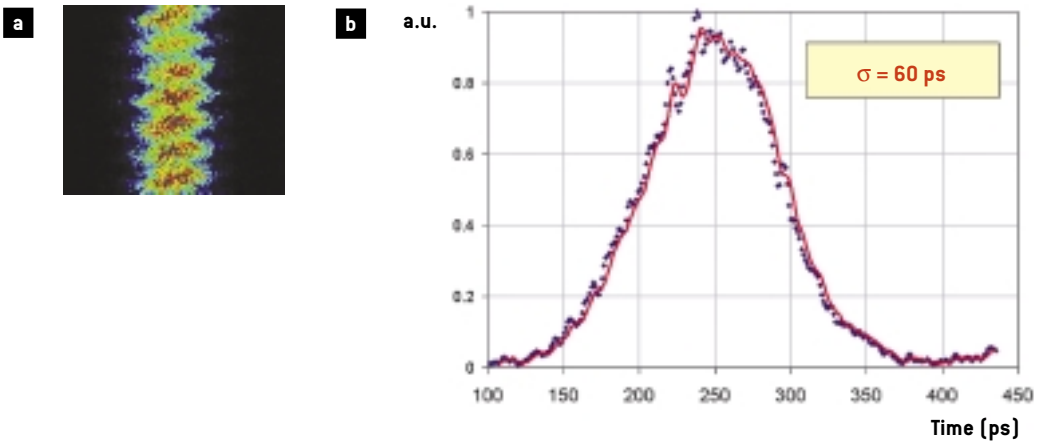

Figure 6. Stable beam with active cavity: stable bunch train **a)**, profile of a lengthened bunch, length 60 ps **b)**.

With the cavity active the final current before the beam dump is doubled with evident benefit to the integrated flux.

The stabilising effect of the cavity is clearly seen in the streak camera images shown in Figures 5 and 6, which have been taken at 250 mA, 2.0 GeV. In Figure 5 a) the beam performs a coherent longitudinal oscillation while the cavity is in its parked position (not active). For the slightly diluted bunches shown in figure 5 a), the average length is between 25 to 35 ps, (Figure 5b). When the cavity is in operation the bunch train becomes stable (Figure 6a). The bunch length, in Figure 6 b), is 60 ps, and is roughly three times the theoretical bunch length i.e. 18 ps. Measurements with the streak camera allow also a characterisation of the phase modulation along the bunch train when a gap of empty buckets is present in the machine. Normally 90% of the 432 buckets are filled, while a gap of about 43 contiguous empty buckets (i.e. 86 ns) is used for ion clearing. This gap induces a phase modulation along the bunch train. Figure 7 shows that, for the minimum detuning of +60 kHz at 320 mA, the phase shift between the first and the last bunch in the train is about 30 degrees. The bunch length changes along the bunch train from 32 ps to 76 ps, with an average value of about 55 ps. The same effect is seen in the streak camera images of Figure 8 where odd and even numbered bunches are mirrored.

CONCLUSIONS

The superconducting 3rd harmonic cavity has been installed and successfully commissioned. Excellent results have been achieved in terms of both an improvement to the beam lifetime, that has increased by up to 3.5 times the theoretical value, and also to the Landau damping of longitudinal instabilities. The SUPER-3HC cavity is in routine operation during User shifts and significantly contributes to the enhancement of beam quality and integrated flux.

ACKNOWLEDGMENTS

The authors would like to thank all colleagues at ELETTRA and at other laboratories which gave a significant contribution to the success of the project.

A particular acknowledgment goes to: P. Marchand of SOLEIL, M. Pedrozzi of SLS,

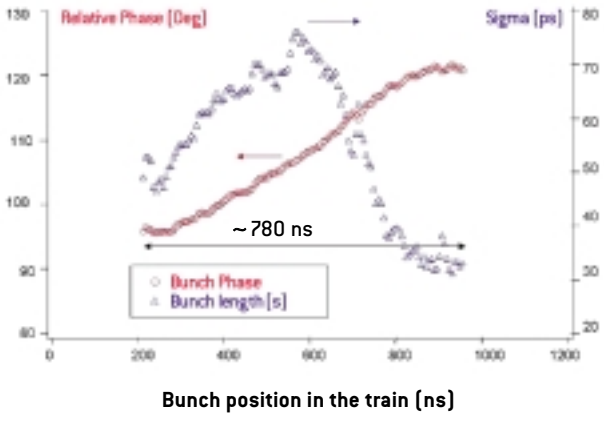

Figure 7. Phase modulation caused by a gap in the bunch train.

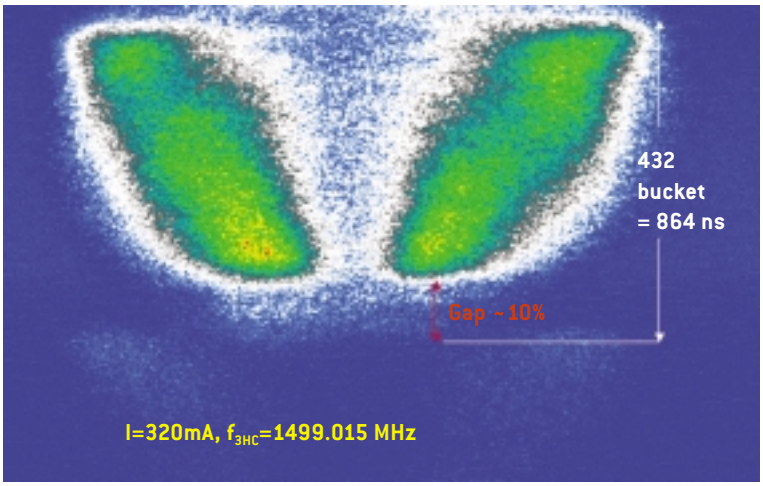

Figure 8. Phase modulation effect as seen on the streak camera.

P. Bosland, P. Bredy, S. Chel, G. Devanz of CEA-SACLAY, A. Anghel of CRPP-EPFL, E. Chiaveri, S. Calatroni, R. Losito, S. Marque of CERN and at ELETTRA, P. Craievich, F. Antoniazzi, L. Battistello, M. Bocciai, M. Chiandone, C. Fava, G. Gaio, A. Gambitta, F. Giacuzzo, M. Giannini, G. Loda, M. Lonza, G. Macho, R. Marizza, D. Morelli, R. Passuello, L. Pivetta, F. Pradal, C. Scafuri, M. Tarlao, E. Turco, R. Visintini, M. Zaccaria, L. Zambon, O. Zoldan.

References

[1] M. Svandrlik et al.; *"The SUPER-3HC Project: an idle superconducting harmoninc cavity for bunch length manipulation";* Proc. European Particle Accelerator Conference, Vienna, Austria, pp. 2052-2054, (2000).

[2] C.J. Bocchetta, *"Machine Status and Developments"*; ELETTRA Highlights 2001-2002, pp. 86-95, (2002).

[3] P. Marchand et al.; *"Cryogenic System for the SLS Third Harmonic RF Cavity"*, Proc. European Particle Accelerator Conference, Paris, France, pp. 2268-2270, (2002).

[4] P. Bosland et al.; *"SUPER-3HC Cryomodule: Layout and First Tests"*, Proc. European Particle Accelerator Conference, Paris, France, pp. 2217-2219, (2002).

FERMI@ELETTRA:
100 NM - 1.2 NM FREE-ELECTRON LASER USER-FACILITY

> R.J. Bakker
Sincrotrone Trieste, S.S. 14, km 163,5 in AREA Science Park, 34012 Basovizza, Trieste, Italy

The FERMI@ELETTRA project is an initiative from ELETTRA, INFM and other Italian institutes, to construct a single-pass Free-Electron Laser (FEL) user-facility for the wavelength range from 100 nm to 1.2 nm next to ELETTRA. It aims to improve the capabilities of the Sincrotrone Trieste S.C.p.A. to levels foreseen for the next generation light-sources. Starting point is the existing 1.2-GeV injector-linac. The merits of this project are:

- Up to nine orders of magnitude higher peak-power (Figure 1).
- Short optical pulses optimized for research of the dynamical properties of materials down to their fundamental limit of femto-seconds.
- A flexible radiation source, similar to the flexibility of a synchrotron.

THE SITE

The site of the project is located along the axis of the existing linac. Free space is available both downstream (1) and upstream (2) of the present infrastructure (Figure 2).

PROJECT STAGES

The project will be implemented in three stages:

1. Construction of a 100 nm to 40 nm FEL with the existing 1.2-GeV S-band linac. Downstream of the linac, the electron is guided to the surface where the undulator- and user hall is located (2, Figure 3).
2. Extension of the wavelength range to 10 nm.
3. Upgrade of the linac to 3-GeV upstream

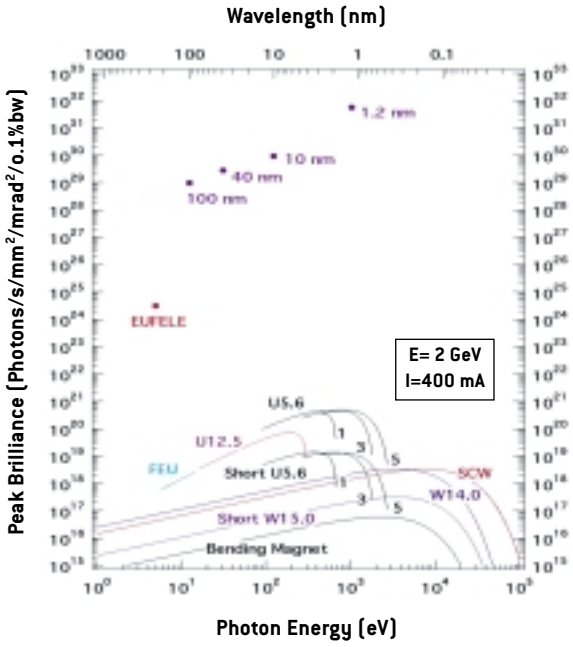

FIGURE 1

FIGURE 2

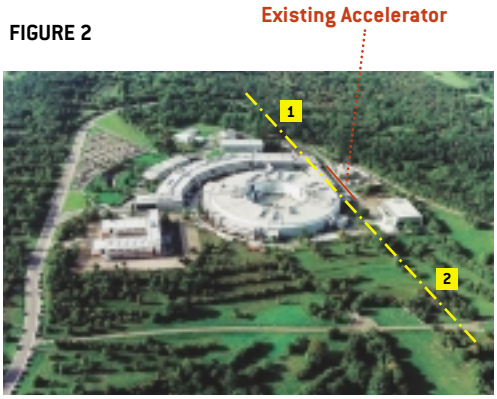

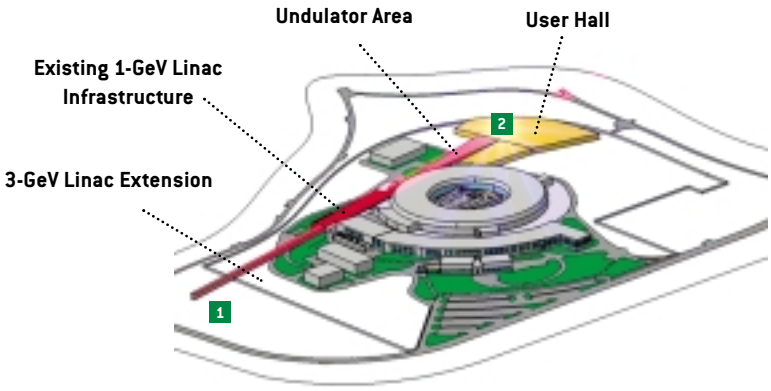

FIGURE 3

of the existing linac (1) to facilitate lasing at 1.24 nm.
For all stages both startup from noise (SASE) and seeded HGHG operation (High-Gain Harmonics Generation) are considered.

THE FIRST STAGE

Presently the implementation of the first stage of the project is planned. Key issues are:

- An upgrade of the linac and the electron gun.
- Implementation of Apple-type undulators for a flexible control of both the wavelength and the polarization.
- Design and implementation of seeding schemes.
- Setup of user-experiments.

MODIFICATIONS TO THE EXISTING LINAC

The existing linac can be transformed into an FEL driver within the existing linac tunnel (Figure 4). The activity issues are:

- Installation of a high brightness electron source in parallel with the present electron gun (1,2).
- The laser driving for the new injector is positioned in an adjacent shielded area (3).
- Moving of two accelerator-sections (6) down-stream to create sufficient space for a magnetic bunch compressor (4,5).
- For phase 2 of the project, i.e., construction of a 10 nm FEL, a second magnetic bunch compressor (7) is needed to boost the beam current into the kA regime.
- The electron beam must be diverted to the surface at the end of the tunnel (8). Simultaneously the linac can fulfill its present task as injector for the storage ring along the tunnel (9).

FIGURE 4 left

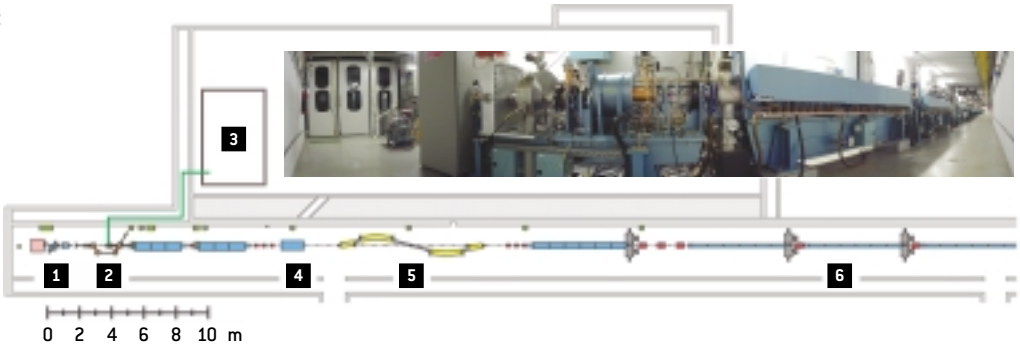

- Minor adjustments to the electron beam optics in the accelerating section as well as the installation of additional diagnostics to monitor electron beam and the bunching process.

A NEW RF PHOTO-INJECTOR

The new RF photo-injector (Figure 5) will be positioned directly behind the linac to obtain the best possible electron-beam quality for FEL operation. In addition the existing electron source will remain operational to guarantee injection into ELETTRA. Since this mode of operation has less restricted demands to the beam-quality, the gun will be moved to a position downstream of the new injector. A double chicane (Figure 6) enables a bypass along the new RF photo-gun into the accelerator.

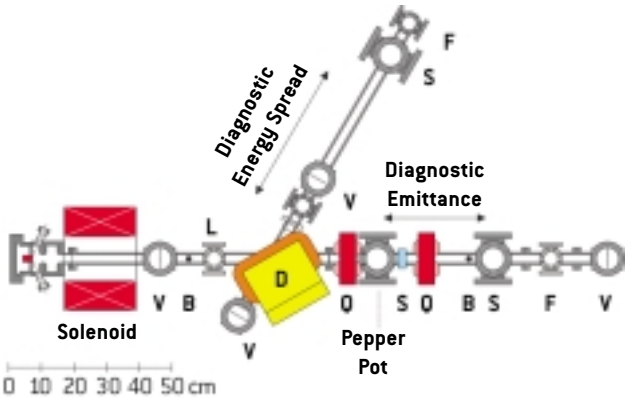

Figure 5. Setup of the stand-alone injector with the RF photo cathode on the left. The major components are labeled: BPM (B), dipole (D), Faraday cup (F), integrated current monitor (I), laser port (L), quadrupole (Q), screen (S), and valve (V).

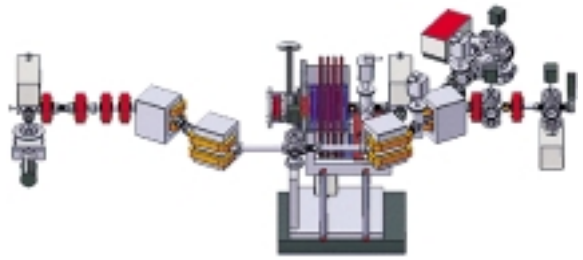

Figure 6. A new RF photo-injector

FIGURE 4 right

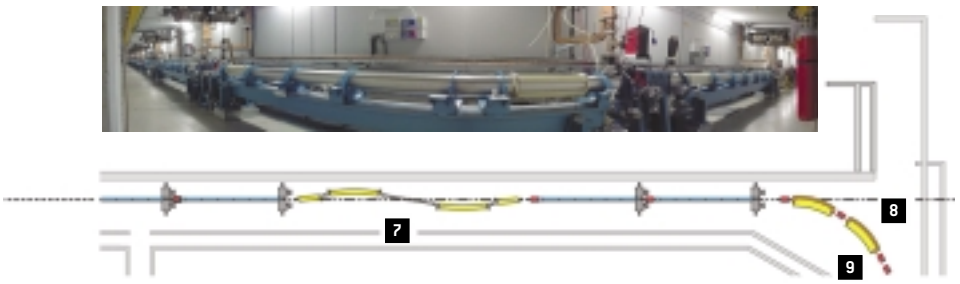

FACTS & FIGURES

ELETTRA BEAMLINE STATUS

(September 2003)

EXIT	BEAMLINE	ACRONYM	PARTNER INSTITUTION
1.2L	Nanospectroscopy		
1.2R	Free-electron Laser	FEL	
2.2L	ESCA Microscopy		
2.2R	SuperESCA		
3.2L	Spectromicroscopy		
3.2R	VUV Photoemission		CNR
4.2	Circularly Polarized Light	POLAR	CNR
5.2L	Small Angle X-ray Scattering	SAXS	Austrian Academy of Sciences
5.2R	X-ray Diffraction	XRD1	CNR
6.1L	Materials Science	MSB	Czech Academy of Sciences, Charles University, Prague
6.1R	SYnchrotron Radiation for MEdical Physics	SYRMEP	University of Trieste
6.2R	Gas Phase		CNR, INFM, INSTM
7.1	Powder Diffraction Beamline	MCX	University of Trento, INSTM
7.2	Advanced Line for Overlayer, Interface and Surface Analysis	ALOISA	INFM
8.1L	Bending magnet for Emission Absorption and Reflectivity	BEAR	INFM
8.1R	Laboratory of Interdisciplinary LIThography	LILIT	CNR, INFM
8.2	Beamline for Advanced DiCHroism	BACH	INFM
9.1	Infrared Synchrotron Radiation Microscopy	IRSR	INFM
9.2	Advanced Photoelectric-effect Experiments	APE	INFM
10.1L	X-ray Microfluorescence		
10.1R	Deep-etch Lithography	DXRL	
10.2	Inelastic Ultra Violet Scattering	IUVS	
11.1	X-ray Absorption Fine Structure	XAFS	ICTP
11.2	X-ray Diffraction	XRD2	

CNR - National Research Council
INFM - National Institute for the Physics of Matter
INFN - National Institute of Nuclear Physics
INSTM - Consortium of Italian Universities for the Science and Technology of Materials

ELETTRA LAYOUT

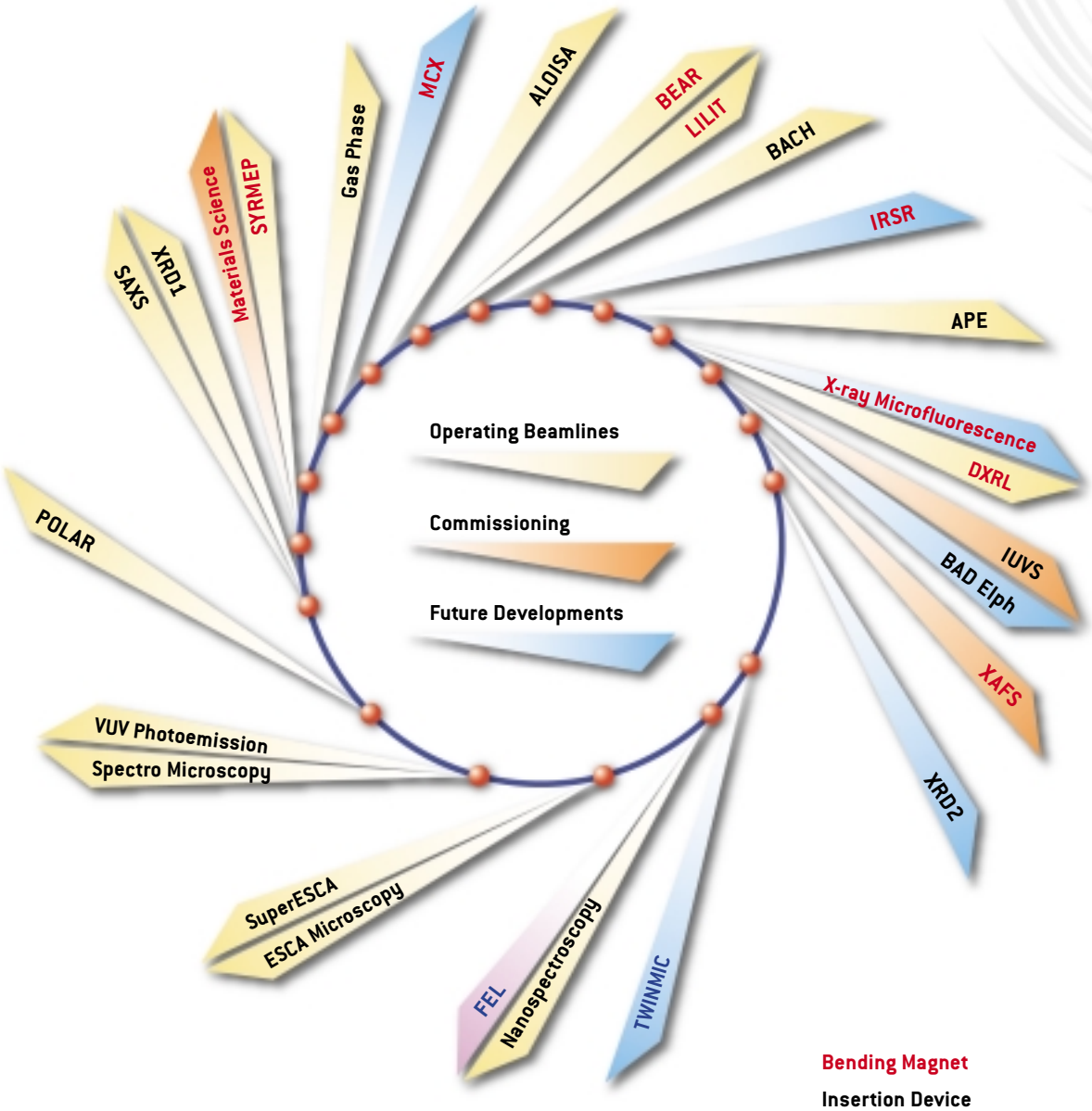

STATISTICS OF PERFORMED MEASUREMENTS

(July 2002 - June 2003)

JULY-DECEMBER 2002

Research Area*	Measurements performed	Shifts used
TOTAL	**143**	**1818**
Atom Molecules and Plasmas	20	258
Catalytic Materials / Surface Sciences	21	353
Environmental and Earth Science	6	42
Hard Condensed Matter - Electronic and Magnetic Structure	23	447
Instrumentation and Technological Materials	5	116
Life and Medical Sciences (excluding Crystallography)	7	121
Protein and Macromolecular Crystallography	31	123
Polymers and Soft Matter	15	186
Hard Condensed Matter - Structure	15	172

** Starting from July 1st 2002, research areas have been updated following more appropriate criteria.*

Measurements Performed

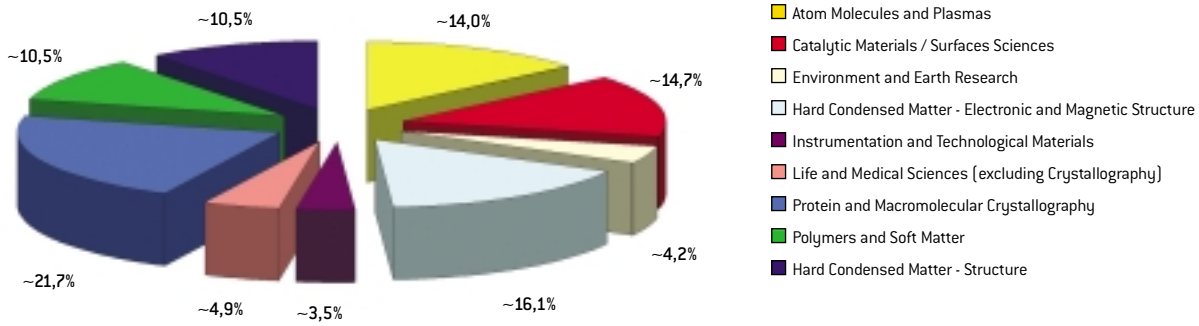

Shifts Used

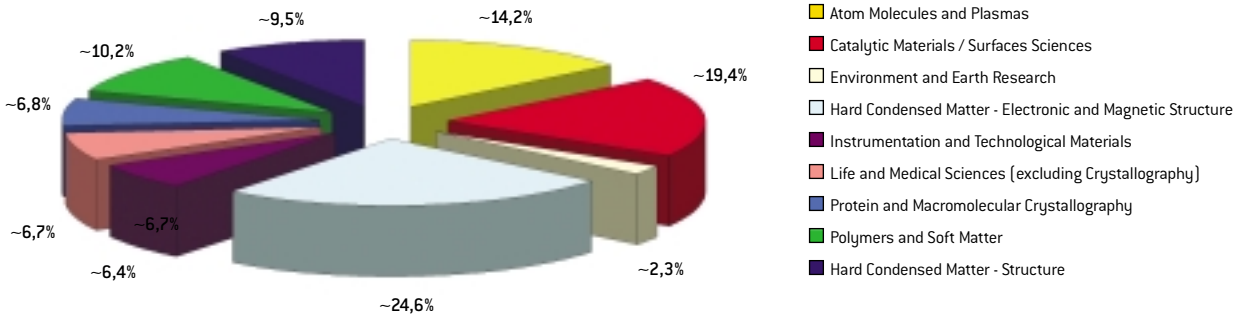

JANUARY-JUNE 2003

Research Area*	Measurements performed	Shifts used
TOTAL	**167**	**2247**
Atom Molecules and Plasmas	26	357
Catalytic Materials / Surface Sciences	28	507
Environmental and Earth Science	4	36
Hard Condensed Matter - Electronic and Magnetic Structure	37	680
Instrumentation and Technological Materials	7	105
Life and Medical Sciences (excluding Crystallography)	12	158
Protein and Macromolecular Crystallography	27	117
Polymers and Soft Matter	6	78
Hard Condensed Matter - Structure	20	209

3 Measurements, with a total of 52 shifts, were performed according to the old categories: physics, life sciences and technology/instrumentation.

Measurements Performed

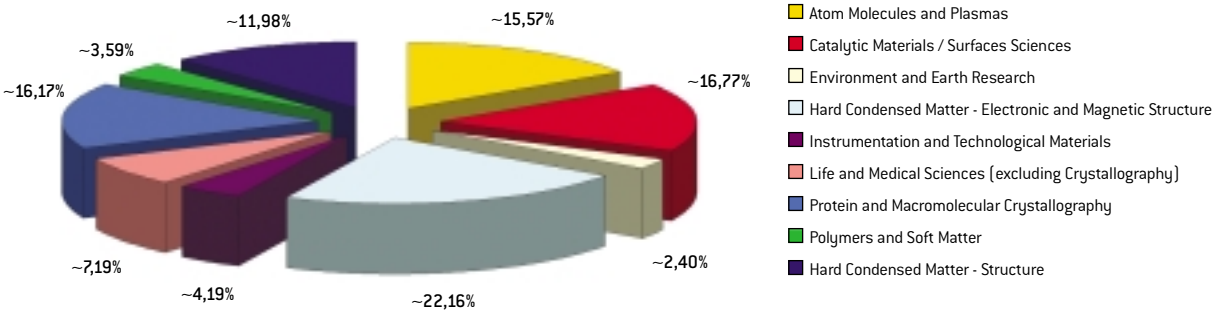

Shifts Used

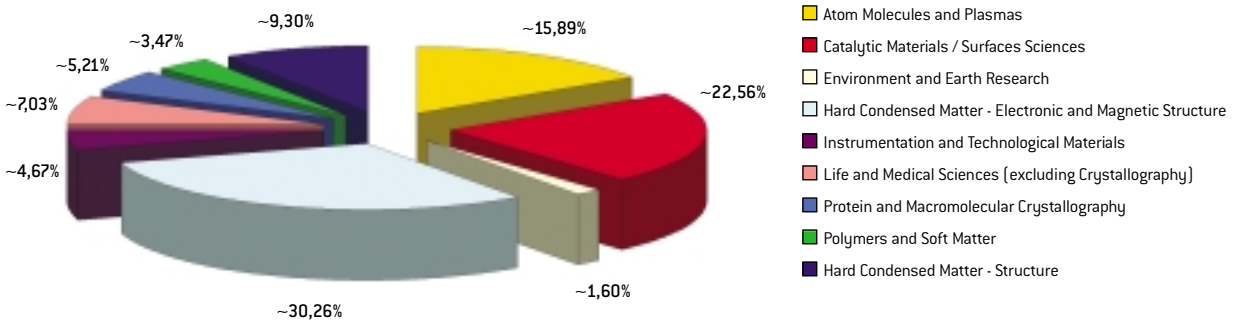

N. USERS
JANUARY-DECEMBER 2002

Total	**841**
Italy	346
European Union	373
Other Countries	122

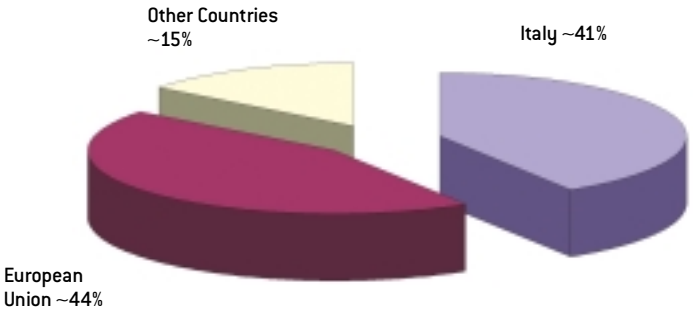

N. USERS
JANUARY-JUNE 2003

Total	**478**
Italy	200
European Union	182
Other Countries	96

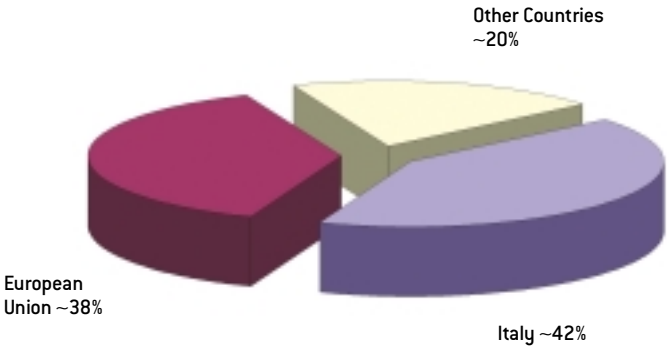

SCIENTISTS FROM DEVELOPING COUNTRIES GAIN ACCESS TO SYNCHROTRON RADIATION

> **Michele Bertolo**, *Sincrotrone Trieste-ELETTRA - S.S. 14 km. 163,5 in AREA Science Park, 34012 Basovizza, Trieste, ITALY*
> **Giovanni Comelli**, *University of Trieste, Trieste, ITALY*

On 23rd November 2001, the International Centre for Theoretical Physics (ICTP) in Trieste, Italy and the Sincrotrone Trieste S.C.p.A. signed an agreement which formed the basis for the ICTP-ELETTRA Users Programme. The mission of the programme is to support access of scientists from developing countries to the synchrotron radiation facility ELETTRA in Trieste for the years 2002-2006.

The allocation of beamtime at ELETTRA for the second semester of 2003 has just been completed, which provides an opportunity to draw up a balance of the first two years of activity of the programme.

The programme was implemented in time to support scientists who had obtained beamtime at ELETTRA in the first semester of 2002 and was announced on the web on 15th February 2002, and duly advertised with a joint ICTP-ELETTRA mailing list, i.e. before the deadline for applications for the second semester of 2002. As can be seen from the graph, the launch of the programme was clearly associated with an increase in the number of beamtime hours allocated to scientists form developing countries, which increased even more in 2003, reaching what appears to be a saturation value of about 1500 hours/semester. This figure corresponds to twice the figure which was envisaged before the launch of the programme (1500 hours/year) and indicates its overwhelming success which was sustained by the generous decision of ICTP to increase its financial support to the programme.

Attention has been devoted also to expanding the range of nations of the supported scientist: the list, which included 4 countries in 2002 (India, Slovenia, Croatia, Belarus), increased to 10 in 2003, with the addition of Brazil, Czech Republic, Moldova, Uruguay, United Arab Emirates, Sultanate of Oman. Particularly noteworthy is the participation of the latter two nations, which belong to the Middle East region, since this marks the potential importance of the ICTP-ELETTRA Users Programme in promoting the training of scientists from that region before SESAME (Synchrotron light for Experimental Science and Applications in the Middle East) begins operation.

For more information on the ICTP-ELETTRA Users Programme, please visit the site http://www.ictp.trieste.it/

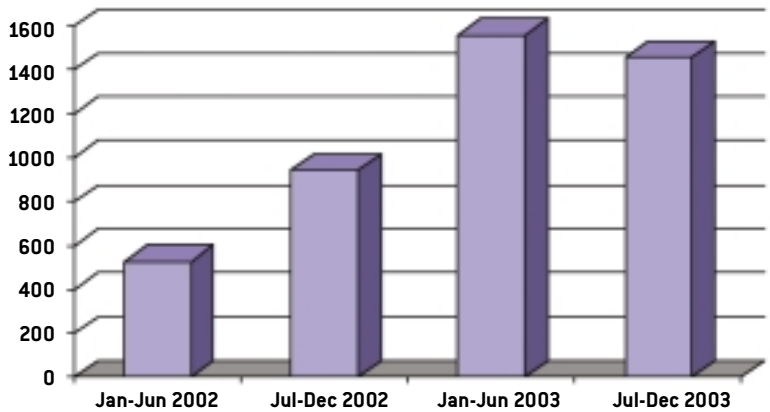

Beamtime hours allocated to scientists from developing countries which received the support of the ICTP-ELETTRA Users Programme

RESOURCES ALLOCATED AT ELETTRA

EXPENDITURE 2002 (MILLIONS OF EURO)

Beamlines, Instruments and In-house Research*	**7,55**
Personnel	3,20
Recurrent	0,75
EU supported projects	1,10
Special Projects	0,10
Investments (new equipment)	2,40

Accelerators	**5,80**
Personnel	3,20
Recurrent	0,50
Investments (new equipment)	2,10

Light Sources	**1,50**
Personnel	0,70
Recurrent	0,30
Investments (new equipment)	0,50

Technical services, Utilities, Buildings and Administration	**13,65**
Personnel	3,60
Recurrent	6,20
Taxes, Adm. Costs	2,30
Investments (new equipment)	1,45
Commercial Activities	0,10

***Additional estimated costs from associated beamline partners (GdR)**	
Personnel	2,12
Recurrent	0,50
Investments (new equipment)	2,80

ELETTRA STAFF

(June 2003)

	Scientists and researchers	Technical personnel	Administrative and clerical personnel	TOTAL
Accelerators sector	12	64	3	**79**
Light sources sector	5	12	1	**18**
Experiments sector	36	33	5	**74**
General services	0	32	11	**43**
Administration	2	9	25	**36**
TOTAL	**55**	**150**	**45**	**250**

Staff Distribution per Sector

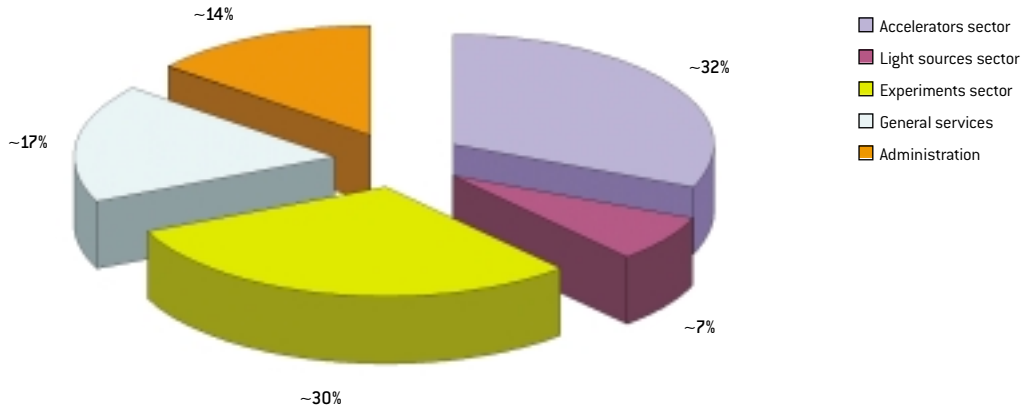

Staff Distribution per Professional Status

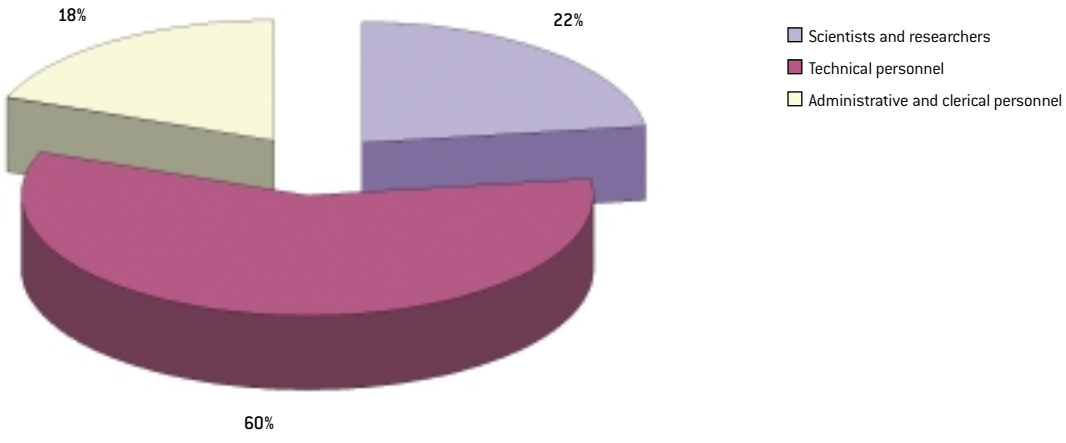

EVENTS

SATELLITE WORKSHOP ON "ULTRAFAST PHENOMENA BY SYNCHROTRON RADIATION"
(TENTH USERS' MEETING, 2002)

> F. Parmigiani
INFM-TASC, Beamline BACH at ELETTRA, Basovizza, Trieste, ITALY
Dipartimento di Matematica e Fisica, Università Cattolica del Sacro Cuore, Brescia, ITALY

> K. C. Prince
Sincrotrone Trieste-ELETTRA - S.S. 14, Km 163,5 in AREA Science Park, 34012 Basovizza, Trieste, ITALY

Looking toward the immediate future, X-ray Free Electron Laser (FEL) sources offer exciting new prospects for future science. These radiation sources differ from conventional lasers in using a relativistic electron beam as its lasing medium, as opposed to bound atomic or molecular states, hence the term "free electron".

FEL facilities are essential for exploring matter using intense and ultrashort (femtosecond) coherent X-ray beams. The knowledge gained from operations of these facilities is critical for providing assessment of many driving forces of science for new experiments in the non-linear regime and the time resolved domain.

In this light the Elettra Users' Meeting, held from October 28-30, 2002, has focused one of the two intensive one-day workshops on "Ultrafast phenomena by Synchrotron Radiation" .

The workshop was opened by D. von der Linde (University of Essen, Germany). He described time domain observations of phonon dynamics, using laboratory based radiation sources, with fast x-ray pulses generated by laser pulses. New insights into the optical phonon modes of bismuth and other materials can be attained in this way. A. Cavalleri (LBNL, Berkeley, USA) continued with studies of vanadium oxide (VO2) which undergoes an insulator-to-metal transition: the big question in this case is the time scale for the dynamics of the transition, and whether it can occur on electronic or atomic vibrational time scales. This question was examined using pulsed laser plasma x-rays and synchrotron radiation to measure the time resolved x-ray absorption spectrum at the vanadium L edge.

Other speakers addressed issues as diverse as the design of new machines for ultrafast studies (W. Barletta), magnetic phenomena (H.C. Siegmann, C.H. Back and D. Pescia) and the possibility of performing X-ray diffraction on a single protein molecule (J. Hajdu.)

The workshop was particularly useful to assess the state of the art of ultrafast spectroscopy, the FEL science case in the VUV and soft X-ray and the capability to deliver tunable, coherent, high power radiation pulses. In particular, seeded FEL sources can have the optical properties characteristic of conventional lasers such as high spatial coherence and a near diffraction limited radiation beam.

All in all, the workshop concluded that there is a strong case for constructing new light sources and that there is much new science to be done.

SATELLITE WORKSHOP ON "PROPERTIES OF MAGNETIC NANOSTRUCTURES" (TENTH USERS' MEETING, 2002)

> G. Panaccione
INFM, Beamline APE, ELETTRA S.S. 14 km 163,5 in AREA Science Park, 34012 Basovizza, Trieste, ITALY

The second satellite workshop of the 9th Users' Meeting, "Properties of Magnetic Nanostructures", chaired by Giancarlo Panaccione, took place on October 30, 2002.

It was opened by the talk of S. Bluegel (IFF-Julich, Germany), who discussed current theoretical progress in describing magnetic properties, such as the size of magnetic moments, the magnetic structure and the magnetisation direction, in the spatial limit.

Results from magnetic STM/STS experiments on nanometer-scale structures were presented by M. Bode (IAP-Hamburg, Germany).

K. Kern (Max Planck- Stuttgart, Germany) illustrated X-ray circular dichroism and STM studies on surfaces nanostructures.

D. Gatteschi (Univ. Florence, INSTM, Italy) introduced the new and fascinating field of Molecular Magnets, which attracts largely increasing interest, as it promises the development of new, unconventional magnetic materials.

The role of spin precession in electron transmission through a ferromagnet was described by W. Weber (IPCMS, Strasbourg, Germany). A detailed understanding of the involved magnetic momentum transfer processes is fundamental for the application of nano-sized magnetic structures.

The significance and future perspectives of magnetic imaging with PEEM and LEEM were discussed by J. Stöhr (SSRL, US) and W. Kuch (Max-Planck, Halle, Germany).

J. Vogel (CNRS, Grenoble, France) presented the first time resolved PEEM studies of magnetisation dynamics at the nanosecond scale, a further important topic for technological application.

1

2

3

TENTH USERS' MEETING (October 28-30, 2002)

1. *Smiling organizing committee.*
2. *A presentation held by D. von der Linde – Phase Transformations and Lattice Dynamics Studied by Femtosecond X-Ray Diffraction.*
3. *Social dinner in a typical Karstic restaurant.*

1

2

3

JOURNALISTS AT ELETTRA

1. *Carlo Rizzuto, President of the Sincrotrone Trieste, inteviewed by a journalist of the Suisse Television (January 24, 2003).*
2. *Giorgio Paolucci, Director of the Experiments Sector, interviewed for a TV programme on medicine (February 19, 2003).*
3. *Managing Director, Massimo Altarelli (left) with Daniel Clery (right), journalist of Science (March 6, 2003).*

1

2

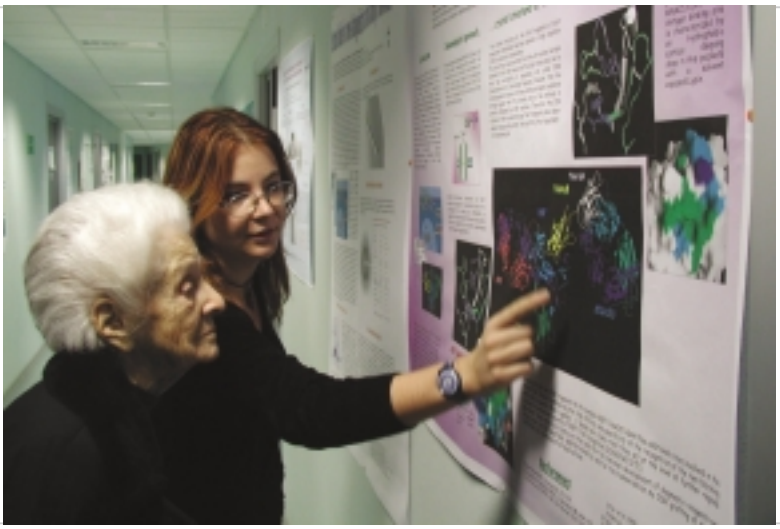

3

NOBEL PRIZES

In the last year the Laboratory has been visited by three winners of the Nobel Prize:

1. *Paul Nurse (Nobel Prize in Physiology or Medicine) during a visit to the XRD1 beamline (October 11, 2002) .*
2. *Rita Levi Montalcini (Nobel Prize in Physiology or Medicine) during her tour at the Cristallography Labs. (November 22, 2002)*
3. *Burton Richter (second from left), Nobel Prize in Physics, with Carlo J. Bocchetta (second from right), Director of the Accelerators Sector (January, 23, 2003).*

1

2

3

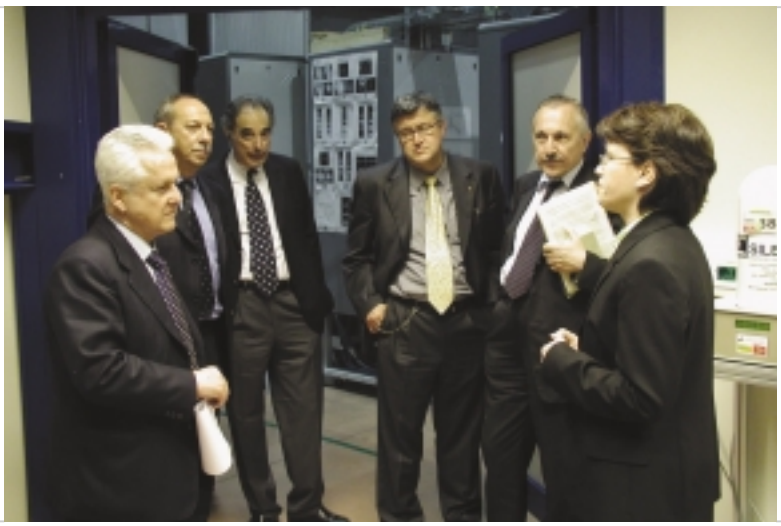

AUTHORITIES...

1. *Vice-ambassador Singh from India, in front of a dipole and a quadrupole magnet (February 21, 2003).*
2. *A delegation of the Croatian Minister of Science and Technology at the APE beamline (February 24, 2003).*
3. *Guido Possa (left), Vice-Minister of Education, University and Research, at the SYRMEP beamline (May 9, 2003).*

1

2

3

... AND UNIVERSITIES

1. *University of Milan "Bicocca" (March 28, 2003).*
2. *University of Trieste. Students of the Postgraduate Specialization School in Archaeology (May 16, 2003).*
3. *University of Bologna. Students of the Department of Chemistry (May 29, 2003).*

1

2

WORKSHOPS

1. *Participants to the 3rd Machine Workshop –SESAME– (December 9-13, 2002).*
2. *Participants to the ICTP-INFM Spring School on "Magnetic Properties of Condensed Matter Investigared by Neutron Scattering and Synchrotron Radiation" (May 19-28, 2003).*

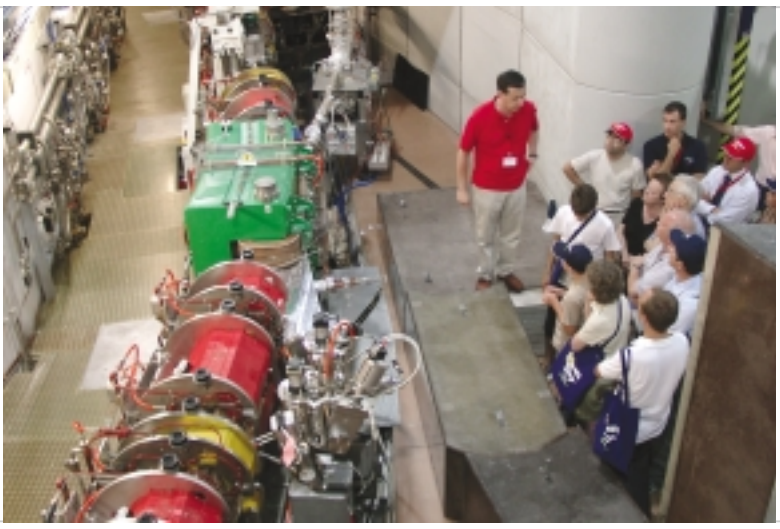

OPEN DAY

The Open Day (June 28, 2003) was organized together with the AREA Science Park Consortium.
Visitors, from the Region, from other Italian regions, as well as from neighbouring countries, had the possibility to take a look at many of the organizations/companies located in the AREA Science Park. Among them, ELETTRA was visited by almost 1000 people throughout the day, who had the exceptional opportunity to see two sections of the ring opened for the event.

AUTHOR INDEX

AREA Science Park

a world for research and innovation

AREA Science Park enjoys a geographic location at hub of an economic area in expansion, between the European single market and the emerging countries of Central-East Europe.
As a system that brings together the worlds of research and business enterprises, AREA is the largest science and technological park in Italy.
The Park is in continuous growth, and comprises over 70 companies and research centres, both national and international, where 1600 persons are engaged in R&D, technology transfer, training and specialised services.
Alongside basic research in physics, material structures, genomics and biotechnology, there is an ever- broadening range of research aimed at applications in the pharmaceutical, automotive, microelectronics, information science, food and space.
AREA is a national research body, under the aegis of the Italian Ministry of the Education, University and Research.
Its mission is:

- the development of the Park, both on a national and international perspective
- exploiting research activities and fostering the dissemination of technological innovation

- offering advanced training for the innovation of enterprises.

Excellence is AREA's key-word: in particular in Molecular Biomedicine – a brand new system of laboratories to be opened soon – and in Technology Transfer to enterprises.
Today, AREA Science Park is a major resource for the entire Friuli Venezia Giulia region, a stimulating specialised environment where scientists of different cultures and nationalities work in synergy with enterprises and with financial and economic organisations, to support local growth based on technological development and innovation.

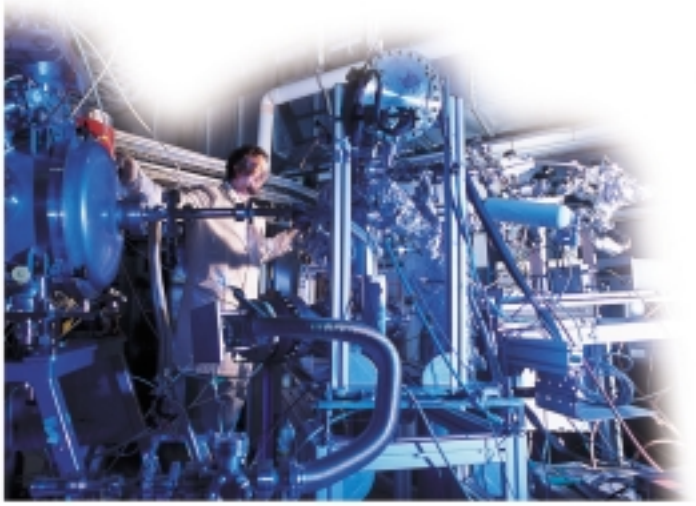

AREA
SciencePark

AREA Science Park
Padriciano 99, 34012 Trieste
Phone (39) 040 375 5111 Fax (39) 040 226698
http://www.area.trieste.it
e-mail: info@area.trieste.it

Sincrotrone Trieste SCpA
S.S. 14 Km. 163,5 in AREA Science Park
34012 Basovizza (Trieste) ITALY
www.elettra.trieste.it - info@elettra.trieste.it